Identification of Unsteady Flight Dynamic Models and Model-based Wind Estimation with Flight Test Validation

Mekonen Haileselassie Halefom

Dissertation submitted to the Faculty of the
Virginia Polytechnic Institute and State University
in partial fulfillment of the requirements for the degree of

Doctor of Philosophy
in
Aerospace Engineering

Craig A. Woolsey, Chair
Mayuresh Patil
Mark L. Psiaki
Shane D. Ross

April 29, 2024
Blacksburg, Virginia

Keywords: Unsteady Flight Dynamics, Aircraft System Identification, Wind Estimation, small Uncrewed Aircraft Systems (UAS), small Unmanned Aircraft Systems (UAS)

Identification of Unsteady Flight Dynamic Models and Model-based Wind Estimation with Flight Test Validation

Mekonen Haileselassie Halefom

ABSTRACT

Numerical weather modeling can benefit from improved wind sensing in the Earth's atmospheric boundary layer (ABL). Small, low-cost, uncrewed aircraft (drones) can be used to measure wind and a distribution of these vehicles could potentially provide measurements with much greater density and resolution, in both space and time, than current methods allow. To measure wind, a drone could be equipped with dedicated wind-measuring sensors, although these can be costly and obtrusive and must be carefully calibrated to account for interference effects. State estimation algorithms that combine a drone's operational measurements with a flight dynamic model can be used to infer wind without a dedicated wind sensor, although the sensor quality affects measurement accuracy. Previous studies have explored the effects of various sensors on wind estimate accuracy, but the effect of flight dynamic model fidelity has received less attention. This dissertation presents analysis of different aerodynamic model-free and model-based wind estimation methods, comparing six wind estimation formulations using experimental flight data from a small, fixed-wing aircraft. Each formulation is implemented using a Kalman filter, an extended Kalman filter, and an unscented Kalman filter. These filters are designed based on different assumptions related to the flight dynamic model, available sensors, and available measurements. Having identified a promising estimation approach, the dissertation next explores the value of incorporating unsteady effects into a flight dynamic model for model-based wind estimation.

An unsteady aerodynamic model for a small, fixed-wing aircraft is developed, identified, and validated using experimental flight data. An extended Kalman filter is then designed and implemented for two motion models – one that includes unsteady effects and another that does not. Analysis of the wind estimates and the estimation differences show that, while the unsteady flight dynamic model better predicts the aircraft motion, the value of incorporating this model for wind estimation is questionable.

Identification of Unsteady Flight Dynamic Models and Model-based Wind Estimation with Flight Test Validation

Mekonen Haileselassie Halefom

GENERAL AUDIENCE ABSTRACT

Wind velocity sensing is crucial to understanding the meteorological processes at low altitudes. The integration of low-cost drones has allowed them to be used as wind-sensing platforms. This is achieved by equipping small drones with dedicated wind-measuring sensors, often costly and infeasible, or inferring wind velocity from the drone's motion. Algorithms designed to infer wind can be used by combining onboard flight sensor measurements with a drone's flight dynamic model to infer wind. However, low-cost drones are usually equipped with low-cost flight sensors, which frequently lead to higher measurement uncertainty and degrade the accuracy of wind estimates. Previous studies have explored the effects of various sensors on wind estimates, but errors due to low-fidelity dynamic models have received less attention. This dissertation first presents a detailed analysis of different flight dynamic model-free and model-based wind estimation methods. It compares six wind estimation formulations. Each formulation is implemented in wind inferring algorithms called a Kalman filter, an extended Kalman filter, and an unscented Kalman filter. These algorithms are designed based on different assumptions related to the flight dynamic model, available flight sensors, and available measurements. Secondly, the value of incorporating a fixed-wing, unsteady flight dynamic model in a wind estimation scheme is analyzed. To this end, an unsteady flight dynamic model for a fixed-wing drone is developed, identified, and validated from data acquired from the drone's flight history. Furthermore, an extended Kalman filter is designed and implemented for two motion models – one that includes unsteady effects and another that does not. The analysis of the time histories of the wind estimates and the wind estimate differences show that both model-based estimators perform equally well.

To my beloved Aunt Minia, who has always believed in me.

Acknowledgments

I would like to express my sincere gratitude to the esteemed members of my Ph.D. committee, Dr. Craig Woolsey, Dr. Mayuresh Patil, Dr. Mark Psiaki, and Dr. Shane Ross, for their invaluable guidance, unwavering support, and encouragement throughout my academic journey. Their mentorship has been instrumental to my success, and I am deeply grateful for their contributions. I would like to convey my appreciation to Dr. Craig Woolsey for his exceptional mentorship, unwavering support, and invaluable guidance. Dr. Woolsey's dedication to advising has played a vital role in shaping my professional growth. I am equally indebted to Dr. Mayuresh Patil for his remarkable mentorship and support throughout my Ph.D. journey. Dr. Patil's insightful guidance and scholarly expertise have significantly shaped my research, and I am sincerely appreciative of his mentorship. I extend my earnest appreciation to Dr. Mark Psiaki for his exceptional teaching and invaluable contributions as a committee member. Dr. Psiaki's profound insights, scholarly guidance, and support have enriched my research journey, and I am profoundly grateful for his mentorship. I am incredibly thankful to Dr. Shane Ross for his support and guidance as a committee member. Dr. Ross's expertise and encouragement have been invaluable throughout my Ph.D. journey.

I want to express my deepest gratitude to my father, Haileselassie Halefom, for his unwavering belief in my abilities and constant encouragement. His guidance and support have inspired me throughout my professional journey, and I am profoundly grateful for his love, wisdom, and encouragement. I am equally thankful to my mother, Aida Gabriel, for her unwavering advocacy and relentless support in all my academic pursuits. Her belief in my potential and tireless efforts to champion my aspirations have been instrumental in all my achievements. I sincerely appreciate her love, encouragement, and unwavering support. I also extend my heartfelt appreciation to my sister, Lula Haileselassie, for her constant support and unwavering belief in my abilities. Her encouragement and belief in me have been a source of motivation and strength, and I am profoundly grateful for her unwavering support, love, and encouragement.

To the love of my life, Hana Ayalew, words cannot fully capture the depth of my gratitude for your unwavering support, belief, and constant encouragement. Your love and support have been my guiding light, especially through the hardest and toughest times. Thank you, Hani, for standing by my side and believing in me even when I doubted myself. Your strength and love have given me the courage to persevere and the motivation to strive for my best. I am forever grateful to have you in my life.

I extend my heartfelt gratitude to my family for their unwavering support throughout my academic journey. To my beloved uncles, aunts, and cousins, your encouragement have been a constant source of strength and inspiration. Your presence in my life has filled it with warmth, laughter, and love, making every challenge easier to overcome and every success sweeter to celebrate. I am profoundly grateful for the invaluable role you have played in shaping both my academic endeavors and my character.

I am immensely grateful to my cherished friends who have stood by my side throughout my academic journey. Your unwavering support, encouragement, and camaraderie have been a constant source of strength and inspiration. Whether through late-night study sessions, brainstorming ideas, or simply being there to lift my spirits during challenging times, you have been my pillars of support. Your friendship has enriched my life in countless ways, and I am deeply thankful for the laughter, memories, and shared experiences we have cherished together. Your friendship has made my academic pursuits more fulfilling and enjoyable, and I am profoundly grateful for your presence in my life.

I am deeply grateful to my esteemed colleagues from the Nonlinear System Laboratory (NSL), who have been my companions throughout the exhilarating and rigorous pursuit of our Ph.D. degrees, research collaborations, and flight tests at the KEAS Lab. I would like to extend my special appreciation to Dr. Javier González-Rocha, Dr. Jean-Michel Fahmi, Dr. Benjamin Simmons, Jeremy Hopwood, Dr. Nazmus Sakib, Dr. Zakia Ahmed, Mohamed Zakaria, Maj Chris “Hula” Gahan, Dennis Marquis, LtCol James ”Nut” Gresham, Ian Wilebeek-LeMair, Dr. Ying-Chun Chen, and Dr. Hisham Shehata for their invaluable contributions to our shared work.

I would also like to express my gratitude to my colleagues at the Center for the Enhancement of Engineering Diversity (CEED), including Dr. Bevlee Watford, Dr. Tremayne O. Waller, Dr. Kim Lester, Dr. DeAnna Katey, Dr. Karis Boyd-Sinkler, Susan Arnold Christian, and Dr. Ashley Taylor, for their unwavering support and encouragement. Their guidance and mentorship have been instrumental in shaping my personal and professional growth.

Contents

List of Figures **xvii**

List of Tables **xxii**

List of Abbreviations **xxiv**

1 Introduction **1**

1.1 Motivation 1

1.2 General Background 4

1.3 Identified Gaps in Literature 6

1.4 Research Contributions 7

1.5 Outline of Dissertation 8

2 Background **10**

2.1 Relevant Mathematical Operations 10

2.1.1 Scalar and Vector Product, Transpose, and Identity Matrix 11

2.1.2 Determinant, Cofactor, Adjoint, and Inverse of Square Matrix 12

2.1.3 Laplace Transform, and the Convolution Integral 14

2.2 System Dynamics 15

2.2.1 Nonlinear Systems 15

2.2.2 Linearization 16

2.2.3 Discretization 17

2.2.4 Process and Measurement Noise Statistics 19

2.2.5 Observability 19

2.3 Particle Dynamics 20

2.3.1 Coordinate Frames 20

2.3.2 Change of Coordinate Frames 21

2.3.3 Rotating Coordinate Frame 23

2.3.4 Velocity and Acceleration in an Arbitrarily Moving Frame 24

2.3.5 Translational and Rotational Dyanmics 26

2.4 Aircraft Equations of Motion 30

2.4.1 Reference Frames 31

2.4.2 Rotation Matrix Parameterization 32

2.4.3 Rigid Body Equations of Motion 34

2.4.4 Air-relative Velocities and Aerodynamic Angles and Forces 40

2.4.5 Aerodynamic Force and Moment 41

2.4.6 Equations of Motion in Wind 42

2.5 Wind Velocity 44

2.5.1 Wind Velocity Vector Field 44

2.5.2 Atmospheric Turbulence 45
2.5.3 Rate of Change of Wind 46

3 Literature Review **49**

3.1 Unsteady Aerodynamics Models 49
3.1.1 Two Dimensional Unsteady Models 53
3.1.2 Three Dimensional Unsteady Models 56
3.1.3 Reduced Order-Model Unsteady Model 60
3.2 Wind Velocity State Estimation 63
3.2.1 Model-based Wind Estimation Methods 64
3.2.2 Model-Free Wind Estimation Methods 68
3.2.3 Combined Wind Estimation Methods 70

4 General Flight Test Experiments **71**

4.1 Experiment Locations and Facilities 71
4.1.1 Kentland Experimental Aerial System (KEAS) Laboratory 72
4.1.2 Open Jet Wind Tunnel 73
4.2 Research Aircraft 74
4.2.1 Aircraft Parameters 75
4.2.2 Aircraft Instruments 75
4.3 Flight Operations 78

4.3.1 Pilot Certification and FAA Waiver 79

4.3.2 QgroundControl and Operation Checklist 80

5 Aircraft System Identification **83**

5.1 Input Design and Data Processing 84

5.1.1 Input Design 84

5.1.2 Data Processing 85

5.2 Data Compatibility 86

5.2.1 Kinematic Consistency 86

5.2.2 Collinearity Diagnostics 87

5.3 Model Structure Determination 88

5.3.1 Nonlinear Aerodynamic Model 89

5.3.2 Unsteady and Quasi-steady Aerodynamic Model 92

5.4 Parameter Identification and Validation 96

5.4.1 Nonlinear Aerodynamic Model 97

5.4.2 Unsteady and Quasi-steady Aerodynamic Models 97

5.4.3 Propulsion Model 99

5.5 Conclusion 103

6 Comparison of Aerodynamic Model-free and Model-based Wind Estimators **105**

6.1 Introduction . . . 106

6.2 Wind Estimation Methods . . . 107

  6.2.1 Aircraft Nonlinear Aerodynamic Model . . . 108

  6.2.2 Wind Estimation Formulations . . . 109

  6.2.3 Estimation Algorithms . . . 114

  6.2.4 Wind Estimation Experiment Flight . . . 117

6.3 Results and Analysis . . . 118

  6.3.1 Filter Setup . . . 119

  6.3.2 General Observations . . . 119

  6.3.3 Error Analysis . . . 124

6.4 Conclusion . . . 128

7 Unsteady Aerodynamics in Estimation 130

7.1 Introduction . . . 130

7.2 Wind Velocity Estimation . . . 132

  7.2.1 Unsteady and Quais-steady Aerodynamic Equations . . . 133

  7.2.2 Augmented Equations of Motion with Wind Disturbance . . . 134

  7.2.3 Measurement Model . . . 136

  7.2.4 Continuous-discrete Extended Kalman Filter . . . 136

7.3 Flight Experiment . . . 139

7.3.1 Experimental Flight Profile 139

7.3.2 Wind Reconstruction from ADU Measurements 140

7.3.3 Reconstructed Wind Results and Analysis 141

7.4 Results and Discussion 143

7.5 Conclusion 149

8 Conclusion **150**

Appendices **153**

Appendix A Modeling and Identification of Unsteady Dynamics from an Artificial Gust Generator **154**

A.1 Introduction 155

A.2 Unsteady Aerodynamic Theoretical Background 156

A.2.1 Unsteady Aerodynamics of a Flat Plate 156

A.2.2 Linear, Unsteady Aerodynamic Model Structure for a Fixed-wing Aircraft 160

A.3 System Identification of the Aerodynamic Parameters 162

A.3.1 System Identification of the Quasi-steady Aerodynamic Coefficients . 162

A.3.2 System Identification of the Empirical Transfer Functions 163

A.4 Flight Test Setup 167

A.4.1 Flight Test Inputs 167

A.4.2 Aircraft Trim Configuration 169

A.4.3 Artificial Gust Generator (AGG) 169

A.4.4 Wind Conditions for Training and Validation Flight 171

A.5 Results and Discussion 174

A.5.1 Quasi-steady Aerodynamic Parameters 174

A.5.2 Unsteady Aerodynamic Parameters 176

A.5.3 Quasi-Steady and Unsteady Aerodynamic Model Predictions in Natural Wind 181

A.6 Conclusion 183

Appendix B Kalman Filter, Extended Kalman Filter, and Unscented Kalman Filter Algorithms 185

Appendix C MTD sUAS Flight Checklist 188

Bibliography 191

List of Figures

1.1 Weather Intelligent Navigation Data and Models for Aviation Planning (WINDMAP) [1]. Image taken from [2]. 3

1.2 Indirect wind estimation method 4

1.3 System identification diagram 6

3.1 Example of aerodynamic models 50

3.2 Airfoil moving through still air 50

3.3 Coefficient of lift and angle of attack 52

3.4 Airfoil moving through upward wind gust 54

3.5 Airfoil pitching about an axis point in unifrom flow 55

4.1 Photographs of KEAS laboratory airstrip and facility 73

4.2 MTD2 instrument test 74

4.3 My twin dream (MTD) 2 aircraft 76

4.4 Frequency response of (a) angle of attack and (b) flank angle vanes. 77

4.5 KEAS laboratory airspace map 80

4.6 Example of QgroundControl telemetry interface 81

5.1 Multisine and doublet inputs. 85

5.2 Sensor correction based on kinematic consistency results. The non-corrected values are shown in black, while the corrected values are indicated by a red dashed line. 88

5.3 Regressor cross plots and pairwise correlations 89

5.4 Model terms selected for C_X and C_Y coefficient of the nonlinear aerodynamic model. The red line indicates the selection threshold. 90

5.5 Model terms selected for C_z and C_l coefficient of the nonlinear aerodynamic model. The red line indicates the selection threshold. 91

5.6 Model terms selected for C_m and C_n coefficient of the nonlinear aerodynamic model. The red line indicates the selection threshold. 91

5.7 Model terms selected for C_X and C_Y coefficient of the quasi-steady and unsteady aerodynamic model. The red line indicates the selection threshold. . . 93

5.8 Model terms selected for C_z and C_l coefficient of the quasi-steady and unsteady aerodynamic model. The red line indicates the selection threshold. . . 94

5.9 Model terms selected for C_m and C_n coefficient of the quasi-steady and unsteady aerodynamic model. The red line indicates the selection threshold. . . 94

5.10 Output validation results from an elevator doublet maneuver. The flight data are given in black, and output predictions are given in the red dashed line. . 98

5.11 Quasi-steady and unsteady aerodynamic model validation 102

6.1 Experimental flight profiles. 118

6.2 Formulation 1 wind velocity estimates. The reconstructed wind is given in black, the KF-based wind estimate is given in blue, the EKF-based wind estimate is given in orange, and the UKF-based wind estimate is given in gold. 124

6.3 Formulation 2 wind velocity estimates. The reconstructed wind is given in black, the KF-based wind estimate is given in blue, the EKF-based wind estimate is given in orange, and the UKF-based wind estimate is given in gold. 125

6.4 Formulation 3 wind velocity estimates. The reconstructed wind is given in black, the KF-based wind estimate is given in blue, the EKF-based wind estimate is given in orange, and the UKF-based wind estimate is given in gold. 125

6.5 Formulation 4 wind velocity estimates. The reconstructed wind is given in black, the KF-based wind estimate is given in blue, the EKF-based wind estimate is given in orange, and the UKF-based wind estimate is given in gold 126

6.6 Formulation 5 wind velocity estimates. The reconstructed wind is given in black, the KF-based wind estimate is given in blue, the EKF-based wind estimate is given in orange, and the UKF-based wind estimate is given in gold 126

6.7 Formulation 6 wind velocity estimates. The reconstructed wind is given in black, the KF-based wind estimate is given in blue, the EKF-based wind estimate is given in orange, and the UKF-based wind estimate is given in gold 127

7.1 (a) Experimental flight profile. (b) The green dots indicate the aircraft's horizontal speed, the blue dots indicate the horizontal wind speed and direction, and the red dot indicates the wind's mean velocity and direction. 140

7.2 (a) Wind velocity components reconstructed from ADU measurements. (b) Power spectra of the reconstructed wind velocity components. 142

7.3 Reconstructed and estimated wind component time histories for north/south flight. 145

7.4 Reconstructed and estimated wind component time histories for east/west flight. 146

7.5 Reconstructed and estimated wind component power spectral density (PSD) over the entire experimental flight profile. 147

7.6 Time histories of difference and root-mean-square difference (RMSD) for the estimated wind components. (Burnt Orange = Unsteady; Gold = Quasi-steady) 148

A.1 Block diagrams of Eq. (A.15) 164

A.2 MTD pass over the AGG 170

A.3 AGG measurement grid, viewed from above. 171

A.4 Artificial gust generator (AGG) visualization 172

A.5 AGG velocity measurement by vertical and lateral station; see Figure A.3. . 172

A.6 Wind conditions for system identification training and validation flights from an Air Data Unit (ADU) 174

A.7 Validation results for the quasi-steady model for an elevator doublet maneuver in calm air. 177

A.8 Validation results for the quasi-steady model for a rudder doublet, then aileron 1-2-1 maneuver. 178

A.9 Unsteady dynamic model system identification training data 179

A.10 Validation flight from an AGG pass 181

A.11 Validation flight in calm winds 182

A.12 Validation flight in light winds 183

A.13 Validation flight in severe conditions 184

List of Tables

4.1 My Twin Dream (MTD) aircraft properties 76

4.2 CubePilot sensor measurement description 78

5.1 My Twin Dream (MTD) nonlinear aerodynamic parameters 99

5.2 MTD aerodynamic force parameters 100

5.3 MTD aerodynamic moment parameters 101

5.4 MTD aerodynamic model domain 101

5.5 Normalized root mean square error (NRMSE) 103

5.6 Propeller model parameter 103

6.1 Unscented Kalman filter tuning parameters 117

6.2 Measurement noise covariance matrices (diag($\boldsymbol{R}$)). 119

6.3 Formulation 1 filter parameters 120

6.4 Formulation 2 and 3 filter parameters 120

6.5 Formulation 4, 5, and 6 filter parameters 121

6.6 Wind velocity root-mean-square difference (RMSD) values 128

7.1 Power spectral density matrices diag($\boldsymbol{S}$) for the unsteady and quasi-steady aerodynamic model-based filters 138

A.1 Aircraft trim condition 169

A.2 AGG technical specifications 170

A.3 Mean velocity and 95 % confidence intervals per coordinate point; see Figure A.3 173

A.4 Quasi-steady model longitudinal parameter estimates 176

A.5 Quasi-steady model lateral-directional parameter estimates 176

A.6 Identified empirical rational transfer functions 178

A.7 Identified empirical rational transfer functions and the state-space representation 179

B.1 Discrete Kalman filter algorithm 186

B.2 Continuous-discrete (hybrid) extended Kalman filter algorithm 186

B.3 Continuous-discrete (hybrid) unscented Kalman filter algorithm 187

List of Abbreviations

α	Angle of attack [rad]
$\bar{c}$	Mean aerodynamic chord [m]
β	sideslip angle [rad]
β_f	flank angle [rad]
$\boldsymbol{\omega}$	Body angular velocity vector [rad/s]
$\boldsymbol{\omega}_\mathrm{r}$	Air-relative body angular velocity vector [rad/s]
$\boldsymbol{\omega}_\mathrm{w}$	Effective flow angular rate of the wind in the body-fixed frame [rad/s]
$\boldsymbol{\Theta}$	Aircraft attitude [rad]
$\tilde{\boldsymbol{x}}$	Unsteady state vector
$\boldsymbol{v}$	Aircraft body velocity vector [m/s]
$\boldsymbol{v}_\mathrm{r}$	Air-relative body velocity vector [m/s]
$\boldsymbol{v}_\mathrm{w}$	Wind velocity expressed in the body-fixed frame [m/s]
$\boldsymbol{x}$	Augmented system state
δ_a	Aileron control surface deflection [rad]
δ_e	Elevator control surface deflection [rad]
δ_rps	Propeller rotation speed [rad/s]

δ_{r}	Rudder control surface deflection [rad]
η_{e}	Propeller efficiency
η_{n}	Number of propellers
ϕ	Roll attitude [rad]
ψ	Yaw attitude [rad]
ρ	Air density [kg/m^3]
ρ	Air density
θ	Pitch attitude [rad]
$\tilde{\boldsymbol{v}}$	Measurement noise vector
$\tilde{\boldsymbol{w}}$	Process noise vector
$A_{(\cdot)_{\tilde{x}}}$	Unsteady aerodynamic parameters: state matrix
b	Wing span [m]
$B_{(\cdot)_{\tilde{x}}}$	Unsteady aerodynamic parameters: input matrix
C_l	Longitudinal axis coefficient of moment acting on the aircraft
C_m	Lateral axis coefficient of moment acting on the aircraft
C_n	Directional axis coefficient of moment acting on the aircraft
C_X	Longitudinal axis coefficient of force acting on the aircraft
C_Y	Lateral axis coefficient of force acting on the aircraft
C_Z	Directional axis coefficient of force acting on the aircraft

D	Aircraft propeller diameter [m]
I_{xx}	Roll aircraft moments of inertia $[\mathrm{kg} \cdot \mathrm{m}^2]$
I_{xz}	Product of inertia $[\mathrm{kg} \cdot \mathrm{m}^2]$
I_{yy}	Pitch aircraft moments of inertia $[\mathrm{kg} \cdot \mathrm{m}^2]$
I_{zz}	Yaw aircraft moments of inertia $[\mathrm{kg} \cdot \mathrm{m}^2]$
m	Mass of aircraft [kg]
p	Angular velocity about the body-fixed x-axis [rad/s]
q	Angular velocity about the body-fixed y-axis [rad/s]
r	Angular velocity about the body-fixed z-axis [rad/s]
S	Wing surface area $[\mathrm{m}^2]$
t	Time [s]
u	Aircraft velocity along the body-fixed x-axis [m/s]
v	Aircraft velocity along the body-fixed y-axis [m/s]
V_r	True airspeed [m/s]
w	Aircraft velocity along the body-fixed z-axis [m/s]
x	Aircraft inertial position along the North axis [m]
y	Aircraft inertial position along the East axis [m]
z	Aircraft inertial position along the Down axis [m]

Chapter 1

Introduction

Uncrewed aerial vehicle (UAV) technology is growing rapidly and being used in civilian, military, and research applications. As the technology advances, there is a growing need to develop more accurate flight dynamic models and identification methodologies to identify flight models from flight data. These models are then used for various applications like control law development, flight simulation, and guidance and navigation solutions. The aim of this dissertation is to present and discuss the development of various flight dynamic models, implement system identification methods to identify the flight dynamic models, and implement the flight dynamic models in state estimation filters.

In this dissertation, an uncrewed aerial vehicle (UAV) is a pilot-less and passenger-less aircraft. An uncrewed aircraft system (UAS) includes the UAV and all its communication and operation systems, such as ground control stations, communication links, and launch and retrieval systems. The designation *small* is used by the Federal Aviation Administration (FAA) to classify all UAVs ranging in weight from 0.5 to 55 pounds.

1.1 Motivation

Various civilian, military, and research sectors are incorporating small UASs at an increasing rate. Small UASs can be used for surveillance, payload delivery, data collection, cinematography, and many more applications. Small UASs are also low-risk alternatives or surrogates for testing aviation technology developed for larger aircraft. The increase in popularity of small UASs is related to the fact that the technology is inexpensive, easily accessible, and easy to operate and maintain.

UAS technologies have recently evolved into the concept of Urban Air Mobility (UAM). UAM uses highly automated aircraft that carry passengers or cargo at lower altitudes in urban and suburban areas. As a result, there is an emerging need in the aviation community to provide weather forecasting to improve the safety of low-altitude aircraft operations can be accomplished by integrating real-time observations from small UASs with numerical weather prediction models; see Figure 1.1 for an illustration. To this end, several technical challenges have been identified [1]:

1. Aircraft (in this case, small UAS and UAM) capable of conducting weather observations accurately and reliably need to be developed.
2. The number and frequency of observations and their sensitivities in data-sparse regions need to be determined.
3. Dense observational data must be assimilated into weather-predicting models with sufficient resolution and accuracy.
4. Novel physics-based reduced-order models capable of incorporating diverse data sets must be developed.
5. Real-time forecasting must be integrated with UAS traffic management (UTM) and detect-and-avoid (DAA) architectures.

This Ph.D. dissertation focuses on the first challenge identified and attempts to develop a method in which a small UAS is used to accurately conduct weather observations, specifically wind velocity values. A small UAS can collect wind velocity values by direct measurements

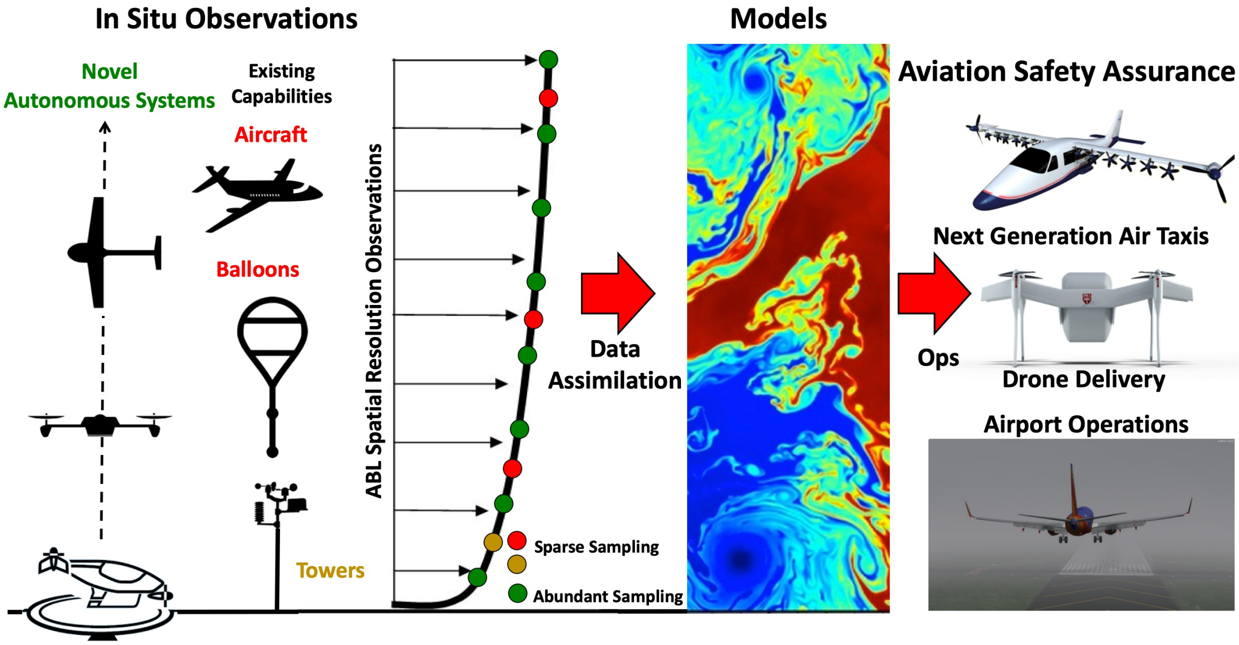

Figure 1.1: Weather Intelligent Navigation Data and Models for Aviation Planning (WINDMAP) [1]. Image taken from [2].

using sensors, such as a vaned air data unit (ADU), or indirectly infer wind velocity values from the aircraft's motion. We focus on the latter point because, in many cases, small UAS are not equipped with an ADU.

Estimation algorithms that combine onboard sensor measurements with aircraft flight dynamic models can be used to infer wind velocity values; see Figure 1.2 for an illustration. However, small UASs are usually equipped with low-cost sensors, which typically means the measurements have high uncertainty. Previous studies have explored the effects of various types of sensors on estimated wind velocity states. However, reconstruction errors due to low-fidelity aircraft dynamic models have received significantly less attention. The work presented in this dissertation aims to develop, demonstrate, and evaluate a method to identify an unsteady flight dynamic model for a fixed-wing aircraft that can used in a model-based wind velocity estimation scheme.

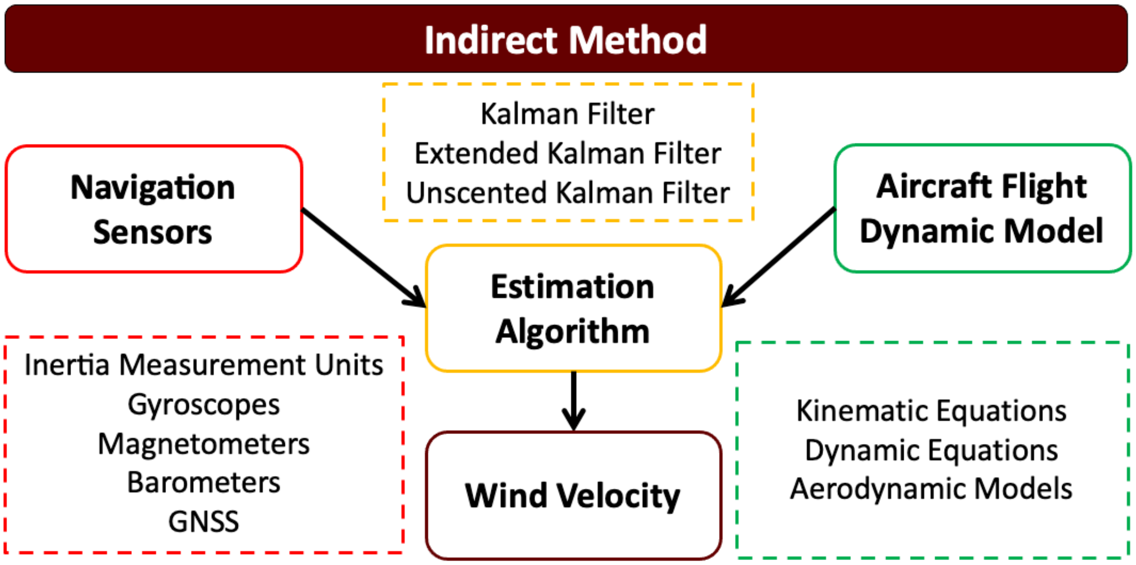

Figure 1.2: Indirect wind estimation method

1.2 General Background

This dissertation describes the identification of unsteady flight dynamic model structure and parameters and the incorporation of an unsteady aerodynamic model in a model-based wind velocity state estimation scheme. Both problems involve an optimal estimator that can best be described as a computational algorithm that utilizes knowledge of a system's dynamics, measurements, noise statistics, and initial condition information to derive a minimum-error estimate of the system's states or parameters. Three types of estimation techniques exist: smoothing, filtering, and prediction. When the desired estimates fall within the available measurement data points, an estimation problem is termed a smoothing problem. If the desired estimates coincide with the most recent measurement data point, it is called filtering. When the desired estimates extend beyond the last available measurement data point, the estimation problem is called a prediction [3]. Generally, aircraft system identification and state estimation techniques utilize various smoothing and filtering techniques.

The aerodynamic models developed in this dissertation are a set of equations that describe the aerodynamic responses of aircraft to perturbations or control inputs. Aerodynamic models have many applications including simulation, control law design, navigation, guidance, and atmospheric sensing. The required accuracy and complexity of the aerodynamic models are determined based on the application.

Aircraft system identification is a multi-step process that results in an aerodynamic model that includes model postulation, experiment design, data collection, data processing and analysis, parameter estimation, and model validation; see Figure 1.3 for an illustration. The model postulation step is done as an initial step and refined in the evaluation phase until an adequate structure is determined. The experiment design is accomplished such that the parameters in the model can sufficiently be excited. Data collection is simply the phase in which the desired measurements are collected from flight or ground tests. In the data processing phase, the collected data are processed as needed and checked for compatibility and collinearity. In data compatibility analysis, kinematic relationships are compared to measured data, and in the data collinearity analysis, the regressors are checked for correlation. In the parameter estimation phase, the desired parameters are estimated using regression techniques such as the least-square or the maximum likelihood approach. Finally, the estimated model is validated using independent measurements. The methodology used in this dissertation is mainly adapted from [4, 5, 6].

Wind velocity state estimation from an aircraft's motion is an established concept [7, 8, 9]. Estimation algorithms that combine onboard sensor measurements with aircraft flight dynamic models have been used to infer wind velocity values [10, 11, 12]. The algorithm uses a series of measurements observed over time to produce estimates of unknown states. Various state estimation algorithms exist; this dissertation uses the Kalman filter, the extended Kalman filter, and the unscented Kalman filter. All three filters aim to estimate system states

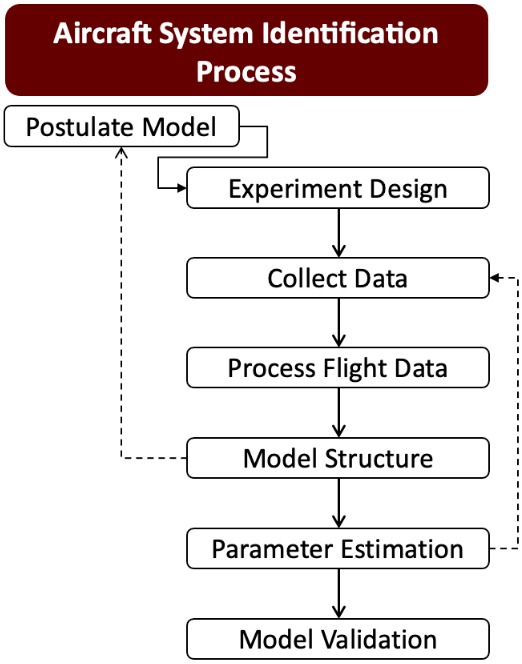

Figure 1.3: System identification diagram

by combining predictions and measurements, but they differ in handling nonlinearity and noise assumptions. The Kalman filter is best for linear systems with Gaussian noise statistics [13]; the extended Kalman filter extends this to nonlinear problems through linearization [14], and the unscented Kalman filter uses sigma points to propagate the system's statistics through a nonlinear function by means of the unscented transformation [15].

1.3 Identified Gaps in Literature

This dissertation investigates whether unsteady aerodynamic model-based wind velocity estimation can resolve more accurate wind velocity states than an approach based on a quasi-steady aerodynamic model. To achieve this, there is a need for a reduced model that sufficiently characterizes the unsteady effects of an aircraft in motion. This implies the necessity of modeling and identifying unsteady aerodynamic parameters of a fixed-wing aircraft from flight test data. Since an unsteady aerodynamic model for a small, fixed-wing aircraft is not available, the notion that an unsteady aerodynamic model-based wind estimation algorithm can resolve more accurate wind states than one based on a quasi-steady or a steady aerodynamic model still needs to be answered. To this end, the author aims to solve the challenge in three parts.

1. Develop a six-degree of freedom unsteady, reduced order model that extends the model given in [16] for a small, fixed-wing aircraft.
2. Develop system identification methods similar to those in [4, 17, 18, 19] to sufficiently excite and identify the unsteady aerodynamic parameters from flight test data.
3. Implement the unsteady aerodynamic model into an estimation algorithm, such as a Kalman Filter (KF), in a similar way as [10, 11, 20, 21] to resolve wind states.

1.4 Research Contributions

The author's primary contributions are listed below.

1. The development of an unsteady aerodynamic model for a small, fixed-wing UAV is presented in [22, 23] and in Chapter 5.
2. The development of a method to identify the unsteady aerodynamic parameters from flight test data is presented in [23] and in Chapter 5.
3. Incorporating an unsteady aerodynamic model of a fixed-wing aircraft in a model-based wind estimation algorithm is presented in [22, 24] and in Chapter 7.

4. Analysis of model-based wind velocity estimation schemes from simulated flight data, subject to a two-dimensional von Kármán turbulence, in a Kalman filter (KF), extended Kalman filter (EKF), and unscented Kalman filter (UKF) is presented in [25].
5. An examination of various wind velocity estimation approaches and formulations utilizing flight test data within three estimation filters (KF, EKF, and UKF) is presented in [26] and in Chapter 6.

The author's collaborative contribution is listed below.

6. A comprehensive literature survey and tutorial review of wind estimation methods are given in [25] and in Chapter 3.

Most flight tests conducted in this dissertation were collaborative endeavors, frequently involving undergraduate and graduate research assistants. These collective experimental initiatives encompassed the construction, instrumentation, and piloting of diverse test aircraft. The author and his collaborators were responsible for executing all flight tests to gather data, which involved preparing the aircraft, outlining mission objectives, ensuring operational safety, and selecting suitable weather conditions. All data analysis in this dissertation was carried out using MATLAB® and involved analytic tools developed by the author and his collaborators and those provided in the System Identification Program for Aircraft (SIDPAC) [27].

1.5 Outline of Dissertation

This dissertation presents the requisite mathematical preliminaries for applying system identification methods, wind estimation methods, and modeling unsteady aerodynamic parameters for a fixed-wing aircraft. A comprehensive literature review on unsteady aerodynamic models, system identification methods, and wind velocity estimation methods is also given. Finally, a detailed summary of all experiments and flight tests conducted and a comprehensive summary of all the contributions (mentioned in Section 1.4) made by the author and his contributors are given. A summary of the dissertation outline is listed below:

- Chapter 2 gives a concise overview of mathematical fundamentals, an in-depth derivation of an aircraft's mathematical model, an overview of system dynamics, and an overview of the wind velocity vector.
- Chapter 3 gives a literature review on aerodynamic modeling, and wind estimation is given.
- Chapter 4 discusses all experiments, locations, facilities, research aircraft, and sensors used in this dissertation.
- Chapter 5 discusses the development, identification, and validation of nonlinear, quasi-steady, and unsteady aerodynamic force and moment models from flight data.
- Chapter 6 discusses various wind velocity estimation schemes and their implementation using flight data.
- Chapter 7 implements and analyzes an unsteady aerodynamic model in a model-based wind velocity estimation scheme.
- Chapter 8 finalizes the dissertation with concluding remarks.

Chapter 2

Background

In this chapter, we present a summary of relevant definitions relevant to the preceding chapters. Additionally, the flight equations of motion are derived, and a summary of the wind velocity vector is given. In Section 2.1, matrix operations, the Laplace transform, and the convolution function are defined. In Section 2.2, the mathematical representation of a nonlinear system, linearization of a nonlinear system, and discretization of both a nonlinear and linear system are discussed. Additionally, the process and measurement noise vectors are established, and finally, the observability condition and observability matrix are given. In Section 2.3, particle dynamics equations are derived. In Section 2.4, the aircraft equations of motion are derived. In Section 2.5, the wind velocity vector is discussed.

2.1 Relevant Mathematical Operations

In this section, we provide some basic mathematical operation definitions that are relevant and used in latter sections and chapters. In Section 2.1.1, the scalar and vector product, matrix transpose, and identity matrix are defined. In Section 2.1.2, the determinant, cofactor, and adjoint of a matrix, and the inverse of a square matrix are defined. Finally, in Section 2.1.3, the Laplace transform and the convolution function are defined.

2.1.1 Scalar and Vector Product, Transpose, and Identity Matrix

Scalar and Vector Product

Let $\boldsymbol{A}$ be a $n \times m$ matrix, $\boldsymbol{b}$ be a $1 \times m$ row matrix, and $\boldsymbol{c}$ be a $1 \times m$ row matrix. The scalar product of two vectors $\boldsymbol{b}$ and $\boldsymbol{c}$ is a scalar:

$$\boldsymbol{b} \cdot \boldsymbol{c} = \boldsymbol{b}^{\mathrm{T}} \boldsymbol{c} = b_1 c_1 + b_2 c_2 + \ldots + b_j c_j \tag{2.1}$$

The vector product of two $\boldsymbol{b}$ and $\boldsymbol{c}$ vectors, whose dimensions are 3×1, is a vector:

$$\boldsymbol{b} \times \boldsymbol{c} = \tilde{\boldsymbol{b}} \boldsymbol{c} \begin{bmatrix} b_2 c_3 - b_3 c_2 \\ b_3 c_1 - b_1 c_3 \\ b_1 c_2 - b_2 c_1 \end{bmatrix} \tag{2.2}$$

where $\tilde{\boldsymbol{b}}$ is a skew-symmetric matrix:

$$\tilde{\boldsymbol{b}} = \begin{bmatrix} 0 & -b_3 & b_2 \\ b_3 & 0 & -b_1 \\ -b_2 & b_1 & 0 \end{bmatrix} \tag{2.3}$$

Transpose

The transpose of vector $\boldsymbol{b}$ is:

$$\boldsymbol{b}^{\mathrm{T}} = [b_1, b_2, \ldots, b_m]^{\mathrm{T}} = \begin{bmatrix} b_1 \\ b_2 \\ \vdots \\ b_m \end{bmatrix} \tag{2.4}$$

The transpose of a matrix $\boldsymbol{A}$ is

$$\boldsymbol{A}^{\mathrm{T}} = \begin{bmatrix} a_{11} & a_{12} & \dots & a_{1m} \\ a_{21} & a_{22} & \dots & \vdots \\ \vdots & \vdots & \ddots & \vdots \\ a_{n1} & \dots & \dots & a_{nm} \end{bmatrix}^{\mathrm{T}} = \begin{bmatrix} a_{11} & a_{21} & \dots & a_{n1} \\ a_{12} & a_{22} & \dots & \vdots \\ \vdots & \vdots & \ddots & \vdots \\ a_{1m} & \dots & \dots & a_{mn} \end{bmatrix} \tag{2.5}$$

Identity Matrix

The identity matrix $\mathbb{I}$ is:

$$\mathbb{I} = \begin{bmatrix} 1 & 0 & \dots & 0 \\ 0 & 1 & \dots & \vdots \\ \vdots & \vdots & \ddots & \vdots \\ 0 & \dots & \dots & 1 \end{bmatrix} \tag{2.6}$$

where $\mathbb{I}$ has entries equal to the Kronecker delta δ_{ij}:

$$\delta_{ij} = \begin{cases} 0 & \text{if} \quad i \neq j \\ 1 & \text{if} \quad i = j \end{cases} \tag{2.7}$$

2.1.2 Determinant, Cofactor, Adjoint, and Inverse of Square Matrix

Determinant

The determinant of a square matrix $\boldsymbol{A}$, whose dimension is $n \times n$, is defined as:

$$|\boldsymbol{A}| = \Sigma_{i=1}^{n} A_{ij} |\boldsymbol{D}^{ij}| (-1)^{i+j} \quad \text{for any} \quad j = 1, \dots, n \tag{2.8}$$

where $\boldsymbol{D}^{ij}$ is the $(n-1) \times (n-1)$ reduced matrix that remains after the i^{th} row and the j^{th} column have been removed from $\boldsymbol{A}$, and A_{ij} is the element in row i^{th} and column j^{th} of matrix $\boldsymbol{A}$. The cofactor A_{ij} is defined as:

$$c_{ij} = (-1)^{i+j} |\boldsymbol{D}^{ij}| \tag{2.9}$$

Cofactor

The matrix formed by all of the cofactors of $\boldsymbol{A}$ is called the cofactor matrix of $\boldsymbol{A}$:

$$\boldsymbol{C} = \begin{bmatrix} c_{11} & c_{12} & \dots & c_{1n} \\ c_{21} & c_{22} & \dots & \vdots \\ \vdots & \vdots & \ddots & \vdots \\ c_{n1} & \dots & \dots & c_{nn} \end{bmatrix} \tag{2.10}$$

Adjoint

The adjoint of matrix $\boldsymbol{A}$ is the transpose of the cofactor matrix $\boldsymbol{C}$:

$$\mathrm{adj(A) = C^T} \tag{2.11}$$

Inverse of Square Matrix

The inverse of $\boldsymbol{A}$ is defined as:

$$\boldsymbol{A}^{-1} = \frac{\mathrm{adj(A)}}{|\boldsymbol{A}|} \tag{2.12}$$

2.1.3 Laplace Transform, and the Convolution Integral

Laplace Transform

Let $f(t)$ be a function defined in the time domain for all values $t > 0$, the Laplace transform of $f(t)$ is

$$\mathcal{L}\{f(t)\} = \int_0^\infty e^{-st} f(t)dt = F(s) \tag{2.13}$$

where s is the complex variable defined in the complex frequency domain (s-domain). The function $f(t)$ can be found formally from its transform $F(s)$ by the application of the inversion theorem. The inverse Laplace transform can be given as:

$$\mathcal{L}^{-1}\{F(s)\} = \frac{1}{2\pi i} \lim_{T\to\infty} \int_{\sigma-iT}^{\sigma+iT} e^{st} F(s)ds = f(t) \tag{2.14}$$

where σ is a real number greater than the real part of all values of s for which $F(s)$ diverges. That is, $s = \sigma$ is a straight line on the s-plabe lying parallel to the imaginary axis and to the right of all the poles of $F(s)$.

The Convolution Integral

The response of any linear system to any arbitrary input $\alpha(t)$ can be obtained from integrals of $\phi(t)$, where $\phi(t)$ is the response to the unit step $\mathbf{1}(t)$. The response to $f(t)$ can be given:

$$f(t) = \int_{\tau=0}^{t} \phi(t-\tau)\dot{\alpha}(\tau)d\tau \tag{2.15}$$

If the system is not assumed to be initially quiescent, the transient of the system is associated with nonzero conditions, such the Equation (2.15) becomes:

$$f(t) = f(0)\phi(t)\int_{\tau=0}^{t} \phi(t-\tau)\dot{\alpha}(\tau)d\tau \tag{2.16}$$

where $f(0)$ is non-zero.

2.2 System Dynamics

In this section, we recall system dynamics notation, definition, and theorems that are relevant to proceeding discussion. In Section 2.2.1, a nonlinear system's mathematical representation is given and discussed. In Section 2.2.2, the linearization of a nonlinear system is discussed. In Section 2.2.3, the discretization of nonlinear and linear systems is explained. In Section 2.2.4, the statistics of the process and measurement noise vector are established. Finally, in Section 2.2.5, the observability condition and oberservabilty matrix are discussed.

2.2.1 Nonlinear Systems

The systems considered in this dissertation are described by a set of continuous ordinary differential as follows:

$$\dot{\boldsymbol{x}}(t) = \boldsymbol{f}\left(t, \boldsymbol{x}(t), \boldsymbol{u}(t), \tilde{\boldsymbol{w}}(t)\right) \tag{2.17a}$$

$$\boldsymbol{y}(t) = \boldsymbol{h}\left(t, \boldsymbol{x}(t), \boldsymbol{u}(t), \tilde{\boldsymbol{v}}(t)\right) \tag{2.17b}$$

where $\boldsymbol{x}(t) \in \mathbb{R}^n$ is the state history, $\boldsymbol{u}(t) \in \mathbb{R}^m$ is the input history, $\boldsymbol{y}(t) \in \mathbb{R}^p$ is the measurement history, $\tilde{\boldsymbol{w}}(t) \in \mathbb{R}^{n_w}$ is the process noise history, $\tilde{\boldsymbol{v}}(t) \in \mathbb{R}^{n_v}$ is the measurement noise history, and t is time. The vector $\boldsymbol{f}$ describes the nonlinear system's dynamics, and the vector $\boldsymbol{h}$ describes the nonlinear system's output measurements. In this dissertation, all systems considered are time-invariant systems and do not depend on time explicitly. The general form of a finite-dimensional, nonlinear, time-invariant system can be given as

$$\dot{\boldsymbol{x}}(t) = \boldsymbol{f}\left(\boldsymbol{x}(t), \boldsymbol{u}(t), \tilde{\boldsymbol{w}}(t)\right) \tag{2.18a}$$

$$\boldsymbol{y}(t) = \boldsymbol{h}\left(\boldsymbol{x}(t), \boldsymbol{u}(t), \tilde{\boldsymbol{v}}(t)\right) \tag{2.18b}$$

Furthermore, all systems considered in this dissertation have a specific structure on the process and measurement equations and are given as follows:

$$\dot{\boldsymbol{x}}(t) = \boldsymbol{f}\left(\boldsymbol{x}(t), \boldsymbol{u}(t)\right) + \tilde{\boldsymbol{w}}(t) \tag{2.19a}$$

$$\boldsymbol{y}(t) = \boldsymbol{h}\left(\boldsymbol{x}(t)\right) + \tilde{\boldsymbol{v}}(t) \tag{2.19b}$$

The dynamic measurement function $\boldsymbol{h}$ does not depend on the input vector $\boldsymbol{u}(t)$; additionally, the process and measurement noise vector have an additive relationship with the dynamic equation and measurement equation, respectively.

2.2.2 Linearization

The system given in Equations (2.19) can be linearized about some equilibrium values. The linearized system can be given as follows:

$$\Delta\dot{\boldsymbol{x}}(t) = \left.\frac{\partial \boldsymbol{f}}{\partial \boldsymbol{x}}\right|_{(\boldsymbol{x}^*, \boldsymbol{u}^*)} \Delta\boldsymbol{x}(t) + \left.\frac{\partial \boldsymbol{f}}{\partial \boldsymbol{u}}\right|_{(\boldsymbol{x}^*, \boldsymbol{u}^*)} \Delta\boldsymbol{u}(t) + \Delta\tilde{\boldsymbol{w}}(t) + \text{h.o.t} \tag{2.20a}$$

$$\Delta\boldsymbol{y}(t) = \left.\frac{\partial \boldsymbol{h}}{\partial \boldsymbol{x}}\right|_{(\boldsymbol{x}^*, \boldsymbol{u}^*)} \Delta\boldsymbol{x}(t) + \Delta\tilde{\boldsymbol{v}}(t) + \text{h.o.t} \tag{2.20b}$$

where the variables with subscripts * are the desired equilibrium points, h.o.t represent all higher order terms, and $\Delta\boldsymbol{x} = \boldsymbol{x} - \boldsymbol{x}^*$, $\Delta\boldsymbol{u} = \boldsymbol{u} - \boldsymbol{u}^*$, $\Delta\tilde{\boldsymbol{w}} = \tilde{\boldsymbol{w}} - \tilde{\boldsymbol{w}}^*$, and $\Delta\tilde{\boldsymbol{v}} = \tilde{\boldsymbol{v}} - \tilde{\boldsymbol{v}}^*$. As a result, the Equations (2.20) can be written in more compact form as follws:

$$\Delta\dot{\boldsymbol{x}}(t) = \boldsymbol{A}\Delta\boldsymbol{x}(t) + \boldsymbol{B}\Delta\boldsymbol{u}(t) + \Delta\tilde{\boldsymbol{w}}(t) + \text{h.o.t} \tag{2.21a}$$

$$\Delta\boldsymbol{y}(t) = \boldsymbol{C}\Delta\boldsymbol{x}(t) + \Delta\tilde{\boldsymbol{v}}(t) + \text{h.o.t} \tag{2.21b}$$

The linearization occurs when $||\boldsymbol{x} - \boldsymbol{x}^*||$, $||\boldsymbol{u} - \boldsymbol{u}^*||$, $||\tilde{\boldsymbol{w}} - \tilde{\boldsymbol{w}}^*||$, and $||\tilde{\boldsymbol{v}} - \tilde{\boldsymbol{v}}^*||$ are assumed to remain small, and as a result, the higher order terms in the Taylor series expansion h.o.t are neglected.

$$\Delta\dot{\boldsymbol{x}}(t) = \boldsymbol{A}\Delta\boldsymbol{x}(t) + \boldsymbol{B}\Delta\boldsymbol{u}(t) + \Delta\tilde{\boldsymbol{w}}(t) \tag{2.22a}$$

$$\Delta\boldsymbol{y}(t) = \boldsymbol{C}\Delta\boldsymbol{x}(t) + \Delta\tilde{\boldsymbol{v}}(t) \tag{2.22b}$$

2.2.3 Discretization

Discretization is concerned with the transformation of continuous differential equations into discrete equations suitable for numerical computing. A discrete-time model of a continuous-time system can modeled by imposing a *zero-order hold* assumption as follows:

$$\boldsymbol{u}(t) = \boldsymbol{u}(t_k) \quad \text{for} \quad t_k \leq t < t_{k+1} \tag{2.23}$$

where the times $t_k, t_{k+1}, t_{k+2}, ...$ are discrete sample times.

Discretization of Nonlinear Systems

The system described by Equations (2.17) can be discretized by implementing a 4^{th} *order Runge-Kutta* numerical integration on the following dynamic equation

$$\boldsymbol{x}(t_{k+1}) = \boldsymbol{x}(t_k) + \int_{t_k}^{t_{k+1}} \boldsymbol{f}\left(\tau, \boldsymbol{x}(\tau), \boldsymbol{u}(\tau), \boldsymbol{w}(\tau)\right) d\tau \tag{2.24}$$

and the discrete measurement equation is given as:

$$\boldsymbol{y}(t_k) = \boldsymbol{h}\left(\tau, \boldsymbol{x}(t_k), \boldsymbol{u}(t_k), \boldsymbol{v}(t_k)\right) \tag{2.25}$$

Discretization of Linear Systems

Similarly, the discretization of the linear-time invariant system can be based on the *zero-hold order* assumption mentioned above. The system described by Equations (2.22) in its discrete form is as follows:

$$\begin{aligned} \Delta\boldsymbol{x}(t_{k+1}) &= \boldsymbol{F}\Delta\boldsymbol{x}(t_k) + \boldsymbol{G}\Delta\boldsymbol{u}(t_k) + \Delta\tilde{\boldsymbol{w}}(t_k) \\ \Delta\boldsymbol{y}(t_k) &= \boldsymbol{H}\Delta\boldsymbol{x}(t_k) + \Delta\tilde{\boldsymbol{v}}(t_k) \end{aligned} \tag{2.26}$$

The state matrix $\boldsymbol{A}$, the input matrix $\boldsymbol{B}$, the output matrix $\boldsymbol{C}$, and the diffusion matrix $\boldsymbol{\Gamma}$ are discretized as follows;

$$\boldsymbol{F} = e^{\boldsymbol{A}T} = \mathcal{L}^{-1}\left[(s\boldsymbol{I} - \boldsymbol{A})^{-1}\right]_{t=T} \tag{2.27a}$$

$$\boldsymbol{G} = \left(\int_{\tau=0}^{T} e^{\boldsymbol{A}\tau} d\tau\right)\boldsymbol{B} = \boldsymbol{A}^{-1}(\boldsymbol{A}_d - \boldsymbol{I})\boldsymbol{B} \tag{2.27b}$$

$$\boldsymbol{H} = \boldsymbol{C} \tag{2.27c}$$

where T is the measurement sample time.

2.2.4 Process and Measurement Noise Statistics

The process noise vector $\tilde{\boldsymbol{w}}(t)$ and measurement noise vector $\tilde{\boldsymbol{v}}(t)$ are assumed to be uncorrelated continuous random processes with white noise statistics.

$$\tilde{\boldsymbol{w}}(t) \sim N(\mathbf{0}, \boldsymbol{S}(t)) \tag{2.28a}$$

$$\tilde{\boldsymbol{v}}(t) \sim N(\mathbf{0}, \boldsymbol{R}_t(t)) \tag{2.28b}$$

where $\boldsymbol{S}(t)$ and $\boldsymbol{R_t}(t)$ are the process and measurement power spectral density matrix, respectively. The discrete process noise $\tilde{\boldsymbol{w}}(t_k)$ and measurement noise vector $\tilde{\boldsymbol{v}}(t_k)$ are assumed to be uncorrelated discrete random processes with white noise statistics.

$$\tilde{\boldsymbol{w}}(t_k) \sim N(\mathbf{0}, \boldsymbol{Q}(t_k)) \tag{2.29a}$$

$$\tilde{\boldsymbol{v}}(t_k) \sim N(\mathbf{0}, \boldsymbol{R}(t_k)) \tag{2.29b}$$

where $\boldsymbol{Q}(t_k)$ and $\boldsymbol{R}(t_k)$ are the process and measurement covariance matrices, respectively.

2.2.5 Observability

The observability matrix corresponding to the system given by Equations (2.22) is:

$$\boldsymbol{\mathcal{O}}\left(\boldsymbol{A}, \boldsymbol{C}\right) = \begin{bmatrix} \boldsymbol{C} & \boldsymbol{C}\boldsymbol{A} & \boldsymbol{C}\boldsymbol{A}^2 & \ldots & \boldsymbol{C}\boldsymbol{A}^{n-1} \end{bmatrix}^{\mathrm{T}} \tag{2.30}$$

A linear time-invariant system is said to be observable if and only if the rank of its observability matrix is full rank [28]; that is:

$$\mathrm{rank}\boldsymbol{\mathcal{O}}\left(\boldsymbol{A},\boldsymbol{C}\right)=n \tag{2.31}$$

2.3 Particle Dynamics

In this section, we recall the derivation of particle dynamics that is relevant to the derivation of the equations of motion that describe the flight dynamics of an aircraft. In Section 2.3.1, a coordinate frame with an origin in space is defined, and in Section 2.3.2 coordinate frame transformation is discussed and explained. In Section 2.3.3, time derivative of rotating coordinate frames is discussed. In Section 2.3.4, the velocity and acceleration of a particle in an arbitrarily moving frame is described. Finally, in Section 2.3.5, the tanslational and rotational dynamics of a particle is described.

2.3.1 Coordinate Frames

A coordinate frame is defined by an origin in space and by three perpendicular unit direction vectors and can be denoted as $\hat{\imath}$, $\hat{\jmath}$, and $\hat{k}$; where

$$\begin{aligned}\hat{\imath}&=\hat{\jmath}\times\hat{k}\\ \hat{\jmath}&=\hat{k}\times\hat{\imath}\\ \hat{k}&=\hat{\imath}\times\hat{\jmath}\end{aligned} \tag{2.32}$$

The components of an arbitrary position vector $\boldsymbol{r}$ whose base is at the origin of the coordinate frame can be expressed as:

$$\begin{aligned} x &= \boldsymbol{r} \cdot \hat{\imath} \\ y &= \boldsymbol{r} \cdot \hat{\jmath} \\ z &= \boldsymbol{r} \cdot \hat{k} \end{aligned} \tag{2.33}$$

where $\boldsymbol{r} = x\hat{\imath} + y\hat{\jmath} + z\hat{k}$. Typically, and in this dissertation, the position vector is written as:

$$\boldsymbol{r} = \begin{bmatrix} x \\ y \\ z \end{bmatrix} \tag{2.34}$$

2.3.2 Change of Coordinate Frames

Let $\mathcal{F}_a$ and $\mathcal{F}_b$ be two different frames with origin a and b, respectively. Let the vector from the origin a to a point of interest P be $\boldsymbol{r}_1$. The vector $\boldsymbol{r}_1$ expressed in F_a is given as

$$\boldsymbol{r}_1^a = \begin{bmatrix} x_1^a \\ y_1^a \\ z_1^a \end{bmatrix} = \begin{bmatrix} \boldsymbol{r}_1 \cdot \hat{\imath}_a \\ \boldsymbol{r}_1 \cdot \hat{\jmath}_a \\ \boldsymbol{r}_1 \cdot \hat{k}_a \end{bmatrix} \tag{2.35}$$

Similarly, let the vector from the origin b to the point P be $\boldsymbol{r}_2$. The vector $\boldsymbol{r}_2$ expressed in F_b is given as

$$\boldsymbol{r}_2^b = \begin{bmatrix} x_2^b \\ y_2^b \\ z_2^b \end{bmatrix} = \begin{bmatrix} \boldsymbol{r}_2 \cdot \hat{\imath}_b \\ \boldsymbol{r}_2 \cdot \hat{\jmath}_b \\ \boldsymbol{r}_2 \cdot \hat{k}_b \end{bmatrix} \tag{2.36}$$

Finally, let the vector from the origin b to the origin a expressed in $\mathcal{F}_b$ be $\boldsymbol{r}^b_{ab}$. By the rules of vector addition, the relationship of the vectors can be given as:

$$\boldsymbol{r}^b_2 = \boldsymbol{r}^a_1 + \boldsymbol{r}^b_{ab} \tag{2.37}$$

The formula for change of coordinate frame from $\mathcal{F}_a$ to $\mathcal{F}_b$ can be derived from Equation (2.37)

$$\begin{bmatrix} x^b_2 \\ y^b_2 \\ z^b_2 \end{bmatrix} = \begin{bmatrix} \boldsymbol{r}^b_2 \cdot \hat{i}_b \\ \boldsymbol{r}^b_2 \cdot \hat{j}_b \\ \boldsymbol{r}^b_2 \cdot \hat{k}_b \end{bmatrix} = \begin{bmatrix} (\boldsymbol{r}^a_1 + \boldsymbol{r}^b_{ab}) \cdot \hat{i}_b \\ (\boldsymbol{r}^a_1 + \boldsymbol{r}^b_{ab}) \cdot \hat{j}_b \\ (\boldsymbol{r}^a_1 + \boldsymbol{r}^b_{ab}) \cdot \hat{k}_b \end{bmatrix} = \begin{bmatrix} (x^a_1 \hat{i}_a + y^a_1 \hat{j}_a + z^a_1 \hat{k}_a + \boldsymbol{r}^b_{ab}) \cdot \hat{i}_b \\ (x^a_1 \hat{i}_a + y^a_1 \hat{j}_a + z^a_1 \hat{k}_a + \boldsymbol{r}^b_{ab}) \cdot \hat{j}_b \\ (x^a_1 \hat{i}_a + y^a_1 \hat{j}_a + z^a_1 \hat{k}_a + \boldsymbol{r}^b_{ab}) \cdot \hat{k}_b \end{bmatrix} \tag{2.38}$$

After distributing the dot products, Equation (2.38) can be re-written as:

$$\begin{bmatrix} x^b_2 \\ y^b_2 \\ z^b_2 \end{bmatrix} = \begin{bmatrix} \hat{i}_a \cdot \hat{i}_b & \hat{j}_a \cdot \hat{i}_b & \hat{k}_a \cdot \hat{i}_b \\ \hat{i}_a \cdot \hat{j}_b & \hat{j}_a \cdot \hat{j}_b & \hat{k}_a \cdot \hat{j}_b \\ \hat{i}_a \cdot \hat{k}_b & \hat{j}_a \cdot \hat{k}_b & \hat{k}_a \cdot \hat{k}_b \end{bmatrix} \begin{bmatrix} x^a_1 \\ y^a_1 \\ z^a_1 \end{bmatrix} + \begin{bmatrix} \boldsymbol{r}^b_{ab} \cdot \hat{i}_b \\ \boldsymbol{r}^b_{ab} \cdot \hat{j}_b \\ \boldsymbol{r}^b_{ab} \cdot \hat{k}_b \end{bmatrix} \tag{2.39}$$

where the 3×3 matrix in Equation (2.39) is called the direction cosine matrix that transforms vectors from frame F_a to frame F_b.

$$\boldsymbol{R}^{ba} = \begin{bmatrix} \hat{i}_a \cdot \hat{i}_b & \hat{j}_a \cdot \hat{i}_b & \hat{k}_a \cdot \hat{i}_b \\ \hat{i}_a \cdot \hat{j}_b & \hat{j}_a \cdot \hat{j}_b & \hat{k}_a \cdot \hat{j}_b \\ \hat{i}_a \cdot \hat{k}_b & \hat{j}_a \cdot \hat{k}_b & \hat{k}_a \cdot \hat{k}_b \end{bmatrix} \tag{2.40}$$

In the case, that frame $\mathcal{F}_a$ and frame $\mathcal{F}_b$ have the same origin but remain two different frames, Equation (2.39) becomes

$$\begin{bmatrix} x^b \\ y^b \\ z^b \end{bmatrix} = \boldsymbol{R}^{ba} \begin{bmatrix} x^a \\ y^a \\ z^a \end{bmatrix} \tag{2.41}$$

the subscripts $_1$ and $_2$ are dropped because, in this case, $\boldsymbol{r}_1^a$ and $\boldsymbol{r}_2^b$ represent the same vector expressed in the two different frames.

2.3.3 Rotating Coordinate Frame

Let $\mathcal{F}_a$ and $\mathcal{F}_b$ have the same origin, and neither origin is accelerating with respect to inertial space, but $\mathcal{F}_b$ is rotating with respect to $\mathcal{F}_a$. Let $\boldsymbol{\omega}^b = [\omega_x^b, \omega_y^b, \omega_z^b]^{\mathrm{T}}$ be the rotation rate vector of frame $\mathcal{F}_b$ with respect to $\mathcal{F}_a$. The time rate of change of Equation (2.41) relative to frame $\mathcal{F}_a$ can be given as:

$$\begin{aligned} \frac{d}{dt}\boldsymbol{r}^b &= \frac{d}{dt}(\boldsymbol{R}^{ba}\boldsymbol{r}^a) \\ &= \frac{d}{dt}\boldsymbol{R}^{ba}\boldsymbol{r}^a + \boldsymbol{R}^{ba}\frac{d}{dt}\boldsymbol{r}^a \\ &= (-\tilde{\boldsymbol{\omega}}^b\boldsymbol{R}^{ba})\boldsymbol{r}^a + \boldsymbol{R}^{ba}\frac{d}{dt}\boldsymbol{r}^a \\ &= -\tilde{\boldsymbol{\omega}}^b(\boldsymbol{R}^{ba}\boldsymbol{r}^a) + \boldsymbol{R}^{ba}\frac{d}{dt}\boldsymbol{r}^a \\ &= -\tilde{\boldsymbol{\omega}}^b\boldsymbol{r}^b + \boldsymbol{R}^{ba}\frac{d}{dt}\boldsymbol{r}^a \\ &= -\boldsymbol{\omega}^b \times \boldsymbol{r}^b + \boldsymbol{R}^{ba}\frac{d}{dt}\boldsymbol{r}^a \end{aligned} \tag{2.42}$$

where $\tilde{\boldsymbol{\omega}}^b$ is the skew-symmetric matrix

$$\tilde{\boldsymbol{\omega}}^b = \begin{bmatrix} 0 & -\omega_z^b & \omega_y^b \\ \omega_z^b & 0 & -\omega_x^b \\ -\omega_y^b & \omega_x^b & 0 \end{bmatrix} \tag{2.43}$$

Note, the derivative of the left side of Equation (2.42) is taken with respect to frame $\mathcal{F}_a$, and the derivative of the right side of Equation (2.42) is taken with respect to frame $\mathcal{F}_b$; however, both side of the Equation (2.42) are expressed in frame $\mathcal{F}_b$.

2.3.4 Velocity and Acceleration in an Arbitrarily Moving Frame

Let, once again, $\mathcal{F}_a$ and $\mathcal{F}_b$ be two different frames with origins a and b, respectively. Let frame $\mathcal{F}_a$ be an inertial frame; that is, it is not translating or rotating. Let $\boldsymbol{\omega}^b = [\omega_x^b, \omega_y^b, \omega_z^b]^{\mathrm{T}}$ be the rotation rate vector of frame $\mathcal{F}_b$ relative to $\mathcal{F}_a$. Additionally, let $\mathcal{F}_b$ be translating and accelerating relative to $\mathcal{F}_a$. Let the position, velocity, and acceleration of some point of interest P relative to $\mathcal{F}_a$ be $\boldsymbol{r}_1^a$, $\boldsymbol{v}_1^a$, and $\boldsymbol{a}_1^a$, respectively. To determine the velocity and acceleration of point P relative to the inertial frame $\mathcal{F}_a$ whose position time history is known in frame $\mathcal{F}_b$, Equation (2.39) can be used:

$$\boldsymbol{r}_2^b = \boldsymbol{R}^{ba}\left(\boldsymbol{r}_1^a - \boldsymbol{r}_{ab}^a\right) \tag{2.44a}$$

$$= \boldsymbol{R}^{ba}\boldsymbol{r}_1^a + \boldsymbol{r}_{ab}^b \tag{2.44b}$$

$$\tag{2.44c}$$

where, $\boldsymbol{r}^b_{ab} = -\boldsymbol{R}^{ba}\boldsymbol{r}^a_{ab}$. The velocity of point P relative to $\mathcal{F}_a$ expressed in frame $\mathcal{F}_b$ is

$$\begin{aligned}
\boldsymbol{v}^b_2 &= \frac{d}{dt}\boldsymbol{r}^b_2 && (2.45a)\\
&= \frac{d}{dt}\left(\boldsymbol{R}^{ba}\left(\boldsymbol{r}^a_1 - \boldsymbol{r}^a_{ab}\right)\right) && (2.45b)\\
&= \frac{d}{dt}\boldsymbol{R}^{ba}\left(\boldsymbol{r}^a_1 - \boldsymbol{r}^a_{ab}\right) + \boldsymbol{R}^{ba}\frac{d}{dt}\left(\boldsymbol{r}^a_1 - \boldsymbol{r}^a_{ab}\right) && (2.45c)\\
&= -\left(\boldsymbol{\omega}^b \times \boldsymbol{R}^{ba}\left(\boldsymbol{r}^a_1 - \boldsymbol{r}^a_{ab}\right)\right) + \boldsymbol{R}^{ba}\left(\boldsymbol{v}^a_1 - \boldsymbol{v}^a_{ab}\right) && (2.45d)\\
&= -\boldsymbol{\omega}^b \times \boldsymbol{r}^b_2 + \boldsymbol{R}^{ba}\left(\boldsymbol{v}^a_1 - \boldsymbol{v}^a_{ab}\right) && (2.45e)
\end{aligned}$$

The acceleration of point P relative to $\mathcal{F}_a$ expressed in frame $\mathcal{F}_b$ is

$$\begin{aligned}
\boldsymbol{a}^b_2 &= \frac{d}{dt}\boldsymbol{v}^b_2 && (2.46a)\\
&= \frac{d}{dt}\left(-\boldsymbol{\omega}^b \times \boldsymbol{r}^b_2\right) + \frac{d}{dt}\left(\boldsymbol{R}^{ba}\left(\boldsymbol{v}^a_1 - \boldsymbol{v}^a_{ab}\right)\right) && (2.46b)\\
&= \frac{d}{dt}\left(-\boldsymbol{\omega}^b\right) \times \boldsymbol{r}^b_2 - \boldsymbol{\omega}^b \times \frac{d}{dt}\left(\boldsymbol{r}^b_2\right) + \frac{d}{dt}\left(\boldsymbol{R}^{ba}\left(\boldsymbol{v}^a_1 - \boldsymbol{v}^a_{ab}\right)\right) && (2.46c)\\
&= -\dot{\boldsymbol{\omega}}^b \times \boldsymbol{r}^b_2 + \boldsymbol{\omega}^b \times \left(\boldsymbol{\omega}^b \times \boldsymbol{r}^b_2\right) - 2\left(\boldsymbol{\omega}^b \times \boldsymbol{R}^{ba}\left(\boldsymbol{v}^a_1 - \boldsymbol{v}^a_{ab}\right)\right) + \boldsymbol{a}^b_1 - \boldsymbol{R}^{ba}\boldsymbol{a}^a_{ab} && (2.46d)
\end{aligned}$$

where,

$$\begin{aligned}
\frac{d}{dt}\left(-\boldsymbol{\omega}\right) \times \boldsymbol{r}^b_2 &= -\dot{\boldsymbol{\omega}}^b \times \boldsymbol{r}^b_2\\
-\boldsymbol{\omega}^b \times \frac{d}{dt}\left(\boldsymbol{r}^b_2\right) &= -\boldsymbol{\omega}^b \times \left(-\boldsymbol{\omega}^b \times \boldsymbol{r}^b_2\right) - \boldsymbol{\omega}^b \times \boldsymbol{R}^{ba}\left(\boldsymbol{v}^a_1 - \boldsymbol{v}^a_{ab}\right)\\
\frac{d}{dt}\left(\boldsymbol{R}^{ba}\left(\boldsymbol{v}^a_1 - \boldsymbol{v}^a_{ab}\right)\right) &= -\boldsymbol{\omega}^b \times \boldsymbol{R}^{ba}\left(\boldsymbol{v}^a_1 - \boldsymbol{v}^a_{ab}\right) + \boldsymbol{a}^b_1 - \boldsymbol{R}^{ba}\boldsymbol{a}^a_{ab}
\end{aligned}$$

After re-arranging Equation (2.46), the inertial acceleration of point P expressed in frame $\mathcal{F}_b$ relative to the inertial frame $\mathcal{F}_a$ can be given as

$$\boldsymbol{a}^b_1 = \boldsymbol{a}^b_2 + \dot{\boldsymbol{\omega}}^b \times \boldsymbol{r}^b_2 - \boldsymbol{\omega}^b \times \left(\boldsymbol{\omega}^b \times \boldsymbol{r}^b_2\right) + 2\boldsymbol{\omega}^b \times \boldsymbol{R}^{ba}\left(\boldsymbol{v}^a_1 - \boldsymbol{v}^a_{ab}\right) + \boldsymbol{R}^{ba}\boldsymbol{a}^a_{ab} \qquad (2.47)$$

where

- $\boldsymbol{R}^{ba}\boldsymbol{a}_{ab}^{a}$ is the acceleration of the origin of $\mathcal{F}_b$ relative to $\mathcal{F}_a$, expressed in $\mathcal{F}_b$.
- $\boldsymbol{a}_2^b$ is the particle's acceleration relative to $\mathcal{F}_b$,expressed in $\mathcal{F}_b$.
- $\dot{\boldsymbol{\omega}}^b \times \boldsymbol{r}_2^b$ is the particle's acceleration due to the rotational acceleration of $\mathcal{F}_b$ relative to $\mathcal{F}_a$, expressed in $\mathcal{F}_b$.
- $\boldsymbol{\omega}^b \times \left(\boldsymbol{\omega}^b \times \boldsymbol{r}_2^b\right)$ is the centripetal acceleration.
- $2\boldsymbol{\omega}^b \times \boldsymbol{R}^{ba}\left(\boldsymbol{v}_1^a - \boldsymbol{v}_{ab}^a\right)$ is the Coriolis acceleration.

The term $\boldsymbol{R}^{ba}\boldsymbol{a}_{ab}^{a}$ describes the acceleration due to the translations and rotational motion of frame $\mathcal{F}_b$ relative to $\mathcal{F}_a$, expressed in $\mathcal{F}_b$; as a result, the term expands to

$$\boldsymbol{R}^{ba}\boldsymbol{a}_{ab}^{a} = \boldsymbol{a}_{ab}^{b} + \boldsymbol{\omega}^b \times \boldsymbol{v}_{ab}^{b} \tag{2.48}$$

If particle P is constrained to the origin of frame $\mathcal{F}_b$, Equation (2.47) becomes

$$\boldsymbol{a}_1^b = \boldsymbol{a}_{ab}^{b} + \boldsymbol{\omega}^b \times \boldsymbol{v}_{ab}^{b} \tag{2.49}$$

where, $\boldsymbol{r}_2^b = 0$ and $\boldsymbol{v}_1^a = \boldsymbol{v}_{ab}^a$.

2.3.5 Translational and Rotational Dyanmics

Let $\mathcal{F}_a$ be an inertial frame of reference with origin a. Consider a collection of N particles, each with a different mass, and located at some distance from the origin of $\mathcal{F}_a$. Let the i^{th} particle have mass m_i and its location expressed in frame $\mathcal{F}_a$ relative to $\mathcal{F}_a$ be denoted by the vector $\boldsymbol{r}_i^a$. Let m denote the total mass of the particles. Let the vector $\boldsymbol{r}_{cm}^a$ denote the location of the center of mass of the collection of particles expressed in frame $\mathcal{F}_a$ relative to the origin of frame $\mathcal{F}_a$. Let the vector $\bar{\boldsymbol{r}}_i^a$ denote the position of the i^{th} particle with respect to the center of mass, expressed in the frame $\mathcal{F}_a$. Finally, suppose that an external force $\boldsymbol{F}_i^a$ acts on the i^{th} particle; and, internal force of interaction $\boldsymbol{F}_{ij}^a$ is exerted by the j^{th} particle on the i^{th} particle. Both $\boldsymbol{F}_i^a$ and $\boldsymbol{F}_{ij}^a$ are expressed in frame $\mathcal{F}_a$ relative to frame $\mathcal{F}_a$.

Translational motion

Newton's second law of motion is applied to the i^{th} and summed over the N particles to determine the translational motion of the particle system.

$$\sum_{i=1}^{N}\left(\boldsymbol{F}_i^a + \sum_{j=1}^{N}\boldsymbol{F}_{ij}^a\right) = \frac{d^2}{dt^2}\sum_{i=1}^{N} m_i \boldsymbol{r}_i^a \tag{2.50}$$

Assuming that the i^{th} particle does not exert a force on itself and that the interaction forces are equal and opposite, Equation (2.50) becomes:

$$\sum_{i=1}^{N}\boldsymbol{F}_i^a = \frac{d^2}{dt^2}\sum_{i=1}^{N} m_i \boldsymbol{r}_i^a \tag{2.51}$$

After completing the sum

$$\boldsymbol{F}_{cm}^a = \frac{d^2}{dt^2}\left(m\boldsymbol{r}_{cm}^a\right) \tag{2.52}$$

where $\boldsymbol{F}_{cm} = \sum_{i=1}^{N}\boldsymbol{F}_i^a$ is the effect of all the forces acting on the center of mass as a single force.

Rotational motion

The angular momentum of the i^{th} particle about $\mathcal{F}_a$ and summed over the N particles is

$$\boldsymbol{H}_a^a = \sum_{i=1}^{N} \left(\boldsymbol{r}_i^a \times m_i \frac{d}{dt} \boldsymbol{r}_i^a \right) \tag{2.53}$$

The superscript in the terms $\boldsymbol{H}_a^a$ denotes the frame in which the angular momentum is expressed, and the subscript denotes the point about which the angular moment is calculated.

$$\begin{aligned} \boldsymbol{H}_a^a = \boldsymbol{r}_{cm}^a \times \left(\sum_{i=1}^{N} m_i \right) \frac{d}{dt} \boldsymbol{r}_{cm}^a + \boldsymbol{r}_{cm}^a \times \frac{d}{dt} \left(\sum_{i=1}^{N} m_i \bar{\boldsymbol{r}}_i^a \right) + \cdots \\ \left(\sum_{i=1}^{N} m_i \bar{\boldsymbol{r}}_i^a \right) \times \frac{d}{dt} \boldsymbol{r}_{cm}^a + \sum_{i=1}^{N} \left(\bar{\boldsymbol{r}}_i^a \times m_i \frac{d}{dt} \bar{\boldsymbol{r}}_i^a \right) \end{aligned} \tag{2.54}$$

where $\boldsymbol{r}_i^a = \boldsymbol{r}_{cm}^a + \bar{\boldsymbol{r}}_i^a$. After recognizing that the middle two terms are equal to zero, we get:

$$\boldsymbol{H}_a^a = \boldsymbol{r}_{cm}^a \times m \frac{d}{dt} \boldsymbol{r}_{cm}^a + \sum_{i=1}^{N} \left(\bar{\boldsymbol{r}}_i^a \times m_i \frac{d}{dt} \bar{\boldsymbol{r}}_i^a \right) \tag{2.55}$$

Differentiating Equation (2.55) and after some algebra, we get:

$$\frac{d}{dt} \boldsymbol{H}_a^a = \boldsymbol{r}_{cm}^a \times m \frac{d^2}{dt^2} \boldsymbol{r}_{cm}^a + \sum_{i=1}^{N} \bar{\boldsymbol{r}}_i^a \times m_i \frac{d^2}{dt^2} \bar{\boldsymbol{r}}_i^a \tag{2.56a}$$

$$= \boldsymbol{r}_{cm}^a \times \boldsymbol{F}_{cm}^a + \sum_{i=1}^{N} \bar{\boldsymbol{r}}_i^a \times \left(\boldsymbol{F}_i^a + \sum_{j=1}^{N} \boldsymbol{F}_{ij}^a \right) \tag{2.56b}$$

Assuming that the i^{th} particle does not exert a force on itself, and that the interaction forces are equal and opposite, Equation (2.56) becomes:

$$\frac{d}{dt} \boldsymbol{H}_a^a = \boldsymbol{r}_{cm}^a \times \boldsymbol{F}_{cm}^a + \sum_{i=1}^{N} \left(\bar{\boldsymbol{r}}_i^a \times \boldsymbol{F}_i^a \right) \tag{2.57}$$

In the case, that angular momentum is taken about the center of mass relative to frame $\mathcal{F}_a$, Equation (2.57) become

$$\frac{d}{dt}\boldsymbol{H}^a_{cm} = \boldsymbol{M}^a_{cm} = \sum_{i=1}^{N} \left(\bar{\boldsymbol{r}}^a_i \times \boldsymbol{F}^a_i\right) \tag{2.58}$$

where $\boldsymbol{M}^a_{cm}$ is the moment of all forces acting about the center of mass, expressed in $\mathcal{F}_a$.

Rigid Body Constraint

If one assumes that the collection of particles from a rigid body and that the rigid body rotates with some angular velocity $\boldsymbol{\omega}^a = [\omega^a_x, \omega^a_y, \omega^a_z]^{\mathrm{T}}$ relative to $\mathcal{F}_a$. The angular momentum of the i^{th} particle summed over the N particles, about the center of mass of the system expressed in $\mathcal{F}_a$ is:

$$\boldsymbol{H}^a_{cm} = \sum_{i=1}^{N} \bar{\boldsymbol{r}}^a_i \times m_i \frac{d}{dt}\bar{\boldsymbol{r}}^a_i \tag{2.59a}$$

$$= \sum_{i=1}^{N} \bar{\boldsymbol{r}}^a_i \times m_i \left(\frac{\partial}{\partial t}\bar{\boldsymbol{r}}^a_i + \boldsymbol{\omega}^a \times \bar{\boldsymbol{r}}^a_i\right) \tag{2.59b}$$

$$= -\sum_{i=1}^{N} \bar{\boldsymbol{r}}^a_i \times m_i \left(\bar{\boldsymbol{r}}^a_i \times \boldsymbol{\omega}^a\right) \tag{2.59c}$$

Note, $\frac{\partial}{\partial t}\bar{\boldsymbol{r}}^a_i = 0$ because the particles are assumed to be fixed relative to the center of mass. One can consider the case where $N \to \infty$ gets an explicit expression of $\boldsymbol{H}^a_{cm}$ in terms of moment of inertia values.

$$\boldsymbol{H}^a_{cm} = -\int \bar{\boldsymbol{r}}^a \times \left(\bar{\boldsymbol{r}}^a \times \boldsymbol{\omega}^a\right) dm \tag{2.60a}$$

$$= \boldsymbol{I}^a \boldsymbol{\omega}^a \tag{2.60b}$$

where $\bar{\boldsymbol{r}}^a = \left[\bar{r}^a_x, \bar{r}^a_y, \bar{r}^a_z\right]^{\mathrm{T}}$, and $\boldsymbol{I}^a$ is the moment of inertia matrix of the rigid body system relative to $\mathcal{F}_a$, expressed in $\mathcal{F}_a$.

$$\boldsymbol{I}^a = \begin{pmatrix} (\bar{r}^a_y)^2 + (\bar{r}^a_z)^2 & -\bar{r}^a_x \bar{r}^a_y & -\bar{r}^a_x \bar{r}^a_z \\ -\bar{r}^a_x \bar{r}^a_y & (\bar{r}^a_x)^2 + (\bar{r}^a_z)^2 & -\bar{r}^a_x \bar{r}^a_z \\ -\bar{r}^a_x \bar{r}^a_z & -\bar{r}^a_x \bar{r}^a_z & (\bar{r}^a_x)^2 + (\bar{r}^a_y)^2 \end{pmatrix} \tag{2.61}$$

Note, $\boldsymbol{I}^a$ varies with the body's rotation because it is expressed in the inertial frame. In Section 2.4, the moment of inertia matrix of a rigid-bodied aircraft is defined in the body-fixed frame, and as a result, the moment of inertia matrix is constant.

2.4 Aircraft Equations of Motion

A mathematical model of an aircraft is a set of equations and parameters that describe the motion of the aircraft. These models are used for a wide range of purposes, including aircraft design, flight simulation, control system development, and performance analysis. Mathematical models of aircraft can vary from simple linear models to highly complex nonlinear models. The choice of model complexity depends on the specific goals and requirements of the analysis or simulation being conducted. The complexity of the model can vary depending on the specific application and level of detail required.

1. **Environmental Factors**: The model may account for environmental factors such as air density, wind speed, and atmospheric conditions, which can affect the aircraft's performance.

2. **Aircraft Geometry**: This includes information about the aircraft's size, shape, and wing.

3. **Mass and Inertia**: This part of the model includes information about the aircraft's mass distribution and moments of inertia.
4. **Aerodynamic Characteristics**: These are the forces and moments generated by the aircraft's wings, tail, and control surfaces as a function of its wind relative angles (angle of attack, sideslip angle) and control inputs (elevator, aileron, rudder deflections).
5. **Propulsion System**: The model includes equations that describe how the aircraft's engines or propellers produce thrust, as well as how engine or propeller performance varies with throttle settings, altitude, and airspeed.
6. **Equations of Motion**: The fundamental equations of motion describe how forces and moments acting on the aircraft result in its translational and rotational motion.
7. **Control Input**: In some models, control input dynamics are included in the equations of motion to map the control inputs to control surface responses.

In Section 2.4.1, the inertial-fixed, north-east-down, and body-fixed reference frames are defined. In Section 2.4.2, the direction cosine matrix parameterized by the Euler angles is defined. In Section 2.4.3, the equations of motion of a rigid-body aircraft are derived and discussed. In section 2.4.4, the aerodynamic angles and forces are defined. In Section 2.4.5, the forces and moments that act on the aircraft are discussed and given. Finally, in Section 2.4.6, the equations of motion of rigid-body aircraft in the wind are derived.

2.4.1 Reference Frames

All reference frames are right-handed with mutually orthogonal axes. We consider three frames: the inertial, the earth-fixed, the body-fixed, and the atmosphere-fixed reference frames [4, 29, 30].

Inertial frame of reference

The *inertial* reference frame is represented by the orthonormal triad ($\hat{i}_x$, $\hat{i}_y$, $\hat{i}_z$). Its origin and orientation are arbitrary, but the frame does not accelerate relative to the distant stars. Newton's laws of motion hold in an inertial reference frame.

North-east-down (NED)

The *north-east-down (NED)* reference frame is represented by an orthonormal triad ($\hat{e}_x$, $\hat{e}_y$, $\hat{e}_z$) based at an arbitrary (non-polar) point on the Earth's surface, with $\hat{e}_x$ pointing north, $\hat{e}_y$ pointing east, and $\hat{e}_z$ pointing down. Over the time and space scales of interest in this paper, the NED frame is assumed to be fixed in inertial space so that Newton's laws of motion hold. We will interchange the terms "NED" and "inertial" in describing this frame. Moreover, we take Earth to be flat and we assume the force of gravity does not vary with position.

Body-fixed frame of reference

The *body-fixed* reference frame is represented by the orthonormal triad ($\hat{b}_x$, $\hat{b}_y$, $\hat{b}_z$). The origin of the body-fixed reference frame is at the aircraft's center of gravity, with the positive $\hat{b}_x$ axis pointing forward through the nose of the aircraft, the positive $\hat{b}_y$ axis pointing out the aircraft's right wing, and the positive $\hat{b}_z$ axis pointing down through the belly of the aircraft.

2.4.2 Rotation Matrix Parameterization

The direction cosine matrix $\boldsymbol{R}^{ab}$ can be parameterized using three independent parameters. This dissertation uses the matrix parameterized by the Euler angles, which is expressed as a product of three right-handed single-axis rotation matrices. The superscript in $\boldsymbol{R}^{ab}$ that denotes the direction of rotation is dropped and replaced by a subscript for convenience in the proceeding sections, where $\boldsymbol{R}^{ab} = \boldsymbol{R}_{ab}$.

Rotation by the roll angle ϕ

A rotation about $\hat{e}_x$ is defined as a rotation matrix parameterized by the roll ϕ, such that:

$$\boldsymbol{R}_1(\phi) = \begin{bmatrix} 1 & 0 & 0 \\ 0 & \cos\phi & \sin\phi \\ 0 & -\sin\phi & \cos\phi \end{bmatrix} \tag{2.62}$$

Rotation by the roll angle θ

A rotation about $\hat{e}_y$ is defined as a rotation matrix parameterized by the pitch θ, such that:

$$\boldsymbol{R}_2(\theta) = \begin{bmatrix} \cos\theta & 0 & -\sin\theta \\ 0 & 1 & \sin\theta \\ \sin\theta & 0 & \cos\theta \end{bmatrix} \tag{2.63}$$

Rotation by the roll angle ψ

A rotation about $\hat{e}_z$ is defined as a rotation matrix parameterized by the yaw ψ, such that:

$$\boldsymbol{R}_3(\psi) = \begin{bmatrix} \cos\psi & \sin\psi & 0 \\ -\sin\psi & \cos\psi & 0 \\ 0 & 0 & 1 \end{bmatrix} \tag{2.64}$$

Rotation from the body-fixed frame to the earth-fixed frame

A rotation of free vectors expressed in the body-fixed reference frame to the earth-fixed reference frame is defined by a rotation matrix denoted $\boldsymbol{R}_{\mathrm{IB}}$, such that:

$$\begin{aligned}
\boldsymbol{R}_{\mathrm{IB}} &= \boldsymbol{R}_3(\psi)\boldsymbol{R}_2(\theta)\boldsymbol{R}_1(\phi) \\
&= \begin{bmatrix} \cos\psi & \sin\psi & 0 \\ -\sin\psi & \cos\psi & 0 \\ 0 & 0 & 1 \end{bmatrix} \begin{bmatrix} \cos\theta & 0 & -\sin\theta \\ 0 & 1 & \sin\theta \\ \sin\theta & 0 & \cos\theta \end{bmatrix} \begin{bmatrix} 1 & 0 & 0 \\ 0 & \cos\phi & \sin\phi \\ 0 & -\sin\phi & \cos\phi \end{bmatrix} \\
&= \begin{bmatrix} \cos\theta\cos\psi & \cos\psi\sin\theta\sin\phi - \cos\phi\sin\psi & \cos\psi\sin\theta\cos\phi + \sin\phi\sin\psi \\ \cos\theta\sin\psi & \sin\phi\sin\theta\sin\psi + \cos\phi\cos\psi & \sin\theta\cos\phi\sin\psi - \sin\phi\sin\psi \\ -\sin\theta & \cos\theta\sin\phi & \cos\theta\cos\phi \end{bmatrix}
\end{aligned} \tag{2.65}$$

Similarly, a rotation of free vectors expressed in the earth-fixed reference frame to the body-fixed reference frame is defined by a rotation matrix denoted $\boldsymbol{R}_{\mathrm{BI}}$, such that:

$$\begin{aligned}
\boldsymbol{R}_{\mathrm{BI}} &= \boldsymbol{R}_{\mathrm{IB}}^{\mathrm{T}} = \boldsymbol{R}_1^{\mathrm{T}}(\phi)\boldsymbol{R}_2^{\mathrm{T}}(\theta)\boldsymbol{R}_3^{\mathrm{T}}(\psi) \\
&= \begin{bmatrix} \cos\theta\cos\psi & \cos\theta\sin\psi & -\sin\theta \\ \cos\psi\sin\theta\sin\phi - \cos\phi\sin\psi & \cos\phi\cos\psi + \sin\theta\sin\phi\sin\psi & \cos\theta\sin\phi \\ \cos\psi\sin\theta\cos\phi + \sin\phi\sin\psi & \sin\theta\cos\phi\sin\psi - \sin\phi\cos\psi & \cos\theta\cos\phi \end{bmatrix}
\end{aligned} \tag{2.66}$$

2.4.3 Rigid Body Equations of Motion

A general derivation of aircraft equations of motion would consider the elasticity, the mass density variation of the aircraft's structure, moving components of various subsystems, and varying weight due to fuel depletion subject to aerodynamic, propulsive, and gravitational forces flying in nonstationary air. Various simplifying assumptions are adopted in this dissertation when deriving the equations of motion of a fixed aircraft. In this dissertation, we implement the following assumptions when developing the equation of motion of the aircraft.

Assumption 1. Fixed-wing, Rigid-body Equations of Motion in Wind

a) The aircraft mass is constant.

b) The aircraft is a rigid body.

c) Earth's surface is flat.

d) The specific force of gravity is constant.

e) Earth is fixed in inertial space.

The assumptions adopted are established for rigid-bodied, electrically powered aircraft that generally fly at low altitudes and cover a small distance over a short flight time.

Translational Kinematic Equations

The translational kinematic (also known as navigation) equations are derived such that the velocity of the aircraft defined in the earth-fixed frame is written as a function of the aircraft's velocity defined in the body-fixed frame.

$$\frac{d}{dt}\begin{bmatrix} x \\ y \\ z \end{bmatrix} = \boldsymbol{R}_{\text{IB}} \begin{bmatrix} u \\ v \\ w \end{bmatrix} \tag{2.67a}$$

$$\frac{d}{dt}\boldsymbol{X} = \boldsymbol{R}_{\text{IB}}\boldsymbol{v} \tag{2.67b}$$

where $\boldsymbol{X}$ is the aircraft position vector defined in the NED reference frame, and $\boldsymbol{v}$ is the aircraft total velocity vector defined in the body-fixed reference frame.

Rotational Kinematic Equations

The rotational kinematic (also known as attitude kinematic) equations are derived by summing the time derivative of the Euler angles in the body-fixed frame.

$$\begin{bmatrix} p \\ q \\ r \end{bmatrix} = \begin{bmatrix} \dot{\phi} \\ 0 \\ 0 \end{bmatrix} + \boldsymbol{R}_1(\phi) \begin{bmatrix} 0 \\ \dot{\theta} \\ 0 \end{bmatrix} + \boldsymbol{R}_1(\phi)\boldsymbol{R}_2(\theta) \begin{bmatrix} 0 \\ 0 \\ \dot{\psi} \end{bmatrix} \tag{2.68a}$$

$$\begin{bmatrix} p \\ q \\ r \end{bmatrix} = \begin{bmatrix} 1 & 0 & -\sin \\ 0 & \cos\theta & \cos\theta\sin\phi \\ 0 & -\sin\phi & \cos\theta\cos\phi \end{bmatrix} \begin{bmatrix} \dot{\phi} \\ \dot{\theta} \\ \dot{\psi} \end{bmatrix} \tag{2.68b}$$

The rotational kinematic equations are:

$$\frac{d}{dt}\begin{bmatrix} \phi \\ \theta \\ \psi \end{bmatrix} = \begin{bmatrix} 1 & \sin\phi\tan\theta & \cos\phi\tan\theta \\ 0 & \cos\phi & -\sin\phi \\ 0 & \sin\phi\sec\theta & \cos\phi\sec\theta \end{bmatrix} \begin{bmatrix} p \\ q \\ r \end{bmatrix} \tag{2.69a}$$

$$\frac{d}{dt}\begin{bmatrix} \phi \\ \theta \\ \psi \end{bmatrix} = \boldsymbol{L}_{\mathrm{IB}} \begin{bmatrix} p \\ q \\ r \end{bmatrix} \tag{2.69b}$$

$$\frac{d}{dt}\boldsymbol{\Theta} = \boldsymbol{L}_{\mathrm{IB}}\boldsymbol{\omega} \tag{2.69c}$$

where $\boldsymbol{\Theta}$ is the aircraft attitude vector defined in the NED reference frame, and $\boldsymbol{\omega}$ is the aircraft angular velocity vector defined in the body-fixed reference frame.

Translational and Rotational Dynamic Equations

Recall the translation dynamic equation Equation (2.52) derived, and note that it is expressed in the inertial-fixed reference frame.

$$\boldsymbol{F}^{a}_{cm} = \frac{d^2}{dt^2}\left(m\boldsymbol{r}^{a}_{cm}\right) \tag{2.70}$$

where the superscript ^{a} denotes the inertial reference frame, and subscript denote $_{cm}$ denotes the center of mass of the aircraft. The aerodynamic forces that act on an aircraft in flight are expressed in the body-fixed reference frame; hence, it is more convenient to reframe the translational dynamic equation Equation (2.70) in the body-fixed frame. Recall Equation (2.49).

$$\boldsymbol{a}^{b}_{1} = \boldsymbol{a}^{b}_{ab} + \boldsymbol{\omega}^{b} \times \boldsymbol{v}^{b}_{ab} \tag{2.71}$$

where the superscript ^{b} denotes the body-fixed reference frame, and subscript $_{ab}$ denotes the origin of the body-fixed frame. In this case, the origin of the body-fixed reference frame is defined such that it coincides with the aircraft's center of mass. As a result, Equation (2.70) and Equation (2.71) can be used to derive the translation dynamic equations of a fixed-wing, rigid body aircraft whose center of mass coincides with the origin of the body-fixed frame expressed in the body-fixed frame relative to the inertial frame.

$$\begin{aligned}
\boldsymbol{R}_{\mathrm{BI}}\boldsymbol{F}^{a}_{cm} &= \boldsymbol{R}_{\mathrm{BI}}\left(\frac{d^2}{dt^2}\left(m\boldsymbol{r}^{a}_{cm}\right)\right) && \text{(2.72a)}\\
&= m\boldsymbol{R}_{\mathrm{BI}}\left(\frac{d^2}{dt^2}\boldsymbol{r}^{a}_{cm}\right) && \text{(2.72b)}\\
&= m\left(\frac{d}{dt}\boldsymbol{v}^{b}_{cm} + \boldsymbol{\omega}^{b} \times \boldsymbol{v}^{b}_{cm}\right) && \text{(2.72c)}\\
&= \boldsymbol{F}^{b}_{cm} && \text{(2.72d)}
\end{aligned}$$

After dropping the superscripts and subscripts, Equation (2.72) can be rewritten to describe the translational dynamic equation that is used in the proceeding sections and chapters.

$$\frac{d}{dt}\boldsymbol{v} = \boldsymbol{v} \times \boldsymbol{\omega} + \frac{1}{m}\boldsymbol{F} \tag{2.73}$$

where $\boldsymbol{v}$ is the aircraft's total velocity vector defined in the body-fixed reference frame, $\boldsymbol{\omega}$ is the aircraft's angular velocity vector defined in the body-fixed reference frame, and $\boldsymbol{F}$ is the force vector of all the forces that act of the aircraft expressed in the body-fixed reference frame.

Rotational Dynamic Equations

Similar to the translational dynamic equations, the rotational dynamic equations derived in Section 2.3.5 are expressed and relative to an inertial-fixed reference frame. However, the aerodynamic moments that act on an aircraft in flight are expressed in the body-fixed reference frame. Additionally, the moment of inertia matrix of a rigid-body system derived in Section 2.3.5 is time-invariant if expressed in the body-fixed frame. As a result, it is convenient to re-frame the rotational dynamic equation Equation (2.60) in the body-fixed reference frame. Recall Equation (2.60).

$$\boldsymbol{H}^a_{cm} = \boldsymbol{I}^a\boldsymbol{\omega}^a \tag{2.74}$$

and Equation (2.58)

$$\boldsymbol{M}^a_{cm} = \frac{d}{dt}\boldsymbol{H}^a_{cm} \tag{2.75}$$

where the superscript ^{a} denotes the inertial-fixed reference frame and subscript denote $_{cm}$ denotes the center of mass. The rotational dynamic equation expressed in the body-fixed reference frame is:

$$\begin{aligned}
\boldsymbol{R}_{\mathrm{BI}}\boldsymbol{H}^{a}_{cm} &= \boldsymbol{R}_{\mathrm{BI}}\left(\boldsymbol{I}^{a}\boldsymbol{\omega}^{a}\right) && \text{(2.76a)}\\
&= \boldsymbol{I}^{b}\boldsymbol{\omega}^{b} && \text{(2.76b)}\\
&= \boldsymbol{H}^{b}_{cm} && \text{(2.76c)}
\end{aligned}$$

where superscript ^{b} denotes body-fixed frame. The time rate of change of the rotational dynamic equation expressed in the body-fixed reference frame

$$\begin{aligned}
\boldsymbol{M}^{b}_{cm} &= \frac{d}{dt}\left(\boldsymbol{R}_{\mathrm{BI}}\boldsymbol{H}^{a}_{cm}\right) && \text{(2.77a)}\\
&= \frac{d}{dt}\boldsymbol{H}^{b}_{cm} + \boldsymbol{\omega}^{b} \times \boldsymbol{H}^{b}_{cm} && \text{(2.77b)}\\
&= \frac{d}{dt}\left(\boldsymbol{I}^{b}\boldsymbol{\omega}^{b}\right) + \boldsymbol{\omega}^{b} \times \boldsymbol{I}^{b}\boldsymbol{\omega}^{b} && \text{(2.77c)}\\
&= \boldsymbol{I}^{b}\frac{d}{dt}\boldsymbol{\omega}^{b} + \boldsymbol{\omega}^{b} \times \boldsymbol{I}^{b}\boldsymbol{\omega}^{b} && \text{(2.77d)}
\end{aligned}$$

After dropping the superscripts and subscripts, Equation (2.72) can be rewritten to describe the rotational dynamic equation used throughout this dissertation.

$$\frac{d}{dt}\boldsymbol{\omega} = \boldsymbol{I}^{-1}\left(\boldsymbol{I}\boldsymbol{\omega} \times \boldsymbol{\omega}\right) + \boldsymbol{I}^{-1}\boldsymbol{M} \tag{2.78}$$

where $\boldsymbol{\omega}$ is the aircraft's angular velocity vector defined in the body-fixed reference frame, $\boldsymbol{I}$ is the aircraft's moment of inertia matrix expressed in the body-fixed reference frame, and $\boldsymbol{M}$ is the moment vector about the aircraft's center of mass defined in the body-fixed reference frame. In summary, the kinematic and dynamic equations of motion of rigid-body aircraft are:

$$\dot{\boldsymbol{X}} = \boldsymbol{R}_{\mathrm{IB}}\boldsymbol{v} \tag{2.79a}$$

$$\dot{\boldsymbol{\Theta}} = \boldsymbol{L}_{\mathrm{IB}}\boldsymbol{\omega} \tag{2.79b}$$

$$\dot{\boldsymbol{v}} = \boldsymbol{v} \times \boldsymbol{\omega} + \frac{1}{m}\boldsymbol{F} \tag{2.79c}$$

$$\dot{\boldsymbol{\omega}} = \boldsymbol{I}^{-1}\left(\boldsymbol{I}\boldsymbol{\omega} \times \boldsymbol{\omega}\right) + \boldsymbol{I}^{-1}\boldsymbol{M} \tag{2.79d}$$

2.4.4 Air-relative Velocities and Aerodynamic Angles and Forces

The total velocity $\boldsymbol{v}$ and angular velocity $\boldsymbol{\omega}$ of an aircraft in motion is

$$\boldsymbol{v} = \boldsymbol{v}_{\mathrm{r}} + \boldsymbol{v}_{\mathrm{w}} \tag{2.80a}$$

$$\boldsymbol{\omega} = \boldsymbol{\omega}_{\mathrm{r}} + \boldsymbol{\omega}_{\mathrm{w}} \tag{2.80b}$$

where, $\boldsymbol{v}_{\mathrm{r}} = [u_{\mathrm{r}}, v_{\mathrm{r}}, w_{\mathrm{r}}]^{\mathrm{T}}$ is the air-relative aircraft velocity vector expressed in the body-fixed reference frame, $\boldsymbol{v}_{\mathrm{w}} = [u_{\mathrm{w}}, v_{\mathrm{w}}, w_{\mathrm{w}}]^{\mathrm{T}}$ is the wind velocity vector expressed in the body-fixed reference frame, $\boldsymbol{\omega}_{\mathrm{r}} = [p_{\mathrm{r}}, q_{\mathrm{r}}, r_{\mathrm{r}}]^{\mathrm{T}}$ is the air-relative angular velocity vector, and $\boldsymbol{\omega}_{\mathrm{w}} = [p_{\mathrm{w}}, q_{\mathrm{w}}, r_{\mathrm{w}}]^{\mathrm{T}}$ is the effective flow angular rate. The air-relative velocity V_{r} of an aircraft is defined as:

$$V_{\mathrm{r}} = \sqrt{u_{\mathrm{r}}^2 + v_{\mathrm{r}}^2 + w_{\mathrm{r}}^2} \tag{2.81}$$

The angle of attack of an aircraft is defined as:

$$\alpha = \tan^{-1}\left(\frac{w_{\mathrm{r}}}{u_{\mathrm{r}}}\right) \tag{2.82}$$

Similarly, the side-slip angle of an aircraft is defined as:

$$\beta = \sin^{-1}\left(\frac{v_{\mathrm{r}}}{\sqrt{u_{\mathrm{r}}^2 + v_{\mathrm{r}}^2 + w_{\mathrm{r}}^2}}\right) \tag{2.83}$$

2.4.5 Aerodynamic Force and Moment

In this dissertation, only the aerodynamic forces $\boldsymbol{F}_A$ and moments $\boldsymbol{M}_A$, propulsion force $\boldsymbol{F}_J$, and gravitational force $\boldsymbol{F}_g$ are assumed to act on the aircraft. The vector $\boldsymbol{F}_G$ is the gravitational force vector defined in the inertial-fixed reference frame:

$$\boldsymbol{F}_G = \begin{bmatrix} 0 \\ 0 \\ mg \end{bmatrix} \tag{2.84}$$

where m is the aircraft's mass, and g is the gravitational acceleration constant 9.81 m/s. The vector $\boldsymbol{F}_A$ is the aerodynamic force vector defined in the body-fixed reference frame:

$$\boldsymbol{F}_A = \begin{bmatrix} F_X(\boldsymbol{v}_r, \boldsymbol{\omega}_r, \boldsymbol{\delta}) \\ F_Y(\boldsymbol{v}_r, \boldsymbol{\omega}_r, \boldsymbol{\delta}) \\ F_Z(\boldsymbol{v}_r, \boldsymbol{\omega}_r, \boldsymbol{\delta}) \end{bmatrix} = \frac{1}{2}\rho\|\boldsymbol{v}_{\mathrm{r}}\|^2 S \begin{bmatrix} C_X(\boldsymbol{v}_r, \boldsymbol{\omega}_r, \boldsymbol{\delta}) \\ C_Y(\boldsymbol{v}_r, \boldsymbol{\omega}_r, \boldsymbol{\delta}) \\ C_Z(\boldsymbol{v}_r, \boldsymbol{\omega}_r, \boldsymbol{\delta}) \end{bmatrix} \tag{2.85}$$

where $\boldsymbol{\delta} = [\delta_{\mathrm{e}}, \delta_{\mathrm{a}}, \delta_{\mathrm{r}}, \delta_{\mathrm{rps}}]^{\mathrm{T}}$ is the conventional elevator, aileron, rudder, and thrust control input vector, $\bar{c}$ is the mean aerodynamic chord, S is the wing planform area, and ρ is the air density. The vector $\boldsymbol{M}_A$ is the aerodynamic moment vector defined in the body-fixed reference frame:

$$\boldsymbol{M}_A = \begin{bmatrix} M_l(\boldsymbol{v}_r, \boldsymbol{\omega}_r, \boldsymbol{\delta}) \\ M_m(\boldsymbol{v}_r, \boldsymbol{\omega}_r, \boldsymbol{\delta}) \\ M_n(\boldsymbol{v}_r, \boldsymbol{\omega}_r, \boldsymbol{\delta}) \end{bmatrix} = \frac{1}{2}\rho \|\boldsymbol{v}_{\mathrm{r}}\|^2 S \begin{bmatrix} bC_l(\boldsymbol{v}_r, \boldsymbol{\omega}_r, \boldsymbol{\delta}) \\ \bar{c}C_m(\boldsymbol{v}_r, \boldsymbol{\omega}_r, \boldsymbol{\delta}) \\ bC_n(\boldsymbol{v}_r, \boldsymbol{\omega}_r, \boldsymbol{\delta}) \end{bmatrix} \tag{2.86}$$

where b is the wingspan. The vector $\boldsymbol{F}_J$ is the propulsion vector defined in the body-fixed reference frame:

$$\boldsymbol{F}_J = D^4 \rho \eta_{\mathrm{e}} \eta_{\mathrm{n}} \delta_{\mathrm{rps}}^2 \begin{bmatrix} C_J(\boldsymbol{\delta}) \\ 0 \\ 0 \end{bmatrix} \tag{2.87}$$

where η_{e} is the efficiency parameter for the aircraft's propellers, η_{n} is the number of propellers of the aircraft, and D is the diameter of the aircraft's propellers. The coefficient of forces (C_X, C_Y, C_Z, C_J) and coefficient moment terms (C_l, C_m, C_n) structure and value are discussed in Chapter 5.

2.4.6 Equations of Motion in Wind

The dynamic equations for a rigid aircraft moving in wind can be obtained by expanding Equation (2.79) to include the aircraft relative velocity $\boldsymbol{v}_r$ and wind velocity $\boldsymbol{v}_w$. Recall Equation (2.80b):

$$\begin{aligned} \boldsymbol{v} &= \boldsymbol{v}_{\mathrm{r}} + \boldsymbol{v}_{\mathrm{w}} \\ \boldsymbol{v} &= \boldsymbol{v}_{\mathrm{r}} + \boldsymbol{R}_{\mathrm{IB}}^{\mathrm{T}} \boldsymbol{V}_{\mathrm{w}} \end{aligned} \tag{2.88}$$

where $\boldsymbol{V}_{\mathrm{w}}$ is the wind velocity vector defined in the inertial-fixed frame. The equations of motion described by Equation (2.79) can be written as:

$$\dot{\boldsymbol{X}} = \boldsymbol{R}_{\mathrm{IB}}\boldsymbol{v}_{\mathrm{r}} + \boldsymbol{V}_{\mathrm{w}} \tag{2.89a}$$

$$\dot{\boldsymbol{\Theta}} = \boldsymbol{L}_{\mathrm{IB}}\boldsymbol{\omega} \tag{2.89b}$$

$$\dot{\boldsymbol{v}}_{\mathrm{r}} = \boldsymbol{v}_{\mathrm{r}} \times \boldsymbol{\omega} + \frac{1}{m}\boldsymbol{F}_A + \frac{1}{m}\boldsymbol{F}_J + \frac{1}{m}\boldsymbol{R}_{\mathrm{IB}}^{\mathrm{T}}\boldsymbol{F}_G - \boldsymbol{R}_{\mathrm{IB}}^{\mathrm{T}}\dot{\boldsymbol{V}}_{\mathrm{w}} \tag{2.89c}$$

$$\dot{\boldsymbol{\omega}} = \boldsymbol{I}^{-1}\left(\boldsymbol{I}\boldsymbol{\omega} \times \boldsymbol{\omega}\right) + \boldsymbol{I}^{-1}\boldsymbol{M}_A \tag{2.89d}$$

where Equation (2.89c) is derived from Newton's second law of motion, written in the non-inertial body-fixed frame, as follows:

$$m\frac{d}{dt}(\boldsymbol{v}_{\mathrm{r}} + \boldsymbol{R}_{\mathrm{IB}}^{\mathrm{T}}\boldsymbol{V}_{\mathrm{w}}) = m(\boldsymbol{v}_{\mathrm{r}} + \boldsymbol{R}_{\mathrm{IB}}^{\mathrm{T}}\boldsymbol{V}_{\mathrm{w}}) \times \boldsymbol{\omega} + \boldsymbol{F}_A + \boldsymbol{F}_J + \boldsymbol{R}_{\mathrm{IB}}^{\mathrm{T}}\boldsymbol{F}_G$$

we compute

$$m\left(\dot{\boldsymbol{v}}_{\mathrm{r}} + \dot{\boldsymbol{R}}_{\mathrm{IB}}^{\mathrm{T}}\boldsymbol{V}_{\mathrm{w}} + \boldsymbol{R}_{\mathrm{IB}}^{\mathrm{T}}\dot{\boldsymbol{V}}_{\mathrm{w}}\right) = m\boldsymbol{v}_{\mathrm{r}} \times \boldsymbol{\omega} + m\boldsymbol{R}_{\mathrm{IB}}^{\mathrm{T}}\boldsymbol{V}_{\mathrm{w}} \times \boldsymbol{\omega} + \boldsymbol{F}_A + \boldsymbol{F}_J + \boldsymbol{R}_{\mathrm{IB}}^{\mathrm{T}}\boldsymbol{F}_G$$

Moving the wind-related terms from the left to the right gives

$$m\dot{\boldsymbol{v}}_{\mathrm{r}} = m\boldsymbol{v}_{\mathrm{r}} \times \boldsymbol{\omega} + m\boldsymbol{v}_{\mathrm{w}} \times \boldsymbol{\omega} + \boldsymbol{F}_A + \boldsymbol{F}_J + \boldsymbol{R}_{\mathrm{IB}}^{\mathrm{T}}\boldsymbol{F}_G - m\boldsymbol{v}_{\mathrm{w}} \times \boldsymbol{\omega} - m\boldsymbol{R}_{\mathrm{IB}}^{\mathrm{T}}\dot{\boldsymbol{V}}_{\mathrm{w}}$$

Simplifying, we find

$$m\dot{\boldsymbol{v}}_{\mathrm{r}} = m\boldsymbol{v}_{\mathrm{r}} \times \boldsymbol{\omega} + \boldsymbol{F}_A + \boldsymbol{F}_J + \boldsymbol{R}_{\mathrm{IB}}^{\mathrm{T}}\boldsymbol{F}_G - m\boldsymbol{R}_{\mathrm{IB}}^{\mathrm{T}}\dot{\boldsymbol{V}}_{\mathrm{w}}$$

Finally, dividing through by mass gives

$$\dot{\boldsymbol{v}}_{\mathrm{r}} = \boldsymbol{v}_{\mathrm{r}} \times \boldsymbol{\omega} + \frac{1}{m}\boldsymbol{F}_A + \frac{1}{m}\boldsymbol{F}_J + \frac{1}{m}\boldsymbol{R}_{\mathrm{IB}}^{\mathrm{T}}\boldsymbol{F}_G - \boldsymbol{R}_{\mathrm{IB}}^{\mathrm{T}}\dot{\boldsymbol{V}}_{\mathrm{w}}$$

In Equation (2.89d), $\boldsymbol{I}$ is the aircraft moment of inertia matrix defined in the body-fixed reference frame.

$$\boldsymbol{I} = \begin{bmatrix} I_{xx} & -I_{xy} & -I_{xz} \\ -I_{xy} & I_{yy} & -I_{yz} \\ -I_{xz} & -I_{yz} & I_{zz} \end{bmatrix} \tag{2.90}$$

For fixed-wing aircraft whose x-z plane is a plane of symmetry, $I_{xy} = I_{yz} = 0$.

2.5 Wind Velocity

In this section, the wind velocity vector field is defined and discussed. In Section 2.5.1, the wind velocity vector field is defined and decomposed into a slowly varying, deterministic mean value and fast-varying, random fluctuation components. In Section 2.5.2, the random fluctuation components of the wind are discussed in more detail. Finally, in Section 2.5.3, the rate of change of the wind velocity is discussed.

2.5.1 Wind Velocity Vector Field

The wind is a three-dimensional vector field that varies in time and space. We denote the wind velocity vector at some position $\boldsymbol{X} = [x, y, z]^{\mathrm{T}}$ and time t as

$$\boldsymbol{W}(\boldsymbol{X}, t) = [W_x(\boldsymbol{X}, t), W_y(\boldsymbol{X}, t), W_z(\boldsymbol{X}, t)]^{\mathrm{T}} \tag{2.91}$$

The wind velocity vector can be decomposed into a slowly varying, deterministic mean value $\bar{\boldsymbol{W}}(\boldsymbol{X}, t)$ and fast-varying, random fluctuations $\tilde{\boldsymbol{W}}(\boldsymbol{X}, t)$ from the mean:

$$\boldsymbol{W}(\boldsymbol{X}, t) = \bar{\boldsymbol{W}}(\boldsymbol{X}, t) + \tilde{\boldsymbol{W}}(\boldsymbol{X}, t) \tag{2.92}$$

2.5.2 Atmospheric Turbulence

Associated with any given point $\boldsymbol{X}$ and time t, there is a 3×3 correlation matrix $\boldsymbol{R}(\boldsymbol{X}, t, \boldsymbol{\zeta}, \tau)$ defined as the ensemble average of the outer product of $\tilde{\boldsymbol{W}}(\boldsymbol{P}, t)$ with $\tilde{\boldsymbol{W}}(\boldsymbol{P}+\boldsymbol{\zeta}, t+\tau)$, where $\boldsymbol{\zeta}$ and τ are the spatial and temporal correlation variables, respectively. The components of the correlation matrix are

$$R_{ij}(\boldsymbol{X}, t, \boldsymbol{\zeta}, \tau) = < \tilde{W}_i(\boldsymbol{X}, t)\tilde{W}_j(\boldsymbol{X} + \boldsymbol{\zeta}, t + \tau) > \tag{2.93}$$

for $i, j \in \{x, y, z\}$, where $< \cdot, \cdot >$ denotes the ensemble average. The component functions R_{ij} provide an incomplete description of the wind turbulence, modeled as a random process, but it is common to characterize turbulence using the information contained in R_{ij}. The functional form of these component functions and the corresponding parameter values depend on meteorological conditions, terrain, and other factors. Atmospheric turbulence is often well characterized by one or more of the following assumptions [30, Ch. 13].

Assumption 2. Common Assumptions Concerning Atmospheric Turbulence

a) The joint probability density functions underlying the correlation functions (2.93) are Gaussian.

b) The process is stationary: R_{ij} does not depend on time t for $i, j \in \{x, y, z\}$.

c) The process is homogeneous: R_{ij} does not depend on position $\boldsymbol{X}$ for $i, j \in \{x, y, z\}$.

d) The process is isotropic: R_{ij} does not depend on the orientation of the frame in which the wind vector is defined. Equivalently, the mean-square velocity components are equal in every direction: $\langle \tilde{W}_x^2 \rangle = \langle \tilde{W}_y^2 \rangle = \langle \tilde{W}_z^2 \rangle = \sigma^2$.

At low altitudes, atmospheric turbulence varies with height; thus, Assumption 1d does not hold.

2.5.3 Rate of Change of Wind

The rate of change of the wind velocity as seen by a particle moving along a trajectory $\boldsymbol{X}(t)$ is

$$\frac{d}{dt}\boldsymbol{W}(\boldsymbol{X}, t) = \frac{\partial}{\partial t}\bar{\boldsymbol{W}} + \nabla\bar{\boldsymbol{W}}\frac{d\boldsymbol{X}}{dt} + \frac{\partial}{\partial t}\tilde{\boldsymbol{W}} + \nabla\tilde{\boldsymbol{W}}\frac{d\boldsymbol{X}}{dt} \tag{2.94}$$

If we assign a body-fixed reference frame to the particle at position $\boldsymbol{X}(t)$ to represent an aircraft, the spatial gradient of the wind velocity vector can be expressed in this frame of reference as

$$\nabla\boldsymbol{v}_{\mathrm{w}} = \boldsymbol{R}_{\mathrm{IB}}^{\mathrm{T}}\nabla\boldsymbol{W}\boldsymbol{R}_{\mathrm{IB}} = \begin{bmatrix} \frac{\partial u_{\mathrm{w}}}{\partial x} & \frac{\partial u_{\mathrm{w}}}{\partial y} & \frac{\partial u_{\mathrm{w}}}{\partial z} \\ \frac{\partial v_{\mathrm{w}}}{\partial x} & \frac{\partial v_{\mathrm{w}}}{\partial y} & \frac{\partial v_{\mathrm{w}}}{\partial z} \\ \frac{\partial w_{\mathrm{w}}}{\partial x} & \frac{\partial w_{\mathrm{w}}}{\partial y} & \frac{\partial w_{\mathrm{w}}}{\partial z} \end{bmatrix} \tag{2.95}$$

where $\boldsymbol{v}_{\mathrm{w}} = [u_{\mathrm{w}}, v_{\mathrm{w}}, w_{\mathrm{w}}]^{\mathrm{T}}$ is the wind velocity vector expressed in the body frame and $\boldsymbol{R}_{\mathrm{IB}}$ is the rotation matrix that maps free vectors from the body frame to the inertial frame. The spatial gradient matrix in Equation (2.95) can be decomposed into a symmetric part representing dilation and a skew-symmetric part representing rotation. For a fixed-wing aircraft, the effect of dilation can be ignored. The effect of rotation is dominated by certain aspects of the aircraft geometry such that the effective flow angular rate $\boldsymbol{\omega}_{\mathrm{w}} = [p_{\mathrm{w}}, q_{\mathrm{w}}, r_{\mathrm{w}}]^{\mathrm{T}}$

felt by the aircraft is [31]

$$p_{\mathrm{w}} = -\frac{\partial w_{\mathrm{w}}}{\partial y} \qquad q_{\mathrm{w}} = \frac{\partial w_{\mathrm{w}}}{\partial x} \qquad r_{\mathrm{w}} = \frac{\partial v_{\mathrm{w}}}{\partial x} \tag{2.96}$$

In this paper, we neglect the gradient of the mean wind velocity $\bar{\boldsymbol{W}}$ due to the nature of the aircraft's flight. For fixed-wing aircraft flying straight and level at a constant speed and altitude, the aircraft speed is often significantly higher than the mean wind velocity and the velocity fluctuations. As a result, the turbulent fluctuations can be treated as a frozen pattern advecting with the mean wind velocity $\bar{\boldsymbol{W}}$ [30, Ch. 13]. Summarizing the points above, we assume the following conditions hold over the scale of the aircraft motion.

Assumption 3. Steady, Uniform Mean Wind and Frozen Turbulence

a) Steady mean wind: The mean wind velocity is constant: $\frac{\partial}{\partial t}\bar{\boldsymbol{W}}(\boldsymbol{X}, t) = \mathbf{0}$.

b) Uniform mean wind: The gradient of the mean wind velocity is zero: $\nabla\bar{\boldsymbol{W}}(\boldsymbol{X}, t) = \mathbf{0}$.

c) Taylor's hypothesis: Atmospheric turbulence is a frozen pattern that varies only in space: $\frac{\partial}{\partial t}\tilde{\boldsymbol{W}}(\boldsymbol{X}, t) = \mathbf{0}$.

The first two assumptions imply that $\bar{\boldsymbol{W}}$ is a constant vector. In practice, the mean wind will vary slowly over the course of a flight. These variations are captured by measurement updates to model-based estimates. In wind estimation, the dynamics of the total wind velocity are often assumed to be driven by a Gaussian white noise process. For the scenario considered here,

$$\frac{d}{dt}\boldsymbol{W}(\boldsymbol{X}, t) = \frac{d}{dt}\left(\bar{\boldsymbol{W}} + \tilde{\boldsymbol{W}}(\boldsymbol{X})\right) = \nabla\tilde{\boldsymbol{W}}\frac{d\boldsymbol{X}}{dt} = \tilde{\boldsymbol{w}}_W \tag{2.97}$$

where the stochastic wind velocity fluctuation $\tilde{\boldsymbol{W}}$ is assumed to be a continuous-time random walk whose generalized derivative $\tilde{\boldsymbol{w}}_W$ is continuous-time white noise [32, Ch. 3]. Finally, we define the apparent wind velocity vector, $\boldsymbol{V}_{\mathrm{w}}(t)$, as the velocity of the wind expressed in the inertial frame at the current aircraft position $\boldsymbol{X}(t)$ assuming that the aircraft is absent. That is, the wind velocity vector $\boldsymbol{V}_{\mathrm{w}}$ is the evaluation of the wind vector field $\boldsymbol{W}$ along the aircraft's trajectory:

$$\boldsymbol{V}_{\mathrm{w}}(t) = [V_{\mathrm{w},x}(t), V_{\mathrm{w},y}(t), V_{\mathrm{w},z}(t)]^{\mathrm{T}} := \boldsymbol{W}(\boldsymbol{X}(t), t) \tag{2.98}$$

Chapter 3

Literature Review

This chapter provides a comprehensive literature review on unsteady aerodynamic models and wind estimation methods. Section 3.1 presents a review of unsteady aerodynamic models, while Section 3.2 discusses wind estimation methods. The literature review presented in Section 3.2 is published in [25], where the author of this dissertation collaborated as a second author.

3.1 Unsteady Aerodynamics Models

The aerodynamic forces and moments that act on an aircraft can be described as algebraic equations; the forces and moments are generally described by non-dimensionalized force and moment coefficients. These equations usually contain stability and control derivatives. See Figure 3.1 for an illustration of an airfoil. Often, the aerodynamic models don't include the unsteady effects, which have dynamics; the models assume instantaneous effects only. In this section, the aerodynamic models that include unsteady effects are reviewed, and the conventional aerodynamic models like the ones shown in Figure 3.1 are extended to include the dynamics of unsteady effects.

Consider an airfoil moving forward with velocity u and downward with velocity w in still air from an origin point O. The angle between the chord axis of the airfoil and the relative wind vector v_w is the angle of attack denoted as α. The lift force that acts on the airfoil can

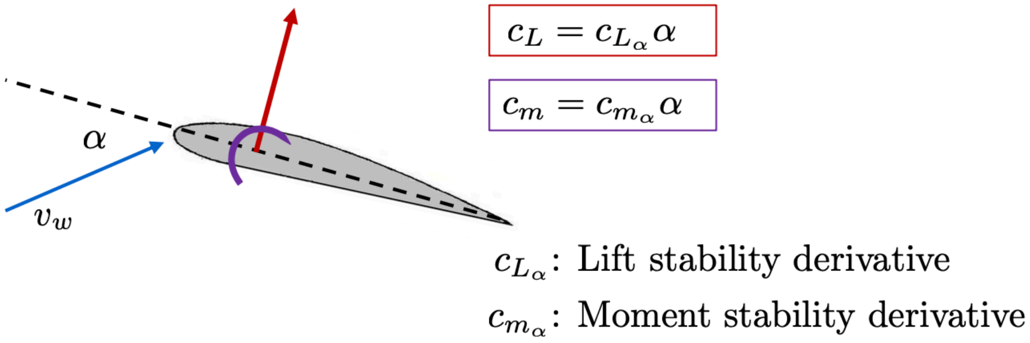

Figure 3.1: Example of aerodynamic models

be described by an aerodynamic lift coefficient c_L. See Figure 3.2 for an illustration.

The lift force acting on the aircraft has unsteady dynamics that conventional aerodynamic models don't include. Instead, the conventional lift coefficient force model assumes that a change in the angle of attack corresponds to an instantaneous change in force; that is, the memory effects (unsteady effects) are ignored. Here, three models that characterize the lift force that is acting on the airfoil, depicted in Figure 3.2, will be discussed [33]: 1) an aerodynamic model that ignores unsteady effects, 2) aerodynamic model that approximated unsteady effects, and 3) aerodynamic model that includes unsteady effects.

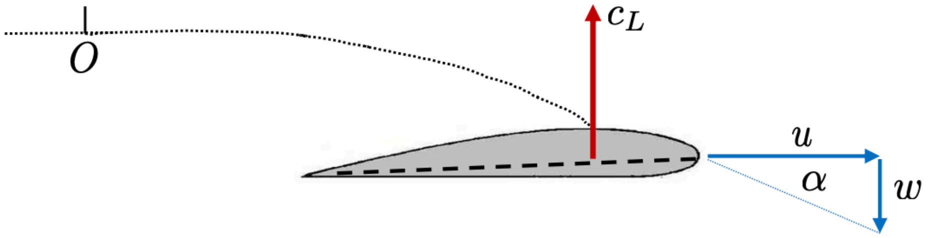

Figure 3.2: Airfoil moving through still air

The aerodynamic model that completely ignores unsteady effects is given as a function of the lift stability derivative with respect to angle of attack c_{L_α} and angle of attack α [33]:

$$c_L = c_{L_\alpha}\alpha \tag{3.1}$$

The coefficient of lift model, given by Equation (3.1), is modeled such that a change in angle of attack corresponds to an instantaneous change in lift force. In this case, unsteady effects (unsteady dynamics) that are present are ignored.

The aerodynamic model that apprpoximates the unsteady effects is given as a fucntion of the different lift stability derivative with respect to angle of attack c_{L_α}, the stability derivative with respect to the rate of angle of attack $c_{L_{\dot{\alpha}}}$, angle of attck α, and the rate of change of angle of attack $\dot{\alpha}$ [33]:

$$c_L = c_{L_\alpha}\alpha + c_{L_{\dot{\alpha}}}\dot{\alpha} \tag{3.2}$$

The lift coefficient model, as given by Equation (3.2), expands upon the aerodynamic model by including a component that approximates unsteady effects. However, it still ignores the dynamics of the unsteady effects acting on the airfoil.

The aerodyanmic model that includes unsteady effect is given as convolution intergral in terms of a time varying indicial fucntion $c_{L_\alpha}(t-\tau)$, and the time varying rate of change of angle of attack $\dot{\alpha}(\tau)$ [33]:

$$c_L = \int_0^t c_{L_\alpha}(t-\tau)\dot{\alpha}(\tau)d\tau \tag{3.3}$$

The lift coefficient model, as given by Equation (3.3), includes a convolution fucntion to charactize the unteady effects induced by airfoil in motion.

In Figure 3.3, a plot of the angle of attack with respect to time and a plot of the aerodynamic lift coefficient with respect to time are given. The purpose of Figure 3.3 is to visually demonstrate Equations (3.1), (3.2), and (3.3). The blue line represents the angle of attack time history, the green line represents the lift coefficient as modeled by Equation (3.1), the red line represents the lift coefficient as modeled by Equation (3.3), and the purple arrow represents the difference between the lift coefficients modeled by Equation (3.1) and Equation (3.3).

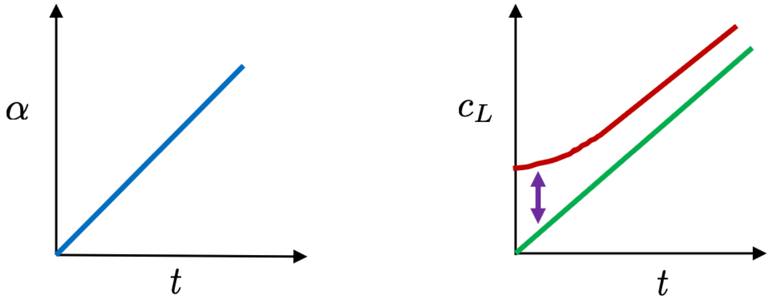

Figure 3.3: Coefficient of lift and angle of attack

Starting from Equation (3.3) and making a few assumtpions one can retrive Equation (3.2) [33, Ch. 4].

$$\begin{aligned}
c_L &= \int_0^t c_{L_\alpha}(t-\tau)\dot{\alpha}(\tau)d\tau \\
c_L &= \dot{\alpha}\int_0^t c_{L_\alpha}(t-\tau)d\tau \\
c_L &= \dot{\alpha}\int_0^t c_{L_\alpha} - F(t-\tau)d\tau \\
c_L &= \dot{\alpha}c_{L_\alpha}t + \dot{\alpha}\int_0^t -F(t-\tau)d\tau \\
c_L &= c_{L_\alpha}\alpha - \dot{\alpha}\int_0^t F(t-\tau)d\tau \\
c_L &= c_{L_\alpha}\alpha + c_{L_{\dot{\alpha}}}\dot{\alpha}
\end{aligned} \tag{3.4}$$

In Equation (3.4), the $\dot{\alpha}$ is assumed to be a time invariant, and $\int_0^t F(t-\tau)d\tau$ is represented by a constant stability derivative. The purple arrow in Figure 3.3 represents $c_{L_{\dot{\alpha}}}\dot{\alpha}$ which accounts for the difference between the lift coefficients modeled by Equation (3.1) and

Equation (3.3).

3.1.1 Two Dimensional Unsteady Models

Here, we briefly discuss Wagner's [34], Kussner's, and Theordorsen's [35] lift formulations. In all three cases, the lift formations include non-circulatory and circulatory components; here, only the circulatory components are discussed. Wagner's lift formulation is given as a convolution function as described above. But to make the comparison between Wagner's, Kussner's and Theodoersen's lift formulation easy, Wagner's indicial function is shown as $\phi_w(t-\tau)$ as opposed to $c_{L_\alpha}(t-\tau)$ in this subsection.

Wagner's Lift Formulation

Wagner's lift formulation [34] is derived for an airfoil that is moving forward with velocity u and downward with velocity w in still air from an origin point O as illustrated in Figure 3.2. The angle between the chord axis of the airfoil and the relative wind vector v_w is the angle of attack denoted as α. The lift force that acts on the airfoil is described by an aerodynamic lift coefficient c_L.

$$c_L = \int_0^t \phi_w(t-\tau)\dot{\alpha}(\tau)d\tau \tag{3.5}$$

where ϕ_w is Wagner's inficial fucntion, and τ is some delayed time such that $\tau < t$.

Kussner's Lift Formulation

Kussner's lift formulation is derived for an airfoil that is moving forward with velcoity u and through an upward wind gust v_w see Figure 3.4. The angle between the chord axis of the airfoil and the relative wind vector v_w is the angle of attack denoted as α. The lift force that acts on the airfoil is described by an aerodynamic lift coefficient c_L.

$$c_L = \int_0^t \phi_k(t-\tau)\dot{\alpha}(\tau)d\tau \tag{3.6}$$

where ϕ_w is Kussner's inficial fucntion, and τ is some delayed time such that $\tau < t$. The differene between Wagner's and Kussner's lift formualtion is the structure and value of the respective indicial functions. That said, both decribed the unsteady effects induced by the motion of the airfoil.

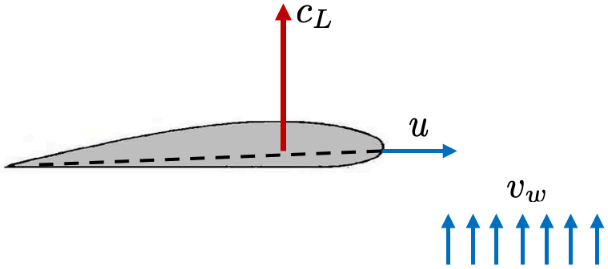

Figure 3.4: Airfoil moving through upward wind gust

Theodorsen's Lift Formulation

Theordorsen's lift formulation [17, 35] is derived for a pitching thin airfoil about an axis point in a unform wind v_w. See Figure 3.5 illustration. The angle between the chord axis of the thin airfoil and the wind vector v_w is the angle of attack denoted as α. The lift force that acts on the airfoil is described by an aerodynamic lift coefficient c_L.

$$c_L = 2\pi\alpha C(k) \tag{3.7}$$

where $C(k)$ is Theodorsen's transfer function defined in the frequency domain. Theodoersen's transfer function $C(k)$ characterizes the transient dynamics of the wake vortices generated

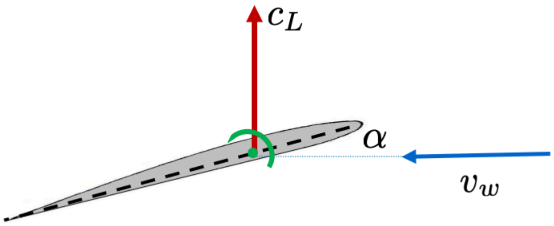

Figure 3.5: Airfoil pitching about an axis point in unifrom flow

aft of the trailing edge in response to an unsteady motion. The quasi-steady terms $2\pi\alpha$, in Equation 3.7, describe the instantaneous lift generated during an unsteady motion, and the wake vortices, captured by $\bar{C}(k)$, have a diminishing and lagging effect on the instantaneous lift. Theodorsen's function $\bar{C}(k)$ is parameterized by the reduced frequency $k = \frac{\omega\bar{c}}{2V_{\mathrm{r}}}$, where ω is the angular rate of the airfoil. Theodorsen's function [35] is:

$$C(k) = \frac{H_1^{(2)}(k)}{H_1^{(2)}(k) + iH_0^{(2)}(k)} \tag{3.8}$$

where $H_x^{(2)} = J_x - iY_x$ is the Hankel function, which is in turn defined in terms of the Bessel functions of the first and second kind, J_x and Y_x, respectively. A reduced frequency of zero describes a steady motion; thus, $C(0) = 1$, in which case c_L is only a function of the angle of attack.

Theodorsen's transfer function can be approximated by a proper rational transfer function [36, 37] $C(s)$, where s is the Laplace variable. The transfer function $C(s)$ is an empirical rational transfer function, where s is a variable defined in the Laplace domain. The reduced frequency k is a single frequency parameter corresponding to harmonic motion; however, the Laplace variable s is an independent variable defined on the entire complex plane, meaning the lift coefficient can be described by linear, time-invariant models. Furthermore, $C(s)$ or the realization of $C(s)$ can be identified empirically from data [17] using system identification methods [4, 5, 24]. In Chapter 5, the parameters of the linear, time-invariant model of $C(s)$ will be identified from flight data for the research aircraft used in this dissertation.

Wagner's Indicial Function and Theodorsen's Function

Wagner's indicial response function and Theodorsen's transfer fucntion function are related by a Laplace transform pair [17, 38, 39].

$$C(s) = s\int_0^\infty \phi(t)e^{-st}dt \tag{3.9}$$

Equation (3.9) shows that Wagner's indicial response function and the Theodorsen transfer function are equivalent ways of representing the effect on the lift of the transient evolution of the wake vortices due to an unsteady motion.

3.1.2 Three Dimensional Unsteady Models

The aerodynamic forces and moments acting on an aircraft in arbitrary motion can be approximated by time-invariant linear or polynomial terms. A longitudinal linear unsteady aerodynamic model in terms of indicial functions was given in [40]. Then, aerodynamic coefficients as functions of state and input variables, which include linear unsteady aerodynamics as a special case, were proposed in [16]. Following [16], the aircraft aerodynamic characteristics [4] can be given as:

$$\begin{aligned} C_a(t) &= C_a[\infty;\boldsymbol{\delta}(t)] \\ &\quad + \int_0^t \boldsymbol{C}_{a_{\zeta_1}}[t-\tau;\boldsymbol{\zeta}(\tau)]^T \frac{d}{d\tau}\boldsymbol{\zeta}_1(\tau)d\tau + \frac{l}{V_{\mathrm{r}}}\int_0^t \boldsymbol{C}_{a_{\zeta_2}}[t-\tau;\boldsymbol{\zeta}(\tau)]^T \frac{d}{d\tau}\boldsymbol{\zeta}_2(\tau)d\tau \end{aligned} \tag{3.10}$$

where $a \in \{X, Z, m, Y, l, n\}$, $\boldsymbol{\delta} = [\delta_a, \delta_e, \delta_r]^T$, $\boldsymbol{\zeta}_1 = [\alpha, \beta]^T$, $\boldsymbol{\zeta}_2 = [p, q, r]^T$, $\boldsymbol{\zeta} = [\boldsymbol{\zeta}_1^T, \boldsymbol{\zeta}_2^T]^T$, $\boldsymbol{l} = [b/2, \bar{c}/2]^T$, $C_a(t)$ is the aerodynamic force or moment coefficient, $C_a[\infty; \boldsymbol{\delta}(t)]$ is the steady-state values of the aerodynamic force or moment bias and control derivative terms, and $\boldsymbol{C}_{a_{\zeta_i}}(t)$ is the vector of indicial functions whose elements are the responses to a unit step in $\boldsymbol{\zeta}$.

Steady-state Assumption on Attitude Rates and Control Inputs

The effects of the attitude rates $\boldsymbol{\zeta}_2$ and control inputs $\boldsymbol{\delta}$ on the aerodynamic force and moment coefficients are assumed to be instantaneous; that is, the unsteady effects due to attitude rates and control inputs are considered to be negligible. As a result, Equation (3.10) can be re-written as follows:

$$C_a(t) = C_a[\infty; \boldsymbol{\delta}(t)] + \frac{l}{V_\mathrm{r}} \boldsymbol{C}_{a_{\zeta_2}}[\infty; \boldsymbol{\zeta}_1(\tau), \mathbf{0}]^T \boldsymbol{\zeta}_2(\tau) + \int_0^t \boldsymbol{C}_{a_{\zeta_1}}[t-\tau; \boldsymbol{\zeta}(\tau)]^T \frac{d}{d\tau} \boldsymbol{\zeta}_1(\tau) d\tau \tag{3.11}$$

Equation (3.11) can be explicitly written in terms of the steady-state stability and control derivative values as follows:

$$\begin{aligned} C_a(t) = {} & C_{a_0}(\infty) + C_{a_{\delta_a}}(\infty)\delta_a(t) + C_{a_{\delta_e}}(\infty)\delta_e(t) + C_{a_{\delta_r}}(\infty)\delta_r(t) + \frac{b}{2V_\mathrm{r}} C_{a_p}(\infty) p(t) \\ & + \frac{\bar{c}}{2V_\mathrm{r}} C_{a_q}(\infty) q(t) + \frac{b}{2V_\mathrm{r}} C_{a_r}(\infty) r(t) + \int_0^t C_{a_\alpha}(t-\tau)\dot{\alpha}(\tau) d\tau \\ & + \int_0^t C_{a_\beta}(t-\tau)\dot{\beta}(\tau) d\tau \end{aligned} \tag{3.12}$$

where $C_{a_0}(\infty)$ is the corresponding steady-state bias term, $C_{a_{\delta_a}}(\infty)$ is the steady-state aileron control derivative term, $C_{a_{\delta_e}}(\infty)$ is the steady-state elevator control derivative term, $C_{a_{\delta_r}}(\infty)$ is the steady-state rudder control derivative term, $C_{a_p}(\infty)$ is the steady-state roll rate stability derivative term, $C_{a_a}(\infty)$ is the steady-state pitch rate stability derivative term, and

$C_{a_r}(\infty)$ is the steady-state yaw rate stability derivative term. For simplicity, the ∞ and t are dropped from Equation (3.12) in proceeding text expect in the terms containing the indicial functions $C_{a_\alpha}(t-\tau)$ and $C_{a_\beta}(t-\tau)$.

$$\begin{aligned} C_a = C_{a_0} + C_{a_{\delta_a}}\delta_a + C_{a_{\delta_e}}\delta_e + C_{a_{\delta_r}}\delta_r + \frac{b}{2V_\mathrm{r}}C_{a_p}p + \frac{\bar{c}}{2V_\mathrm{r}}C_{a_q}q + \frac{b}{2V_\mathrm{r}}C_{a_r}r \\ + \int_0^t C_{a_\alpha}(t-\tau)\dot{\alpha}(\tau)d\tau + \int_0^t C_{a_\beta}(t-\tau)\dot{\beta}(\tau)d\tau \end{aligned} \tag{3.13}$$

The Use of Deficiency Functions for Modeling Unsteady Dynamics

The indicial function approaches steady-state as the argument $(t-\tau)$ increases to infinity; therefore, the indicial function [4] can be expressed as:

$$\boldsymbol{C}_{a_{\zeta_i}}[t-\tau;\boldsymbol{\zeta}(\tau)] = \boldsymbol{C}_{a_{\zeta_i}}[\infty;\boldsymbol{\zeta}(\tau)] - \boldsymbol{F}_{a_{\zeta_i}}[t-\tau;\boldsymbol{\zeta}(\tau)] \tag{3.14}$$

where $C_{a_{\zeta_j}}[\infty;\boldsymbol{\zeta}(\tau)]$ is the steady-state sensitivity of the coefficient C_a to changes in $\boldsymbol{\zeta}_j$, with the remaining variables in $\boldsymbol{\zeta}$ fixed at the instantaneous values $\boldsymbol{\zeta}(\tau)$, and $F_{a_{\zeta_j}}[t-\tau;\boldsymbol{\zeta}(\tau)]$ is the deficiency function, which approaches zero as $(t-\tau)\rightarrow\infty$. Equation (3.14) can be substituted into Equation (3.13), and the steady-state parameters can be integrated over time to give

$$\begin{aligned} C_a = C_{a_0} + C_{a_{\delta_a}}\delta_a + C_{a_{\delta_e}}\delta_e + C_{a_{\delta_r}}\delta_r + \frac{b}{2V_\mathrm{r}}C_{a_p}p + \frac{\bar{c}}{2V_\mathrm{r}}C_{a_q}q + \frac{b}{2V_\mathrm{r}}C_{a_r}r \\ + \int_0^t \left(C_{a_\alpha}(\infty) - F_{a_\alpha}(t-\tau)\right)\dot{\alpha}(\tau)d\tau + \int_0^t \left(C_{a_\beta}(\infty) - F_{a_\beta}(t-\tau)\right)\dot{\beta}(\tau)d\tau \end{aligned} \tag{3.15}$$

where $C_{a_\alpha}(\infty)$ and $C_{a_\beta}(\infty)$ are the steady-state stability derivative with respect to α and β, and $F_{a_\alpha}(t-\tau)$ and $F_{a_\beta}(t-\tau)$ are the deficiency functions. As a result, Equation (3.15) can be explicitly written as follows:

$$\begin{aligned} C_a = {} & C_{a_0} + C_{a_{\delta_a}}\delta_a + C_{a_{\delta_e}}\delta_e + C_{a_{\delta_r}}\delta_r + \frac{b}{2V_\mathrm{r}}C_{a_p}p + \frac{\bar{c}}{2V_\mathrm{r}}C_{a_q}q + \frac{b}{2V_\mathrm{r}}C_{a_r}r \\ & + C_{a_\alpha}\alpha + C_{a_\beta}\beta - \int_0^t F_{a_\alpha}(t-\tau)\dot{\alpha}(\tau)d\tau - \int_0^t F_{a_\beta}(t-\tau)\dot{\beta}(\tau)d\tau \end{aligned} \tag{3.16}$$

Longitudinal and Lateral-Directional Decoupling of the Unsteady Models

A fixed-wing aircraft is symmetric about its $x-z$ plane; as a result, the unsteady aerodynamic model can be written such that the longitudinal terms and lateral-directional terms are decoupled. The symmetric force and moment coefficients C_X, C_Z, and C_m are assumed to be independent from asymmetric variables β, p, r, δ_a, δ_r and $\dot{\beta}$. The asymmetric force and moment coefficients C_Y, C_l, C_n are assumed to be independent from symmetric variables α, q, δ_e, and $\dot{\alpha}$. Hence, both the indicial function-based equation, Equations 3.13, and the deficiency-based equation, 3.16, can be written as follows:

$$C_b = C_{b_0} + C_{b_{\delta_e}}\delta_e + \frac{\bar{c}}{2V_\mathrm{r}}C_{b_q}q + \int_0^t C_{b_\alpha}(t-\tau)\dot{\alpha}(\tau)d\tau \tag{3.17a}$$

$$C_c = C_{c_0} + C_{c_{\delta_a}}\delta_a + C_{c_{\delta_r}}\delta_r + \frac{b}{2V_\mathrm{r}}C_{c_p}p + \frac{b}{2V_\mathrm{r}}C_{c_r}r + \int_0^t C_{c_\beta}(t-\tau)\dot{\beta}(\tau)d\tau \tag{3.17b}$$

where $b \in \{X, Z, m\}$ and $c \in \{Y, l, n\}$.

$$C_b = C_{b_0} + C_{b_{\delta_e}}\delta_e + \frac{\bar{c}}{2V_\mathrm{r}}C_{b_q}q + C_{b_\alpha}\alpha - \int_0^t F_{b_\alpha}(t-\tau)\dot{\alpha}(\tau)d\tau \tag{3.18a}$$

$$C_c = C_{c_0} + C_{c_{\delta_a}}\delta_a + C_{c_{\delta_r}}\delta_r + \frac{b}{2V_\mathrm{r}}C_{c_p}p + \frac{b}{2V_\mathrm{r}}C_{c_r}r + C_{c_\beta}\beta - \int_0^t F_{c_\beta}(t-\tau)\dot{\beta}(\tau)d\tau \tag{3.18b}$$

(3.18c)

In the following section, Equations (3.17) will be used to develop the unsteady reduced-order model for the research aircraft in this dissertation. However, other significant works have been done on developing an unsteady reduced-order model using Equations (3.18). For completeness, the development of a deficiency function-based reduced-order unsteady model will also be presented in the following section.

3.1.3 Reduced Order-Model Unsteady Model

Tobak and Shiff's unsteady [16, 40] have been used to develop a reduced-order unsteady model [41, 42, 43, 44]. The deficiency function-based reduced-order unsteady model begins with establishing a structure to the deficiency function [44]. For simplicity, only Equation (3.18b) is used to demonstrate the development of the deficiency function-based reduced-order unsteady model.

$$F_{b_\alpha}(t-\tau) = a_1 e^{-b_1 t} \tag{3.19a}$$

$$\eta(t) = \int_0^t e^{-b_1(t-\tau)} \hat{\dot{\alpha}}(\tau) d\tau \tag{3.19b}$$

The structure of the deficiency shown in Equations (3.19), can then be used to develop the reduced order model. Using Equation (3.19), Equation (3.18b) can written as follows:

$$\dot{\eta} = -b_1 \eta + \hat{\dot{\alpha}} \tag{3.20a}$$

$$C_b = C_{b_0} + C_{b_{\delta_e}} \delta_e + \frac{\bar{c}}{2V_\mathrm{r}} C_{b_q} q + C_{b_\alpha} \alpha - a_1 \eta \tag{3.20b}$$

The same approach applies to the lateral-directional equation given by Equation (3.18c) to get the corresponding reduced-order model.

Indificial Function based Reduced-Order Unsteady Model

The longitudinal and lateral-directional indicial function-based unsteady model given by Equation (3.17) is used to develop a reduced-order model as well. In this dissertation, this approach is preferred because it doesn't require knowledge angle of attack rate and sideslip rate, which will be significant for system identification and wind estimation work presented in the following chapters.

Based on the discussion given in Section 3.1.1, the indicial functions in Equations (3.17) have corresponding transfer functions.

$$C_{b_\alpha}(s) = s\int_0^\infty C_{b_\alpha}(t)e^{-st}dt \tag{3.21a}$$

$$C_{c_\alpha}(s) = s\int_0^\infty C_{c_\beta}(t)e^{-st}dt \tag{3.21b}$$

$$\tag{3.21c}$$

As a result, Equations (3.17) can be written in terms of proper rational transfer functions.

$$C_b = C_{b_0} + C_{b_{\delta_e}}\delta_e + \frac{\bar{c}}{2V_\mathrm{r}}C_{b_q}q + \mathcal{L}^{-1}\left\{C_{b_\alpha}(s)\alpha(s)\right\} \tag{3.22a}$$

$$C_c = C_{c_0} + C_{c_{\delta_a}}\delta_a + C_{c_{\delta_r}}\delta_r + \frac{b}{2V_\mathrm{r}}C_{c_p}p + \frac{b}{2V_\mathrm{r}}C_{c_r}r + \mathcal{L}^{-1}\left\{C_{c_\beta}(s)\beta(s)\right\} \tag{3.22b}$$

The state-space realizations of the transfer functions used to construct the unsteady reduced order model are:

$$C_{b_\alpha}(s) \longrightarrow \left[\begin{array}{c|c} A_{b_{\tilde{x}}} & B_{b_\alpha} \\ \hline C_{b_{\tilde{x}}} & C_{b_\alpha} \end{array}\right] \tag{3.23a}$$

$$C_{c_\beta}(s) \longrightarrow \left[\begin{array}{c|c} A_{c_{\tilde{x}}} & B_{c_\beta} \\ \hline C_{c_{\tilde{x}}} & C_{c_\beta} \end{array}\right] \tag{3.23b}$$

Finally, the longitudinal and lateral-directional indicial function-based unsteady model can be written in terms of the state-space parameters given in Equations (3.23). The longitudinal reduced order unsteady model is given as follows:

$$\dot{\tilde{x}}_b = A_{b_{\tilde{x}}}\tilde{x}_b + B_{b_\alpha}\alpha \tag{3.24a}$$

$$C_b = C_{b_0} + C_{b_{\delta_e}}\delta_e + C_{b_q}\hat{q} + C_{b_{\tilde{x}}}\tilde{x}_b + C_{b_\alpha}\alpha \tag{3.24b}$$

where $\hat{q} = \frac{q\bar{c}}{2V_\mathrm{r}}$ is the nondimensionalized pitch rate, and $\tilde{x}_b$ are the longitudinal unsteady state variables. Similarly, the lateral-directional reduced order unsteady model is given as follows:

$$\dot{\tilde{x}}_c = A_{c_{\tilde{x}}}\tilde{x}_c + B_{c_\beta}\beta \tag{3.25a}$$

$$C_c = C_{c_0} + C_{c_{\delta_a}}\delta_a + C_{c_{\delta_r}}\delta_r + C_{c_p}\hat{p} + C_{c_r}\hat{r} + C_{c_{\tilde{x}}}\tilde{x}_c + C_{c_\beta}\beta \tag{3.25b}$$

where $\hat{p} = \frac{p\bar{c}}{2V_\mathrm{r}}$ is the nondimensionalized roll rate, $\hat{r} = \frac{r\bar{c}}{2V_\mathrm{r}}$ is the nondimensionalized yaw rate, and $\tilde{x}_c$ are the lateral-directional unsteady state variables.

The reduced-order unsteady longitudinal and lateral-directional models given by Equations (3.24) and (3.25) are used in Chapter 5 and in Chapter 7. In Chapter 5, the stability derivatives, control derivatives, and unsteady parameters are identified from flight data collected using the research aircraft presented in Chapter 4. Furthermore, the identified reduced-order unsteady longitudinal and lateral-directional models in Chapter 5 are then used in Chapter 7 for unsteady aerodynamic model-based wind estimation.

3.2 Wind Velocity State Estimation

Two primary methods for estimating wind velocity using uncrewed aerial vehicles (UAVs) are direct measurement of relative wind velocity and indirect wind estimation from an aircraft's motion. The validation of indirect methods involves comparing the estimated wind velocity with a reliable source, such as direct measurements obtained from dedicated sensors on the aircraft [24, 45]. Wind velocity inferred from an aircraft's motion is derived from inertial and air-relative velocity measurements through the wind triangle relationship. The wind velocity can be divided into steady and turbulent components, as outlined in Section 2.5.1. The Dryden and von Kármán turbulence models are commonly employed to model air turbulence effects on aircraft motion [46]. As seen in [47] and [48], integrating turbulence models into indirect estimation schemes often utilizes the Dryden model. While other models, such as the Kaimal model [49] and the Mann model [50], exist, they are not extensively utilized for UAV wind estimation. Additionally, turbulent wind can be represented as a Gauss-Markov sequence [51] or as a random walk process [24]. Indirect wind estimation methods using UAVs, which involve solving the wind triangle, can be categorized as either model-based or model-free. Model-based techniques rely on aircraft kinematic and dynamic equations, while model-free methods do not depend on the aircraft's dynamic model. These approaches make use of various estimators and necessitate data from onboard sensors, typically including global navigation satellite system (GNSS) receivers, inertial measurement units (IMUs), magnetometers, Pitot probes, and, at times, flow vanes or multihole Pitot probes for the angle of attack and sideslip measurements, collectively known as an air data unit (ADU). Furthermore, both methods are employed in various estimation algorithms, such as a Kalman filter, extended Kalman filter, unscented Kalman filter, and other deterministic observers.

3.2.1 Model-based Wind Estimation Methods

Model-based methods for estimating wind generally require ground testing for inertial properties, wind tunnel testing for propulsion models [52], and both experimental and computational model identification for aerodynamic forces and moments [22, 24, 53]. These techniques apply to deterministic and non-deterministic systems and linear and nonlinear dynamic models. Additionally, alternative wind estimation methods involve optimization techniques to solve nonlinear optimal control problems, such as multi-objective optimization and model predictive static programming [54, 55]. Additionally, the tilt-based wind estimation methods utilizing multirotor aircraft are discussed in [56, 57, 58, 59]. These methods rely on the deviation of the multirotor's attitude from a trim hover condition and necessitate only attitude and position data from onboard GNSS and IMU sensors. Palomaki *et al.* [56] compare direct wind measurements using a sonic anemometer on a hexacopter with indirect model-based estimates from a hovering quadcopter. Segales *et al.* [57] utilize the CopterSonde for remote sensing in the atmospheric boundary layer, computing wind velocity from pitch angle measurements by having the aircraft hover in "wind vane" mode. Neumann *et al.* [58] develop a quadcopter aerodynamic model through wind tunnel testing and perform real-time wind estimation using GNSS-based inertial velocity measurements and the identified aerodynamic model with IMU and magnetometer data. Shelekhov *et al.* [59] estimate atmospheric turbulence using three multirotor aircraft hovering at different altitudes and compare their results with anemometer measurements.

Kalman and Extended Kalman Filter-Based Model-Based Wind Estimation

In [53, 60, 61], the wind is modeled is assumed to be dterministic, and the system's linearized motion equations are employed for wind estimation through a deterministic observer. In [60], a quadcopter's kinematic particle, dynamic particle, and rigid body models are introduced and used to estimate wind velocity by solving the wind triangle relationship with GNSS, IMU, magnetometer, and barometer data measurements. In [53], wind velocity estimates from the three quadcopter models are compared against sonic anemometer measurements. The study demonstrates that higher model fidelity improves wind speed estimates, with the rigid body model performing the best. Finally, in [61], the rigid body model-based wind estimates are acquired from a hover and steady ascent quadcopter, utilizing aerodynamic force and moment models identified from flight test data. This study also compares wind estimates in hover and ascent to SoDAR measurements.

Studies have investigated model-based wind estimation methods using either a Kalman Filter (KF) or an Extended Kalman Filter (EKF) [10, 11, 20, 21, 24, 62, 62, 63, 63, 64]. Both filters necessitate linearizing nonlinear system equations: a Kalman filter requires a linearized model around a nominal state, whereas an extended Kalamn filter linearizes around the current state estimate at each time step.

Hattenberger *et al.* [62] employs a dynamic particle model of a multirotor in a Kalman filter to infer wind estimates, assuming slow wind field variation relative to the aircraft. In another study, Xiang *et al.* [63] present quadcopter-based wind estimation from a steady flight in a straight line and steady hover flight using a Kalman filter. The estimated results closely matched anemometer measurements.

Petrich *et al.* [64] apply a two-state Kalman Filter, starting with a position estimate based on GNSS measurements and subsequently estimating orientation, airspeed, angular rate, and

3D wind velocity using measurements from an IMU and ADU, assuming a constant wind field. Langelaan *et al.* [10] implements a Kalman filter assuming a polynomial structure for the wind state, making it easier to implement a Kalman Filter for state estimation to enable real-time wind field querying to support autonomous dynamic soaring.

Torgesen *et al.* [65] use an error-state Kalman filter to estimate steady and turbulent air wake components on a hexacopter tethered behind a cruising vessel. Chen *et al.* [21] develop an invariant-extended Kalman filter that leverages the invariant dynamics of quadcopter kinematics and translational dynamics to generate error estimates consistent with the system's symmetries [66]. Tian *et al* [21] propose a method for modeling wind as a random walk process and employ a two-stage extended Kalman filter: the first extended Kalamn filter estimates angle of attack and angle of sideslip, while the second extended Kalman filter estimates air-relative velocity, orientation, and wind velocity based on GNSS, IMU, and Pitot probe measurements.

Sun *et al.* [20] have introduced a method for estimating wind for a tail-sitter UAV that operates in rotary, transitional, and wing-borne flight modes. This approach models wind as a random walk process and utilizes a cascaded extended Kalman filter. Pappu *et al.* [67] have employed an extended Kalman filter to estimate wind gusts for a hovering quadcopter, using only GNSS, IMU, and control actuation sensors while assuming gusts as filtered white noise. Lie *et al.* [11] present an approach for estimating wind that relies solely on GNSS and INS measurements and using a cascaded extended Kalman filter. Halefom *et al.* [24] presents an unsteady aerodynamic model-based wind estimator for a small fixed-wing aircraft in an extended Kalman filter.

Unscented Kalman Filter-Based Model-Based Wind Estimation

The unscented Kalman filter is used for model-based wind estimation in [12, 47, 52, 68, 69, 70]. The unscented Kalman filter does not require analytical linearization of the nonlinear equations of motion about a nominal state. Condomines *et al.* [52] present wind estimation and aircraft parameter identification based on flight experiments using a fixed-wing UAV where a square root unscented Kalman filter-based approach is proposed for wind velocity estimation. Larrabee *et al.* [12] investigate the use of a stand-alone unscented Kalman filter and a cooperative unscented Kalman filter for a leader-follower formation of fixed-wing aircraft where the follower senses the wake of the leader. Rhudy *et al.* [68] estimates wind velocity, assuming the wind acceleration is a random walk process using an unscented Kalman filter. Rhudy *et al.* [69] compares wind velocity estimates under two different wind models: (1) a random walk and (2) a Gauss-Markov process. Lee *et al.* [47] use a square-root unscented Kalman filter for wind and aircraft state estimation where the aircraft is exposed to time-varying prevailing wind and turbulence modeled using the Dryden model. Cooper *et al.* [70] perform quadcopter wind estimation using an unscented Kalman filter for source localization in two scenarios: (1) a hovering quadcopter and (2) a quadcopter that hovers for 10 seconds then moves to a sequence of two waypoints, loitering at each for 10 seconds.

Optimization Methods-Based and Alternative Approaches for Model-based Wind Estimation

The use of optimization methods, such as multi-objective optimization and model predictive static programming, have been used for model-based wind estimation [54, 55, 71]. Velasco-Carrau *et al.* [71] employed multi-objective optimization for wind estimation and aircraft model identification. Hong *et al.* in [55] implemented a generalized model predictive static programming, while in a subsequent work [54], Hong *et al.* utilized tracking model predictive static programming for wind estimation without using airspeed measurements. The generalized model predictive static programming method in [55] treated wind as a virtual input and minimized terminal errors between measured and predicted states. In [54], the wind vector was estimated by treating it as an input to the aircraft model, thus reducing the error between the measured and predicted kinematic states of the aircraft.

Alternative approaches to model-based wind estimation encompass several techniques: estimating wind gusts using a frequency-based nonlinear disturbance observer [72], employing an unknown input observer for wind gust estimation in a quasi-hovering quadrotor [73], direct calculation of wind velocities [74], leveraging Gaussian process regression for wind velocity estimation [75], determining time-varying wind parameters from quadrotor data via finite time estimation [76], utilizing a moving horizon estimator for wind velocity and aircraft aerodynamic coefficient estimation [48], and estimating ambient wind with an active particle filter based on data from radio-controlled helicopters [77].

3.2.2 Model-Free Wind Estimation Methods

The techniques used to estimate wind without relying on a flight dynamic model are referred to as model-free methods. These methods typically rely on airspeed data from a Pitot tube and inertial velocity derived from GNSS. One of the key advantages of model-free methods is their ability to eliminate the need for extensive model identification processes. However, they often require continuous aircraft motion to accurately determine the air-relative velocity from the Pitot probe's scalar airspeed readings. The topic of model-free wind estimation from UAV flights is discussed in [78, 79, 80, 81, 82].

The selection of a wind estimation method is influenced by the operational sensors available on an aircraft. Model-free wind estimation techniques depend on GNSS and Pitot probe data, as discussed in [79] and [78]. Cho *et al.* [79] propose a model-free wind estimation method using a single GNSS antenna/receiver and a Pitot probe, assuming a constant 2D wind field. They utilize sustained aircraft excitation through banking turns and circling maneuvers to calculate air-relative velocities using an extended Kalman filter. Balmer *et al.* [78] employ a Kalman filter for wind estimation, assuming a constant wind field and integrating pseudo-measurements of the angle of attack and angle of sideslip to compute air-relative velocity. These pseudo-measurements represent the equilibrium values of the angle of attack and the angle of the sideslip, assuming that pitch and yaw stability maintains only minor deviations from these equilibrium values. This approach eliminates the need for sustained excitation or significant attitude changes typically required in model-free wind estimation.

In addition to GNSS and Pitot probe measurements, model-free wind estimation can utilize data from an IMU, magnetometer, and ADU. Rautenberg *et al.* [80] discuss wind estimation using a fixed-wing UAV equipped with a multihole Pitot probe, IMU, and GNSS receiver, comparing the accuracy of estimates when including air-relative velocity measurements in the filter versus estimates obtained using persistent excitation without flow sensor data. Zhang *et al.* [82] use GNSS, IMU, Pitot probe, and barometric pressure measurements for real-time Pitot probe calibration and wind field estimation with a hovering quadcopter. Witte *et al.* [81] employ GNSS, IMU, magnetometer, and multihole Pitot probe data from a fixed-wing UAV to estimate wind velocity, using GNSS measurements for inertial velocity and the multihole Pitot probe for the three components of air-relative velocity. Combined with attitude estimates from the IMU and magnetometer, these measurements solve the wind triangle to determine wind velocity [81]. Rhudy *et al.* [83] present and compare four different wind estimation formulations using an unscented Kalman filter, including two model-free methods and two model-based methods, utilizing GNSS, IMU, and ADU measurements.

3.2.3 Combined Wind Estimation Methods

Combined wind estimation methods employ extended Kalman filters [84], deterministic observers [85], or moving horizon estimators [48, 86]. Wenz *et al.* [84] utilize an extended Kalman filter with GNSS, IMU, and Pitot probe data to estimate both steady wind and turbulent fluctuations, requiring attitude adjustments during flight to maintain observability. Borup *et al.* [85] implement a nonlinear observer for model-free wind estimation, eliminating the need for persistent excitation by incorporating a simple aerodynamic model updated with propeller speed and Pitot probe measurements. Benders *et al.* [86] apply a moving horizon estimator, integrating wind velocity-based path planning with wind velocity estimation using the Dryden turbulence model. This approach necessitates aircraft attitude changes during flight to maintain observability and is considered a combined method since the aerodynamic coefficients are determined online. Similarly, Wenz *et al.* [48] use a moving horizon estimator with the Dryden turbulence model to estimate wind velocity and turbulence, requiring persistent excitation to differentiate between aerodynamic coefficient changes and wind velocity.

Chapter 4

General Flight Test Experiments

In this chapter, we present a description of the facilities used for conducting all experiments and flight tests, the research aircraft and its instruments utilized for conducting flight tests, and a comprehensive explanation of all flight operation-related procedures, certifications, and software used. In Section 4.1, the laboratories and facilities are described. In Section 4.2, the research aircraft parameters and instruments are described. Finally, in Section 4.3, the pilot certification process and FAA waiver utilized for conducting the fight tests, the QgrounfControl software, and the flight operation checklist developed and utilized are discussed.

4.1 Experiment Locations and Facilities

This section provides detailed information about the two main facilities used for conducting all the experiments required for data collection. Virginia Tech is the owner and operator of both the Kentland Experimental Aerial System (KEAS) Laboratory and the 0.7 m open jet wind tunnel. The KEAS Laboratory is primarily used for conducting UAS flights and ground tests, and it operates in full compliance with CFR 14 Part 107 regulations. On the other hand, the open jet wind tunnel is utilized to perform all air data unit (ADU) dynamic characterization experiments. These facilities have been designed and equipped with equipment to ensure that all experiments are carried out safely and effectively.

4.1.1 Kentland Experimental Aerial System (KEAS) Laboratory

All the flight-test research operations carried out to collect data were conducted at the Kentland Experimental Aerial Systems (KEAS) Laboratory [87], located at Virginia Tech's Kentland Farm agricultural research facility. Covering about 1800 acres of university-owned farmland in a sparsely populated area southwest of the main campus, the KEAS Laboratory is a state-of-the-art research facility that supports small unmanned aerial vehicle (UAV) flight operations. The laboratory offers a 300 ft by 70 ft paved airstrip located at the center of the farm, which is ideal for conducting flight tests of small UAVs. The airstrip is equipped with a wind sock to indicate wind speed and direction, ensuring safe and efficient flight operations. In addition to the airstrip, the airfield includes a state-of-the-art weather station that logs meteorological data, providing researchers with valuable information to plan and conduct their experiments. The KEAS Laboratory has a hangar to facilitate storage, rapid aircraft repair, flight test preparations, and post-flight work. This hangar is fully equipped with all the necessary tools and equipment to support flight research operations, ensuring that researchers can conduct their experiments safely and efficiently. Moreover, the laboratory has a wireless network covering the area that provides direct internet access at all times, enabling researchers to access and analyze their data in real time. This network also supports collaboration among university faculty, students, and affiliates, which is the laboratory's primary objective. The KEAS Laboratory provides a safe, efficient, and collaborative environment for conducting flight-test research operations involving UAVs. Please see Figure 4.1 for a visual representation of the KEAS Laboratory.

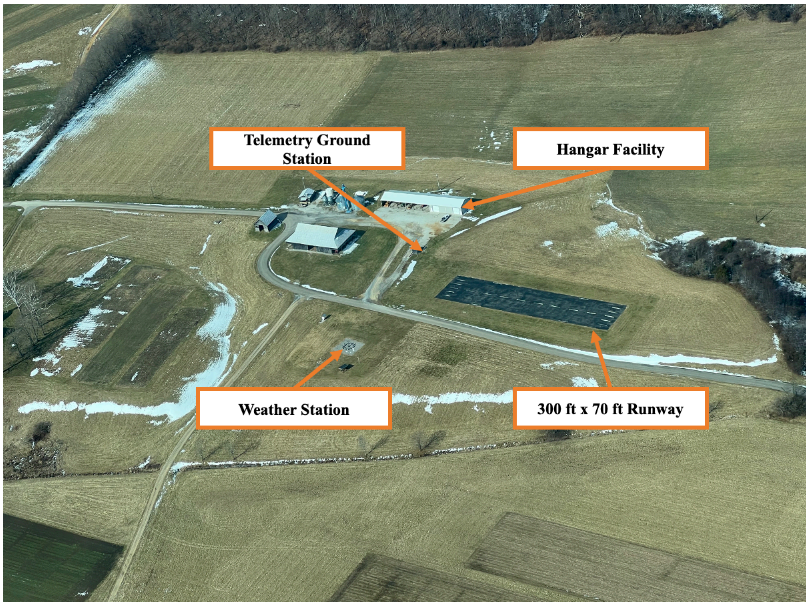

Figure 4.1: Photographs of KEAS laboratory airstrip and facility

4.1.2 Open Jet Wind Tunnel

All wind tunnel tests that aimed to characterize the sensors instrumented on the research aircraft were conducted in an open jet subsonic wind tunnel [88]. The wind tunnel, an open-circuit blower type, stands on a sturdy steel base and is constructed with lightweight aluminum composite panels and an extruded aluminum frame. Its power source is a 30 hp BC-SW Size 365 Twin City centrifugal fan, capable of generating an airflow of up to 15 m^3/s. The airflow is discharged into a diffuser and enters a settling chamber. A combination of a honeycomb and three turbulence reduction screens within the settling chamber reduces turbulence to achieve a uniform flow. The flow then exits into the atmosphere through a contraction nozzle. An AF-600 General Electric variable frequency drive regulates the flow velocity in the wind tunnel. At its maximum fan speed of 1180 RPM, the flow exits the contraction exit chamber at 30 m/s. Flow velocity measurement is achieved through static pressure taps located at the exit of the settling chamber, with a manometer mounted on the side of the tunnel measuring the pressure difference between the settling chamber and

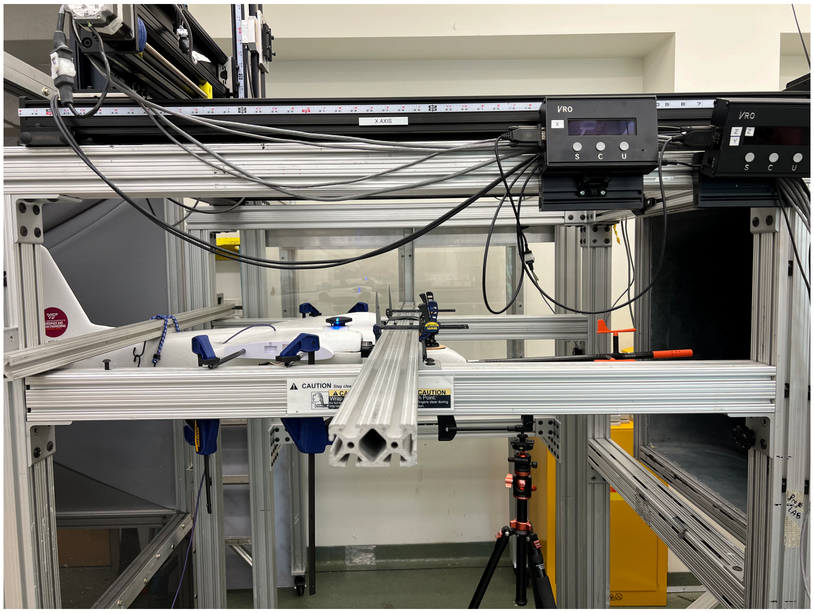

Figure 4.2: MTD2 instrument test

atmospheric pressure. To ensure the comfort and safety of the laboratory environment, a jet catcher is installed downstream of the contraction exit chamber, as depicted. This device, constructed from an extruded aluminum frame with composite panels, incorporates two fiberglass high-loss screens to redirect the flow toward the ground and ceiling. Additional high-loss screens situated at the top and bottom of the jet catcher further reduce the flow velocity before it enters the room, effectively mitigating the impact of the airflow in the laboratory. The tunnel is equipped with a versatile adjustable support frame for model mounting. This frame, constructed from extruded aluminum beams, offers numerous slots for flexible model positioning to accommodate various research needs. See Figure 4.2.

4.2 Research Aircraft

This section gives a comprehensive overview of the research aircraft utilized for conducting flight tests in this dissertation. The description comprises detailed information about the aircraft's constant parameters, weight, and characteristic lengths. Additionally, the moment of inertia of the UAS is discussed. Furthermore, the flight computers used to manage the aircraft's flight during the tests are described. This section also describes the aircraft's instruments that were collectively used to collect flight data during the tests, including their specifications and functionality.

4.2.1 Aircraft Parameters

The research aircraft used, the My Twin Dream (MTD), is a radio-controlled (RC) twin-engine, electrically powered, and foam-structured fixed-wing aircraft manufactured by My Fly Dream. The aircraft is powered by a four-cell 14.8 V 6750 mAh Lithium-polymer battery with a counter-rotating twin propeller configuration. See Figure 4.3. The MTD is chosen for its simple construction, benign flight dynamics, greater than 20 minutes of endurance, and sufficient payload to incorporate the desired instrumentation package and onboard co-computer. The MTD aircraft is instrumented with a Pixhawk flight computer (Cube Orange flight controller), specifically a Pixhawk 2.1 Cube Orange Flight Controller running PX4 firmware and an air data unit (ADU) for data collection. The moments of inertia (MoI) were measured experimentally using the compound pendulum technique presented in [89], and the product of inertia I_{xz} was determined using a fourth test as described in [4]. The remaining products of inertia, I_{xy} and I_{yz}, were assumed to be zero based on lateral symmetry. Table 4.1 shows the mass and geometric properties of the aircraft.

4.2.2 Aircraft Instruments

The MTD is instrumented with the CubePilot autopilot, which runs PX4 firmware with an ecosystem that includes a Global Navigation Satellite System (GNSS) sensor with RTK

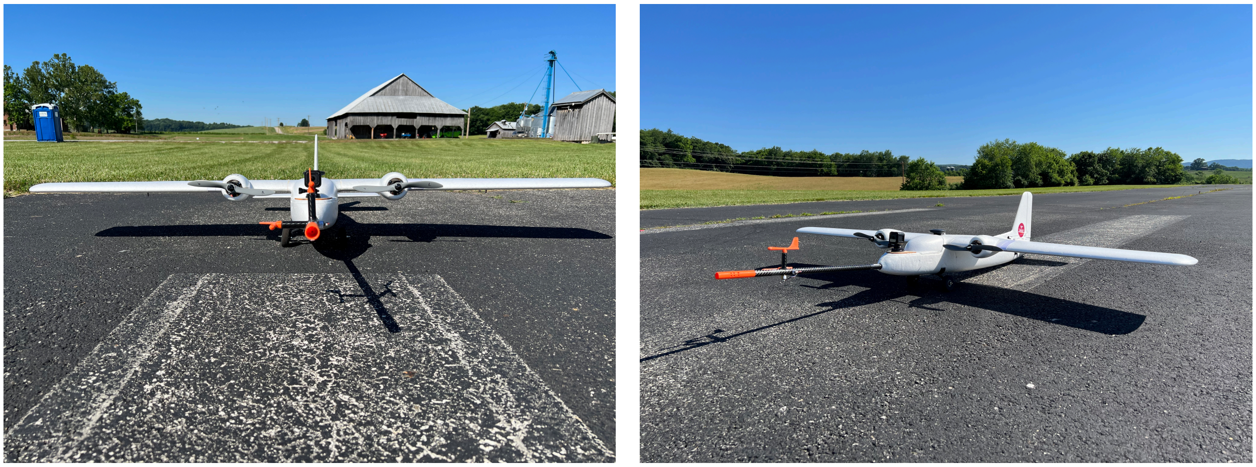

(a) Front view of MTD2. (b) Left view of MTD2.

Figure 4.3: My twin dream (MTD) 2 aircraft

Table 4.1: My Twin Dream (MTD) aircraft properties

Property	**Symbol**	**Value**	**Units**
Mass	m	3.311	kg
Mean aerodynamic chord	$\bar{c}$	0.254	m
Projected wing span	b	1.80	m
Wing reference area	S	0.457	m^2
Roll moment of inertia	I_{xx}	0.319	kg-m^2
Pitch moment of inertia	I_{yy}	0.267	kg-m^2
Yaw moment of inertia	I_{zz}	0.471	kg-m^2
Product of inertia	I_{xz}	0.024	kg-m^2

capability. From the GNSS sensor, the position and total velocity expressed in the NED frame are available. The CubePilot includes barometers and Inertial Measurement Unit (IMU) sensors (which contain accelerometers, gyroscopes, and magnetometers). The PX4 firmware runs a sensor-fusion algorithm in an extended Kalman filter to resolve the aircraft's attitude, inertial position, inertial total velocity, accelerometer bias, gyroscope bias, and magnetometer bias. Hence, the aircraft's specific force, angular rate, and attitude are available. Additionally, the aircraft is instrumented with an air data unit (ADU) that contains a pitot probe, angle of attack vanes, and flank angle vane linked to the CubePilot to measure the aircraft's true airspeed, angle of attack, and sideslip angle. The MTD also carries a vaned ADU for measuring air-relative velocity. The ADU, visible in Figure 4.3, gives the aircraft's true airspeed (V_r), angle of attack (α), and flank angle (β_f). The dynamic response of the angle of attack and flank angle vanes at different airspeeds can be inferred from Figure 4.4, which was obtained from data collected in an open-jet wind tunnel. The process involved applying impulse perturbations to the vane angles at different free-stream velocities and then recording the damped, harmonic subsidence from these perturbations. The logarithmic decrement method was used to determine the vanes' damping ratios and natural frequencies at different velocities. The bandwidth of the α and β_f vanes is approximately 6 Hz for a free-stream velocity of 12.33 m/s, which is approximately the stall speed of the MTD. The sensor bandwidth increases up to about 14 Hz for a free-stream velocity of 23.61 m/s. The cutoff frequency for the ADU vanes is at least two times higher than the MTD's short-period mode natural frequency of about 3 Hz at the nominal cruise speed

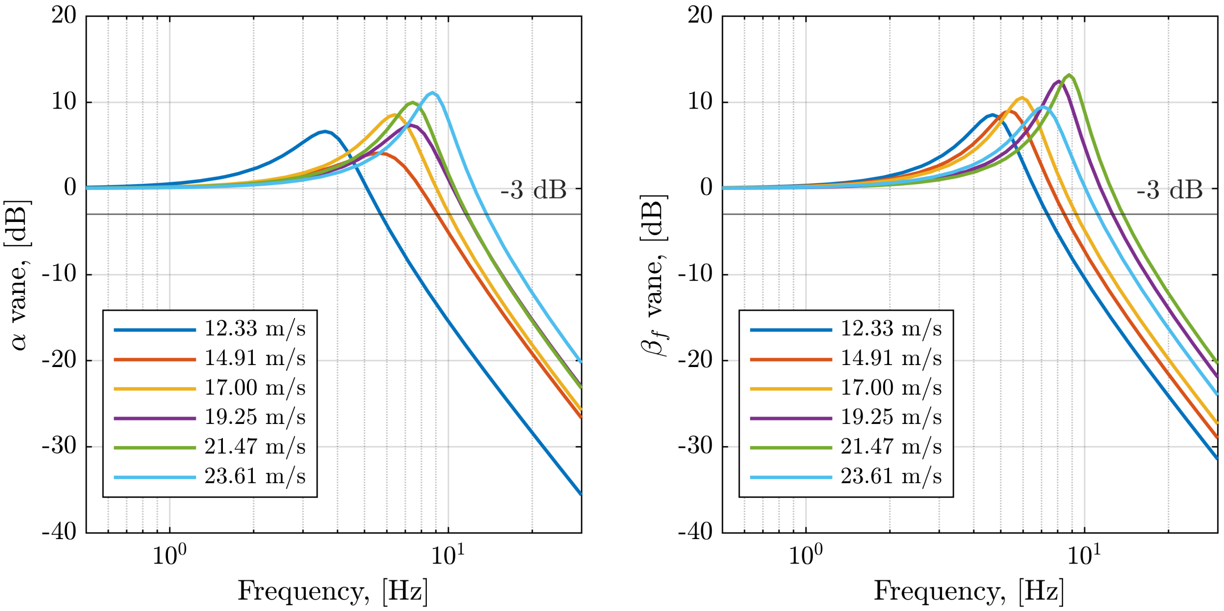

(a) Angle of attack vane.

(b) Flank angle vane.

Figure 4.4: Frequency response of (a) angle of attack and (b) flank angle vanes.

of 18 m/s. Aerodynamic angle measurements are used only to validate the wind estimates generated using other measurement data. Typically, the sensors have different sampling rates. The IMU has the fastest sampling rate, and the GNSS sensor has the slowest one. In this paper, the data from the various sensors were synchronized using a shape-preserving piecewise cubic interpolation to maintain an overall sampling rate of 50 Hz.

Table 4.2: CubePilot sensor measurement description

Measurement	**Name & Units**	**Frame of Reference or Location Relative to c.g.**	**Sensor**
$\boldsymbol{X} = [x, y, x]^{\mathrm{T}}$	Position [m]	NED frame	GNSS & PX4
$\boldsymbol{V} = [V_x, V_y, V_z]^{\mathrm{T}}$	Total Velocity [m/s]	NED frame	GNSS & PX4
$\boldsymbol{f}_a = [a_x, a_y, a_z]^{\mathrm{T}}$	Specific Force [m/s^2]	Body-fixed frame	IMU & PX4
$\boldsymbol{\omega} = [p, q, r]^{\mathrm{T}}$	Angular Rate [rad/s]	Body-fixed frame	IMU & PX4
$\boldsymbol{\Theta} = [\phi, \theta, \phi]^{\mathrm{T}}$	Attitude [rad]	NED frame	IMU & PX4
$\boldsymbol{\delta} = [\delta_a, \delta_e, \delta_r]^{\mathrm{T}}$	Control Signals [μs (mapped to rad)]	—	PX4
α_{v}	Angle of Attack [μs (mapped to rad)]	$[x_{\alpha_{\mathrm{v}}}, y_{\alpha_{\mathrm{v}}}, z_{\alpha_{\mathrm{v}}}]$	ADU
$\beta_{f_{\mathrm{v}}}$	Flank Angle [μs (mapped to rad)]	$[x_{\beta_{f_{\mathrm{v}}}}, y_{\beta_{f_{\mathrm{v}}}}, z_{\beta_{f_{\mathrm{v}}}}]$	ADU
V_{t}	True Airspeed [m/s]	—	ADU & PX4

4.3 Flight Operations

This section provides a comprehensive explanation of the certification process for UAS pilots, along with the necessary requirements and procedures that should be followed to obtain certification to operate a UAS. Furthermore, it discusses the FAA waiver that has been granted for operating up to 700 AGL. The section also includes a detailed overview of QgroundControl, a software tool that is used for mission planning, telemetry monitoring, flight control, and data analysis. Lastly, the section covers the flight operations checklist, explaining and discussing its various aspects.

4.3.1 Pilot Certification and FAA Waiver

The author and research collaborators involved in operating the research aircraft for data collection are CFR 14 Part 107 certified and meet Virginia Tech's UAS operation guidelines and training. The certification and Virginia Tech's training program involve rigorous testing and training to ensure that the operators are qualified and competent to operate the UAS safely and efficiently. The flight operations were conducted at KEAS, a UAS test site in Virginia that is authorized by the Federal Aviation Administration (FAA). The KEAS test site is designed to provide a safe and secure environment for UAS flight testing and research. The flight operations were conducted in accordance with the CFR 14 Part 107 regulations, which specify the requirements for UAS operations, including pilot certification, UAS registration, and airspace restrictions.

In addition to adherence to the CFR 14 Part 107 regulations, the nonlinear system laboratory (NSL) applied for Part 107.51 (b) waiver application and is certified to operators up to 700 AGL [90]. This waiver allowed the NSL's certified pilots to operate the UAS at a higher altitude than the 400 AGL mandated by the CRF 14 Part 107 regulations. The altitude of 700 AGL was selected because KEAS is located between two airports: Virginia Tech/Montgomery Executive Airport (KBCB) and New River Valley (KPSK) airports, which are surrounded by a Class E airspace that starts at 700 AGL; see Figure 4.5. The higher altitude allowed flexibility in UAS operation while maintaining a low risk of interfering with manned aircraft operations in the surrounding airspace. Before each UAS flight, the pilot in command (PIC) is responsible for all UAS preflight tasks, including maintenance and flight preparations, weather monitoring, NOTAM filing, mission briefs, adherence to crew resource management (CRM) practices, and establishment of emergency procedures for the flight. These preflight tasks are crucial to ensure safe and efficient UAS flight operations. The PIC must also ensure that the UAS is in compliance with all applicable regulations.

The safety and success of UAS flight operations depend on careful planning, preparation, and execution by the PIC and the UAS team.

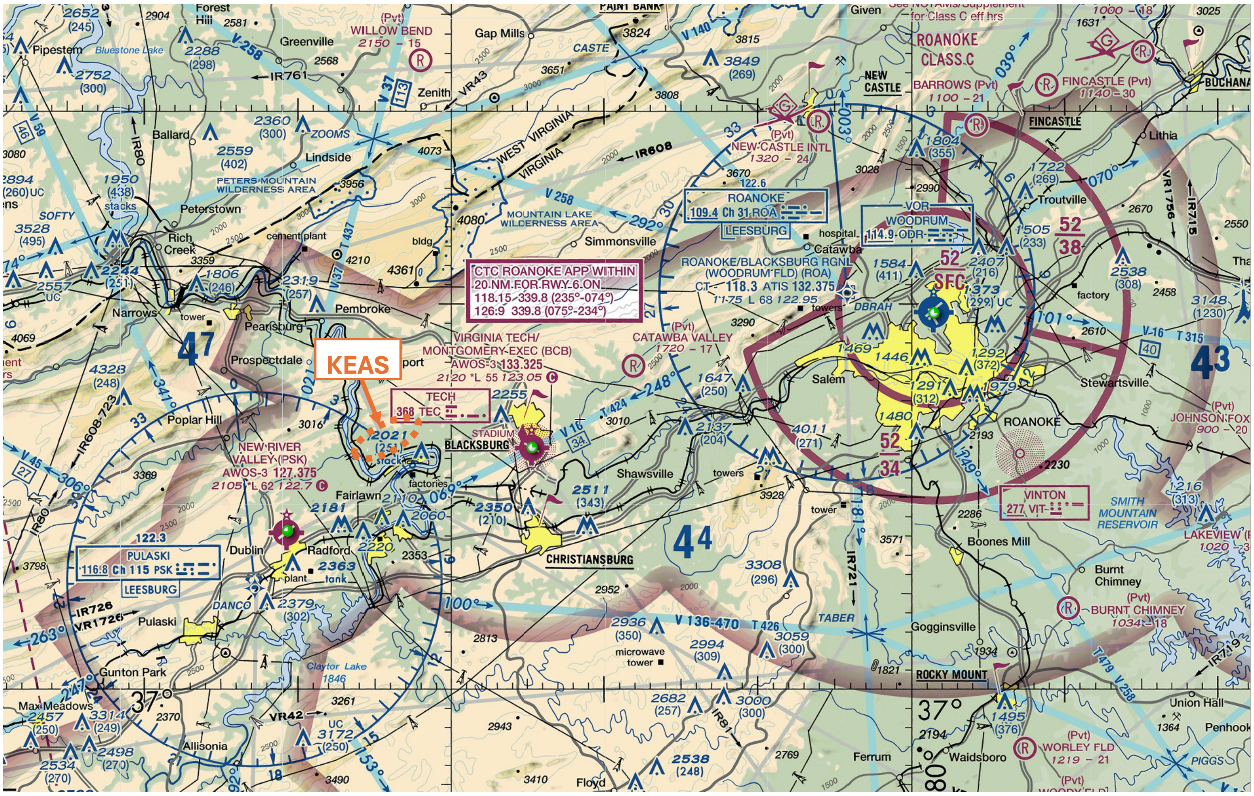

Figure 4.5: KEAS laboratory airspace map

4.3.2 QgroundControl and Operation Checklist

In this dissertation, QGroundControl is used as the primary software for all UAS flight operations. It acts as a bridge between the operator and the UAS during flight. This software offers a range of advanced features to manage various aspects of UAS flight operations, such as mission planning, telemetry monitoring, flight control, and data analysis; see Figure 4.6. QGroundControl offers a user-friendly interface that enables users to plan and manage drone missions efficiently. For example, users can define waypoints, altitude, speed, and other parameters to plan the route of the drone. This feature allows for a more accurate and efficient operation. Moreover, QGroundControl receives telemetry data from the UAS during flight operations, such as GPS position, altitude, battery status, and sensor readings, in real-time. This data is critical for executing predefined missions and maintaining a specific flight pattern for data collection. After completing a flight mission, QGroundControl allows users to analyze, review, and download flight data. During UAS flights, it is crucial to maintain a high level of safety and efficiency. To achieve this, the Pilot-In-Command (PIC) utilizes a flight checklist, which serves as a procedural tool to ensure that critical tasks are completed accurately and in the correct sequence during various phases of flight. The primary purpose of the checklists is to enhance flight safety by systematically guiding the UAS team through essential tasks before, during, and after flight. Every UAS flight involves a complex set of tasks that need to be carefully executed to ensure a safe and successful outcome. To achieve this, the PIC and the UAS team rely on checklists to ensure that all necessary procedures are appropriately completed. By following the checklists, the team reduces the likelihood of

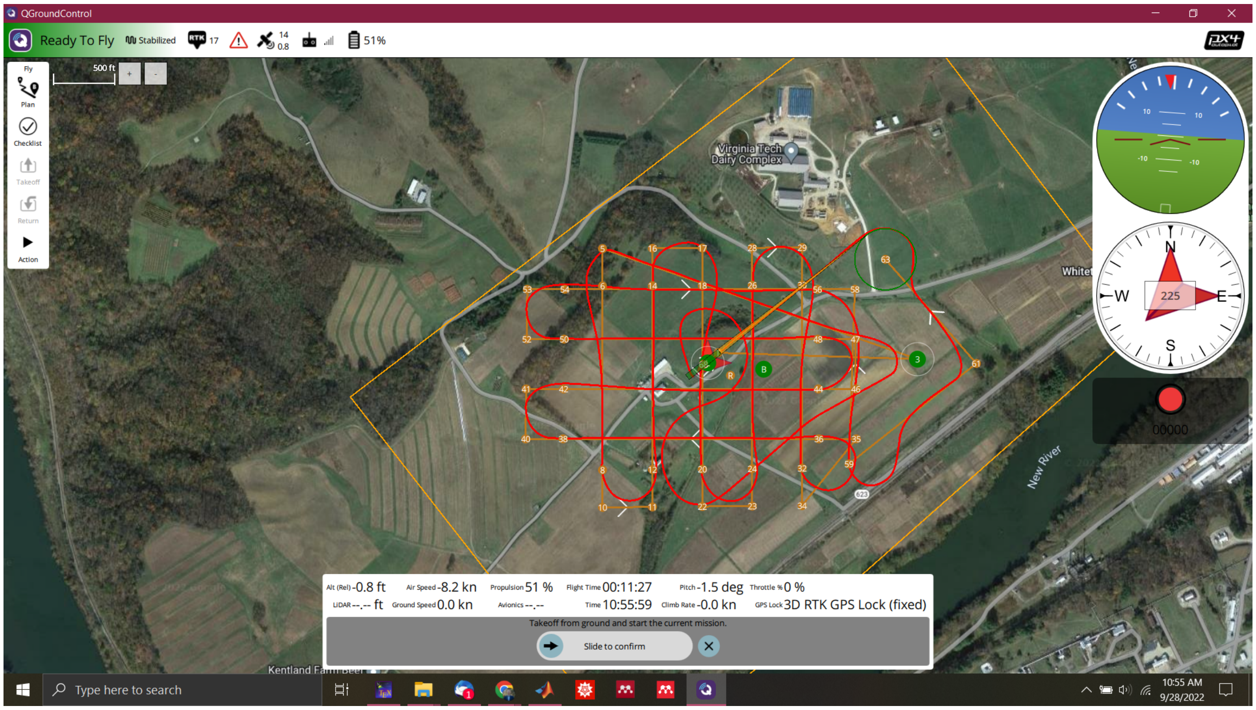

Ready To Fly
Stabilized
RTK 17
14 0.8
51%

Alt (Rel) -0.8 ft
Air Speed -8.2 kn
Propulsion 51 %
Flight Time 00:11:27
Pitch -1.5 deg
Throttle % 0 %
LiDAR --.-- ft
Ground Speed 0.0 kn
Avionics --.--
Time 10:55:59
Climb Rate -0.0 kn
GPS Lock 3D RTK GPS Lock (fixed)

Takeoff from ground and start the current mission.

Figure 4.6: Example of QgroundControl telemetry interface

human error, which can have potentially severe consequences. In addition to improving flight safety, checklists also help to improve the workflow and organize research tasks related to flight data collection into manageable steps. By breaking the process down into smaller, more manageable steps, the team can complete the research tasks more efficiently and effectively. The checklist document used in the UAS flight conducted in the dissertation is available in Section C. It includes a detailed set of tasks that the PIC and the UAS team need to complete before, during, and after the flight. These tasks include pre-flight checks, equipment testing, flight planning, data collection, and post-flight analysis. By following this checklist, the UAS team can ensure that every critical step is completed accurately and in the correct sequence, minimizing the possibility of errors and ensuring a safe and successful UAS flight.

Chapter 5

Aircraft System Identification

The research aircraft, My Twin Dream (MTD) described in Section 4.2, is used throughout this dissertation for experiment based work, including system identification and wind estimation, which are the main subject of this dissertation. In this chapter, the system identification methodology is implemented to develop flight dynamic models for the MTD. These models are used in Chapters 6 and 7.

The MATLAB® toolbox called System Identification Programs for Aircraft (SIDPAC), which is associated with [4], is used for the development and validation of three flight dynamic models for a small, fixed-wing aircraft are discussed in detail here. The first model is a generic nonlinear aerodynamic model similar to [19]. The second model is a linear aerodynamic model similar to the nonlinear model, but this linear model does not include nonlinear regression. Finally, the third model is a linear, unsteady aerodynamic model.

The aircraft system identification approach follows the methods described in [4, 5, 6], beginning with the design and implementation of input excitations – longitudinal and lateral-directional doublets and multisine waves – followed by checks for kinematic consistency and data collinearity. The structure of the aerodynamic model is determined using multivariate-orthogonal-function (MOF) modeling [91] or is based on unsteady flight dynamic physics [44]. The aerodynamic model parameters are then determined using the output-error method applied to data obtained over several flights. Finally, the identified model is validated using independent data.

The system identification input design, data processing, kinematic consistency test, and collinearity test are identical for all three models. That is, the data collected to train the nonlinear aerodynamic model can be used for the linear unsteady aerodynamic model. That said, even though some aerodynamic parameters appear in all three models, the values to which these parameters converge are different.

The chapter begins with Section 5.1 where the input design and data processing are discussed, followed by Section 5.2 where the kinematic consistency and collinearity test are discussed. In Section 5.3, the model structures of the three models are described and explained in detail. In Section 5.4, the aerodynamic parameter identification and validation are discussed, and the identified aerodynamic parameters results of all three flight dynamic models are given.

5.1 Input Design and Data Processing

The input design and data processing step of the system identification methodology used are described here. The implementation of these steps is identical for all three model identification processes. A short and thorough description of the input design and data processing is described in this section.

5.1.1 Input Design

The maneuvers used to identify the MTD's aerodynamic model include multiple orthogonal phase-optimized multisine inputs for data training and actuator doublets for validation [4]. In all cases, the perturbation input $\Delta\delta$ is applied to each input in the control surface deflection vector ($\Delta\delta_a$,$\Delta\delta_e$,$\Delta\delta_r$). For the effort described in this paper, six multisine data sets, two longitudinal doublet sets, and two lateral-directional doublet sets were collected. See Fig. 5.1

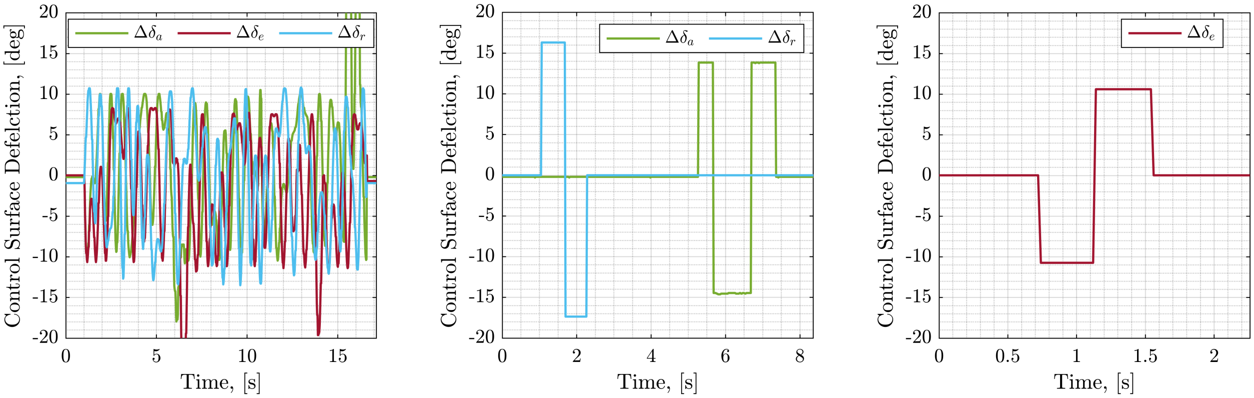

(a) Orthogonal multisine.
(b) Lat-dir doublet.
(c) Lon doublet.

Figure 5.1: Multisine and doublet inputs.

for an example of multisine inputs and doublet inputs.

5.1.2 Data Processing

The flight data required for system identification is acquired from the aircraft's flight computer discussed in Section 4.2. The data collected for system identification was filtered using a Butterworth lowpass filter at 6 Hz as recommended in [92]. The nondimensional aerodynamic force and moment coefficients are constructed from the data collected as follows:

$$C_X = \frac{2m}{\rho V_0^2 S} a_x \tag{5.1a}$$

$$C_Y = \frac{2m}{\rho V_0^2 S} a_y \tag{5.1b}$$

$$C_Z = \frac{2m}{\rho V_0^2 S} a_z \tag{5.1c}$$

$$C_l = \frac{2}{\rho V_0^2 S b} \left(I_{xx}\dot{p} - I_{xz}\dot{r} + (I_{zz} - I_{xz})qr - I_{xz}pq \right) \tag{5.1d}$$

$$C_m = \frac{2}{\rho V_0^2 S b} \left(I_{xx}\dot{p} - I_{xz}\dot{r} + (I_{zz} - I_{xz})qr - I_{xz}pq \right) \tag{5.1e}$$

$$C_n = \frac{2}{\rho V_0^2 S b} \left(I_{xx}\dot{p} - I_{xz}\dot{r} + (I_{zz} - I_{xz})qr - I_{xz}pq \right) \tag{5.1f}$$

where ρ is the air density, V_0 is the aircraft's nominal cruise airspeed, $\dot{\boldsymbol{\omega}} = [\dot{p}, \dot{q}, \dot{r}]^{\mathrm{T}}$ is the smoothed numerical differentiated angular rate vector. For the purpose of system identification, the aircraft angle of attack α and sideslip angle β are reconstructed from the aircraft's velocity expressed in the body-fixed frame. Flight tests for model identification were conducted on a calm day so that $\boldsymbol{v} = \boldsymbol{v}_{\mathrm{r}}$ and $\boldsymbol{\omega} = \boldsymbol{\omega}_{\mathrm{r}}$ and we have

$$\alpha = \tan^{-1}\left(\frac{w}{u}\right) \tag{5.2a}$$

$$\beta = \sin^{-1}\left(\frac{v}{V}\right) \tag{5.2b}$$

$$V = \sqrt{u^2 + v^2 + w^2} \tag{5.2c}$$

The remaining explanatory variables are nondimensionalized as follows:

$$\hat{p} = \frac{pb}{2V_0} \tag{5.3a}$$

$$\hat{q} = \frac{qc}{2V_0} \tag{5.3b}$$

$$\hat{r} = \frac{rb}{2V_0} \tag{5.3c}$$

5.2 Data Compatibility

The data collected for regression was first checked for data compatibility by assessing kinematic consistency and data collinearity as suggested in [4].

5.2.1 Kinematic Consistency

For the kinematic consistency analysis, the kinematic equations were evaluated using accelerometer $\boldsymbol{f}_a$ and gyroscope $\boldsymbol{\omega}$ measurements as inputs, and the aircraft's states $\boldsymbol{v}$ and

$\boldsymbol{\Theta}$ as measurements. Bias terms $\boldsymbol{b}_{f_a} = [b_{a_x}, b_{a_y}, b_{a_z}]^{\mathrm{T}}$ and $\boldsymbol{b}_{\omega} = [b_p, b_q, b_r]^{\mathrm{T}}$ were included to account for bias in the accelerometer and gyroscope measurement, respectively. These bias terms were estimated using the output-error method and were used to correct the accelerometer and gyroscope measurements, as recommended in [4]. The kinematic equations used in the kinematic consistency analyses are as follows:

$$\dot{u} = (r - b_r)v - (q - b_q)w - g\sin\theta + a_x - b_{a_x} \tag{5.4a}$$

$$\dot{v} = (p - b_p)w - (r - b_r)u + g\sin\theta\sin\phi + a_y - b_{a_y} \tag{5.4b}$$

$$\dot{w} = (q - b_q)u - (p - b_p)v + g\cos\theta\cos\phi + a_z - b_{a_z} \tag{5.4c}$$

$$\dot{\phi} = (p - b_p) + \tan\theta\sin\phi(q - b_q) + \tan\theta\cos\phi(r - b_r) \tag{5.4d}$$

$$\dot{\theta} = \cos\phi(q - b_q) - \sin\phi(r - b_r) \tag{5.4e}$$

$$\dot{\phi} = \sin\phi\sec\theta(q - b_q) + \cos\phi\sec\theta(r - b_r) \tag{5.4f}$$

Figure 5.2 illustrates an example of bias-corrected and non-corrected accelerometer and gyroscope measurements.

5.2.2 Collinearity Diagnostics

A low pairwise correlation between individual explanatory variables is necessary for identifying each variable's contribution to aircraft dynamic response in system identification. Analysis of regressor pairwise correlation is one technique to identify regressor pairs that may not be well suited for modeling. The correlation coefficient between data vectors for a pair of regressors x and y is calculated as follows:

$$r_{xy} = \frac{(x - \bar{x})^{\mathrm{T}}(y - \bar{y})}{\sqrt{(x - \bar{x})^{\mathrm{T}}(x - \bar{x})\,(y - \bar{y})^{\mathrm{T}}(y - \bar{y})}} \tag{5.5}$$

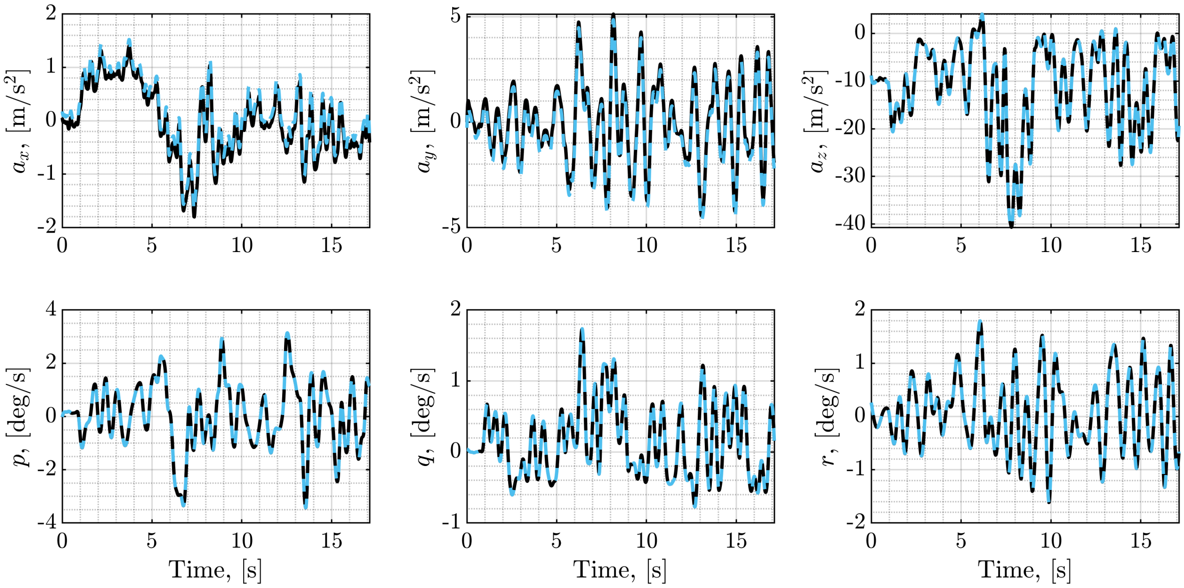

Figure 5.2: Sensor correction based on kinematic consistency results. The non-corrected values are shown in black, while the corrected values are indicated by a red dashed line.

where x and y are the mean values of the respective data sets. The correlation pairwise coefficient, r, will have a value in the range $[-1, 1]$, with 0, meaning no correlation or orthogonal data vectors. Figure 5.2 illustrates an example of c used in the assessment presented below.Figure 5.2 displays regressor cross plots and pairwise correlation values of a multisine dataset.

5.3 Model Structure Determination

The longitudinal and lateral-directional regressors considered in the models given in this section are perturbations from nominal values. That is, the variables that denote perturbations from nominal state and control values are defined as follows:

$$\Delta u_{\mathrm{r}} = u_{\mathrm{r}} - u_{\mathrm{r,nom}} \quad \Delta\alpha = \alpha - \alpha_{\mathrm{nom}} \quad \Delta\beta = \beta - \beta_{\mathrm{nom}}$$

$$\Delta\delta_a = \delta_a - \delta_{a,\mathrm{nom}} \quad \Delta\delta_e = \delta_e - \delta_{e,\mathrm{nom}} \quad \Delta\delta_r = \delta_r - \delta_{r,\mathrm{nom}}$$

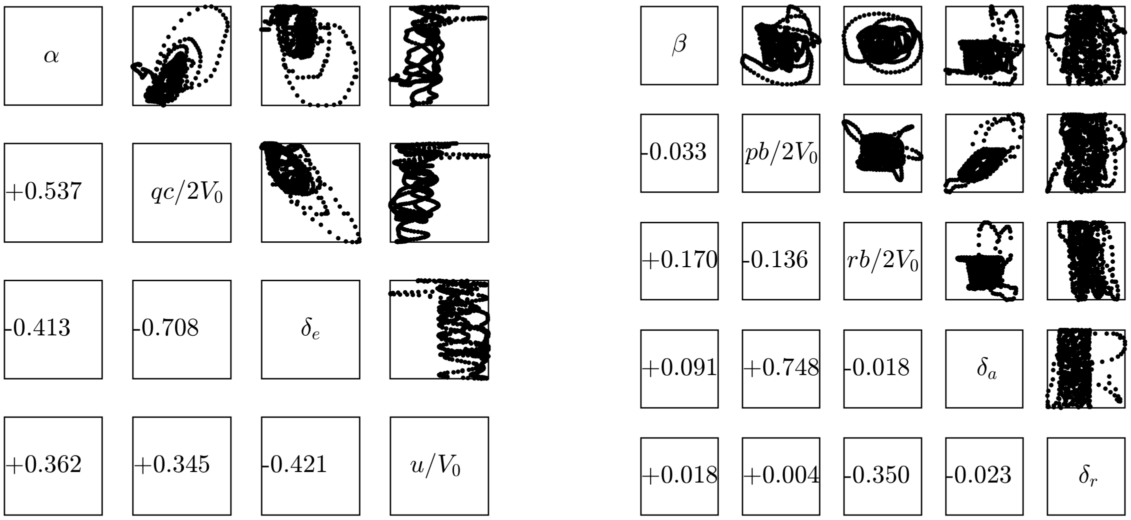

(a) Collinearity diagnostics: Longitudinal (b) Collinearity diagnostics: Lateral-directional

Figure 5.3: Regressor cross plots and pairwise correlations

The nondimensional state variables are defined as follows:

$$J = \frac{u_r}{\delta_{\text{rps}} D} \quad \alpha = \tan^{-1}\left(\frac{w_r}{u_r}\right) \quad \beta = \sin^{-1}\left(\frac{w_r}{\|\boldsymbol{v}_{\text{r}}\|}\right) \quad \hat{p} = \frac{pb}{2V_0} \quad \hat{q} = \frac{q\bar{c}}{2V_0} \quad \hat{r} = \frac{rb}{2V_0}$$

5.3.1 Nonlinear Aerodynamic Model

The model structure of the nonlinear aerodynamic model is determined using the multivariate orthogonal function (MOF) method described in [93]. The longitudinal regressors $\Delta\alpha$, $\hat{q}$, and $\Delta\delta_e$, the lateral-directional regressors $\Delta\beta$, $\hat{p}$, $\hat{r}$, $\Delta\delta_a$, and $\Delta\delta_r$ were multiplied in all possible combinations up to the third order, for example, $\Delta\alpha$, $\hat{q}$, δ_e,$\hat{r}$, $\Delta\delta_a$, $\Delta\beta^3$ etc., to form the candidate regressor pool. An additional regressor $\Delta\hat{u}_r = \frac{\Delta u_r}{V_0}$ was included when determining the structure of C_X to account for the velocity variations. Two doublets and six multisines were used to run the MOF based structure determination process, and the regressors that occurred at least seven times were selected. Figures 5.4 to 5.6 display the selected aerodynamic model terms, which were chosen based on their frequency of occurrence.

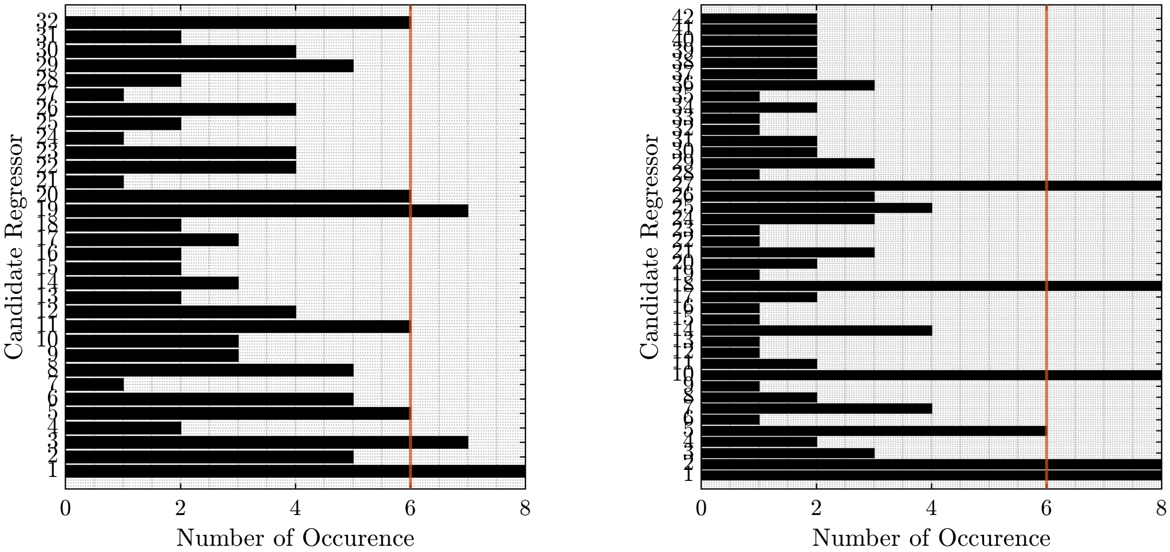

(a) Model terms selected for C_X (b) Model terms selected for C_Y

Figure 5.4: Model terms selected for C_X and C_Y coefficient of the nonlinear aerodynamic model. The red line indicates the selection threshold.

The numbers on the y-axis in Figures 5.4 to 5.6 correspond to longitudinal and lateral-directional combination regressors up to the third order. The red lines in Figures 5.4 to 5.6 denote the threshold for selecting terms, where only the ones with more than six occurrences were included in the model. Any term that occurred less than six times was not included in the model. Based on the MOF analysis, the final nonlinear aerodynamic model structure

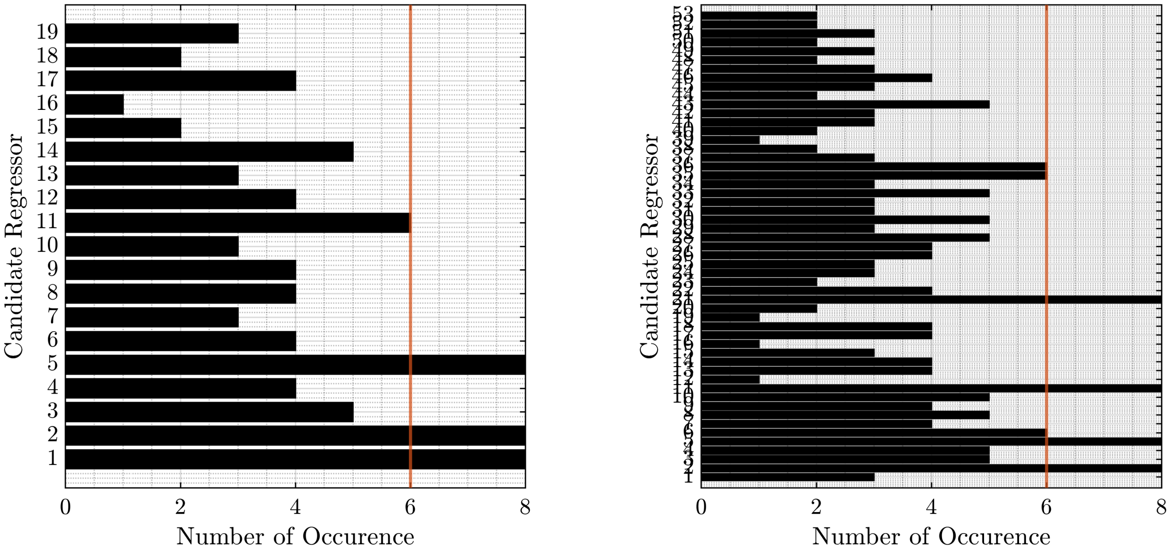

(a) Model terms selected for C_Z (b) Model terms selected for C_l

Figure 5.5: Model terms selected for C_z and C_l coefficient of the nonlinear aerodynamic model. The red line indicates the selection threshold.

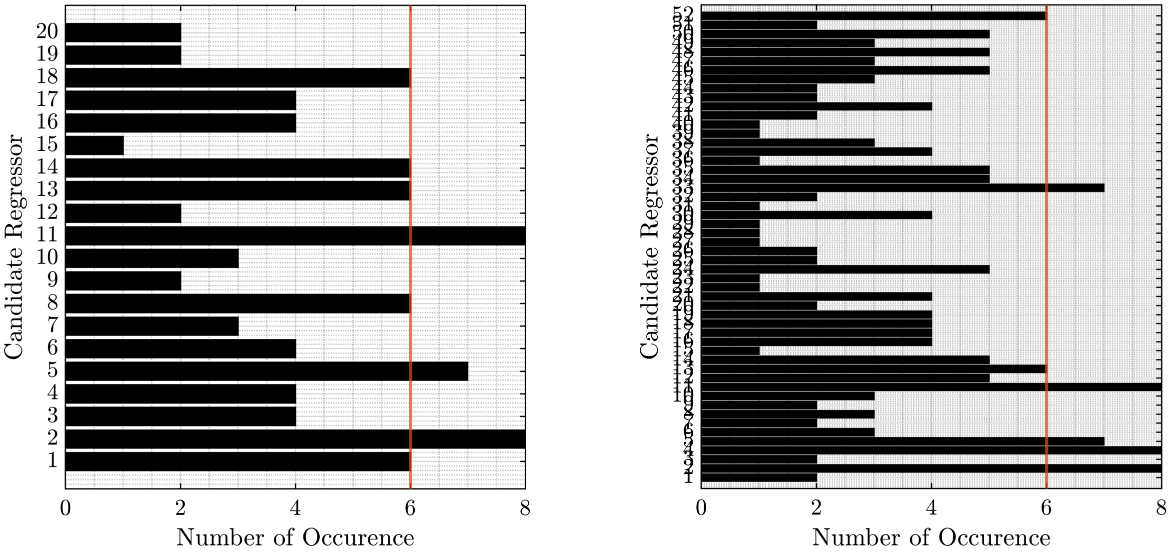

(a) Model terms selected for C_m (b) Model terms selected for C_n

Figure 5.6: Model terms selected for C_m and C_n coefficient of the nonlinear aerodynamic model. The red line indicates the selection threshold.

is as follows:

$$C_J = C_{J_0} + C_J J + C_{J^2} J^2 \tag{5.6a}$$

$$C_X = C_{X_0} + C_{X_{\alpha^2}} \Delta\alpha^2 + C_{X_{u_r}} \Delta\hat{u}_r \tag{5.6b}$$

$$C_Y = C_{Y_0} + C_{Y_\beta} \Delta\beta + C_{Y_r} \hat{r} + C_{Y_{\delta_a}} \Delta\delta_a + C_{Y_{\delta_r}} \Delta\delta_r \tag{5.6c}$$

$$C_Z = C_{Z_0} + C_{Z_\alpha} \Delta\alpha + C_{Z_q} \hat{q} \tag{5.6d}$$

$$C_l = C_{l_\beta} \Delta\beta + C_{l_p} \hat{p} + C_{l_r} \hat{r} + C_{l_{\delta_a}} \Delta\delta_a \tag{5.6e}$$

$$C_m = C_{m_\alpha} \Delta\alpha + C_{m_q} \hat{q} + C_{m_{\delta_e}} \Delta\delta_e \tag{5.6f}$$

$$C_n = C_{n_\beta} \Delta\beta + C_{n_{\beta^3}} \Delta\beta^3 + C_{n_p} \hat{p} + C_{n_r} \hat{r} + C_{n_{\delta_r}} \Delta\delta_r \tag{5.6g}$$

5.3.2 Unsteady and Quasi-steady Aerodynamic Model

The unsteady aerodynamic model structure is determined using MOF method as well. Expect here, the longitudinal and the lateral-directional regressors are first-order combinations, for example, $\Delta\alpha$, $\hat{q}$, δ_e, $\hat{r}$, $\Delta\delta_a$, etc., to form the candidate regressor pool. The additional regressor $\Delta\hat{u}_r = \frac{\Delta u_r}{V_0}$ is also included here when determining the structure of C_X to account for the velocity variations. Six multisines were used to run the MOF based structure determination process, and the regressors that occurred at least two times were selected. Figures 5.7 to 5.9 display the selected aerodynamic model terms, which were chosen based on their frequency of occurrence. The numbers on the y-axis in Figures 5.7 to 5.9 correspond to the first-order combinations of longitudinal and lateral-directional regressors. The red lines in Figures 5.7 to 5.9 denote the threshold for selecting terms, where only the ones with more than two occurrences were included in the model. Any term that occurred less than two times was not included in the model.

The unsteady explanatory variables $\tilde{x}_Y$, $\tilde{x}_Z$, $\tilde{x}_l$, $\tilde{x}_m$, and $\tilde{x}_n$ are not measurable; as a result,

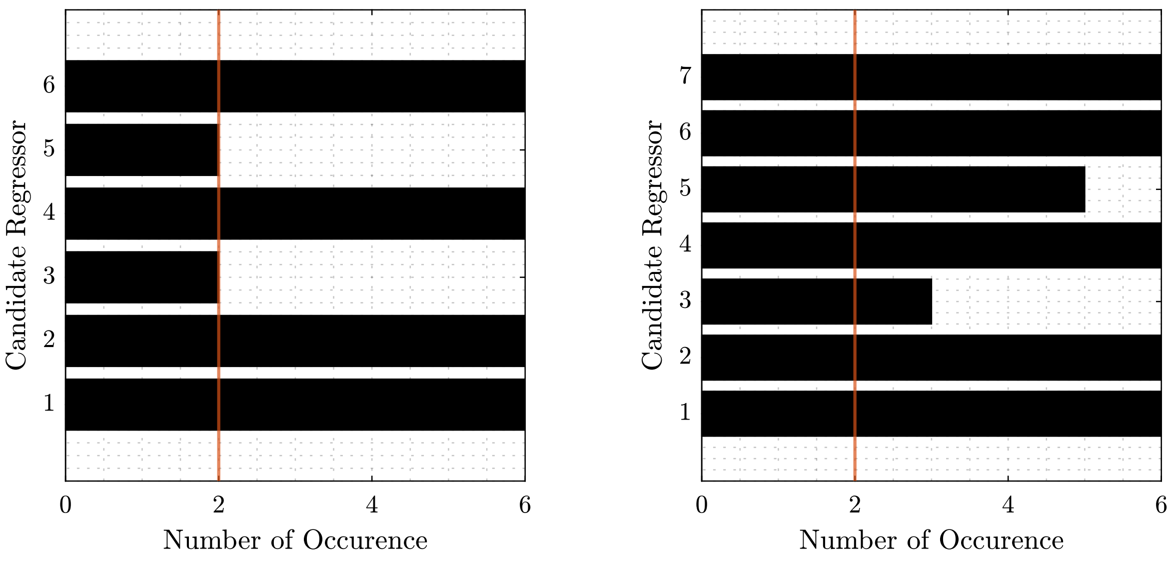

(a) Model terms selected for C_X

(b) Model terms selected for C_Y

Figure 5.7: Model terms selected for C_X and C_Y coefficient of the quasi-steady and unsteady aerodynamic model. The red line indicates the selection threshold.

the unsteady explanatory variables can not be included in the MOF analysis. Instead, the explanatory variables that generally approximate unsteady effects, such as the rate of change of angle of attack $\dot{\alpha}$ and rate of change of sideslip angle $\dot{\beta}$, can be added into the MOF analysis. In this case, the regular longitudinal and lateral-directional explanatory variables, such as $\delta\alpha$, $\delta\beta$, $\Delta\hat{u_r}$, $\Delta\delta_a$, $\Delta\delta_e$, $\Delta\delta_r$, $\hat{p}$, $\hat{q}$, and $\hat{r}$ are considered along $\dot{\alpha}$ and $\dot{\beta}$ explanatory variable to determine the structure of the unsteady model. Once the structure is determined, the explanatory variables that approximate unsteady effects ($\dot{\alpha}$ and $\dot{\beta}$) are replaced by the unsteady explanatory variables ($\tilde{x}_Y$, $\tilde{x}_Z$, $\tilde{x}_l$, $\tilde{x}_m$ and $\tilde{x}_n$). Based on the MOF analysis, the

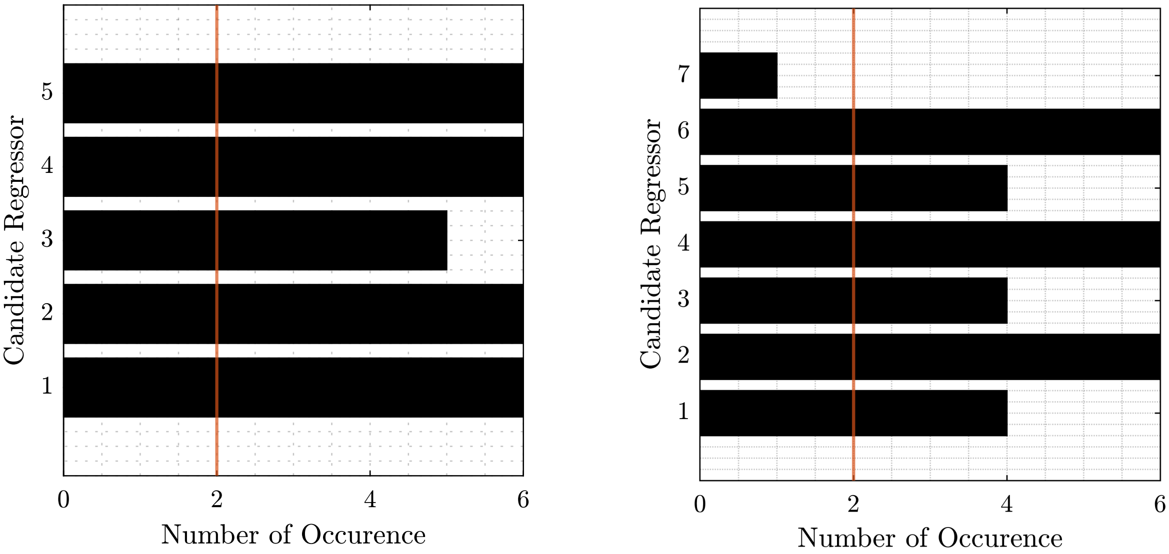

(a) Model terms selected for C_Z (b) Model terms selected for C_l

Figure 5.8: Model terms selected for C_z and C_l coefficient of the quasi-steady and unsteady aerodynamic model. The red line indicates the selection threshold.

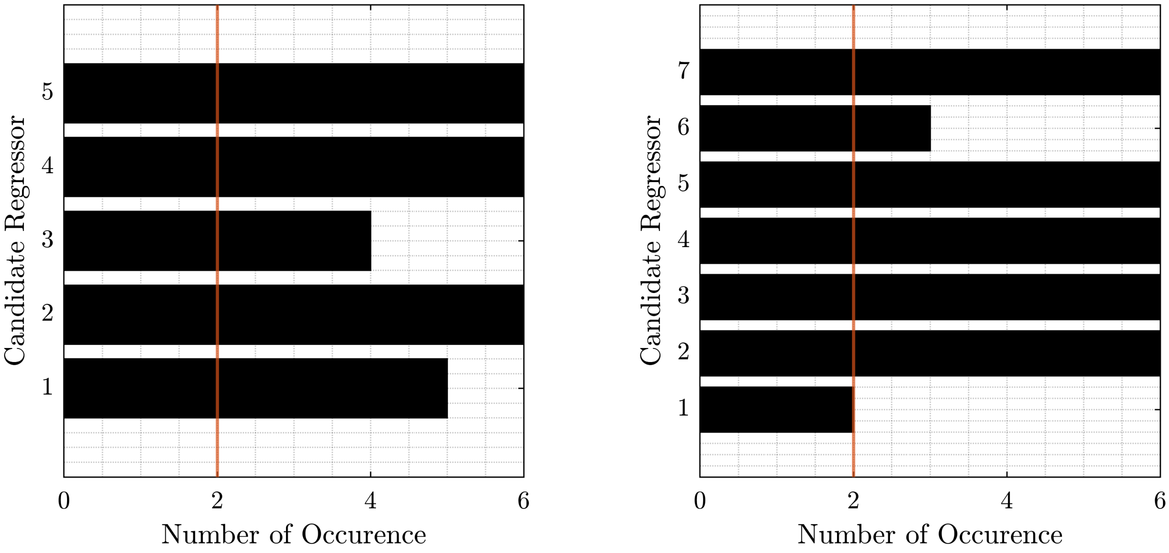

(a) Model terms selected for C_m (b) Model terms selected for C_n

Figure 5.9: Model terms selected for C_m and C_n coefficient of the quasi-steady and unsteady aerodynamic model. The red line indicates the selection threshold.

final unsteady aerodynamic model structure is as follows:

$$C_J = C_{J_0} + C_J J + C_{J^2} J^2 \tag{5.7a}$$

$$C_X = C_{X_0} + C_{X_\alpha} \Delta\alpha + C_{X_q} \hat{q} + C_{X_{u_\mathrm{r}}} \Delta u_\mathrm{r} \tag{5.7b}$$

$$C_Y = C_{Y_{\tilde{x}}} \tilde{x}_Y + C_{Y_0} + C_{Y_\beta} \Delta\beta + C_{Y_p} \hat{p} + C_{Y_r} \hat{r} + C_{Y_{\delta_a}} \Delta\delta_a + C_{Y_{\delta_r}} \Delta\delta_r \tag{5.7c}$$

$$C_Z = C_{Z_{\tilde{x}}} \tilde{x}_Z + C_{Z_0} + C_{Z_\alpha} \Delta\alpha + C_{Z_q} \hat{q} + C_{Z_{\delta_e}} \Delta\delta_e \tag{5.7d}$$

$$C_l = C_{l_{\tilde{x}}} \tilde{x}_l + C_{l_0} + C_{l_\beta} \Delta\beta + C_{l_p} \hat{p} + C_{l_r} \hat{r} + C_{l_{\delta_a}} \Delta\delta_a \tag{5.7e}$$

$$C_m = C_{m_{\tilde{x}}} \tilde{x}_m + C_{m_0} + C_{m_\alpha} \Delta\alpha + C_{m_q} \hat{q} + C_{m_{\delta_e}} \Delta_e \tag{5.7f}$$

$$C_n = C_{n_{\tilde{x}}} \tilde{x}_n + C_{n_\beta} + C_{n_p} \hat{p} + C_{n_r} \hat{r} + C_{n_{\delta_a}} \Delta\delta_a + C_{n_{\delta_r}} \Delta\delta_r \tag{5.7g}$$

The vector $\boldsymbol{\tilde{x}} = [\tilde{x}_Y, \tilde{x}_Z, \tilde{x}_l, \tilde{x}_m, \tilde{x}_n]^\mathrm{T}$ is the nondimensional unsteady aerodynamic state vector with dynamics described by the following equations:

$$\dot{\tilde{x}}_Y = A_{Y_{\tilde{x}}} \tilde{x}_Y + B_{Y_{\tilde{x}}} \Delta\beta \tag{5.8a}$$

$$\dot{\tilde{x}}_Z = A_{Z_{\tilde{x}}} \tilde{x}_Z + B_{Z_{\tilde{x}}} \Delta\alpha \tag{5.8b}$$

$$\dot{\tilde{x}}_l = A_{l_{\tilde{x}}} \tilde{x}_l + B_{l_{\tilde{x}}} \Delta\beta \tag{5.8c}$$

$$\dot{\tilde{x}}_m = A_{m_{\tilde{x}}} \tilde{x}_m + B_{m_{\tilde{x}}} \Delta\alpha \tag{5.8d}$$

$$\dot{\tilde{x}}_n = A_{n_{\tilde{x}}} \tilde{x}_n + B_{n_{\tilde{x}}} \Delta\beta \tag{5.8e}$$

where $A_{(\cdot)_{\tilde{x}}}$ and $B_{(\cdot)_{\tilde{x}}} = 1\ \mathrm{s}^{-1}$ parameterize the unsteady aerodynamics. For compactness, the unsteady dynamic equations given above are combined as follows:

$$\dot{\tilde{\boldsymbol{x}}} = \underbrace{\begin{bmatrix} A_{Y_{\tilde{x}}} & 0 & 0 & 0 & 0 \\ 0 & A_{Z_{\tilde{x}}} & 0 & 0 & 0 \\ 0 & 0 & A_{l_{\tilde{x}}} & 0 & 0 \\ 0 & 0 & 0 & A_{m_{\tilde{x}}} & 0 \\ 0 & 0 & 0 & 0 & A_{n_{\tilde{x}}} \end{bmatrix}}_{\bar{\boldsymbol{A}}} \tilde{\boldsymbol{x}} + \underbrace{\begin{bmatrix} 0 & 1 \\ 1 & 0 \\ 0 & 1 \\ 1 & 0 \\ 0 & 1 \end{bmatrix}}_{\bar{\boldsymbol{B}}} \underbrace{\begin{bmatrix} \Delta\alpha \\ \Delta\beta \end{bmatrix}}_{\tilde{\boldsymbol{u}}} \tag{5.9}$$

The quasi-steady aerodynamic model is structurally identical to Equation (5.7), except that the $\tilde{x}$ terms are omitted because the model is quasi-steady.

$$C_J = C_{J_0} + C_J J + C_{J^2} J^2 \tag{5.10a}$$

$$C_X = C_{X_0} + C_{X_\alpha}\Delta\alpha + C_{X_q}\hat{q} + C_{X_{u_\mathrm{r}}}\Delta u_\mathrm{r} \tag{5.10b}$$

$$C_Y = C_{Y_0} + C_{Y_\beta}\Delta\beta + C_{Y_p}\hat{p} + C_{Y_r}\hat{r} + C_{Y_{\delta_a}}\Delta\delta_a + C_{Y_{\delta_r}}\Delta\delta_r \tag{5.10c}$$

$$C_Z = C_{Z_0} + C_{Z_\alpha}\Delta\alpha + C_{Z_q}\hat{q} + C_{Z_{\delta_e}}\Delta\delta_e \tag{5.10d}$$

$$C_l = C_{l_0} + C_{l_\beta}\Delta\beta + C_{l_p}\hat{p} + C_{l_r}\hat{r} + C_{l_{\delta_a}}\Delta\delta_a \tag{5.10e}$$

$$C_m = C_{m_0} + C_{m_\alpha}\Delta\alpha + C_{m_q}\hat{q} + C_{m_{\delta_e}}\Delta_e \tag{5.10f}$$

$$C_n = C_{n_\beta} + C_{n_p}\hat{p} + C_{n_r}\hat{r} + C_{n_{\delta_a}}\Delta\delta_a + C_{n_{\delta_r}}\Delta\delta_r \tag{5.10g}$$

5.4 Parameter Identification and Validation

The aerodynamic parameters were identified using the output-error method. The output-error method was run on three different multisine data sets, and a weighted mean of the identified parameters and standard error were calculated. The output-error algorithm is initialized with parameter values and covariance matrices identified using equation-error on each data set.

$$w_i = \frac{1}{\sigma_i^2} \tag{5.11a}$$

$$\hat{\theta} = \frac{\Sigma_{i=1}^{n} w_i \hat{\theta}_i}{\Sigma_{i=1}^{n} w_i} \tag{5.11b}$$

$$\sigma = \left(\Sigma_{i=1}^{n} w_i\right)^{-1/2} \tag{5.11c}$$

where σ_i is the standard error of each parameter estimate for individual maneuvers accounting for colored residuals, θ_i is the parameter estimate for individual maneuvers, and n is the number of maneuvers. The model parameters are validated on a separate dataset from the one used for training, which includes an elevator doublet and aileron-rudder doublets.

5.4.1 Nonlinear Aerodynamic Model

The aerodynamic parameter estimates of the nonlinear model given by Equations (5.6) are given in Table 5.1, and the validation results are given in Figure 5.10. The model parameters are validated on a separate dataset from the one used for training, which includes an elevator doublet and aileron-rudder doublets.

5.4.2 Unsteady and Quasi-steady Aerodynamic Models

Tables 5.2 and 5.3 contain the aerodynamic force and moment parameters of the unsteady and quasi-steady aerodynamic models given in Section 5.3.2. The identified models are assumed to be valid for the flight domain indicated by Table 5.4. These explanatory variable upper and lower bounds were taken to be the minimum and maximum values, respectively,

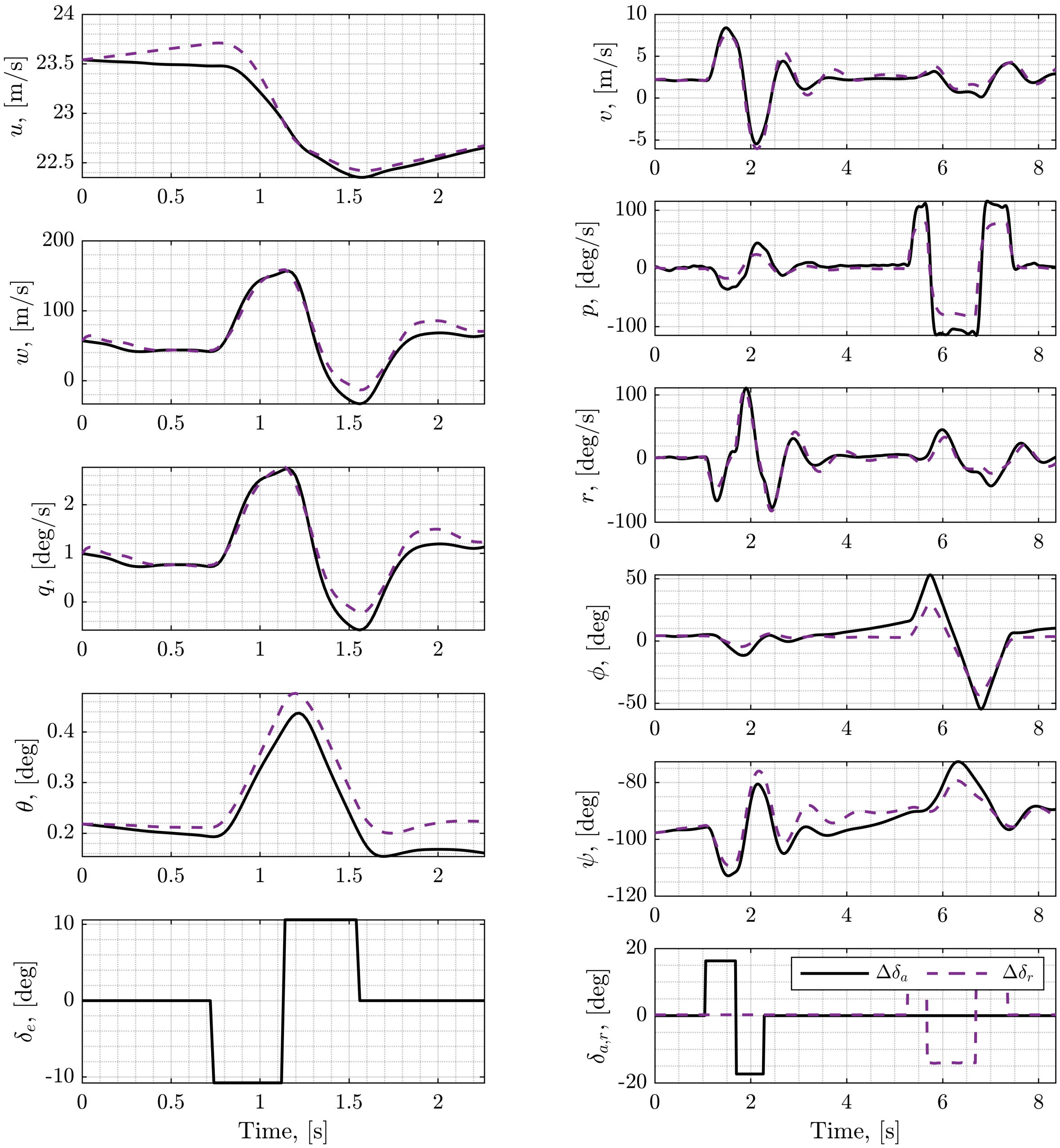

(a) Longitudinal output prediction (b) Lateral-direcional output prediction

Figure 5.10: Output validation results from an elevator doublet maneuver. The flight data are given in black, and output predictions are given in the red dashed line.

Table 5.1: My Twin Dream (MTD) nonlinear aerodynamic parameters

Parameter	$\hat{\theta} \pm \sigma$	Parameter	$\hat{\theta} \pm \sigma$	Parameter	$\hat{\theta} \pm \sigma$
C_{X_0}	+0.0145 ± 0.0025	C_{Y_0}	+0.0040 ± 0.0018	C_{Z_0}	-0.2531 ± 0.0026
$C_{X_{\alpha^2}}$	+3.5996 ± 0.6020	C_{Y_β}	-0.4512 ± 0.0142	C_{Z_α}	-6.0055 ± 0.2582
C_{X_V}	-0.1803 ± 0.0132	C_{Y_r}	+0.4197 ± 0.0602	C_{Z_q}	-15.409 ± 3.1685
		$C_{Y_{\delta_a}}$	-0.0376 ± 0.0088		
		$C_{Y_{\delta_r}}$	+0.1298 ± 0.0136		
Parameter	$\hat{\theta} \pm \sigma$	Parameter	$\hat{\theta} \pm \sigma$	Parameter	$\hat{\theta} \pm \sigma$
C_{l_β}	-0.0377 ± 0.0030	C_{m_α}	-0.4782 ± 0.0279	C_{n_β}	+0.0811 ± 0.0033
C_{l_p}	-0.2942 ± 0.0237	C_{m_q}	-6.2964 ± 0.4981	$C_{n_{\beta^3}}$	+0.0543 ± 0.0931
C_{l_r}	+0.0236 ± 0.0147	$C_{m_{\delta_e}}$	-0.3126 ± 0.0122	C_{n_p}	-0.0433 ± 0.0060
$C_{l_{\delta_a}}$	+0.0858 ± 0.0059			C_{n_r}	-0.1756 ± 0.0080
				$C_{n_{\delta_r}}$	-0.0517 ± 0.0021

in the training data set after outlier removal using MATLAB command `rmoutliers`[1]. The model validation results are presented in Figure 5.11, and their normalized root-mean-square error (NRMSE) is provided in Table 5.5. The NRMSE used is calculated as follows:

$$\text{NRMSE} = \frac{1}{\max(\boldsymbol{z}_{\text{flight}}) - \min(\boldsymbol{z}_{\text{flight}})} \sqrt{\frac{(\boldsymbol{z}_{\text{flight}} - \hat{\boldsymbol{y}}_{\text{model}})^{\mathrm{T}}(\boldsymbol{z}_{\text{flight}} - \hat{\boldsymbol{y}}_{\text{model}})}{N}} \tag{5.12}$$

where is $\boldsymbol{z}_{\text{flight}}$ is the measured output from flight data, $\hat{\boldsymbol{y}}_{\text{model}}$ is the response of the model, and N is the number of data points in $\boldsymbol{z}_{\text{flight}}$ and $\hat{\boldsymbol{y}}_{\text{model}}$. The time histories and NRMSE values for the validation data reflect nearly identical performance for the two models.

5.4.3 Propulsion Model

The propulsion model was developed using a least-squares polynomial fit in advance ratio from UIUC wind tunnel data [94] for the APC 10x6E propellers. The propeller model is given below.

$$C_J = C_{J_0} + C_J J + C_{J^2} J^2 \tag{5.13}$$

---

[1] Data more than three scaled median absolute deviations from the median are removed. See `https://www.mathworks.com/help/matlab/ref/rmoutliers.html` (Accessed Jan 2024) for more information.

Table 5.2: MTD aerodynamic force parameters

Unsteady model		**Quasi-steady model**	
Term	$\hat{\theta} \pm \mathrm{std}$	Term	$\hat{\theta} \pm \mathrm{std}$
C_{X_0}	-0.4048 ± 0.0001	C_{X_0}	-0.4045 ± 0.0002
C_{X_α}	+0.2610 ± 0.0040	C_{X_α}	+0.2625 ± 0.0061
C_{X_q}	+2.0675 ± 0.0432	C_{X_q}	+2.0856 ± 0.0674
$C_{X_{u_\mathrm{r}}}$	-0.1923 ± 0.0007	$C_{X_{u_\mathrm{r}}}$	-0.1935 ± 0.0011
$A_{Y_{\tilde{x}}}$	-1.2739 ± 0.0424		
$C_{Y_{\tilde{x}}}$	+0.1238 ± 0.0076		
C_{Y_0}	+0.0007 ± 0.0001	C_{Y_0}	+0.0004 ± 0.0002
C_{Y_β}	-0.5585 ± 0.0014	C_{Y_β}	-0.5524 ± 0.0019
C_{Y_p}	+0.1928 ± 0.0041	C_{Y_p}	+0.1936 ± 0.0065
C_{Y_r}	+0.4311 ± 0.0052	C_{Y_r}	+0.4731 ± 0.0069
$C_{Y_{\delta_a}}$	-0.1052 ± 0.0014	$C_{Y_{\delta_a}}$	-0.1050 ± 0.0022
$C_{Y_{\delta_r}}$	+0.1644 ± 0.0012	$C_{Y_{\delta_r}}$	+0.1637 ± 0.0018
$A_{Z_{\tilde{x}}}$	-0.3524 ± 0.0228		
$C_{Z_{\tilde{x}}}$	+0.4179 ± 0.0375		
C_{Z_0}	-0.3690 ± 0.0010	C_{Z_0}	-0.3642 ± 0.0015
C_{Z_α}	-5.7611 ± 0.0340	C_{Z_α}	-5.6419 ± 0.0507
C_{Z_q}	-42.712 ± 0.4680	C_{Z_q}	-42.975 ± 0.7844
$C_{Z_{\delta_e}}$	-0.4581 ± 0.0115	$C_{Z_{\delta_e}}$	-0.4515 ± 0.0180

Table 5.3: MTD aerodynamic moment parameters

Unsteady Model		Quasi-steady Model	
Term	$\hat{\theta} \pm$ std	Term	$\hat{\theta} \pm$ std
$A_{l_{\tilde{x}}}$	-0.9815 ± 0.0444		
$C_{l_{\tilde{x}}}$	-0.0052 ± 0.0023		
C_{l_0}	-0.0006 ± 0.0001	C_{l_0}	-0.0006 ± 0.0001
C_{l_β}	-0.0314 ± 0.0005	C_{l_β}	-0.0316 ± 0.0006
C_{l_p}	-0.2882 ± 0.0014	C_{l_p}	-0.2881 ± 0.0022
C_{l_r}	+0.0684 ± 0.0016	C_{l_r}	+0.0669 ± 0.0021
$C_{l_{\delta_a}}$	+0.1283 ± 0.0005	$C_{l_{\delta_a}}$	+0.1281 ± 0.0008
$A_{m_{\tilde{x}}}$	-1.0186 ± 0.0426		
$C_{m_{\tilde{x}}}$	+0.1908 ± 0.0142		
C_{m_0}	+0.0032 ± 0.0002	C_{m_0}	+0.0039 ± 0.0002
C_{m_α}	-0.6273 ± 0.0056	C_{m_α}	-0.5930 ± 0.0077
C_{m_q}	-5.6897 ± 0.0725	C_{m_q}	-5.7774 ± 0.1202
$C_{m_{\delta_e}}$	-0.3544 ± 0.0018	$C_{m_{\delta_e}}$	-0.3525 ± 0.0028
$A_{n_{\tilde{x}}}$	-1.4365 ± 0.0381		
$C_{n_{\tilde{x}}}$	-0.0759 ± 0.0024		
C_{n_β}	+0.0947 ± 0.0004	C_{n_β}	+0.0904 ± 0.0005
C_{n_p}	-0.0323 ± 0.0011	C_{n_p}	-0.0328 ± 0.0018
C_{n_r}	-0.0871 ± 0.0015	C_{n_r}	-0.1118 ± 0.0019
$C_{n_{\delta_a}}$	-0.0011 ± 0.0004	$C_{n_{\delta_a}}$	-0.0014 ± 0.0006
$C_{n_{\delta_r}}$	-0.0587 ± 0.0003	$C_{n_{\delta_r}}$	-0.0584 ± 0.0005

Table 5.4: MTD aerodynamic model domain

	Minimum	Mean	Maximum	Units
u_r	12.504	21.096	30.527	m/s
α	-0.0861	0.0412	0.1735	rad
β	-0.2626	0.0524	0.3672	rad
p	-3.1770	0.0045	3.1405	rad/s
q	-1.5367	0.1143	1.6566	rad/s
r	-1.9676	-0.0252	1.9204	rad/s
δ_a	-0.4745	0.0114	0.4854	rad
δ_e	-0.4657	-0.0105	0.4486	rad
δ_r	-0.3013	0.0081	0.3306	rad
J	0.2064	0.3423	0.4368	–

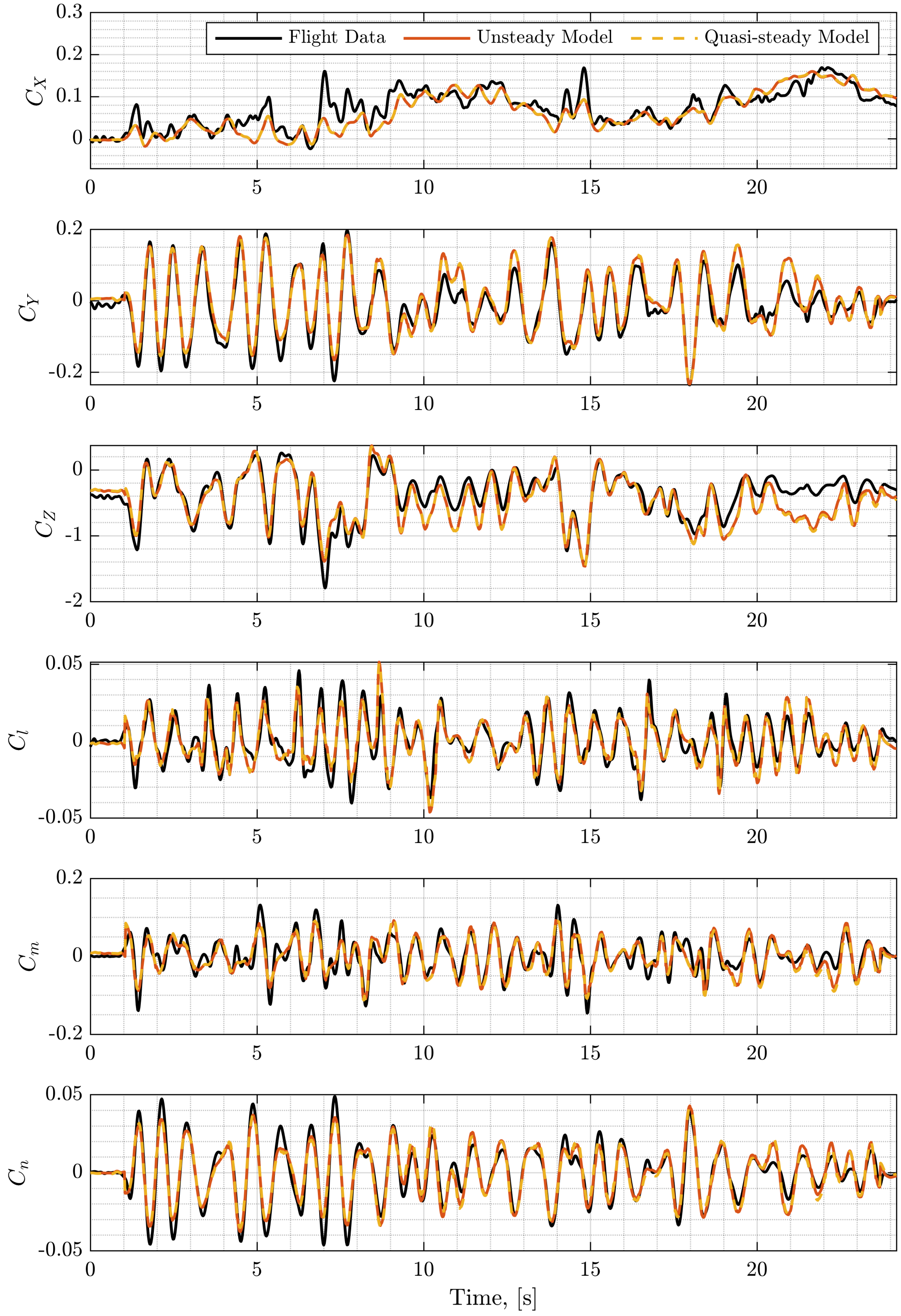

Figure 5.11: Quasi-steady and unsteady aerodynamic model validation

Table 5.5: Normalized root mean square error (NRMSE)

	Unsteady Aerodynamic Model	Quasi-steady Aerodynamic Model
C_X	0.3129	0.3163
C_Y	0.0624	0.0636
C_Z	0.1093	0.1165
C_l	0.0744	0.0745
C_m	0.0853	0.0874
C_n	0.0631	0.0703

where $J = \frac{u}{\delta_{\text{rps}} D}$ is the propeller advanced ratio, δ_{rps} is the propeller rotation speed, and D is the diameter of the aircraft's propeller. The propeller model parameters are given in Table 5.6.

Table 5.6: Propeller model parameter

Term	$\hat{\theta} \pm \sigma$
C_{J_0}	+0.116 ± 0.0002
C_J	-0.040 ± 0.0013
C_{J^2}	-0.131 ± 0.0015

5.5 Conclusion

In summary, three aerodynamic models were developed for the research aircraft described in Chapter 4: a nonlinear, a quasi-steady, and an unsteady aerodynamic model. The nonlinear aerodynamic model is used for the work presented in Chapter 6, and the quasi-steady and nonlinear aerodynamic model are used for the work presented in Chapter 7. A propulsion model is also developed and used along the nonlinear, quasi-steady, and unsteady aerodynamic models. The objective of the work presented in Chapter 6 is to compare various existing wind estimation schemes. As a result, a nonlinear aerodynamic model of the research aircraft suffices the effort's needs. However, in Chapter 7, the objective is to include an unsteady aerodynamic model in a wind estimation scheme, which is a novel contribution of this dissertation, and compare the estimate to a quasi-steady aerodynamic model-based wind estimate. As a result, an unsteady and quasi-steady aerodynamic model for the research aircraft is developed. The following chapters present wind estimation methods and the implementation of the aerodynamic models presented in this chapter.

Chapter 6

Comparison of Aerodynamic Model-free and Model-based Wind Estimators

In this chapter, six wind estimation formulations using experimental flight data obtained from a small, fixed-wing, uncrewed aircraft are compared. For every formulation, three filters are developed – a Kalman filter, an extended Kalman filter, and an unscented Kalman filter. Each formulation adopts different assumptions about the flight dynamic model and available measurements. The first three formulations use no aerodynamic model: the wind triangle and a rigid motion model with either six measurements (inertial and air-relative velocity) or nine measurements (the previous six plus attitude). The latter three formulations include an aerodynamic model. The chapter discusses the selection of initial state estimates and filter parameters, including the selection of process and measurement noise matrices. An air data unit with wind vanes and a pitot tube is used to reconstruct the local wind velocity for validation. The chapter presents wind estimate error analysis for all three filters as applied for each formulation in comparison with the reconstructed wind velocity.

6.1 Introduction

The development and application of unmanned aircraft systems (UAS) and the push towards urban air mobility (UAM) have introduced the need and opportunity to measure characteristics of the lower atmosphere that are important for atmospheric science and weather forecasts, such as pressure, temperature, humidity, and wind velocity [1, 8, 9, 25, 46, 80, 95]. This chapter compares a number of methods for estimating atmospheric wind using a fixed-wing aircraft. The aircraft is equipped with a satellite navigation sensor that provides absolute velocity and with an air data unit that provides air-relative velocity in the form of total airspeed and two aerodynamic angles. While all of the estimation formulations use the absolute velocity measurements, not all of them use air-relative velocity. The formulations that do not use air-relative velocity are of particular interest. If these methods are accurate, then they enable indirect wind estimation without the need for a sophisticated air data unit or on-board anemometer [25].

Direct wind measurement relies on sensors dedicated to measuring wind, e.g., an anemometer, SoDAR, or LiDAR. SoDAR and LiDAR sensors are ground-based instruments that can provide wind velocity profiles. In practice, these devices average high rate measurements over a user-specified period of time – on the order of minutes – to produce time-averaged measurements at particular heights over a specific location. Anemometers provide real-time point measurements of wind velocity, either at a fixed ground location or on-board an aircraft [56, 96]. Indirect wind estimation, as mentioned above, uses no direct measurement of the wind, but leverages an aircraft's motion model and its operational sensor data to infer wind velocity [11, 47, 60, 79, 82, 83, 97]; essentially, the aircraft itself is the wind sensor.

For indirect wind estimation using an aircraft motion model, one may choose whether to incorporate a model of the aerodynamic effects into the estimator [25]. Aerodynamic model-free [79, 82, 83] and model-based [11, 20, 47, 53, 97] approaches have been a subject of interest in in recent years.

This chapter compares aerodynamic model-free and model-based wind velocity estimation results obtained using flight data from small, fixed-wing aircraft. A selection of wind estimation formulations, involving different model and measurement information, are implemented using three estimation filters: a Kalman filter [28], an extended Kalman filter [14], and an unscented Kalman filter [15]. Accordingly, the chapter describes the various state propagation and measurement models, the measurement and control input data, filter initialization, and selection of process and measurement noise covariance matrices.

Wind estimates obtained using the various model-based formulations and filters discussed above are compared with direct measurements obtained using the wind triangle. When interpreting these comparisons, though, it is important to keep in mind that the wind triangle measurements are not necessarily "truth" data. They are direct measurements, but they are obtained using sensors that can exhibit uncharacterized bias, noise, and nonlinearity. By incorporating additional measurements, one could credibly produce a *more* accurate estimate of the wind velocity than is provided by the wind triangle. For this reason, we regard comparisons between the estimated wind velocity and measured wind velocity as "differences" rather than "errors." Accordingly, the chapter presents root-mean-squared *difference* (RMSD) values for each of the formulations and filters that are described.

6.2 Wind Estimation Methods

In this section, six wind estimation formulations are described. All six formulations leverage the wind triangle relationship. They at least require the aircraft's total velocity expressed in the NED frame and a component of its relative velocity expressed in the body-fixed frame. The availability of sensors typically guides the construction of any wind estimation formulation.

6.2.1 Aircraft Nonlinear Aerodynamic Model

The aerodynamic model used in this chapter is described in detail in Section 5.3.1.

$$C_J = C_{J_0} + C_J J + C_{J^2} J^2 \tag{6.1a}$$

$$C_X = C_{X_0} + C_{X_{\alpha^2}} \Delta\alpha^2 + C_{X_{u_r}} \Delta\hat{u}_r \tag{6.1b}$$

$$C_Y = C_{Y_0} + C_{Y_\beta}\Delta\beta + C_{Y_r}\hat{r} + C_{Y_{\delta_a}}\Delta\delta_a + C_{Y_{\delta_r}}\Delta\delta_r \tag{6.1c}$$

$$C_Z = C_{Z_0} + C_{Z_\alpha}\Delta\alpha + C_{Z_q}\hat{q} \tag{6.1d}$$

$$C_l = C_{l_\beta}\Delta\beta + C_{l_p}\hat{p} + C_{l_r}\hat{r} + C_{l_{\delta_a}}\Delta\delta_a \tag{6.1e}$$

$$C_m = C_{m_\alpha}\Delta\alpha + C_{m_q}\hat{q} + C_{m_{\delta_e}}\Delta\delta_e \tag{6.1f}$$

$$C_n = C_{n_\beta}\Delta\beta + C_{n_{\beta^3}}\Delta\beta^3 + C_{n_p}\hat{p} + C_{n_r}\hat{r} + C_{n_{\delta_r}}\Delta\delta_r \tag{6.1g}$$

The variables that denote perturbations from nominal state and control values given in Equation (6.1) are defined as follows:

$$\Delta u_{\mathrm{r}} = u_{\mathrm{r}} - u_{\mathrm{r,nom}} \quad \Delta\alpha = \alpha - \alpha_{\mathrm{nom}} \quad \Delta\beta = \beta - \beta_{\mathrm{nom}}$$

$$\Delta\delta_a = \delta_a - \delta_{a,\mathrm{nom}} \quad \Delta\delta_e = \delta_e - \delta_{e,\mathrm{nom}} \quad \Delta\delta_r = \delta_r - \delta_{r,\mathrm{nom}}$$

The nondimensional state variables given in Equation (6.1) are defined as follows:

$$J = \tfrac{u_r}{\delta_{\mathrm{rps}} D} \quad \alpha = \tan^{-1}\left(\tfrac{w_r}{u_r}\right) \quad \beta = \sin^{-1}\left(\tfrac{w_r}{\|\boldsymbol{v}_{\mathrm{r}}\|}\right) \quad \hat{p} = \tfrac{pb}{2V_0} \quad \hat{q} = \tfrac{q\bar{c}}{2V_0} \quad \hat{r} = \tfrac{rb}{2V_0}$$

6.2.2 Wind Estimation Formulations

The wind estimation formulations described have a dynamic and measurement model with white, uncorrelated process and measurement noise statistics that are constructed as follows:

$$\dot{\boldsymbol{x}}(t) = \boldsymbol{f}(t, \boldsymbol{x}(t), \boldsymbol{u}(t)) + \tilde{\boldsymbol{w}}(t) \tag{6.2a}$$

$$\boldsymbol{z}(t_k) = \boldsymbol{h}(t_k, \boldsymbol{x}(t_k)) + \tilde{\boldsymbol{v}}(t_k) \tag{6.2b}$$

The measurement model is discrete with a sampling period Δt, where $t_k = t_0 + k\Delta t$. The vector $\boldsymbol{f}(t, \boldsymbol{x}(t), \boldsymbol{u}(t), \tilde{\boldsymbol{w}}(t))$ is the system's dynamic function, the vector $\boldsymbol{h}(t_k, \boldsymbol{x}(t_k))$ is the system's measurement model, $\boldsymbol{x}$ is the system's $n \times 1$ state vector, $\boldsymbol{u}$ is the system's $m \times 1$ input vector, and $\boldsymbol{z}$ is the system's $p \times 1$ measurement vector. The process and measurement noise are assumed to be described by Gaussian distributions with $\tilde{\boldsymbol{w}}(t) \sim \mathcal{N}(\boldsymbol{0}, \boldsymbol{S})$ and $\tilde{\boldsymbol{v}}(t_k) \sim \mathcal{N}(\boldsymbol{0}, \boldsymbol{R})$, respectively.

Formulation 1: Wind Triangle Aerodynamic Model-free

Formulation 1 solely relies on the wind triangle, where the system's states include the wind velocity expressed in the NED frame, a lumping parameter (ζ) to estimate the effect of the angle of attack (α), and sideslip angle (β), and the aircraft's total velocity expressed in the NED frame. The dynamics of wind velocity, lumping parameter, and total velocity are modeled as a random walk process. The aircraft's total velocity and the aircraft's true airspeed V_t are used as measurements. The formulation presented here is similar to the one introduced in [79] and later in [83]. However, the formulation given in [79, 83] includes the aircraft's total velocity as part of the system's input, while here, it is considered as part of the system's measurement. The system's dynamic function is constructed as follows:

$$\dot{\boldsymbol{x}} = \begin{bmatrix} \dot{\boldsymbol{V}}_{\mathrm{w}} \\ \dot{\zeta} \\ \dot{\boldsymbol{V}} \end{bmatrix} = \begin{bmatrix} \boldsymbol{0} + \tilde{\boldsymbol{w}}_{\mathrm{w}} \\ \boldsymbol{0} + \tilde{w}_{\zeta} \\ \boldsymbol{0} + \tilde{w}_{V} \end{bmatrix} \tag{6.3}$$

where $\boldsymbol{x} = [\boldsymbol{V}_{\mathrm{w}}, \zeta, \boldsymbol{V}]^{\mathrm{T}}$ is a 7×1 state vector, $\tilde{\boldsymbol{w}} = [\tilde{\boldsymbol{w}}_{\mathrm{w}}, \tilde{w}_{\zeta}, \tilde{\boldsymbol{w}}_{V}]^{\mathrm{T}}$ is a 7×1 process noise vector. The measurement model of the system is constructed as follows:

$$\boldsymbol{z} = \begin{bmatrix} \zeta\sqrt{(V_x - V_{\mathrm{w},x})^2 + (V_y - V_{\mathrm{w},y})^2 + (V_z - V_{\mathrm{w},z})^2} \\ \boldsymbol{V} \end{bmatrix} + \begin{bmatrix} \tilde{v}_{V_{\mathrm{t}}} \\ \tilde{\boldsymbol{v}}_{V} \end{bmatrix} \tag{6.4}$$

where $\boldsymbol{z}$ is a 4×1 measurement vector, $\tilde{\boldsymbol{v}} = [\tilde{v}_{V_{\mathrm{r}}}, \tilde{\boldsymbol{v}}_{V}]^{\mathrm{T}}$ is a 4×1 measurement noise vector.

Formulation 2: 15-State and 6-Measurement Aerodynamic Model-free

The wind estimation method given here is one that was formulated in [83, 98]. This formulation state vector includes the aircraft's relative velocity expressed in the body-fixed frame, attitude, and the wind velocity expressed in the NED frame. The aircraft's measured specific force and angular rate values are used as inputs. The specific force and angular rate are acquired from IMU sensors, which are prone to bias. Hence, the IMU's bias terms are augmented onto the system's state vector and modeled as a random walk process to account for sensor bias. The aircraft's total velocity history, expressed in the NED frame, is used as a measurement along with the aircraft's true airspeed, angle of attack, and sideslip angle.

The system's dynamic model is constructed as follows:

$$\dot{\boldsymbol{x}} = \begin{bmatrix} \dot{\boldsymbol{v}}_{\mathrm{r}} \\ \dot{\boldsymbol{\Theta}} \\ \dot{\boldsymbol{V}}_{\mathrm{w}} \\ \dot{\boldsymbol{b}}_{f_a} \\ \dot{\boldsymbol{b}}_{\omega} \end{bmatrix} = \begin{bmatrix} \boldsymbol{v}_{\mathrm{r}} \times (\boldsymbol{\omega} - \boldsymbol{b}_{\omega}) + (\boldsymbol{f}_a - \boldsymbol{b}_a) + g\boldsymbol{R}_{\mathrm{IB}}^{\mathrm{T}}\boldsymbol{e}_z + \tilde{\boldsymbol{w}}_{v_{\mathrm{r}}} \\ \boldsymbol{L}_{\mathrm{IB}}\left(\boldsymbol{\omega} - \boldsymbol{b}_{\omega}\right) + \tilde{\boldsymbol{w}}_{\Theta} \\ \boldsymbol{0} + \tilde{\boldsymbol{w}}_{\mathrm{w}} \\ \boldsymbol{0} + \tilde{\boldsymbol{w}}_{f_a} \\ \boldsymbol{0} + \tilde{\boldsymbol{w}}_{\omega} \end{bmatrix} \tag{6.5}$$

where $\boldsymbol{b}_{f_a} = [b_{a_x}, b_{a_y}, b_{a_z}]^{\mathrm{T}}$ is the accelerometer bias vector with 3×1 dimension, $\boldsymbol{b}_{\omega} = [b_p, b_q, b_r]^{\mathrm{T}}$ is the gyroscope bias vector with 3×1 dimension, $\boldsymbol{x} = [\boldsymbol{v}_{\mathrm{r}}, \boldsymbol{\Theta}, \boldsymbol{V}_{\mathrm{w}}, \boldsymbol{b}_{f_a}, \boldsymbol{b}_{\omega}]^{\mathrm{T}}$ is an 15×1 state vector, $\boldsymbol{u} = [\boldsymbol{f}_a, \boldsymbol{\omega}]^{\mathrm{T}}$ is the 6×1 input vector, and $\tilde{\boldsymbol{w}} = [\tilde{\boldsymbol{w}}_{v_{\mathrm{r}}}, \tilde{\boldsymbol{w}}_{\Theta}, \tilde{\boldsymbol{w}}_{\mathrm{W}}, \tilde{\boldsymbol{w}}_{f_a}, \tilde{\boldsymbol{w}}_{\omega}]^{\mathrm{T}}$ is the 15×1 process noise vector. The process noise $\tilde{\boldsymbol{w}}_{v_{\mathrm{r}}}$ accounts for accelerometer noise, gyroscope noise, errors due to linearization if applicable, and error due to ignoring the $\boldsymbol{R}_{\mathrm{IB}}^{\mathrm{T}}\dot{\boldsymbol{V}}_{\mathrm{W}}$ term. The process noise $\tilde{\boldsymbol{w}}_{\Theta}$ accounts for gyroscope noise and errors due to linearization, if applicable. The process noise vectors $\tilde{\boldsymbol{w}}_{f_a}$, and $\tilde{\boldsymbol{w}}_{\omega}$ account for the noise signals that drive the bias random walk processes associated with the accelerometer and gyroscope sensors, respectively. The system's measurement model is constructed as follows:

$$\boldsymbol{z} = \begin{bmatrix} \boldsymbol{V} \\ V_{\mathrm{t}} \\ \alpha \\ \beta \end{bmatrix} = \begin{bmatrix} \boldsymbol{R}_{\mathrm{IB}}\boldsymbol{v}_{\mathrm{r}} + \boldsymbol{V}_{\mathrm{w}} + \tilde{\boldsymbol{v}}_{V} \\ u_{\mathrm{r}} + \tilde{\boldsymbol{v}}_{V_{\mathrm{r}}} \\ \tan^{-1}\left(\frac{w_{\mathrm{r}}}{u_{\mathrm{r}}}\right) + \tilde{v}_{\alpha} \\ \sin^{-1}\left(\frac{v_{\mathrm{r}}}{\|\boldsymbol{v}_{\mathrm{r}}\|}\right) + \tilde{v}_{\beta} \end{bmatrix} \tag{6.6}$$

where $\boldsymbol{z} = [\boldsymbol{V}, V_{\mathrm{r}}, \alpha, \beta]^{\mathrm{T}}$ is the 6×1 measurement vector, and $\tilde{\boldsymbol{v}} = [\tilde{\boldsymbol{v}}_{V}, \tilde{v}_{V_{\mathrm{r}}}, \tilde{v}_{\alpha_{\mathrm{v}}}, \tilde{v}_{\beta\mathrm{v}}]$ is the 6×1 measurement noise vector. Note the angle of attack and sideslip angle measurement history are computed using data acquired from the ADU vanes mounted away from the aircraft's center of gravity as suggested in [99].

Formulation 3: 15-State and 9-Measurement Aerodynamic Model-free

The wind estimation formulation described here expands formulation 2 to include the aircraft's attitude as measurement. The system measurement model is constructed such that $\boldsymbol{z} = [\boldsymbol{V}, \boldsymbol{\Theta}, V_{\mathrm{r}}, \alpha_{\mathrm{v}}, \beta_{f_{\mathrm{v}}}]^{\mathrm{T}}$ is a 9×1 measurement vector, and $\tilde{\boldsymbol{v}} = [\tilde{\boldsymbol{v}}_V, \tilde{\boldsymbol{v}}_\Theta, \tilde{v}_{V_{\mathrm{r}}}, \tilde{v}_\alpha, \tilde{v}_\beta]$ is the system's 9×1 measurement noise vector.

Formulation 4: Model-based

Formulation 4 is distinct from formulations 1, 2, and 3 in that it incorporates the aircraft's aerodynamic force and moment model into the system's model framework. Moreover, the system includes the aircraft's position, as expressed in the NED frame, and angular rate histories as measurements. Notably, the system does not consider the aircraft's true airspeed, angle of attack, and sideslip as measured variables. The system's dynamic model is constructed as follows:

$$\dot{\boldsymbol{x}} = \begin{bmatrix} \dot{\boldsymbol{X}} \\ \dot{\boldsymbol{\Theta}} \\ \dot{\boldsymbol{v}}_{\mathrm{r}} \\ \dot{\boldsymbol{\omega}} \\ \dot{\boldsymbol{V}}_{\mathrm{w}} \end{bmatrix} = \begin{bmatrix} \boldsymbol{v}_{\mathrm{r}} + \boldsymbol{R}_{\mathrm{IB}}^{\mathrm{T}} \boldsymbol{V}_{\mathrm{w}} + \tilde{\boldsymbol{w}}_P \\ \boldsymbol{L}_{\mathrm{IB}} \boldsymbol{\omega} + \tilde{\boldsymbol{w}}_\Theta \\ \boldsymbol{v}_{\mathrm{r}} \times \boldsymbol{\omega} + \frac{1}{m} \boldsymbol{F}_{\mathrm{A}}(\boldsymbol{v}_{\mathrm{r}}, \boldsymbol{\omega}, \boldsymbol{u}) + \boldsymbol{R}_{\mathrm{IB}}^{\mathrm{T}} g \boldsymbol{e}_z + \tilde{\boldsymbol{w}}_{v_{\mathrm{r}}} \\ \boldsymbol{I}^{-1} \left(\boldsymbol{I} \omega \times \omega \right) + \boldsymbol{I}^{-1} \boldsymbol{M}_{\mathrm{A}}(\boldsymbol{v}_{\mathrm{r}}, \boldsymbol{\omega}, \boldsymbol{u}) + \tilde{\boldsymbol{w}}_\omega \\ \tilde{\boldsymbol{w}}_{\mathrm{w}} \end{bmatrix} \tag{6.7}$$

where $\boldsymbol{x} = [\boldsymbol{X}, \boldsymbol{\Theta}, \boldsymbol{v}_{\mathrm{r}}, \boldsymbol{\omega}, \boldsymbol{V}_{\mathrm{w}}]^{\mathrm{T}}$ is a 15×1 state vector, $\tilde{\boldsymbol{w}} = [\tilde{\boldsymbol{w}}_P, \tilde{\boldsymbol{w}}_\Theta, \tilde{\boldsymbol{w}}_v, \tilde{\boldsymbol{w}}_\omega, \tilde{\boldsymbol{w}}_{\mathrm{w}}]^{\mathrm{T}}$ is a 15×1 is a process noise vector. The process noise signals $\tilde{\boldsymbol{w}}_P$ and $\tilde{\boldsymbol{w}}_\Theta$ account errors due to linearization. The process noise signals $\tilde{\boldsymbol{w}}_{v_{\mathrm{r}}}$ accounts for errors due to linearization if applicable, aerodynamic modeling error in $\boldsymbol{F}_{\mathrm{A}}$, and ignoring the $\boldsymbol{R}_{\mathrm{IB}}^{\mathrm{T}} \dot{\boldsymbol{V}}_{\mathrm{W}}$ term. The process noise signals $\tilde{\boldsymbol{w}}_\omega$ accounts for errors due to linearization if applicable and aerodynamic modeling error in

$\boldsymbol{M}_{\mathrm{A}}$. The system's measurement model is constructed as follows:

$$\boldsymbol{z} = \begin{bmatrix} \boldsymbol{X} \\ \boldsymbol{\Theta} \\ \boldsymbol{V} \\ \boldsymbol{\omega} \end{bmatrix} = \begin{bmatrix} \boldsymbol{X} + \tilde{\boldsymbol{v}}_X \\ \boldsymbol{\Theta} + \tilde{\boldsymbol{v}}_\Theta \\ \boldsymbol{R}_{\mathrm{IB}}\boldsymbol{v}_{\mathrm{r}} + \boldsymbol{V}_{\mathrm{w}} + \tilde{\boldsymbol{v}}_V \\ \boldsymbol{\omega} + \tilde{\boldsymbol{v}}_\omega \end{bmatrix} \tag{6.8}$$

where $\boldsymbol{z} = [\boldsymbol{X}, \boldsymbol{\Theta}, \boldsymbol{V}, \boldsymbol{\omega}]^{\mathrm{T}}$ is the 12×1 measurement vector, and $\tilde{\boldsymbol{v}} = [\tilde{\boldsymbol{v}}_X, \tilde{\boldsymbol{v}}_\Theta, \tilde{\boldsymbol{v}}_V, \tilde{\boldsymbol{v}}_\omega]$ is the 12×1 measurement noise vector.

Formulation 5: 15-State and 13-Measurement Aerodynamic Model-based

The wind estimation formulation described here expands formulation 4 to include true airspeed V_{r} as part of the measurement vector. The system's measurement model is constructed as follows:

$$\boldsymbol{z} = \begin{bmatrix} \boldsymbol{X} \\ \boldsymbol{\Theta} \\ \boldsymbol{V} \\ \boldsymbol{\omega} \\ V_{\mathrm{t}} \end{bmatrix} = \begin{bmatrix} \boldsymbol{X} + \tilde{\boldsymbol{v}}_X \\ \boldsymbol{\Theta} + \tilde{\boldsymbol{v}}_\Theta \\ \boldsymbol{R}_{\mathrm{IB}}\boldsymbol{v}_{\mathrm{r}} + \boldsymbol{V}_{\mathrm{w}} + \tilde{\boldsymbol{v}}_V \\ \boldsymbol{\omega} + \tilde{\boldsymbol{v}}_\omega \\ \sqrt{u_r^2 + v_r^2 + w_r^2} + \tilde{v}_{V_{\mathrm{t}}} \end{bmatrix} \tag{6.9}$$

where $\boldsymbol{z} = [\boldsymbol{X}, \boldsymbol{\Theta}, \boldsymbol{V}, \boldsymbol{\omega}, V_{\mathrm{t}}]^{\mathrm{T}}$ is a 13×1 measurement vector, and $\tilde{\boldsymbol{v}} = [\tilde{\boldsymbol{v}}_X, \tilde{\boldsymbol{v}}_\Theta, \tilde{\boldsymbol{v}}_V, \tilde{\boldsymbol{v}}_\omega, \tilde{v}_{V_{\mathrm{t}}}]$ is the system's 13×1 measurement noise vector.

Formulation 6: 15-State and 15-Measurement Aerodynamic Model-based

The wind estimation formulation described here expands formulation 4 to include true airspeed V_{r}, angle of attack α, and sideslip angle β as part of the measurement vector. The system's measurement model is constructed as follows:

$$\boldsymbol{z} = \begin{bmatrix} \boldsymbol{X} \\ \boldsymbol{\Theta} \\ \boldsymbol{V} \\ \boldsymbol{\omega} \\ V_{\mathrm{t}} \\ \alpha \\ \beta \end{bmatrix} = \begin{bmatrix} \boldsymbol{X} + \tilde{\boldsymbol{v}}_X \\ \boldsymbol{\Theta} + \tilde{\boldsymbol{v}}_\Theta \\ \boldsymbol{R}_{\mathrm{IB}}\boldsymbol{v}_{\mathrm{r}} + \boldsymbol{V}_{\mathrm{w}} + \tilde{\boldsymbol{v}}_V \\ \boldsymbol{\omega} + \tilde{\boldsymbol{v}}_\omega \\ \sqrt{u_r^2 + v_r^2 + w_r^2} + \tilde{v}_{V_{\mathrm{r}}} \\ \tan^{-1}\left(\frac{w_{\mathrm{r}}}{u_{\mathrm{r}}}\right) + \tilde{v}_\alpha \\ \sin^{-1}\left(\frac{v_{\mathrm{r}}}{\|\boldsymbol{v}_{\mathrm{r}}\|}\right) + \tilde{v}_\beta \end{bmatrix} \tag{6.10}$$

where $\boldsymbol{z} = [\boldsymbol{X}, \boldsymbol{\Theta}, \boldsymbol{V}, \boldsymbol{\omega}, V_{\mathrm{r}}, \alpha, \beta]^{\mathrm{T}}$ is a 15×1 measurement vector, and $\tilde{\boldsymbol{v}} = [\tilde{\boldsymbol{v}}_X, \tilde{\boldsymbol{v}}_\Theta, \tilde{\boldsymbol{v}}_V, \tilde{\boldsymbol{v}}_\omega, \tilde{v}_{V_{\mathrm{r}}}, \tilde{v}_\alpha, \tilde{v}_\beta]^{\mathrm{T}}$ is the system's 15×1 measurement noise vector.

6.2.3 Estimation Algorithms

The six formulations described above are implemented in three filters: the continuous-discrete Kalman filter (KF), the continuous-discrete extended Kalman filter (EKF), and the continuous-discrete unscented Kalman filter (UKF). The continuous model and discretized measurement functions are:

$$\boldsymbol{x}(t) = \boldsymbol{f}\left(t, \boldsymbol{x}(t), \boldsymbol{u}(t)\right) + \tilde{\boldsymbol{w}}(t) \tag{6.11a}$$

$$\boldsymbol{z}(t_k) = \boldsymbol{h}\left(t_k, \boldsymbol{x}(t_k)\right) + \tilde{\boldsymbol{v}}(k) \tag{6.11b}$$

For a constant sampling period Δt, one has $t_k = t_0 + k\Delta t$, however the filter algorithms do not require a fixed sample rate. The linearized and continuous-discrete system functions are:

$$\boldsymbol{x}(t) = \boldsymbol{A}\boldsymbol{x}(t) + \boldsymbol{B}\boldsymbol{u}(t) + \boldsymbol{\Gamma}\tilde{\boldsymbol{w}}(t) \tag{6.12a}$$

$$\boldsymbol{z}(t_k) = \boldsymbol{H}\boldsymbol{x}(t_k) + \tilde{\boldsymbol{v}}(t_k) \tag{6.12b}$$

where $\boldsymbol{A}$, $\boldsymbol{B}$, $\boldsymbol{\Gamma}$, and $\boldsymbol{H}$ are time-invariant Jacobian matrices of the system dynamics and measurement functions about some nominal state and input vectors. The filter algorithms use a numerical integration scheme to propagate the state estimate and its covariance from one sample time to the next. In this case, the fourth-order Runge-Kutta integration scheme is used.

State and State Covariance Initialization

The initial estimates and error covariance of position $\hat{\boldsymbol{X}}(t_0)$, total velocity $\hat{\boldsymbol{V}}(t_0)$ and attitude $\hat{\boldsymbol{\Theta}}(t_0)$ are selected from the flight computer navigation solution. The initial estimate of angular velocity $\hat{\boldsymbol{\omega}}(t_0)$ is chosen from the gyroscope measurement, and its initial error state covariance is equal to the covariance of the residual between the measurement and smoothed measurement values. For this computation, the Matlab function `cov` is used. The relative velocity initial estimate $\hat{\boldsymbol{v}}_{\mathrm{r}}(t_0)$ is computed using the rotation matrix constructed from $\hat{\boldsymbol{\Theta}}(t_0)$ along with the measured inertial velocity $\hat{\boldsymbol{V}}(t_0)$ from the autopilot assuming that $\hat{\boldsymbol{V}}_{\mathrm{W}}(t_0)$ is zero. The initial estimate of the scale factor $\hat{\zeta}(t_0)$ is set to be one, and its error covariance is selected such that it reflects a high confidence in the initial state. Likewise, the bias initial states $\hat{\boldsymbol{b}}_{f_a}(t_0)$ and $\hat{\boldsymbol{b}}_{\omega}(t_0)$ estimates are selected to be zeros, and their error covariance is selected to reflect high confidence in the initial state guesses. However, the initial estimates of wind velocity $\hat{\boldsymbol{V}}_{\mathrm{W}}(t_0)$ were taken to be zero with error covariance that reflects low confidence in the initial state guess.

Measurement Time History and Noise Covariance Matrix

The measurement vectors for all formulation $\boldsymbol{z}(t_k)$ are obtained from the flight computer's low-level navigation solution – except for angular velocity, which is obtained directly from the vehicle's angular rate gyroscopes. The associated measurement noise covariance $\boldsymbol{R}(t_k)$ is taken to be diagonal with entries corresponding to the state estimate variances reported by the flight computer. For the gyroscope readings, the measurement noise covariance is considered constant and is estimated by smoothing historical data as explained above.

Process Noise Power Spectral Density Matrix

The constant process noise power spectral density $\boldsymbol{S}$ is obtained by computing the power spectral density of the residuals of the true and modeled state derivative from historical flight data. The residuals are computed as follows:

$$\boldsymbol{\nu} = \dot{\boldsymbol{x}}_{\text{truth}} - \boldsymbol{f}\left(t, \boldsymbol{x}_{\text{truth}}, \boldsymbol{u}_{\text{truth}}\right) \tag{6.13}$$

The constant power spectral density of the residual is computed using the Matlab function `pwelch` function as follows:

$$\boldsymbol{S} = \max\left(\texttt{pwelch}\left(\boldsymbol{\nu}, [], [], [], \mathrm{f_s}\right)\right) \tag{6.14}$$

where $\mathrm{f_s}$ is the sampling frequency.

Unscented Kalman Filter Tuning Parameters

The unscented Kalman filter has additional tuning parameters denoted as α_{ukf}, κ_{ukf}, and β_{ukf}. The tuning parameter α_{ukf} determines the spread of the sigma points around the mean of $\hat{\boldsymbol{x}}$ and is usually set to a small positive value. The tuning parameter κ_{ukf} is also a scaling parameter that influences the weight given to the predicted covariance matrix. A common choice is to set kappa to a value between 0 to 3. Finally, the tuning parameter β_{ukf} is used to incorporate prior knowledge of the distribution of $\hat{\boldsymbol{x}}$.

Table 6.1: Unscented Kalman filter tuning parameters

UKF Parameters	Selected Value	Description
α_{ukf}	$1e{-3}$	–
κ_{ukf}	0	–
β_{ukf}	2	For Gaussian distributions

6.2.4 Wind Estimation Experiment Flight

This section describes two flight profiles used to demonstrate the estimation schemes described. The flight was conducted at Virginia Tech's Kentland Experimental Aerial Systems (KEAS) Laboratory. The aircraft was flown at an altitude of 210 m above ground level (AGL) with a cruise speed of 18.00 m/s in the grid pattern. The mission was automated, except for the take-off and landing phases. The mean wind velocity throughout the flight was 7.55 m/s from northwest to southeast, gusting between 3 m/s and 12 m/s. The estimation schemes were implemented on two sections of this flight profile: a constant altitude, wings-level straight leg (referred to as *straight leg*) and a constant altitude, turning leg (referred to as *turning leg*). Both the straight leg and the turning leg used in the estimation schemes are shown in Figure 6.1.

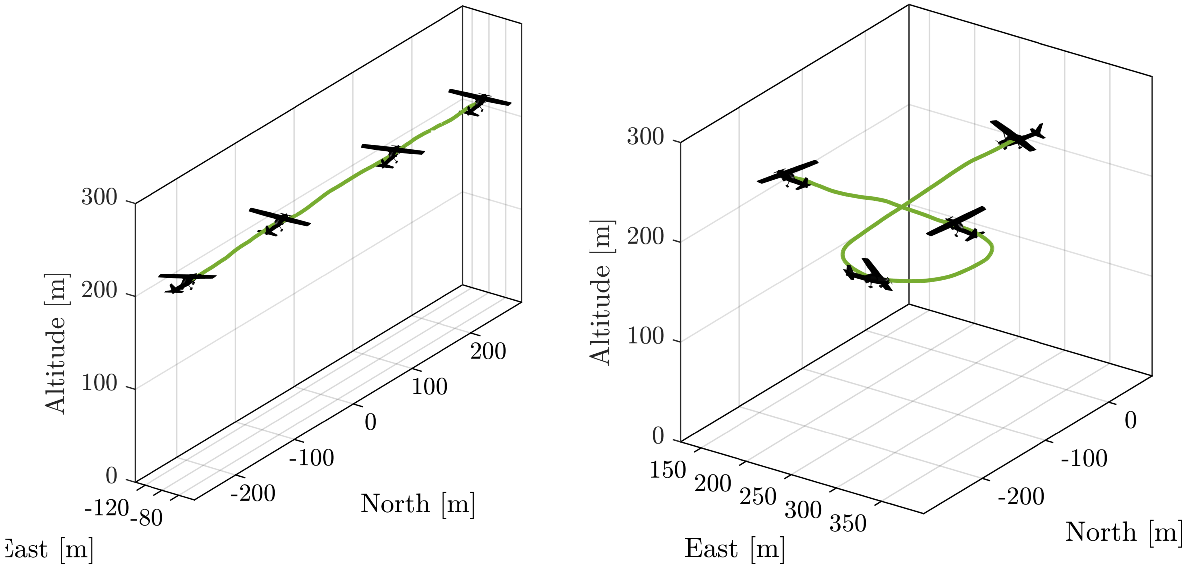

(a) Straight leg.

(b) Turning leg.

Figure 6.1: Experimental flight profiles.

6.3 Results and Analysis

This section presents the results of implementing six wind estimation formulations mentioned in Section 6.2.2. The implementation was done using a KF, an EKF, and a UKF on two flight profiles that are illustrated in Figure 6.1. The flight profiles were chosen to evaluate the performance of different filters under constant altitude and wings-level flight conditions, as well as constant altitude and turning flight conditions. The KF uses a linearized model of nonlinear aircraft dynamics around the equilibrium states and inputs. The EKF recursively linearizes the nonlinear aircraft dynamics about the previous state estimates. On the other hand, the UKF relies on sigma points to propagate the nonlinear function rather than linearization. The selection of the initial states and initial covariance matrix, and the tuning of the measurement noise matrix, process noise matrix, and UKF parameters are discussed below.

6.3.1 Filter Setup

The initial state $\hat{\boldsymbol{x}}(t_0)$, the initial error covariance $\hat{\boldsymbol{P}}(t_0)$, the measurement noise covariance $\boldsymbol{R}$, and the process noise power spectral density matrix $\boldsymbol{S}$ used for all formulation are given here. In Section 6.2.3, a detailed discussion on how to select and calculate the initial state vector, initial error covariance matrices, the measurement noise covariance, and the process noise power spectral density matrix is given. And, in Tables 6.2 to 6.5, the selected and calculated values are given. In Table 6.2, the diagonal of the measurement covariance matrices used to generate the results in Figure 6.2 to 6.7 are given. In Tables 6.3 to 6.5, the initial state, initial error covariance, and the power spectral density matrices used to generate the results in Figure 6.2 to 6.7 are given.

Table 6.2: Measurement noise covariance matrices (diag($\boldsymbol{R}$)).

	Formulation 1	Formulation 2	Formulation 3	Formulation 4	Formulation 5	Formulation 6
V_x	10^{-4}	10^{-4}	10^{-4}	10^{-4}	10^{-4}	10^{-4}
V_y	10^{-4}	10^{-4}	10^{-4}	10^{-4}	10^{-4}	10^{-4}
V_z	10^{-4}	10^{-4}	10^{-4}	10^{-4}	10^{-4}	10^{-4}
V_t	10^{-4}	10^{-4}	10^{-4}	–	10^{-4}	10^{-4}
α	–	10^{-5}	10^{-5}	–	–	10^{-5}
β	–	10^{-5}	10^{-5}	–	–	10^{-5}
ϕ	–	–	10^{-5}	10^{-5}	10^{-5}	10^{-5}
θ	–	–	10^{-5}	10^{-5}	10^{-5}	10^{-5}
ψ	–	–	10^{-3}	10^{-3}	10^{-3}	10^{-3}
x	–	–	–	10^{-2}	10^{-2}	10^{-2}
y	–	–	–	10^{-2}	10^{-2}	10^{-2}
z	–	–	–	10^{-1}	10^{-1}	10^{-1}
p	–	–	–	10^{-4}	10^{-4}	10^{-4}
q	–	–	–	10^{-5}	10^{-5}	10^{-5}
r	–	–	–	10^{-6}	10^{-6}	10^{-6}

6.3.2 General Observations

In Figures 6.2 to 6.6, we compare the wind velocity estimates that we obtained from the KF, EKF, and UKF to algebraically reconstructed wind. The wind velocity estimates that

Table 6.3: Formulation 1 filter parameters

	Initial state Estimate $\hat{\boldsymbol{x}}(t_0)$		Initial error Covariance Estimate $\hat{\boldsymbol{P}}(t_0)$	Process Noise Power Spectral Density Matrix diag($\boldsymbol{S}$)
	Straight	Turning	Both	Both
$V_{\mathrm{w,x}}$	0	0	10^{+1}	1.46
$V_{\mathrm{w,y}}$	0	0	10^{+1}	3.86
$V_{\mathrm{w,z}}$	0	0	10^{+1}	3.39
ζ	1	1	10^{-8}	0
V_x	13.7	-22.5	10^{-4}	0.69
V_y	2.54	-0.350	10^{-4}	0.27
V_z	0.450	1.63	10^{-4}	2.06

Table 6.4: Formulation 2 and 3 filter parameters

	Initial state Estimate $\hat{\boldsymbol{x}}(t_0)$		Initial error Covariance Estimate $\hat{\boldsymbol{P}}(t_0)$	Process Noise Power Spectral Density Matrix diag($\boldsymbol{S}$)
	Straight	Turning	Both	Both
u_r	13.4	21.6	10^{+1}	1.67
v_r	3.50	-5.58	10^{+1}	3.68
w_r	1.56	-0.33	10^{+1}	3.52
ϕ	-0.21	-0.09	10^{-5}	$3.23e{-4}$
θ	0.03	0.02	10^{-5}	$1.49e{-5}$
ψ	-0.09	-2.79	10^{-3}	$3.13e{-5}$
$V_{\mathrm{w,x}}$	0	0	10^{+1}	1.45
$V_{\mathrm{w,y}}$	0	0	10^{+1}	3.86
$V_{\mathrm{w,z}}$	0	0	10^{+1}	3.39
b_{a_x}	0	0	10^{-8}	0
b_{a_y}	0	0	10^{-8}	0
b_{a_z}	0	0	10^{-8}	0
b_p	0	0	10^{-8}	0
b_q	0	0	10^{-8}	0
b_r	0	0	10^{-8}	0

are acquired from the KF are not included in Figures 6.2b, 6.3b, 6.4b, 6.5b, 6.6b, and 6.7b because the KF is only valid for small perturbation flights from the nominal condition, which is not the case in turning flights, leading to diverging results. In Figures 6.2 to 6.7, the reconstructed wind velocity is assumed to be the true wind velocity and is given in black, while the wind estimates acquired from the KF, EKF, and UKF are given in blue, orange, and gold, respectively.

Table 6.5: Formulation 4, 5, and 6 filter parameters

	Initial state estimate $\hat{\boldsymbol{x}}(t_0)$		Initial error covariance estimate $\hat{\boldsymbol{P}}(t_0)$	Process Noise Power Spectral Density Matrix diag($\boldsymbol{S}$)
	Straight	Turning	Both	Both
x	-244	44.8	10^{-2}	$2.20e{-3}$
y	-91.6	267	10^{-2}	$1.31e{-3}$
z	-216	-214	10^{-1}	$1.66e{-3}$
ϕ	$-2.09e{-1}$	$-8.78e{-2}$	10^{-5}	$3.22e{-4}$
θ	$2.60e{-2}$	$2.67e{-2}$	10^{-5}	$1.49e{-5}$
ψ	$-8.92e{-2}$	-2.79	10^{-3}	$3.14e{-5}$
u_r	13.4	$2.16e{+1}$	10^{+1}	8.00
v_r	3.50	-5.58	10^{+1}	3.85
w_r	1.56	$-3.29e{-1}$	10^{+1}	3.36
p	$-4.95e{-3}$	$-2.22e{-1}$	10^{-4}	3.12
q	$-3.35e{-3}$	$-1.49e{-1}$	10^{-5}	$1.52e{-1}$
r	$1.71e{-1}$	$1.18e{-1}$	10^{-6}	$1.76e{-1}$
$V_{\mathrm{w,x}}$	0	0	10^{+1}	1.45
$V_{\mathrm{w,y}}$	0	0	10^{+1}	3.86
$V_{\mathrm{w,z}}$	0	0	10^{+1}	3.39

The measured true airspeed (V_{r}), flank angle (β_{f_v}), and angle of attack (α_v) were used to reconstruct the three-dimensional body-fixed wind velocities [19] as follows:

$$\boldsymbol{V}_{\mathrm{w}} = \boldsymbol{V} - \boldsymbol{R}_{\mathrm{IB}}(\boldsymbol{\Theta})\left(\boldsymbol{v}_{\mathrm{ADU}} - \boldsymbol{\omega} \times \boldsymbol{r}_{\mathrm{ADU}}\right) \tag{6.15}$$

Here $\boldsymbol{v}_{\mathrm{ADU}} = \boldsymbol{R}_{\mathrm{BW}}(\alpha_v, \beta_v)[V_{\mathrm{r}},\ 0,\ 0]^{\mathrm{T}}$ is the air-relative velocity at the geometric center of the ADU vanes, whose position in the body frame is denoted $\boldsymbol{r}_{\mathrm{ADU}}$. The rotation matrix

$$\boldsymbol{R}_{\mathrm{BW}} = \begin{bmatrix} \cos(\alpha_v)\cos(\beta_v) & -\cos(\alpha_v)\sin(\beta_v) & -\sin(\alpha_v) \\ \sin(\beta_v) & \cos(\beta_v) & 0 \\ \sin(\alpha_v)\cos(\beta_v) & -\sin(\alpha_v)\sin(\beta_v) & \cos(\alpha_v) \end{bmatrix}$$

maps free vectors from the wind frame to the body frame. Note that the sideslip angle can be computed from the flank angle as $\beta_v = \tan^{-1}(\tan(\beta_{\mathrm{f}_v})\cos(\alpha_v))$. The aircraft attitude $\boldsymbol{\Theta}$ and angular velocity $\boldsymbol{\omega}$ are acquired from the aircraft's flight computer navigation solution and rate gyroscopes, respectively.

Figure 6.2 shows wind velocity estimates generated by the KF, EKF, and UKF based on formulation 1. In general, the three filter-based wind estimates do not track the reconstructed wind velocity on both the straight and turning flights. However, $V_{\mathrm{w,x}}$ obtained from the Kalman filter on the straight leg tracks the reconstructed wind velocity's forward component. This formulation does not depend on ADU measurements or the aircraft dynamic model, and it only requires total velocity measurement, typically acquired from a GNSS sensor. Formulation 1 directly solves the wind triangle relationship, making it the most straightforward formulation for wind velocity estimation.

Figure 6.3 and 6.4 show wind velocity estimates generated by the KF, EKF, and UKF based on formulations 2 and 3, respectively. The difference between the two formulations is that formulation 3 includes aircraft attitude measurements. These formulations include air data unit (ADU) measurements, which have significantly improved the accuracy of the wind estimates. Based on the results shown in Figure 6.3 and 6.4, formulations 2 and 3 yield better wind velocities estimates in all three components ($V_{\mathrm{w,x}}$, $V_{\mathrm{w,y}}$, $V_{\mathrm{w,z}}$) than formulation 1 and 4. Additionally, including aircraft attitude measurements as part of the filters' measurement step improves wind velocity estimates significantly. Unfortunately, the problem of indirect wind velocity estimation is often related to inferring wind velocity estimates in cases where air data unit (ADU) measurements are not available; as a result, this approach is often not applicable to many indirect wind velocity estimation problems.

Figure 6.5 shows wind velocity estimates generated by the KF, EKF, and UKF based on formulations 4, respectively. This method involves identifying an aerodynamic model from flight data, as explained in Chapter 5. During the straight flight, all three filters track the reconstructed wind velocity. However, during the turning leg, the KF estimate diverges because the aircraft is perturbed from the equilibrium flight condition that the aircraft dynamics are linearized about. On the other hand, the EKF and UKF estimates do not diverge, but the EKF tracks the reconstructed wind velocity the best. Formulation 4 does not rely on ADU measurements but depends on the aircraft dynamic to solve the wind triangle relationship. However, it requires the additional step of identifying the test aircraft's aerodynamic force and moment models. This technique is the most practical wind estimation method if ADU measurements are unavailable. That said, other sensors such as the GNSS sensor, attitude and heading reference system (AHRS), and gyroscope sensor may be required to achieve desirable results.

Figure 6.6 shows wind velocity estimates generated by the KF, EKF, and UKF based on formulations 5, respectively. This method, like formulation 4, is a model-based approach, but unlike formulation 4, it includes true airspeed measurement as part of its measurement model. The results in Figure 6.6b indicate an overall improvement in wind velocity estimate accuracy during the turning flight profile. Furthermore, the results in Figure 6.6a indicate a significant improvement in $V_{\mathrm{w,x}}$ estimate, which suggests that the wind component parallel to the direction of the aircraft's motion is improved as a result of adding true airspeed in the formulation's measurement model.

Figure 6.7 shows wind velocity estimates generated by the KF, EKF, and UKF based on formulations 6, respectively. This method expands formulation 6 to include angle of attack and sideslip measurements. The results in Figure 6.7 indicate a significant improvement in wind velocity estimate accuracy. This difference between formualtion 6 and formulation 3 is that formulation 6 includes an aerodynamic model.

The KF is a simple and widely used filtering method that provides reliable and accurate estimates of linear system states. On the other hand, the UKF is a more complex and computational approach that can provide more accurate results but requires more tuning. The EKF is a compromise between the two, being more straightforward to implement than

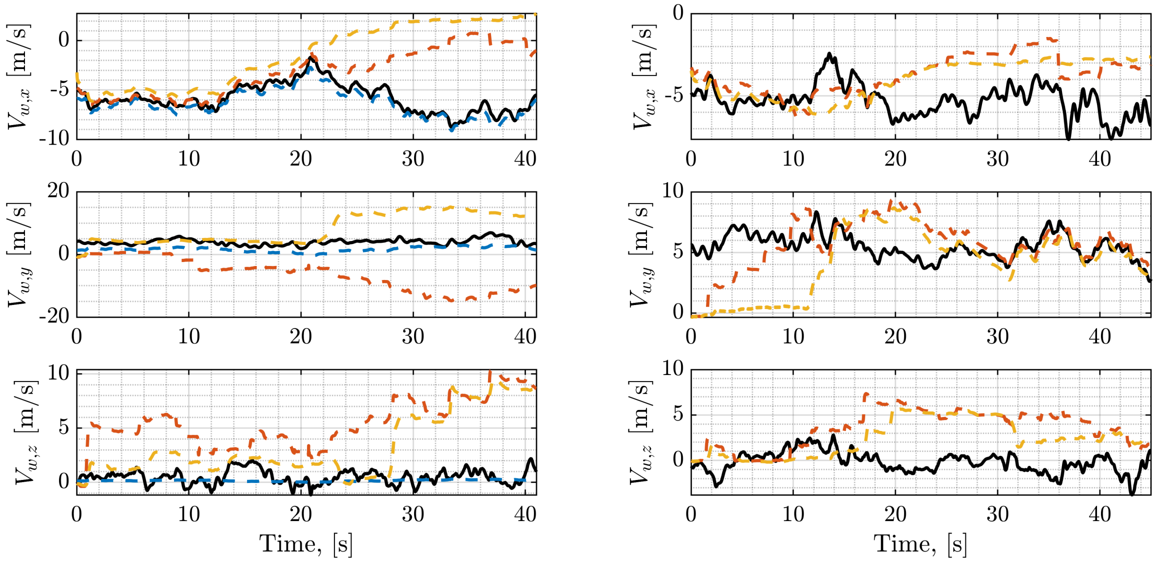

(a) Straight leg flight profile.

(b) Turning flight profile.

Figure 6.2: Formulation 1 wind velocity estimates. The reconstructed wind is given in black, the KF-based wind estimate is given in blue, the EKF-based wind estimate is given in orange, and the UKF-based wind estimate is given in gold.

the UKF but requiring additional calculations of the system's Jacobians. For flight profiles that are not straight and level, the EKF and UKF are better suited due to their ability to handle nonlinearities. However, for wind estimation problems, the EKF is the better choice because of its ease of implementation and tuning compared to the UKF. It is worth noting that the benefit of using a UKF for wind velocity estimation is not always apparent when compared to the EKF, which is a simpler and more straightforward alternative.

6.3.3 Error Analysis

Table 6.6 provides the RMSD values of the wind velocity estimates from each of the three filters in all six wind estimation formulations for the two flight test data sets. It is observed that the KF wind estimates have the highest error in the turning flight data, which is expected as the nonlinear dynamics are linearized about straight and level flight in the KF

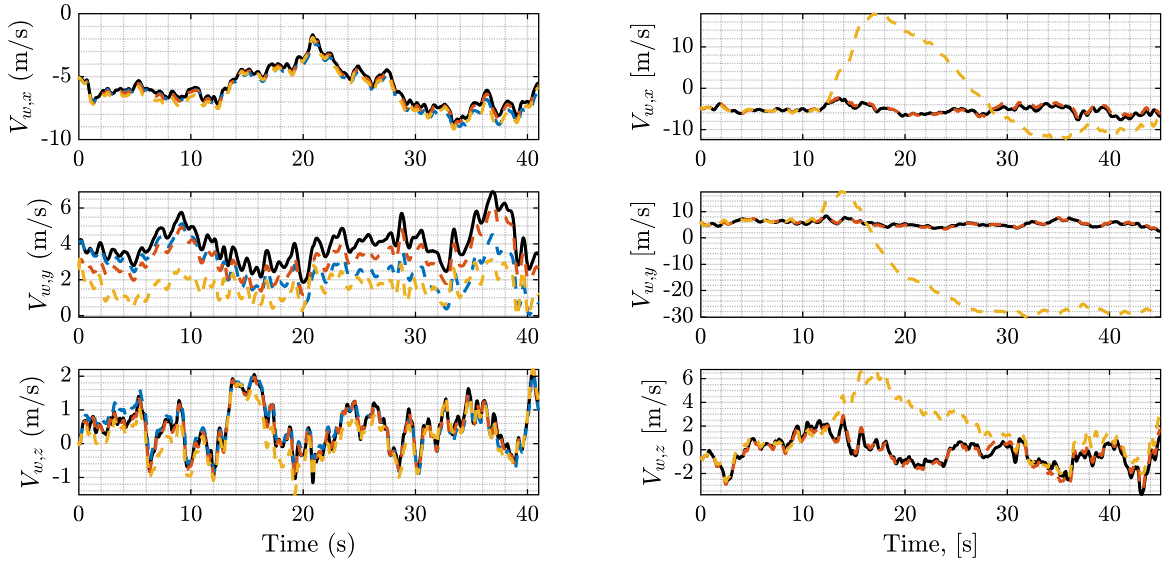

(a) Straight leg flight profile.

(b) Turning flight profile.

Figure 6.3: Formulation 2 wind velocity estimates. The reconstructed wind is given in black, the KF-based wind estimate is given in blue, the EKF-based wind estimate is given in orange, and the UKF-based wind estimate is given in gold.

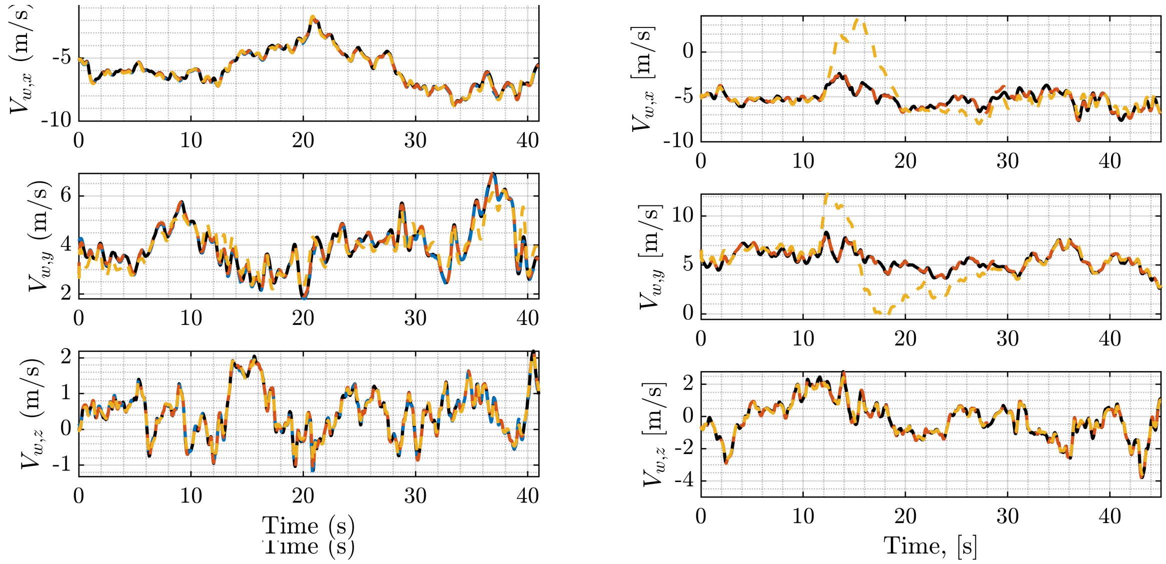

(a) Straight leg flight profile.

(b) Turning flight profile.

Figure 6.4: Formulation 3 wind velocity estimates. The reconstructed wind is given in black, the KF-based wind estimate is given in blue, the EKF-based wind estimate is given in orange, and the UKF-based wind estimate is given in gold.

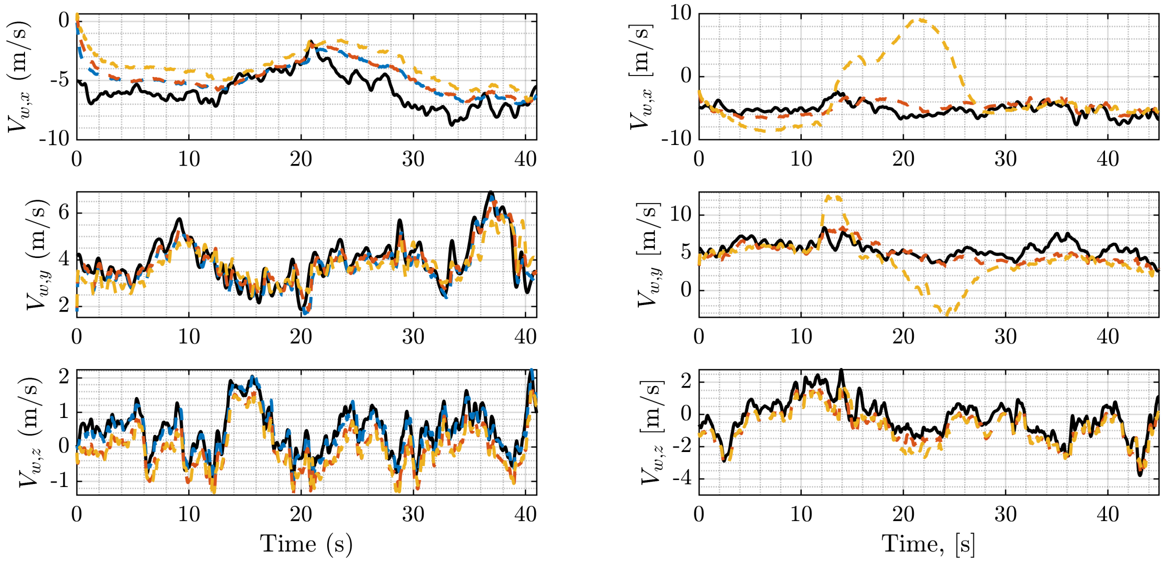

(a) Straight leg flight profile.

(b) Turning flight profile.

Figure 6.5: Formulation 4 wind velocity estimates. The reconstructed wind is given in black, the KF-based wind estimate is given in blue, the EKF-based wind estimate is given in orange, and the UKF-based wind estimate is given in gold

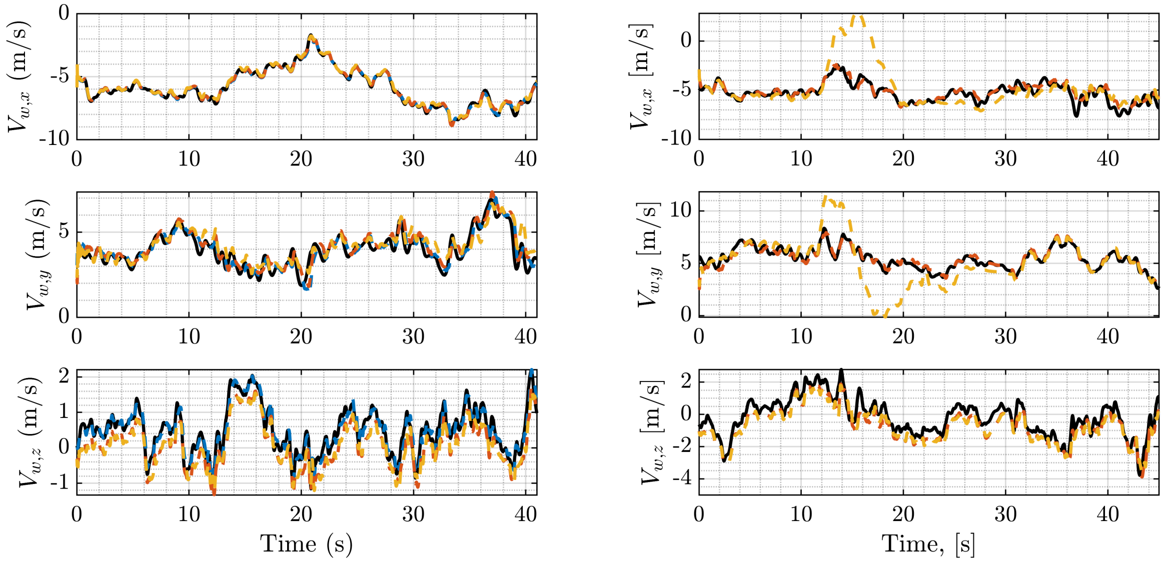

(a) Straight leg flight profile.

(b) Turning flight profile.

Figure 6.6: Formulation 5 wind velocity estimates. The reconstructed wind is given in black, the KF-based wind estimate is given in blue, the EKF-based wind estimate is given in orange, and the UKF-based wind estimate is given in gold

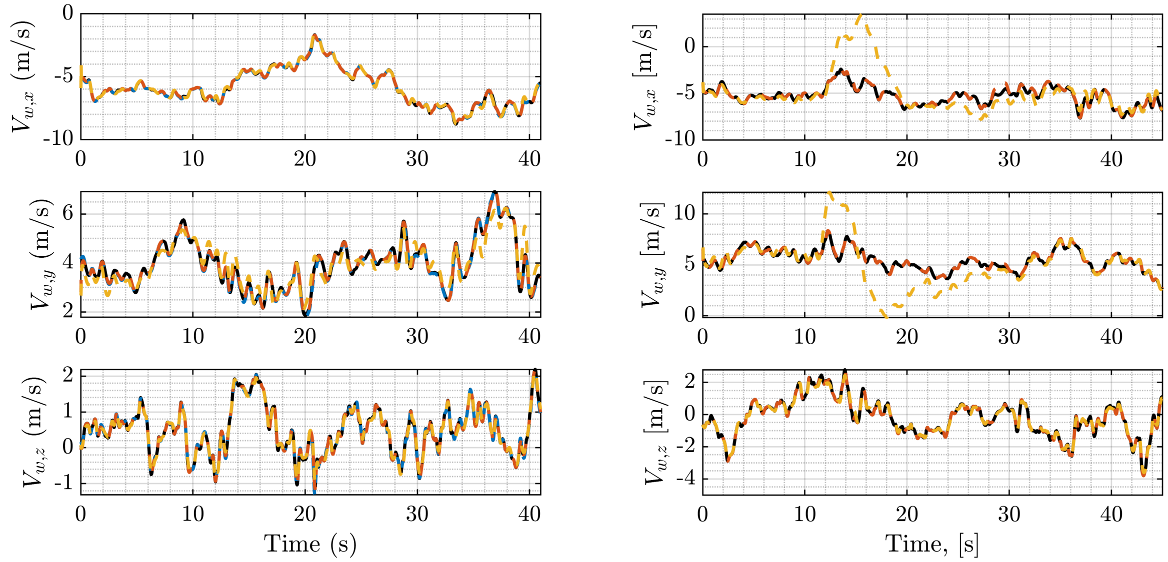

(a) Straight leg flight profile.

(b) Turning flight profile.

Figure 6.7: Formulation 6 wind velocity estimates. The reconstructed wind is given in black, the KF-based wind estimate is given in blue, the EKF-based wind estimate is given in orange, and the UKF-based wind estimate is given in gold

implementation. The EKF is the most consistent in providing wind velocity estimates, and it does not diverge from the reconstructed wind, whereas the UKF is seen to diverge in Figure 6.4b. Formulations 3 and 6 appear to have the best results in terms of RMSD values in both the straight leg and turning data when the EKF and UKF are implemented. The RMSD is calculated as follows:

$$\mathrm{RMSD} = \sqrt{\frac{\sum_{i=1}^{N}\left(V_{\mathrm{w},(.)}^{\mathrm{Reconstructed}} - V_{\mathrm{w},(.)}^{\mathrm{Estimate}}\right)^2}{N}} \tag{6.16}$$

where N is the number of data points, $(.)$ denotes the x, y, or z components of the wind velocity, $V_{\mathrm{w},(.)}^{\mathrm{Reconstructed}}$ is a component of the reconstructed velocity, and $V_{\mathrm{w},(.)}^{\mathrm{Estimate}}$ is a component of the estimated wind velocity.

Table 6.6: Wind velocity root-mean-square difference (RMSD) values

Wind Velocity Components	Estimation Filters Algorithm	Formulation 1: Wind Triangle Aerodynamic Model-free		Formulation 2: 15 States 6 Measurement Aerodynamic Model-free		Formulation 3: 15 States 9 Measurement Aerodynamic Model-free	
		Straight	Turning	Straight	Turning	Straight	Turning
$V_{\mathrm{w,x}}$	KF	0.61	3.32	0.41	10.70	0.09	18.20
	EKF	4.01	2.21	0.20	0.42	0.04	0.13
	UKF	5.77	2.19	0.48	9.70	0.15	1.97
$V_{\mathrm{w,y}}$	KF	2.48	15.36	1.54	55.30	0.07	33.50
	EKF	11.60	2.33	0.80	0.27	0.06	0.09
	UKF	6.21	3.35	2.40	23.80	0.38	1.89
$V_{\mathrm{w,z}}$	KF	0.73	1.28	0.18	6.23	0.04	0.24
	EKF	5.49	4.57	0.06	0.29	0.02	0.03
	UKF	4.09	3.64	0.32	2.51	0.07	0.12

Wind Velocity Components	Estimation Filters Algorithm	Formulation 4: Aircraft Aerodynamic Model-based		Formulation 5: 15 States 13 Measurement Aerodynamic Model-based		Formulation 6: 15 States 15 Measurement Aerodynamic Model-based	
		Straight	Turning	Straight	Turning	Straight	Turning
$V_{\mathrm{w,x}}$	KF	1.33	17.00	0.11	18.20	0.05	18.20
	EKF	1.48	1.10	0.11	0.42	0.02	0.13
	UKF	2.28	5.72	0.19	1.79	0.15	1.83
$V_{\mathrm{w,y}}$	KF	0.49	32.90	0.45	33.40	0.06	33.50
	EKF	0.43	1.10	0.47	0.34	0.04	0.08
	UKF	0.65	2.87	0.57	1.70	0.37	1.77
$V_{\mathrm{w,z}}$	KF	0.19	0.36	0.17	0.36	0.04	0.23
	EKF	0.53	0.65	0.45	0.59	0.02	0.03
	UKF	0.60	0.76	0.48	0.63	0.08	0.12

6.4 Conclusion

In this chapter, we compare the performance of six different wind estimation methods in three commonly used state estimators. The six wind estimation methods are wind triangle aerodynamic model-free, 15-state and 6-measurement aerodynamic model-free, 15-state and 9-measurement aerodynamic model-free, aerodynamic model-based, aerodynamic model-based with a true airspeed measurement, and aerodynamic model-based with a true airspeed, angle of attack, and sideslip measurements. We implement these methods in three filters: a Kalman filter, an extended Kalman filter, and an unscented Kalman filter. We provide information on the tuning processes and initialization of each filter. To provide a baseline for comparison, we compute the algebraic wind velocity reconstruction from measurements obtained from a vaned air data unit. We compare the wind estimates to the algebraically reconstructed wind and calculate their root-mean-square error. Our findings show that the wind triangle aerodynamic model-free method is the least accurate, while the 15-state and 9-measurement aerodynamic model-free method yields the best wind estimation results, but requires vaned air data unit measurements. The 15-state and 6-measurement aerodynamic model-free method performs better than the wind triangle method but underperforms when compared to the 15-state and 9-measurement aerodynamic model-free method because it does not include the aircraft's attitude measurement. The aerodynamic model-based method yields the next-best wind velocity estimates and is ideal for situations where the aircraft is not equipped with a vaned air data unit. That said, the aerodynamic model-based method with true airspeed measurement significantly improves the results achieved from the aerodynamic model-based method and is ideal for situations where the aircraft is not equipped with air data vanes but with a pitot tube sensor. Furthermore, the aerodynamic model-based method with true airspeed, angle of attack, and sideslip measurements yields the best results but requires the aircraft to be equipped with a vaned air data unit (ADU). The Kalman filter is the easiest to tune and implement but is limited to nominal flight trajectories due to its linearity. The unscented Kalman filter is the hardest to tune and is computationally more expensive than the Kalman filter and extended Kalman filter. However, the unscented Kalman filter does not show a significant improvement in wind estimates compared to the other two filters. The extended Kalman filter yields the best results.

Chapter 7

Unsteady Aerodynamics in Estimation

This chapter examines the value of incorporating unsteady aerodynamics in a model-based wind estimator for a small, fixed-wing aircraft and presents results of an experimental implementation. An extended Kalman filter is designed for two motion models identified from flight data – one that includes unsteady effects and another that does not. An air data unit with wind vanes and a Kiel probe is used to reconstruct the local wind velocity for validation. Analysis of the time histories of the wind estimates and the wind estimate difference relative to the reconstructed wind velocity shows that the two model-based estimators perform equally well. The power spectral densities of the reconstructed wind and the estimated wind, computed using either estimator, follow Kolmogorov's $-5/3$ law. The work presented in this chapter is published in [24].

7.1 Introduction

Small uncrewed aircraft can serve as sensor platforms to measure atmospheric properties *in situ* [8, 9]. Inferring atmospheric wind using aircraft-mounted sensors is a well-established concept [7] in which estimation algorithms combine onboard sensor measurements with a motion model; see, for example, [48, 74, 84, 85, 86]. References [78, 79, 80, 81, 82] describe wind estimation where measurements are combined with a kinematic motion model. Others have incorporated full dynamic motion models [10, 12, 20, 21, 47, 62, 63, 65, 66, 67, 68, 69].

Wind estimation schemes can be classified into direct and indirect measurements. Direct measurements provide the vehicle's air-relative velocity whose vector difference from the total velocity is the wind velocity [83]. Indirect measurements, on the other hand, use various motion data to infer the wind velocity using a well-designed estimation algorithm [11]. Small, low-cost, uncrewed aircraft are usually equipped with low-cost sensors with a high measurement uncertainty that affects the accuracy of state estimates. Several studies have explored using different sensors for wind estimation to address this issue.

In [57], only an inertial measurement unit (IMU) was utilized, while [56] incorporated both an IMU and magnetometers. In [54] and [62], a combination of global navigation satellite system (GNSS) data and barometric pressure sensors improved wind estimate results. In [20, 21, 47, 53, 58, 73, 76, 82, 100], various combinations of IMU, magnetometer, GNSS, barometer, and air data unit (ADU) sensors were employed to estimate wind velocity and improve the accuracy of the estimates.

Prior studies have also explored the effect of various estimation algorithms on wind estimate accuracy. Linear state estimators, such as the Kalman filter [10, 62, 63, 64] and the H_∞ filter [45], have been widely used for wind velocity estimation, though they are only expected to be effective for small perturbations from a nominal flight condition. Nonlinear estimators, such as the extended Kalman filter, have also been employed in several studies to combat the shortcomings of linear approaches [20, 21, 65, 66, 67]. The unscented Kalman filter has also been used to infer wind velocity, having the benefit of not requiring computations of Jacobians and better handling of statistical propagation through nonlinearities [12, 47, 68, 69, 70]. Recently, other nonlinear approaches have been used that aim to provide stronger convergence guarantees by leveraging the nonlinear system dynamics [101, 102]. Wind velocity estimation error due to low-fidelity dynamic models has received less attention. In [103], the effect of linearizing a quasi-steady, nonlinear flight dynamic model and ignoring non-uniform flow effects on wind estimation accuracy was explored.

In this chapter, the effect of dynamic modeling assumptions on reconstructed wind field states is revisited, except that the model-based estimator – an extended Kalman filter – is based on an unsteady aerodynamic model. We compare the results of wind velocity estimation obtained using the unsteady aerodynamic model-based approach with those obtained using a quasi-steady aerodynamic model. Furthermore, we compare both approaches with the reconstructed wind velocity derived from measurements obtained using an ADU. Additionally, we analyze and compare the power spectra of the estimated wind velocity and the reconstructed wind velocity.

In Section 7.2, we present the augmented equations of motion, including the extended state variables that represent the wind velocity estimates, the measurement model, and the initialization and tuning parameters for the estimator. In Section 7.3, we describe the test aircraft and its instrumentation, the flight profile flown by the test aircraft, and the reconstruction technique for obtaining the “true” wind velocity from ADU measurements, including analysis of the reconstructed wind velocity. Section 7.4 presents the model-based estimation results. Conclusions are presented in Section 7.5.

7.2 Wind Velocity Estimation

This section describes the augmented motion equations used as the estimator’s propagation model. The measurement model is then described, followed by the design and tuning of the filter.

7.2.1 Unsteady and Quais-steady Aerodynamic Equations

The aerodynamic model used in this chapter is described in detail in Section 5.3.2. Recall, the aerodynamic model given below:

$$C_J = C_{J_0} + C_J J + C_{J^2} J^2 \tag{7.1a}$$

$$C_X = C_{X_0} + C_{X_\alpha}\Delta\alpha + C_{X_q}\hat{q} + C_{X_{u_\mathrm{r}}}\Delta u_\mathrm{r} \tag{7.1b}$$

$$C_Y = C_{Y_{\tilde{x}}}\tilde{x}_Y + C_{Y_0} + C_{Y_\beta}\Delta\beta + C_{Y_p}\hat{p} + C_{Y_r}\hat{r} + C_{Y_{\delta_a}}\Delta\delta_a + C_{Y_{\delta_r}}\Delta\delta_r \tag{7.1c}$$

$$C_Z = C_{Z_{\tilde{x}}}\tilde{x}_Z + C_{Z_0} + C_{Z_\alpha}\Delta\alpha + C_{Z_q}\hat{q} + C_{Z_{\delta_e}}\Delta\delta_e \tag{7.1d}$$

$$C_l = C_{l_{\tilde{x}}}\tilde{x}_l + C_{l_0} + C_{l_\beta}\Delta\beta + C_{l_p}\hat{p} + C_{l_r}\hat{r} + C_{l_{\delta_a}}\Delta\delta_a \tag{7.1e}$$

$$C_m = C_{m_{\tilde{x}}}\tilde{x}_m + C_{m_0} + C_{m_\alpha}\Delta\alpha + C_{m_q}\hat{q} + C_{m_{\delta_e}}\Delta_e \tag{7.1f}$$

$$C_n = C_{n_{\tilde{x}}}\tilde{x}_n + C_{n_\beta} + C_{n_p}\hat{p} + C_{n_r}\hat{r} + C_{n_{\delta_a}}\Delta\delta_a + C_{n_{\delta_r}}\Delta\delta_r \tag{7.1g}$$

The variables that denote perturbations from nominal state and control values given in Equation (7.1) are defined as follows:

$$\Delta u_\mathrm{r} = u_\mathrm{r} - u_{\mathrm{r,nom}} \quad \Delta\alpha = \alpha - \alpha_\mathrm{nom} \quad \Delta\beta = \beta - \beta_\mathrm{nom}$$
$$\Delta\delta_a = \delta_a - \delta_{a,\mathrm{nom}} \quad \Delta\delta_e = \delta_e - \delta_{e,\mathrm{nom}} \quad \Delta\delta_r = \delta_r - \delta_{r,\mathrm{nom}}$$

The nondimensional state variables given in Equation (7.1) are defined as follows:

$$J = \frac{u_r}{\delta_\mathrm{rps} D} \quad \alpha = \tan^{-1}\left(\frac{w_r}{u_r}\right) \quad \beta = \sin^{-1}\left(\frac{w_r}{\|\boldsymbol{v}_\mathrm{r}\|}\right) \quad \hat{p} = \frac{pb}{2V_0} \quad \hat{q} = \frac{q\bar{c}}{2V_0} \quad \hat{r} = \frac{rb}{2V_0}$$

The vector $\tilde{\boldsymbol{x}} = [\tilde{x}_Y, \tilde{x}_Z, \tilde{x}_l, \tilde{x}_m, \tilde{x}_n]^{\mathrm{T}}$ is the nondimensional unsteady aerodynamic state vector with dynamics described by the following equations:

$$\dot{\tilde{x}}_Y = A_{Y_{\tilde{x}}}\tilde{x}_Y + B_{Y_{\tilde{x}}}\Delta\beta \tag{7.2a}$$

$$\dot{\tilde{x}}_Z = A_{Z_{\tilde{x}}}\tilde{x}_Z + B_{Z_{\tilde{x}}}\Delta\alpha \tag{7.2b}$$

$$\dot{\tilde{x}}_l = A_{l_{\tilde{x}}}\tilde{x}_l + B_{l_{\tilde{x}}}\Delta\beta \tag{7.2c}$$

$$\dot{\tilde{x}}_m = A_{m_{\tilde{x}}}\tilde{x}_m + B_{m_{\tilde{x}}}\Delta\alpha \tag{7.2d}$$

$$\dot{\tilde{x}}_n = A_{n_{\tilde{x}}}\tilde{x}_n + B_{n_{\tilde{x}}}\Delta\beta \tag{7.2e}$$

where $A_{(\cdot)_{\tilde{x}}}$ and $B_{(\cdot)_{\tilde{x}}} = 1\ \mathrm{s}^{-1}$ parameterize the unsteady aerodynamics. For compactness, the unsteady dynamic equations is given as follows:

$$\dot{\tilde{\boldsymbol{x}}} = \underbrace{\begin{bmatrix} A_{Y_{\tilde{x}}} & 0 & 0 & 0 & 0 \\ 0 & A_{Z_{\tilde{x}}} & 0 & 0 & 0 \\ 0 & 0 & A_{l_{\tilde{x}}} & 0 & 0 \\ 0 & 0 & 0 & A_{m_{\tilde{x}}} & 0 \\ 0 & 0 & 0 & 0 & A_{n_{\tilde{x}}} \end{bmatrix}}_{\tilde{\boldsymbol{A}}} \tilde{\boldsymbol{x}} + \underbrace{\begin{bmatrix} 0 & 1 \\ 1 & 0 \\ 0 & 1 \\ 1 & 0 \\ 0 & 1 \end{bmatrix}}_{\tilde{\boldsymbol{B}}} \underbrace{\begin{bmatrix} \Delta\alpha \\ \Delta\beta \end{bmatrix}}_{\tilde{\boldsymbol{u}}} \tag{7.3}$$

The quasi-steady aerodynamic model is structurally identical to Equation (7.1), except that the $\tilde{x}$ terms are omitted.

7.2.2 Augmented Equations of Motion with Wind Disturbance

To estimate wind velocity, the state variable $\boldsymbol{V}_{\mathrm{w}}$ is appended to the original state vector to represent the unknown wind velocity in the dynamic model. As discussed in Chapter 2, the wind dynamics are modeled as a continuous-time random walk in Equation (2.97). The wind-augmented system model, with and without unsteady aerodynamic terms, is used as the dynamic propagation model in an extended Kalman filter. The augmented motion model is

$$\dot{\boldsymbol{X}} = \boldsymbol{R}_{\mathrm{IB}}\boldsymbol{v}_{\mathrm{r}} + \boldsymbol{V}_{\mathrm{w}} \tag{7.4a}$$

$$\dot{\boldsymbol{\Theta}} = \boldsymbol{L}_{\mathrm{IB}}\boldsymbol{\omega} \tag{7.4b}$$

$$\dot{\boldsymbol{v}}_{\mathrm{r}} = \boldsymbol{v}_{\mathrm{r}} \times \boldsymbol{\omega} + \frac{1}{m}\boldsymbol{F}_A(\boldsymbol{v}_{\mathrm{r}}, \boldsymbol{\omega}, \boldsymbol{\delta}, \tilde{\boldsymbol{x}}) + \frac{1}{m}\boldsymbol{F}_J(\boldsymbol{\delta}) + \frac{1}{m}\boldsymbol{R}_{\mathrm{IB}}^{\mathrm{T}}\boldsymbol{F}_G - \boldsymbol{R}_{\mathrm{IB}}^{\mathrm{T}}\dot{\boldsymbol{V}}_{\mathrm{w}} \tag{7.4c}$$

$$\dot{\boldsymbol{\omega}} = \boldsymbol{I}^{-1}\left(\boldsymbol{I}\boldsymbol{\omega} \times \boldsymbol{\omega}\right) + \boldsymbol{I}^{-1}\boldsymbol{M}_A(\boldsymbol{v}_{\mathrm{r}}, \boldsymbol{\omega}, \boldsymbol{\delta}, \tilde{\boldsymbol{x}}) \tag{7.4d}$$

$$\dot{\tilde{\boldsymbol{x}}} = \bar{\boldsymbol{A}}\tilde{\boldsymbol{x}} + \bar{\boldsymbol{B}}\tilde{\boldsymbol{u}}(\boldsymbol{v}_{\mathrm{r}}) \tag{7.4e}$$

$$\dot{\boldsymbol{V}}_{\mathrm{w}} = \tilde{\boldsymbol{w}}_w \tag{7.4f}$$

In Equation (7.4a), $\boldsymbol{V}_{\mathrm{w}}$ is treated as part of the system state as opposed to an external disturbance. The augmented equations of motion can be written in the compact form:

$$\dot{\boldsymbol{x}} = \boldsymbol{f}(t, \boldsymbol{x}, \boldsymbol{\delta}) + \tilde{\boldsymbol{w}} \tag{7.5}$$

where $\boldsymbol{x} = [\boldsymbol{X}^{\mathrm{T}}, \boldsymbol{\Theta}^{\mathrm{T}}, \boldsymbol{v}_{\mathbf{r}}^{\mathrm{T}}, \boldsymbol{\omega}^{\mathrm{T}}, \tilde{\boldsymbol{x}}^{\mathrm{T}}, \boldsymbol{V}_{\mathrm{w}}^{\mathrm{T}}]^{\mathrm{T}}$ is the 20×1 augmented state vector and $\tilde{\boldsymbol{w}} = [\tilde{\boldsymbol{w}}_X, \tilde{\boldsymbol{w}}_\Theta, \tilde{\boldsymbol{w}}_{v_{\mathrm{r}}}, \tilde{\boldsymbol{w}}_\omega, \tilde{\boldsymbol{w}}_{\tilde{x}}, \tilde{\boldsymbol{w}}_w]^T$ is a corresponding 20×1 disturbance vector of stationary, zero-mean, Gaussian white noise. The 3×1 vectors $\tilde{\boldsymbol{w}}_X$ and $\tilde{\boldsymbol{w}}_\Theta$ are process noise signals which help account for error due to the linearization of Equations (7.4a) and (7.4b). Similarly, the 3×1 process noise vectors $\tilde{\boldsymbol{w}}_{v_{\mathrm{r}}}$ and $\tilde{\boldsymbol{w}}_\omega$ are intended to account for error due to the linearization of Equations (7.4c) and (7.4d), as well as aerodynamic modeling error in $\boldsymbol{F}_A$ and $\boldsymbol{M}_A$. Additionally, we lump the random process $-\boldsymbol{R}_{\mathrm{IB}}^{\mathrm{T}}\dot{\boldsymbol{V}}_{\mathrm{w}}$ in Equation (7.4c) together with $\tilde{\boldsymbol{w}}_{v_{\mathrm{r}}}$. Finally, the 5×1 signal $\tilde{\boldsymbol{w}}_{\tilde{x}}$ accounts for modeling error in the unsteady aerodynamic approximation (7.4e).

7.2.3 Measurement Model

The measurements provided to the estimator are the aircraft position, attitude, inertial velocity (denoted $\boldsymbol{V}$), and body angular velocity. Note that the 12×1 measurement vector $\boldsymbol{z}$ and the augmented state vector $\boldsymbol{x}$ have a nonlinear relationship because of the attitude dependent wind triangle expression:

$$\boldsymbol{z}(t) = \boldsymbol{h}(\boldsymbol{x}) + \tilde{\boldsymbol{v}}(t) = \begin{bmatrix} \boldsymbol{X} \\ \boldsymbol{\Theta} \\ \boldsymbol{R}_{\mathrm{IB}}\boldsymbol{v}_{\mathrm{r}} + \boldsymbol{V}_{\mathrm{w}} \\ \boldsymbol{\omega} \end{bmatrix} + \tilde{\boldsymbol{v}} = \begin{bmatrix} \boldsymbol{X} \\ \boldsymbol{\Theta} \\ \boldsymbol{V} \\ \boldsymbol{\omega} \end{bmatrix} + \tilde{\boldsymbol{v}} \tag{7.6}$$

where $\tilde{\boldsymbol{v}}$ is the 12×1 measurement noise vector assumed to be zero-mean, Gaussian, white noise. Local observability of the system (7.5) with measurements (7.6) was verified along the nominal aircraft motion of steady, wings level flight at constant speed and altitude for both the quasi-steady and unsteady system.

7.2.4 Continuous-discrete Extended Kalman Filter

Because the experimental aircraft is a sampled data system, we adopt the hybrid (continuous-discrete) extended Kalman filter (hEKF); the algorithm is briefly provided in Appendix B. The system dynamics (7.5) are continuous-time but the measurement model is discrete-time:

$$\dot{\boldsymbol{x}}(t) = \boldsymbol{f}\left(t, \boldsymbol{x}(t), \boldsymbol{\delta}(t)\right) + \tilde{\boldsymbol{w}}(t), \qquad \boldsymbol{x}(t_0) = \boldsymbol{x}_0 \tag{7.7a}$$

$$\boldsymbol{z}(t_k) = \boldsymbol{h}\left(t_k, \boldsymbol{x}(t_k)\right) + \tilde{\boldsymbol{v}}(t_k), \qquad t_k \in \{t_0, t_1, t_2, \ldots\} \tag{7.7b}$$

For a constant sampling period Δt, one has $t_k = t_0 + k\Delta t$, however the algorithm does not require a fixed sample rate. The hybrid extended Kalman filter's algorithm uses a numerical integration scheme to propagate the state estimate and its covariance from one sample time to the next. The process and measurement noise are assumed to be described by Gaussian distributions with $\tilde{\boldsymbol{w}}(t) \sim \mathcal{N}(\boldsymbol{0}, \boldsymbol{S})$ and $\tilde{\boldsymbol{v}}(t_k) \sim \mathcal{N}(\boldsymbol{0}, \boldsymbol{R}(t_k))$, respectively. The measurements $\boldsymbol{z}(t_k)$ are obtained from the flight computer's low-level navigation solution – except for angular velocity, which is obtained directly from the vehicle's angular rate gyroscopes. The associated measurement noise covariance $\boldsymbol{R}(t_k)$ is taken to be diagonal with entries corresponding to the state estimate variances reported by the flight computer. For the gyroscope readings, the measurement noise covariance is considered constant and is estimated by smoothing historical data. The initial state estimate $\hat{\boldsymbol{x}}(t_0)$ and the initial state estimate error covariance $\boldsymbol{P}(t_0)$ are similarly chosen based on the flight computer's navigation solution. Specifically, the initial estimates and error covariance of position $\hat{\boldsymbol{X}}(t_0)$ and attitude $\hat{\boldsymbol{\Theta}}(t_0)$ are taken from the flight computer navigation solution. The initial estimate of angular velocity $\hat{\boldsymbol{\omega}}(t_0)$ is taken from the vehicle's gyroscope with a covariance equal to that of its measurement noise. The relative velocity initial estimate $\hat{\boldsymbol{v}}_{\mathrm{r}}(t_0)$ is computed using the rotation matrix constructed from $\hat{\boldsymbol{\Theta}}(t_0)$ along with the measured inertial velocity $\boldsymbol{V}$ from the autopilot. Finally, the initial estimates of wind velocity $\hat{\boldsymbol{V}}_{\mathrm{w}}(t_0)$ and of the unsteady states $\hat{\mathring{\boldsymbol{x}}}(t_0)$ were taken to be zero with covariances appropriate for their typical magnitudes.

The constant process noise power spectral density $\boldsymbol{S}$ is obtained by computing the power spectral density of the residuals of the true and modeled state derivative from historical flight data. The residuals are computed as follows:

$$\boldsymbol{\nu} = \dot{\boldsymbol{x}}_{\text{truth}} - \boldsymbol{f}\left(t, \boldsymbol{x}_{\text{truth}}, \boldsymbol{\delta}_{\text{truth}}\right) \tag{7.8}$$

The constant power spectral density of the residual is computed using the Matlab function `pwelch` function as follows:

$$\boldsymbol{S} = \max\left(\texttt{pwelch}\left(\boldsymbol{\nu}, [], [], [], \mathrm{f_s}\right)\right) \tag{7.9}$$

where $\mathrm{f_s}$ is the sampling frequency. Because their true values are unknown, the unsteady states in $\boldsymbol{x}_{\text{truth}}$ are set to zero when computing $\boldsymbol{S}$. The values of the process noise power spectral density matrices $\boldsymbol{S}$ calculated to obtain the results shown in Figure 7.3a are given in Table 7.1. Equation (7.8) and (7.9) are used to calculate the values given in Table 7.1. The process noise power spectral density matrices calculated to obtain the results shown in Figure 7.3b, Figure 7.4a, and Figure 7.4b are not shown, but the results are similar to the ones reported in Table 7.1 and are obtained using Equation (7.8) and (7.9) as well.

Table 7.1: Power spectral density matrices diag($\boldsymbol{S}$) for the unsteady and quasi-steady aerodynamic model-based filters

	Unsteady Model-based Filter diag($\boldsymbol{S}$)	Quasi-steady Model-based Filter diag($\boldsymbol{S}$)
x	$2.20e-3$	$2.20e-3$
y	$1.31e-3$	$1.31e-3$
z	$1.66e-3$	$1.66e-3$
ϕ	$1.66e-3$	$1.66e-3$
θ	$1.49e-5$	$1.49e-5$
ψ	$3.13e-5$	$3.13e-5$
u_r	8.07	8.07
v_r	4.18	4.18
w_r	3.36	3.36
p	3.61	3.61
q	$1.46e-1$	$1.46e-1$
r	$3.24e-1$	$3.24e-1$
$V_{\mathrm{w,x}}$	1.46	1.46
$V_{\mathrm{w,y}}$	3.86	3.86
$V_{\mathrm{w,z}}$	3.39	3.39
$\tilde{x}_Y$	$8.74e-4$	–
$\tilde{x}_Z$	$8.42e-5$	–
$\tilde{x}_l$	$8.74e-4$	–
$\tilde{x}_m$	$8.42e-5$	–
$\tilde{x}_n$	$8.74e-4$	–

The process noise errors associated with the kinematic equations are minimal, as expected, unlike the dynamic equations, which have considerable uncertainty because of aerodynamic model mismatch. The extended Kalman filter preserves the nonlinear kinematics, so there aren't nonlinearities for the process noise to account for. That said, the extended Kalman filter used in this dissertation approximates the nonlinearities using a first-order Taylor series approximation; as a result, process noise associated with the kinematic equations is included to account for errors due to linearization.

In the case that Equations (7.8) and (7.9) can not be used to calculate $\boldsymbol{S}$ an iterative approach where values proportional in magnitude to the values given in Table 7.1 should be used until desirable results are achieved. Generally, $\tilde{\boldsymbol{w}}_\mathrm{w}$ is the most challenging process noise to tune, especially in the lower atmosphere where representative wind data are limited. In practice, one may select the magnitude based on the general wind conditions. If the wind conditions are severe, for example, one should choose high magnitudes for the elements of the power spectral density matrix related to $\tilde{\boldsymbol{w}}_\mathrm{w}$; if the wind conditions are calm, one should choose low magnitudes.

7.3 Flight Experiment

This section describes the research aircraft and its instrumentation as well as the flight test in which wind data were collected to compare the two model-based wind estimators.

7.3.1 Experimental Flight Profile

The flight test in which wind data were collected to support comparative analysis of the two model-based wind estimators was conducted at Virginia Tech's Kentland Experimental

Aerial Systems (KEAS) Laboratory. The aircraft was flown at an altitude of 210 meters above ground level with a cruise speed of 18 m/s in the grid pattern shown in Figure 7.1a. The mission was automated, except for take-off and landing. Figure 7.1b shows the measured horizontal wind velocity, where the radial distance from the origin to a data point indicates wind speed, and the azimuth angle indicates wind direction in degrees from true north. The blue dots represent individual wind measurements; the red dot indicates the mean wind velocity. The wind was blowing from the northwest to the southeast throughout the flight, with a mean wind speed of 7.55 m/s, varying between 3 and 12 m/s. See Section 7.3.2 for more details on the reconstruction of wind velocity from flight data.

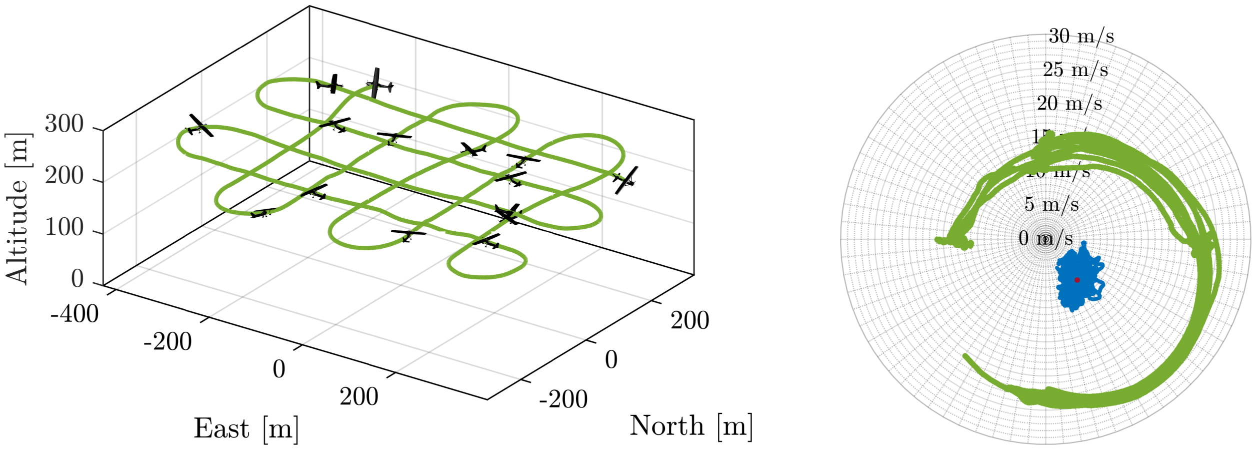

(a)

(b)

Figure 7.1: (a) Experimental flight profile. (b) The green dots indicate the aircraft's horizontal speed, the blue dots indicate the horizontal wind speed and direction, and the red dot indicates the wind's mean velocity and direction.

7.3.2 Wind Reconstruction from ADU Measurements

The ADU measurements were collected to reconstruct the wind velocity following the approach of [19]. The measured true velocity ($V_\mathrm{r} = \|\boldsymbol{v}_\mathrm{r}\|$), flank angle ($\beta_\mathrm{f}$), and angle of attack

(α) were used to reconstruct the three-dimensional body-fixed wind velocities as follows:

$$\boldsymbol{V}_{\mathrm{w}} = \boldsymbol{V} - \boldsymbol{R}_{\mathrm{IB}}(\boldsymbol{\Theta})\left(\boldsymbol{v}_{\mathrm{ADU}} - \boldsymbol{\omega} \times \boldsymbol{r}_{\mathrm{ADU}}\right) \tag{7.10}$$

Here $\boldsymbol{v}_{\mathrm{ADU}} = \boldsymbol{R}_{\mathrm{BW}}(\alpha, \beta)[V_{\mathrm{r}},\ 0,\ 0]^{\mathrm{T}}$ is the air-relative velocity at the geometric center of the ADU vanes, whose position in the body frame is denoted $\boldsymbol{r}_{\mathrm{ADU}}$. The rotation matrix

$$\boldsymbol{R}_{\mathrm{BW}} = \begin{bmatrix} \cos(\alpha)\cos(\beta) & -\cos(\alpha)\sin(\beta) & -\sin(\alpha) \\ \sin(\beta) & \cos(\beta) & 0 \\ \sin(\alpha)\cos(\beta) & -\sin(\alpha)\sin(\beta) & \cos(\alpha) \end{bmatrix}$$

maps free vectors from the wind frame to the body frame. Note that the sideslip angle can be computed from the flank angle as $\beta = \tan^{-1}(\tan(\beta_f)\cos(\alpha))$. The aircraft attitude $\boldsymbol{\Theta}$ and angular velocity $\boldsymbol{\omega}$ are acquired from the aircraft's flight computer navigation solution and rate gyroscopes, respectively. Figure 7.2 concerns the reconstructed wind velocity over the entire flight depicted in Figure 7.1. The reconstructed inertial wind velocity components (blue) and their time averages (red) are shown in Figure 7.2a. The power spectra (solid) and the Kolmogorov $10^{-5/3}$ reference (dashed) are shown in Figure 7.2b.

7.3.3 Reconstructed Wind Results and Analysis

Wind data were collected in a grid pattern flight at constant altitude as shown in Figure 7.1a. Assumptions 3a) and 3b) concerning the temporal and spatial derivatives of the mean wind $\bar{\boldsymbol{W}}$ are satisfied by construction since the mean wind is computed as a time-average of the full data set. All variation from the mean wind is attributed to turbulent fluctuations.

Assumption 3c), which states that the wind velocity fluctuations $\tilde{\boldsymbol{W}}$ vary in space but not in time, relates to the relative time scales of aircraft and atmospheric motion. The

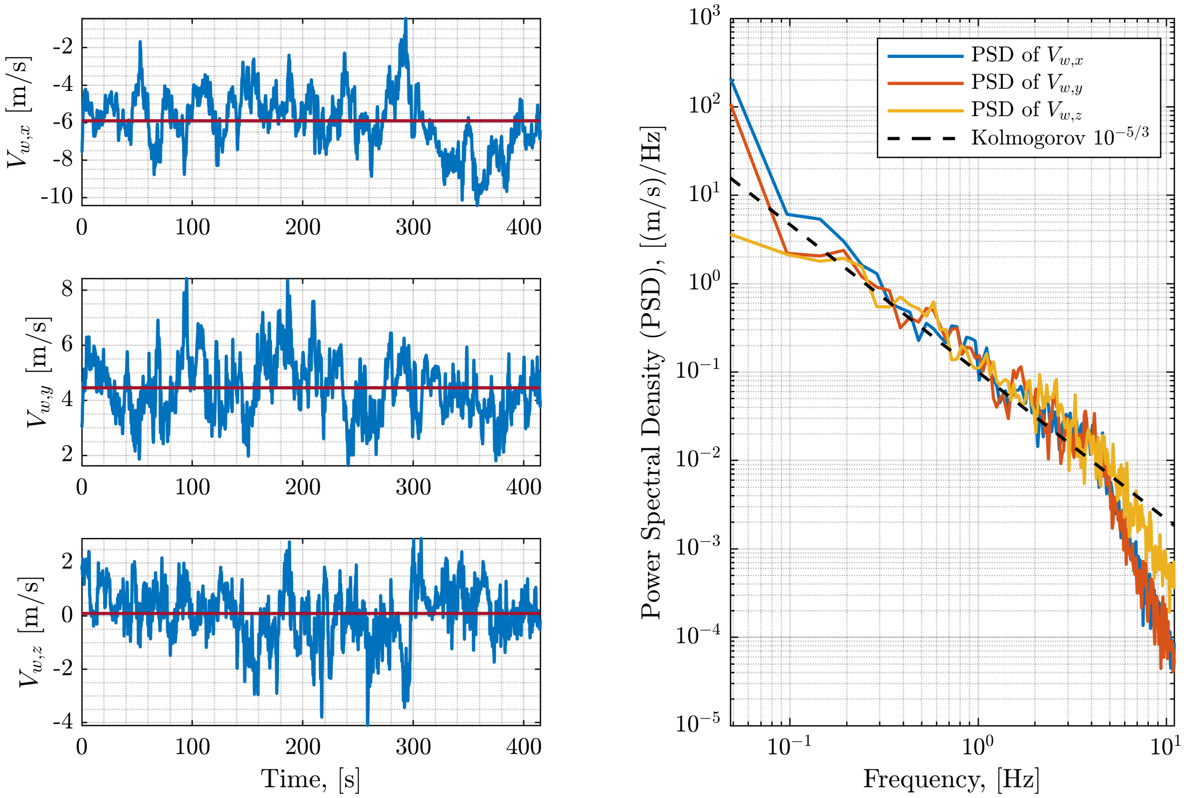

(a)

(b)

Figure 7.2: (a) Wind velocity components reconstructed from ADU measurements. (b) Power spectra of the reconstructed wind velocity components.

frozen turbulence assumption is appropriate, for example, for a fixed-wing aircraft flying straight and level, at a constant altitude, and at a speed much higher than the wind velocity. Figure 7.1b shows the aircraft's speed and the measured wind velocity throughout the flight that is depicted in Figure 7.1a. The nominal speed of the aircraft is about four times larger than the measured wind velocity, supporting Assumption 3c) that $\boldsymbol{W}$ is a "frozen" vector field advecting with the mean wind.

7.4 Results and Discussion

This section compares model-based estimates of wind velocity and power spectra using unsteady and quasi-steady aerodynamic models. As shown in Figure 7.1a, the aircraft is flown in a grid pattern. Only four legs of the flight are used in the analysis described here, corresponding to northward, southward, eastward, and westward flight. The reconstructed wind velocity and power spectra are taken as true values to which the unsteady and quasi-steady model-based wind velocity and power spectrum estimates are compared.

In the proceeding plots, true values are shown in blue, the quasi-steady aerodynamic model-based wind estimates in gold, and the unsteady aerodynamic model-based wind estimates in burnt orange. The dashed black reference lines in the power spectrum plots have a slope of $10^{-5/3}$. For the time histories of wind estimates shown in Figures 7.3a, 7.3b, 7.4a, and 7.4b, shaded regions indicating ±1 standard deviation bounds are shown in the respective colors. These standard deviations were computed numerically by propagating samples of normally distributed uncertain values through Equation (7.10). Specifically, the standard deviations of $\boldsymbol{\Theta}$, $\boldsymbol{V}$, and $\boldsymbol{\omega}$ were chosen in the same way as explained in Section 7.2.4, and the standard deviations of the vane angles and differential pressure sensor-based airspeed measurements were obtained from manufacturer specifications.

In Figures 7.3a to 7.4b, the estimated wind velocities, given in gold and burnt orange, are compared to the reconstructed wind velocity given in blue. These values are established from the northward, southward, eastward, and westward legs. The unsteady aerodynamic and quasi-steady aerodynamic model-based wind estimates track the reconstructed wind velocity comparably well.

Figure 7.5 shows a comparison between the power spectral density of the estimated wind velocities and the reconstructed wind velocity. A large dataset is needed to visualize the energy content of wind velocities. Hence, the entire flight experiment profile was used to generate the plot in this case. The power spectral density plots for the wind estimates based on both aerodynamic models track the power spectral density of the reconstructed wind. The slope of both the reconstructed and estimated power spectral densities track the dashed black lines with a slope of $10^{-5/3}$, reflecting physically reasonable wind characteristics. Vertical lines in Figure 7.5 indicate the aircraft short period mode (around 3 Hz) and the ADU vane cutoff frequency (around 11 Hz). The spectral properties computed for the quasi-steady and unsteady model-based wind estimates are considered most accurate below 3 Hz. Conversely, the spectral properties of the reconstructed wind velocity values are considered unreliable above 11 Hz.

The plots given in Figure 7.6 indicate that the difference of both aerodynamic model-based wind estimates relative to the reconstructed wind velocity are low. The bar graphs showing root-mean-square difference (RMSD) suggest that the unsteady and the quasi-steady aerodynamic model-based wind estimates are comparable, but the quasi-steady results consistently show slightly lower differences with the reconstructed wind.

The direction of flight with respect to the direction of the wind affected the performance of the filters. During the field experiment, the measured wind was blowing from the northwest to the southeast with a mean wind velocity of 7.55 m/s, gusting between 3 m/s and 12 m/s. The $V_{w,x}$ estimates improved when the aircraft flew from west to east and from east to west. Similarly, the $V_{w,y}$ estimates improved when the aircraft flew from north to south and from south to north. This suggests the wind component perpendicular to the direction of aircraft motion is estimated more accurately. The (horizontal) direction of aircraft motion did not affect the $V_{w,z}$ wind estimates.

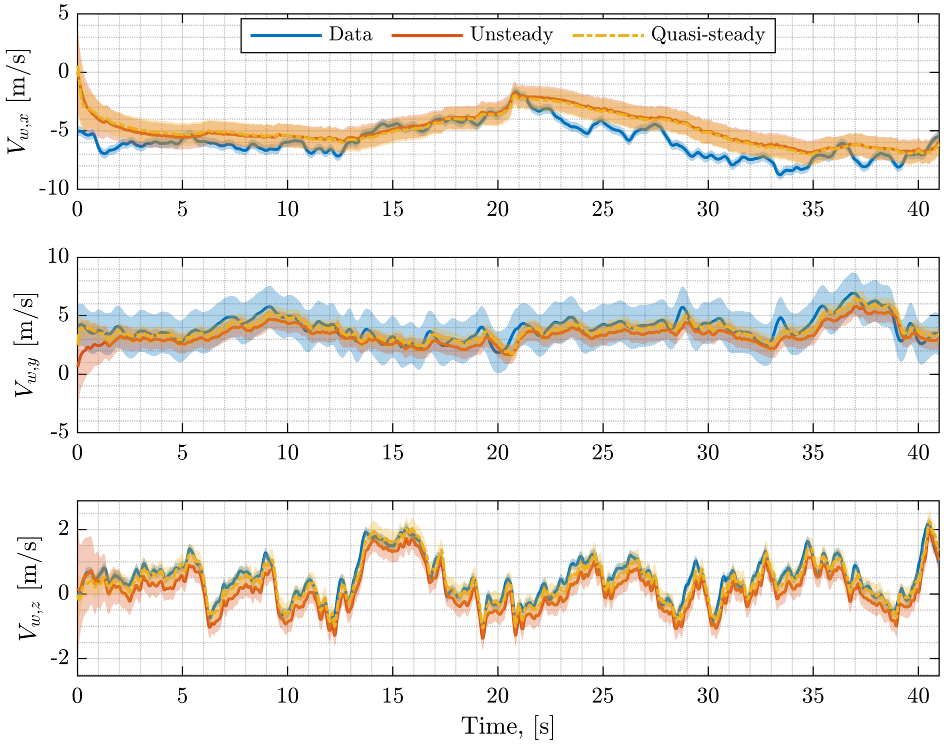

(a) Northward flight.

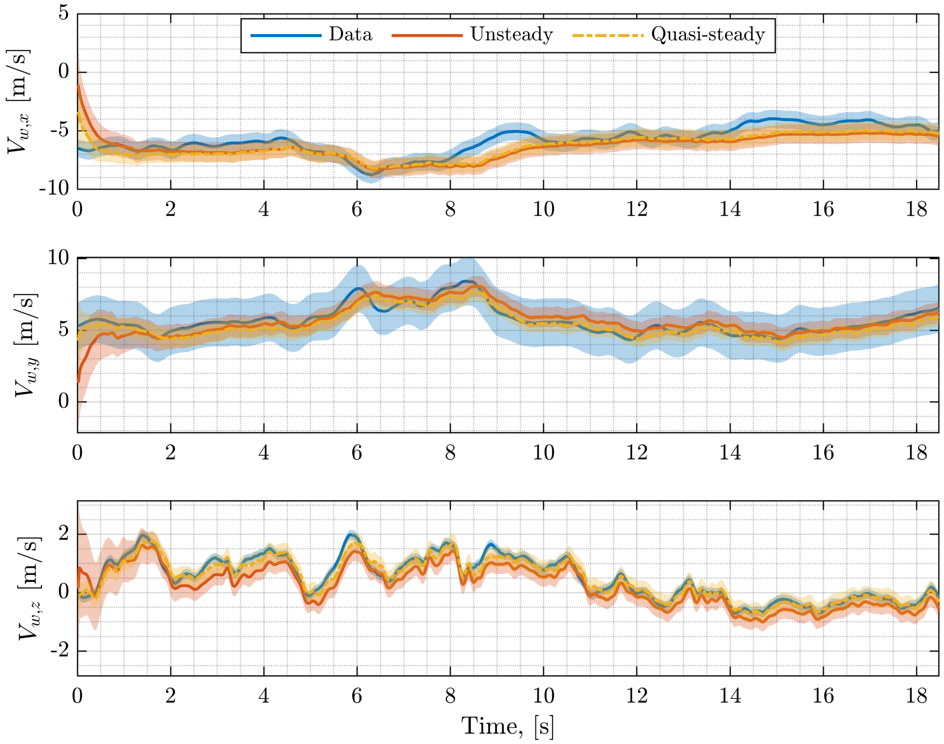

(b) Southward flight.

Figure 7.3: Reconstructed and estimated wind component time histories for north/south flight.

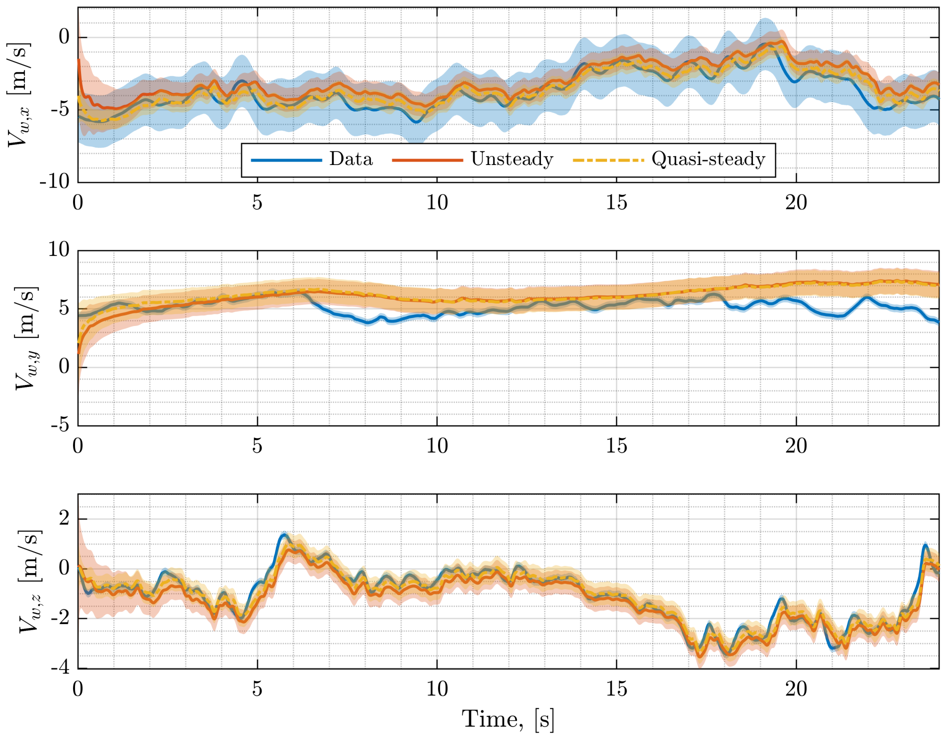

(a) Eastward flight.

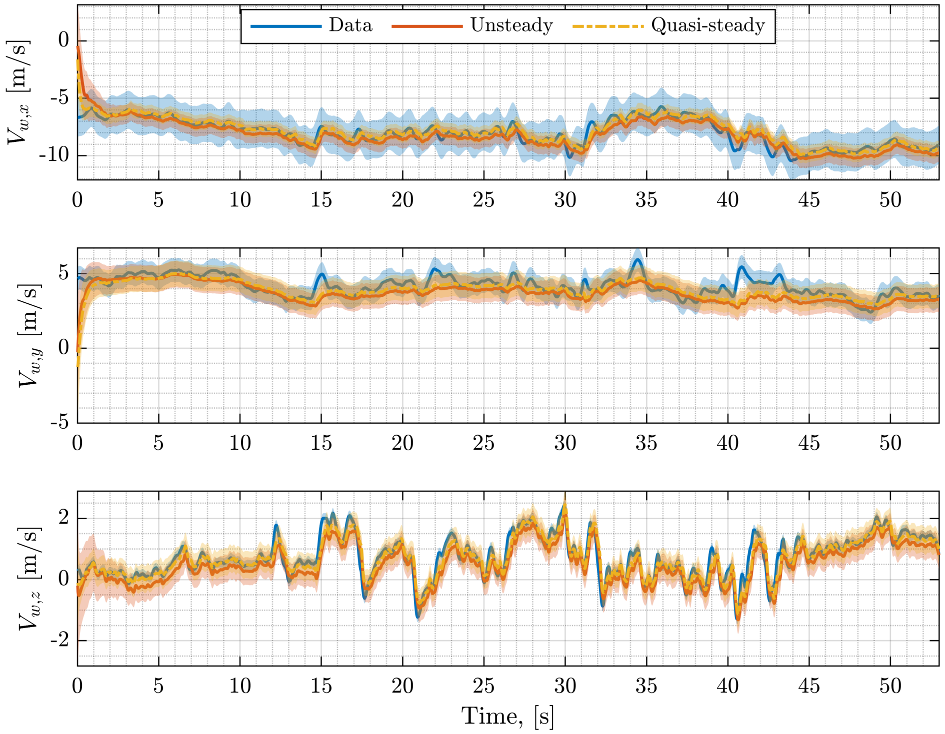

(b) Westward flight.

Figure 7.4: Reconstructed and estimated wind component time histories for east/west flight.

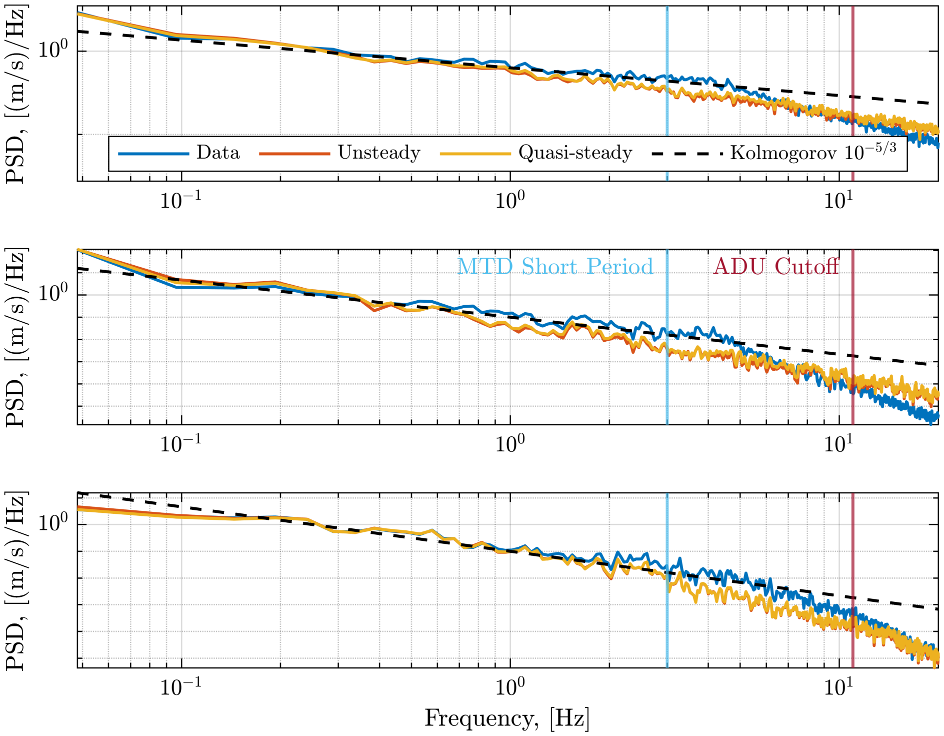

Figure 7.5: Reconstructed and estimated wind component power spectral density (PSD) over the entire experimental flight profile.

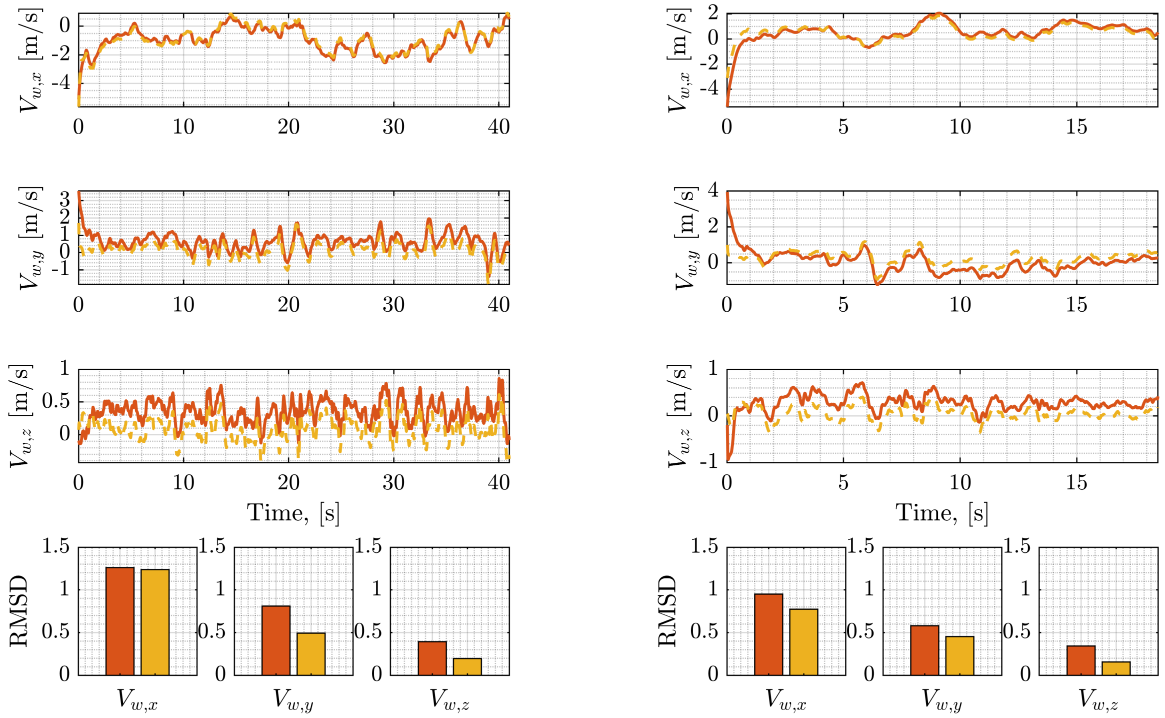

(a) Northward flight.

(b) Southward flight.

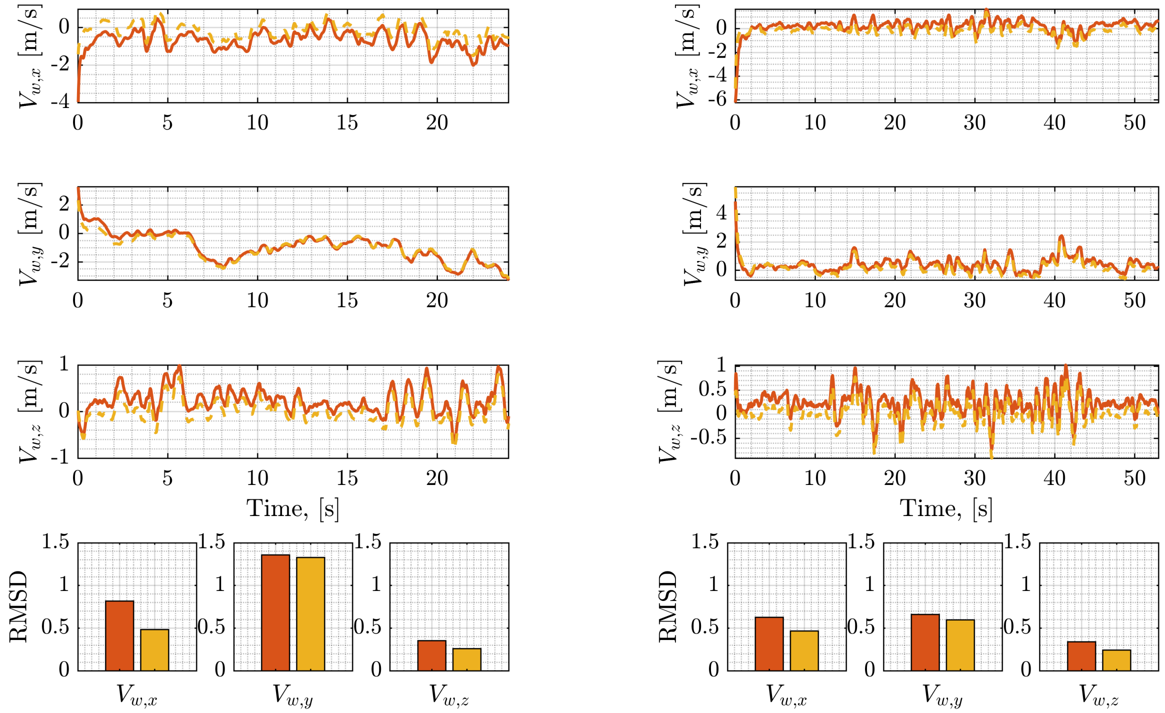

(c) Eastward flight.

(d) Westward flight.

Figure 7.6: Time histories of difference and root-mean-square difference (RMSD) for the estimated wind components. (Burnt Orange = Unsteady; Gold = Quasi-steady)

7.5 Conclusion

The performance of two model-based wind estimators for a small, fixed-wing aircraft were compared. In one estimator, the flight dynamic model incorporated unsteady aerodynamics identified from flight test data, while the other estimator used a quasi-steady flight dynamic model. To provide a baseline for this comparison, the wind velocity was reconstructed from measurements obtained using a vaned air data unit. The measurements from this sensor were not incorporated into the model-based wind estimates. The unsteady and quasi-steady aerodynamic model-based wind velocity estimates performed similarly in comparison with the reconstructed wind velocity, with the quasi-steady model-based estimates showing marginally lower root-mean-square difference. The power spectral density of both model-based wind estimates agree with the power spectral density of the reconstructed wind velocity, and all three power spectra exhibit Kolmogorov's $10^{-5/3}$ slope, consistent with expectations. It has been shown how unsteady aerodynamic effects may be incorporated into a model-based wind estimation scheme for a fixed-wing aircraft. For the aircraft and flight data considered here, the procedure did not improve wind estimate accuracy, compared with results obtained using a quasi-steady aerodynamic model. It is possible, though, that incorporating unsteady effects could improve model-based wind estimates for other vehicle configurations, environmental conditions, or scenarios where unsteady aerodynamics become important.

Chapter 8

Conclusion

This dissertation discusses the development and validation of three flight dynamic models for a small, fixed-wing aircraft using the MATLAB® toolbox known as System Identification Programs for Aircraft (SIDPAC). The first model is a generic nonlinear aerodynamic model, the second is a linear aerodynamic model, and the third is a linear, unsteady aerodynamic model. The aircraft system identification process starts with designing and implementing input excitations such as longitudinal and lateral-directional doublets and multisine waves. Afterward, checks for kinematic consistency and data collinearity are performed. The aerodynamic model's structure is determined using multivariate-orthogonal-function (MOF) modeling, and its parameters are then identified using the output-error method applied to data obtained over several flights. Finally, the identified model is validated using independent data. The input design, data processing, kinematic consistency test, and collinearity test are identical for all three models. The data collected to train the nonlinear aerodynamic model is used for the linear unsteady aerodynamic model. However, although some aerodynamic parameters appear in all three models, the values to which these parameters converge are different.

Additionally, this dissertation compares the performance of six different wind estimation methods in three commonly used state estimators. It provides detailed information on the tuning processes and initialization of each filter to help researchers and engineers better understand the methods used for wind estimation. The six wind estimation methods that were compared are wind triangle aerodynamic model-free, 15-state and 6-measurement aerodynamic model-free, 15-state and 9-measurement aerodynamic model-free, aerodynamic model-based, aerodynamic model-based with a true airspeed measurement, and aerodynamic model-based with a true airspeed, angle of attack, and sideslip measurements. These methods are implemented in three filters: a Kalman filter, an extended Kalman filter, and an unscented Kalman filter. To provide a baseline for comparison, a wind velocity reconstruction from measurements obtained from a vaned air data unit is calculated. The wind estimates are then compared to the reconstructed wind and their root-mean-square difference are calculated. It is observed that the wind triangle aerodynamic model-free method is the least accurate, while the 15-state and 9-measurement aerodynamic model-free method yields the best wind estimation results. However, the latter method requires vaned air data unit measurements. The 15-state and 6-measurement aerodynamic model-free method performs better than the wind triangle method. Still, it underperforms compared to the 15-state and 9-measurement aerodynamic model-free methods because it does not include the aircraft's attitude measurement. The aerodynamic model-based method yields the next-best wind velocity estimates and is ideal for situations where the aircraft is not equipped with a vaned air data unit. However, the aerodynamic model-based method with true airspeed measurement significantly improves the results of the aerodynamic model-based method. It is ideal when the aircraft is not equipped with air data vanes but a pitot tube sensor. Furthermore, the aerodynamic model-based method with true airspeed, angle of attack, and sideslip measurements yields the best results but enforces the need for the aircraft to be equipped with a vaned air data unit (ADU). It is also found that the Kalman filter is the easiest to tune and implement, but due to its linearity, it is limited to nominal flight trajectories. The unscented Kalman filter is the hardest to tune and computationally more expensive than the Kalman and extended Kalman filters. However, the unscented Kalman filter does not significantly improve wind estimates compared to the other two filters. The extended Kalman filter yields the best results.

Finally, this dissertation compares the performance of two model-based wind estimators for a small, fixed-wing aircraft. The first estimator utilizes a flight dynamic model that incorporates an unsteady aerodynamic model. The second estimator uses a quasi-steady flight dynamic model. To provide a baseline for this comparison, the wind velocity is reconstructed from measurements obtained using a vaned air data unit. It is worth noting that the measurements from the sensor were not incorporated into the model-based wind estimates in this analysis. Both the unsteady and quasi-steady aerodynamic model-based wind velocity estimates performed similarly when compared with the reconstructed wind velocity. However, the quasi-steady model-based estimates showed marginally lower root-mean-square difference. The power spectral density of both model-based wind estimates agreed with the power spectral density of the reconstructed wind velocity. Furthermore, all three power spectra exhibit Kolmogorov's $10^{-5/3}$ slope, which is expected. The study found that incorporating unsteady aerodynamic effects into the model-based wind estimation scheme did not improve wind estimate accuracy compared with results obtained using a quasi-steady aerodynamic model. It is possible, though, that incorporating unsteady effects could improve model-based wind estimates for other vehicle configurations, environmental conditions, or scenarios where unsteady aerodynamics become important.

Appendices

Appendix A

Modeling and Identification of Unsteady Dynamics from an Artificial Gust Generator

This chapter describes the development, identification, and validation of unsteady aerodynamic force and moment models for a small, fixed-wing, uncrewed aircraft. The development and characterization of an outdoor artificial gust generator used to identify the unsteady aerodynamic parameters is also discussed. The identified unsteady flight dynamic model is compared to a quasi-steady dynamic model using validation data obtained from independent flights through the turbulent jet of the gust generator. The results show the unsteady model better captures the aircraft's dynamic response to the turbulent jet from the gust generator. As a preliminary exploration of model-based wind estimation, the identified quasi-steady and unsteady models are then used to estimate the response to natural winds. The results indicate that estimation using the unsteady model is slightly more accurate, but the estimation error increases with increasingly severe wind fluctuations suggesting additional modeling effort is required to accurately infer wind velocity fluctuations. Additionally, the usage of an outdoor artificial gust generator for system identification proved to be difficult to repeat and, therefore, contributed to modeling error.

A.1 Introduction

Small uncrewed aircraft systems (sUAS) have become an attractive sensor platform to measure atmospheric quantities [7, 8, 9, 81]. A sUAS offers an accessible, low-cost method for measuring wind, especially at lower altitudes where atmospheric conditions vary rapidly in space and time. To infer wind, estimation algorithms that combine onboard sensor measurements with aircraft flight dynamic models have been used; see, for example, [11, 74, 85]. Small UAS are usually equipped with low-cost sensors, which typically means the measurements have higher uncertainty. Previous studies have explored the effects of various types of sensors on estimated states [78, 79, 82, 83]. Reconstruction errors due to low fidelity dynamic models have received less attention, although the effect of linearizing a quasi-steady, nonlinear flight dynamic model and of ignoring non-uniform flow effects on wind estimation accuracy was explored in [103]. Here, a linear, unsteady flight dynamic model is developed, and its parameters are identified to improve the accuracy of the dynamic model for model-based estimation of wind velocity from unsteady aircraft motion.

Unsteady aerodynamic formulations were first given by Wagner in the time domain [34], and Theodorsen in the frequency domain [35]. Garrick and Jones [38] later observed that Wagner's and Theodorsen's models are equivalent and that they are related by a Laplace transform. Tobak [40] introduced longitudinal linear unsteady aerodynamic equations in terms of indicial functions [40], and later Tobak and Schiff [16] introduced linear unsteady aerodynamic equations as a function of aircraft state and input variables.

Although Theodorsen's model was originally intended to describe flutter at high velocities, the theory is valuable in characterizing unsteady aerodynamic force and moment more generally. Both Wagner's and Theodorsen's formulations include an added mass component, a quasi-steady component, and a function that models the effect of the wake vortex. Both

Wagner's and Theodorsen's theories are restricted to ideal flow theory assumptions. In [17], an empirical rational transfer function of the Theodorsen's function and its state-space representation are presented. In [30, 33], Theodorsen's equations are given in the form of stability derivatives, and in [4, 18] system identification maneuvers to identify the quasi-steady aerodynamic parameters are discussed. This chapter describes the development and identification of a six-degree-of-freedom unsteady aerodynamic model for a small, fixed-wing aircraft as originally presented in [22].

In Section A.2, we present the theoretical background of unsteady aerodynamic models. In Section A.3, we describe the formulation of a linear unsteady aerodynamic model in terms of aircraft states and inputs. In Section A.4, we describe the test aircraft and the flight test experiment, which includes the development of an artificial gust generator (AGG). In Section A.5, we present the system identification results of the modeled unsteady parameters. Finally, the conclusions are discussed in Section A.6.

A.2 Unsteady Aerodynamic Theoretical Background

We begin by reviewing Wagner's and Theodorsen's unsteady lift models for a flat plate in Section A.2.1., extending these concepts to a rigid aircraft in Section A.2.2.

A.2.1 Unsteady Aerodynamics of a Flat Plate

Wagner's Formulation of Unsteady Lift Model

Wagner's lift model for a flat plate is formulated in the time domain. The model assumes inviscid, and incompressible flow [17, 33]. The model includes a convolution integral, with the indicial response function $\phi(\hat{t})$, where $\hat{t} = t\frac{2V_r}{\bar{c}}$, that describes the effect of wake vortices generated due to unsteady motion. Wagner's lift model [17, 33] is

$$c_l(\hat{t}) = \pi\delta(\hat{t}) + \int_0^{\hat{t}} \phi(\hat{t}-\tau)\dot{\alpha}(\tau)d\tau \tag{A.1}$$

where $\delta(\hat{t})$ is the added-mass for a step input in angle of attack. The first term is the non-circulatory component, and the second term is the circulatory component. Neglecting the non-circulatory component of lift, and based on [33, Ch. 5], the response of $c_l(\hat{t})$ to a change in the angle of attack can be written as:

$$c_l(\hat{t}) = c_{l_\alpha}\alpha(\hat{t}) - \hat{\dot{\alpha}} \int_0^{\hat{t}} f(\hat{t}-\tau)d\tau \tag{A.2}$$

where $\alpha(\hat{t}) = \hat{\dot{\alpha}}\hat{t}$, $\hat{\dot{\alpha}} = \frac{\dot{\alpha}\bar{c}}{2V_\mathrm{r}}$, and $f(\hat{t})$ is the lift deficiency function. If the effects due to unsteady motion are neglected, and the quasi-steady assumption is enforced, Eq. (A.2) can be written in terms of stability derivatives

$$c_l = c_{l_\alpha}\alpha + c_{l_{\dot{\alpha}}}\hat{\dot{\alpha}} \tag{A.3}$$

where $c_{l_{\dot{\alpha}}} = -\int_0^{\hat{t}} f(\hat{t}-\tau)d\tau$. Eq. (A.3) is a quasi-steady model; the value of c_l depends only on the instantaneous values of α and $\dot{\alpha}$.

Theodorsen's Formulation of Unsteady Lift Model

Theodorsen's aerodynamic force given in [104] accounts for heaving and pitching motion of a flat plate. For our purposes, we will only consider the effect due to the flat plate's motion, ignoring the effect of a control surface, which Theodorsen [35] included. Theodorsen's coefficient of lift force acting on an infinite-span flat plate that is plunging and pitching in a horizontal flow is:

$$c_l(t) = \underbrace{\frac{\pi}{2}\left(\dot{\alpha}(t)\frac{\bar{c}}{V_\mathrm{r}} - \ddot{h}(t)\frac{\bar{c}}{V_\mathrm{r}^2} + \ddot{\alpha}(t)\frac{\bar{c}^2}{V_\mathrm{r}^2}\left(\frac{1}{2} - \frac{a}{\bar{c}}\right)\right)}_{\text{non-circulatory component}} + \underbrace{\underbrace{2\pi\left(\alpha(t) - \frac{\dot{h}(t)}{V_\mathrm{r}} + \dot{\alpha}(t)\frac{\bar{c}}{V_\mathrm{r}}\left(\frac{3}{4} - \frac{a}{\bar{c}}\right)\right)}_{\text{quasi-steady component}}\bar{C}(k)}_{\text{circulatory component}} \tag{A.4}$$

In Eq. (A.4), a is the pitching axis location about which the pitch moment is taken, measured aft of the leading edge, h is the downward vertical displacement of the point a with respect to a fixed point, and α is the flat plate's angle of attack with respect to the free stream. The terms in the non-circulatory component capture the added mass effect due to an unsteady motion. The terms in the circulatory component account for quasi-steady lift and the transient dynamics of the wake vortices generated aft of the trailing edge in response to an unsteady motion, which is captured by Theodorsen's function $\bar{C}(k)$. If the non-circulatory component is neglected, Eq. (A.4) becomes:

$$c_l(t) = 2\pi\left(\alpha(t) - \frac{\dot{h}(t)}{V_\mathrm{r}} + \dot{\alpha}(t)\frac{\bar{c}}{V_\mathrm{r}}\left(\frac{3}{4} - \frac{a}{\bar{c}}\right)\right)\bar{C}(k) \tag{A.5}$$

The quasi-steady terms describe the instantaneous lift generated during an unsteady motion, and the wake vortices, captured by $\bar{C}(k)$, have a diminishing and lagging effect on the instantaneous lift. Theodorsen's function $\bar{C}(k)$ is parameterized by the reduced frequency $k = \frac{\omega\bar{c}}{2V_\mathrm{r}}$, where ω is the frequency of harmonic oscillation. Theodorsen's function [35] is:

$$\bar{C}(k) = \frac{H_1^{(2)}(k)}{H_1^{(2)}(k) + iH_0^{(2)}(k)} \tag{A.6}$$

where $H_x^{(2)} = J_x - iY_x$ is the Hankel function, which is in turn defined in terms of the Bessel functions of the first and second kind, J_x and Y_x, respectively. A reduced frequency of zero describes a steady motion; thus, $\bar{C}(0) = 1$, in which case c_l is only a function of the effective angle of attack.

Theodorsen's classical theory was developed from ideal flow theory with assumptions that limit its application. An empirical approach to relax limitations such as inviscid flow, flat plate geometry, and harmonic motion is given in [17]. The empirical model of Eq. (A.5) is:

$$c_l(t) = \left(c_{l_\alpha}\alpha(t) + c_{l_{\dot{\alpha}}}\hat{\dot{\alpha}}(t)\right)\bar{C}(s) \tag{A.7}$$

where c_{l_α} and $c_{l_{\dot{\alpha}}}$ are stability derivatives and $\bar{C}(s)$ is a generalized Theodorsen's function defined in the Laplace domain. Note that Eq. (A.7) incorporates a common abuse of notation, in which an s-domain transfer function multiplies a time-domain signal; a time-domain realization of the transfer function is used in numerical models. The contribution of $\dot{h}$ is present in Eq. (A.7) as part of the effective angle of attack for the entire airfoil. If the unsteady effects are ignored, Eq. (A.7) reduces to the quasi-steady model (A.3).

Wagner's Indicial Function and Theodorsen's Function

Wagner's indicial response function and Theodorsen's function are related by a Laplace transform pair [17, 38, 39].

$$\bar{C}(s) = s\int_0^\infty \phi(t)e^{-st}dt \tag{A.8}$$

Eq. (A.8) shows that Wagner's indicial response function and the Theodorsen function are equivalent ways of representing the effect on the lift of the transient evolution of the wake vortices due to an unsteady motion.

A.2.2 Linear, Unsteady Aerodynamic Model Structure for a Fixed-wing Aircraft

The aerodynamic forces and moments acting on an aircraft in arbitrary motion can be approximated by time-invariant linear or polynomial terms. A longitudinal linear unsteady aerodynamic model in terms of indicial functions was given in [40]. Aerodynamic coefficients as functions of state and input variables, which include linear unsteady aerodynamics as a special case, were proposed in [16]. Here, we summarize the presentation in [4, Ch. 3] of the analysis provided in [16]. Let $C_a(t)$ represent a given nondimensional force or moment coefficient where $a \in \{X, Z, m, Y, l, n\}$. Also let $C_a[\infty, \boldsymbol{\delta}(t)]$ represent the steady-state value of this coefficient in response to control commands $\boldsymbol{\delta} = [\delta_a, \delta_e, \delta_r]^T$

$$C_a(t) = C_a[\infty; \boldsymbol{\delta}(t)] + \int_0^t \boldsymbol{C}_{a_{\zeta_1}}[t-\tau; \boldsymbol{\zeta}(\tau)]^T \frac{d}{d\tau}\boldsymbol{\zeta}_1(\tau)d\tau + \frac{l}{V_\mathrm{r}}\int_0^t \boldsymbol{C}_{a_{\zeta_2}}[t-\tau; \boldsymbol{\zeta}(\tau)]^T \frac{d}{d\tau}\boldsymbol{\zeta}_2(\tau)d\tau \tag{A.9}$$

where $\boldsymbol{\zeta}_1 = [\alpha, \beta]^T$, $\boldsymbol{\zeta}_2 = [p, q, r]^T$, $\boldsymbol{\zeta} = [\boldsymbol{\zeta}_1^T, \boldsymbol{\zeta}_2^T]^T$, and $\boldsymbol{C}_{a_{\zeta_i}}(t)$ is the vector of indicial functions whose elements are the responses to a change in $\boldsymbol{\zeta}_i$. Following the presentation in [4, Ch. 3], Eq. (A.9) can be expanded and written as:

$$\begin{aligned} C_a(t) = C_{a_0} + C_{a_{\delta_a}}\delta_a(t) + C_{a_{\delta_e}}\delta_e(t) + C_{a_{\delta_r}}\delta_r(t) + C_{a_p}\hat{p}(t) + C_{a_q}\hat{q}(t) + C_{a_r}\hat{r}(t) + \\ C_{a_\alpha}\alpha(t) - \int_0^t F_{a_\alpha}(t-\tau)\hat{\dot{\alpha}}(\tau)d\tau + C_{a_\beta}\beta(t) - \int_0^t F_{a_\beta}(t-\tau)\hat{\dot{\beta}}(\tau)d\tau \end{aligned} \tag{A.10}$$

where the nondimensional terms in Eq. (A.10) are

$$\hat{p}(t) = \tfrac{p(t)b}{2V_\mathrm{r}} \quad \hat{q}(t) = \tfrac{q(t)\bar{c}}{2V_\mathrm{r}} \quad \hat{r}(t) = \tfrac{r(t)b}{2V_\mathrm{r}} \quad \hat{\dot{\alpha}} = \tfrac{\dot{\alpha}\bar{c}}{2V_\mathrm{r}} \quad \hat{\dot{\beta}} = \tfrac{\dot{\beta}b}{2V_\mathrm{r}}$$

and where $\bar{c}$ is the aerodynamic mean chord, b is the wingspan, and V_r is the freestream velocity. In Eq. (A.10), the vector of indicial functions, $\boldsymbol{C}_{a_{\zeta_1}}[t-\tau]^T$, whose elements are the terms in the vector $\boldsymbol{\zeta}_1$ is expanded into the steady-state coefficients of C_a with respect to α and β, and the convolution functions which include the deficiency functions F_{a_α} and F_{a_β}. Following Section A.2.1, these indicial functions are related to transfer functions by a Laplace transform pair

$$\bar{C}_{a_{\zeta_{1_{(\cdot)}}}}(s) = s\int_0^\infty C_{a_{\zeta_{1_{(\cdot)}}}}(t)e^{-st}dt \tag{A.11}$$

where $(\cdot)$ denotes α or β. The transfer functions given in Eq. (A.11) are s-domain representations of the impulse response of $C_a(t)$ to changes in α and β. Based on Eq. (A.10) and Eq. (A.11), a linear, unsteady aerodynamic model of a fixed-wing aircraft in terms of stability derivatives and corresponding deficiency functions replaced by their respective transfer functions is:

$$C_X(t) = C_{X_0} + C_{X_q}\hat{q}(t) + C_{X_{\delta_e}}\delta_e(t) + \Big(C_{X_\alpha}\alpha(t) + C_{X_{\dot\alpha}}\hat{\dot\alpha}(t)\Big)\bar{C}_{X_\alpha}(s) \tag{A.12a}$$

$$C_Z(t) = C_{Z_0} + C_{Z_q}\hat{q}(t) + C_{Z_{\delta_e}}\delta_e(t) + \Big(C_{Z_\alpha}\alpha(t) + C_{Z_{\dot\alpha}}\hat{\dot\alpha}(t)\Big)\bar{C}_{Z_\alpha}(s) \tag{A.12b}$$

$$C_m(t) = C_{m_0} + C_{m_q}\hat{q}(t) + C_{m_{\delta_e}}\delta_e(t) + \Big(C_{m_\alpha}\alpha(t) + C_{m_{\dot\alpha}}\hat{\dot\alpha}(t)\Big)\bar{C}_{m_\alpha}(s) \tag{A.12c}$$

$$C_Y(t) = C_{Y_0} + C_{Y_p}\hat{p}(t) + C_{Y_r}\hat{r}(t) + C_{Y_{\delta_a}}\delta_a(t) + C_{Y_{\delta_r}}\delta_r(t) + \Big(C_{Y_\beta}\beta(t) + C_{Y_{\dot\beta}}\hat{\dot\beta}(t)\Big)\bar{C}_{Y_\beta}(s) \tag{A.12d}$$

$$C_l(t) = C_{l_0} + C_{l_p}\hat{p}(t) + C_{l_r}\hat{r}(t) + C_{l_{\delta_a}}\delta_a(t) + C_{l_{\delta_r}}\delta_r(t) + \Big(C_{l_\beta}\beta(t) + C_{l_{\dot\beta}}\hat{\dot\beta}(t)\Big)\bar{C}_{l_\beta}(s) \tag{A.12e}$$

$$C_n(t) = C_{n_0} + C_{n_p}\hat{p}(t) + C_{n_r}\hat{r}(t) + C_{n_{\delta_a}}\delta_a(t) + C_{n_{\delta_r}}\delta_r(t) + \Big(C_{n_\beta}\beta(t) + C_{n_{\dot\beta}}\hat{\dot\beta}(t)\Big)\bar{C}_{n_\beta}(s) \tag{A.12f}$$

Note, for a fixed-wing aircraft the symmetric force and moment coefficients C_X, C_Z, and C_m are assumed to be independent from asymmetric variables v, p, r, β, and $\dot\beta$. The asymmetric force and moment coefficients C_Y, C_l, C_n are assumed to be independent from symmetric variables u, w, q, α, and $\dot{\alpha}$.

A.3 System Identification of the Aerodynamic Parameters

A.3.1 System Identification of the Quasi-steady Aerodynamic Coefficients

This section briefly describes a model identification methodology for determining the quasi-steady stability derivatives given in Eq. (A.12) from data obtained in experimental flight tests. The quasi-steady terms are identified before the transfer function parameters discussed in Section A.2.2 are determined. The process of determining which parameters in Eq. (A.19) are significant enough to include in the model is adapted from [4]. This effort was implemented in [105, 106] for a research aircraft that is similar to the one used in this chapter. Here we seek to determine which parameters in Eq. (A.19) adequately describe the aircraft's motion or response (output) to controls or small perturbations (inputs). The quasi-steady model used in this chapter does not capture propulsion effects as discussed in [107], and the propeller was feathered with idle throttle setting for the data collected to identify the quasi-steady model. The quasi-steady model is valid near the nominal trim conditions described later in Section A.4.2. Note, the quasi-steady aerodynamic coefficients are identified separately from the empirical transfer functions by setting $\bar{C}_{Z_\alpha}(s) = 1$, $\bar{C}_{X_\alpha}(s) = 1$, $\bar{C}_{m_\alpha}(s) = 1$, $\bar{C}_{Y_\beta}(s) = 1$, $\bar{C}_{l_\beta}(s) = 1$, and $\bar{C}_{n_\beta}(s) = 1$. Hence, the quasi-steady longitudinal and lateral-directional quasi-steady aerodynamic coefficients can be written as follows:

$$C_X(t) = C_{X_0} + C_{X_q}\hat{q}(t) + C_{X_{\delta_e}}\delta_e(t) + C_{X_\alpha}\alpha(t) + C_{X_{\dot{\alpha}}}\hat{\dot{\alpha}}(t) \tag{A.13a}$$

$$C_Z(t) = C_{Z_0} + C_{Z_q}\hat{q}(t) + C_{Z_{\delta_e}}\delta_e(t) + C_{Z_\alpha}\alpha(t) + C_{Z_{\dot{\alpha}}}\hat{\dot{\alpha}}(t) \tag{A.13b}$$

$$C_m(t) = C_{m_0} + C_{m_q}\hat{q}(t) + C_{m_{\delta_e}}\delta_e(t) + C_{m_\alpha}\alpha(t) + C_{m_{\dot{\alpha}}}\hat{\dot{\alpha}}(t) \tag{A.13c}$$

$$C_Y(t) = C_{Y_0} + C_{Y_p}\hat{p}(t) + C_{Y_r}\hat{r}(t) + C_{Y_{\delta_a}}\delta_a(t) + C_{Y_{\delta_r}}\delta_r(t) + C_{Y_\beta}\beta(t) + C_{Y_{\dot{\beta}}}\hat{\dot{\beta}}(t) \tag{A.13d}$$

$$C_l(t) = C_{l_0} + C_{l_p}\hat{p}(t) + C_{l_r}\hat{r}(t) + C_{l_{\delta_a}}\delta_a(t) + C_{l_{\delta_r}}\delta_r(t) + C_{l_\beta}\beta(t) + C_{l_{\dot{\beta}}}\hat{\dot{\beta}}(t) \tag{A.13e}$$

$$C_n(t) = C_{n_0} + C_{n_p}\hat{p}(t) + C_{n_r}\hat{r}(t) + C_{n_{\delta_a}}\delta_a(t) + C_{n_{\delta_r}}\delta_r(t) + C_{n_\beta}\beta(t) + C_{n_{\dot{\beta}}}\hat{\dot{\beta}}(t) \tag{A.13f}$$

A.3.2 System Identification of the Empirical Transfer Functions

The work presented here is an extension of [22]. Let the subscript $b \in \{X, Z, m\}$ and let subscript $c \in \{Y, l, n\}$ so that we may write a given aerodynamic force or moment coefficient as

$$C_b(t) = C_{b_0} + C_{b_q}\hat{q}(t) + C_{b_{\delta_e}}\delta_e(t) + \Big(C_{b_\alpha}\alpha(t) + C_{b_{\dot{\alpha}}}\hat{\dot{\alpha}}(t)\Big)\,\bar{C}_{b_\alpha}(s) \tag{A.14a}$$

$$C_c(t) = C_{c_0} + C_{c_p}\hat{p}(t) + C_{c_r}\hat{r}(t) + C_{c_{\delta_a}}\delta_a(t) + C_{c_{\delta_r}}\delta_r(t) + \Big(C_{c_\beta}\beta(t) + C_{c_{\dot{\beta}}}\hat{\dot{\beta}}(t)\Big)\,\bar{C}_{c_\beta}(s) \tag{A.14b}$$

Here, we assume that we have measured the force and moment coefficients on the left side of Eq. (A.14) directly from flight tests, or reconstructed these coefficients from measured data, as well as the state variables that appear on the right. Additionally, we assume that the stability derivatives on the right are known, e.g., from the process summarized in Section A.3.2. If we consider the coefficients of the transfer functions in Eq. (A.14) as the input signals to those transfer functions, then the resulting output signals are the circulatory components. Rearranging (A.14) to isolate these circulatory components, we have

$$\tilde{C}_b(t) = \left(C_{b_\alpha}\alpha(t) + C_{b_{\dot{\alpha}}}\hat{\dot{\alpha}}(t)\right)\bar{C}_{b_\alpha}(s) = C_b(t) - C_{b_0} - C_{b_q}\hat{q}(t) - C_{b_{\delta_e}}\delta_e(t) \tag{A.15a}$$

$$\tilde{C}_c(t) = \left(C_{c_\beta}\beta(t) + C_{c_{\dot{\beta}}}\hat{\dot{\beta}}(t)\right)\bar{C}_{c_\beta}(s) = C_c(t) - C_{c_0} - C_{c_p}\hat{p}(t) - C_{c_r}\hat{r}(t) - C_{c_{\delta_a}}\delta_a(t) - C_{c_{\delta_r}}\delta_r(t) \tag{A.15b}$$

To illustrate the relationship between the circulatory component (output) and the quasi-steady component (input) of the empirical transfer functions in Eq. (A.15) a block diagram representation is given in Figure A.1.

(a) Quasi-steady and unsteady α dependent terms

(b) Quasi-steady and unsteady β dependent terms

Figure A.1: Block diagrams of Eq. (A.15)

In Figure A.1, $C_{(\cdot)}^{\text{circ}}$ is the circulatory aerodynamic force or moment, and $C_{(\cdot)}^{\text{QS}}$ is the quasi-steady aerodynamic force or moment. The output $C_a^{\text{circ}}(t)$ is known from flight data. That is, we assume that $C_a^{\text{circ}}(t) \approx \tilde{C}_a(t)$. Hence, the empirical transfer function can be written as follows:

$$\bar{C}_{b_\alpha}(s) = \frac{\mathcal{L}[C_b^{\text{circ}}]}{\mathcal{L}[C_b^{\text{QS}}]} = \frac{\mathcal{L}[\tilde{C}_b(t)]}{\mathcal{L}[C_{b_\alpha}\alpha(t) + C_{b_{\dot{\alpha}}}\hat{\dot{\alpha}}(t)]} \tag{A.16a}$$

$$\bar{C}_{c_\beta}(s) = \frac{\mathcal{L}[C_c^{\text{circ}}]}{\mathcal{L}[C_c^{\text{QS}}]} = \frac{\mathcal{L}[\tilde{C}_c(t)]}{\mathcal{L}[C_{c_\beta}\beta(t) + C_{c_{\dot{\beta}}}\hat{\dot{\beta}}(t)]} \tag{A.16b}$$

In order to finalize the six degrees of freedom unsteady aerodynamic force and moment coefficients given in Section A.2.2, Eq. (A.12) needs to be written using a state-space realization of the transfer functions given in Eq. (A.16). The state-space realizations of Eq. (A.16) with state vectors x_{b_α} and x_{c_β}, respectively, can be written as:

$$\bar{C}_{b_\alpha}(s) \rightarrow \left[\begin{array}{c|c} \bar{\boldsymbol{A}}_{b_\alpha} & \bar{\boldsymbol{B}}_{b_\alpha} \\ \hline \bar{\boldsymbol{C}}_{b_\alpha} & \bar{D}_{b_\alpha} \end{array}\right] \qquad \bar{C}_{c_\beta}(s) \rightarrow \left[\begin{array}{c|c} \bar{\boldsymbol{A}}_{c_\beta} & \bar{\boldsymbol{B}}_{c_\beta} \\ \hline \bar{\boldsymbol{C}}_{c_\beta} & \bar{D}_{c_\beta} \end{array}\right] \tag{A.17}$$

The dynamic equations for these state-space representations are:

$$\dot{\tilde{\boldsymbol{x}}}_{Z_\alpha}(t) = \bar{\boldsymbol{A}}_{Z_\alpha}\tilde{\boldsymbol{x}}_{Z_\alpha}(t) + \bar{\boldsymbol{B}}_{Z_\alpha}(C_{Z_\alpha}\alpha(t) + C_{Z_{\dot{\alpha}}}\hat{\dot{\alpha}}(t)) \tag{A.18a}$$

$$\dot{\tilde{\boldsymbol{x}}}_{X_\alpha}(t) = \bar{\boldsymbol{A}}_{X_\alpha}\tilde{\boldsymbol{x}}_{X_\alpha}(t) + \bar{\boldsymbol{B}}_{X_\alpha}(C_{X_\alpha}\alpha(t) + C_{X_{\dot{\alpha}}}\hat{\dot{\alpha}}(t)) \tag{A.18b}$$

$$\dot{\tilde{\boldsymbol{x}}}_{m_\alpha}(t) = \bar{\boldsymbol{A}}_{m_\alpha}\tilde{\boldsymbol{x}}_{m_\alpha}(t) + \bar{\boldsymbol{B}}_{m_\alpha}(C_{m_\alpha}\alpha(t) + C_{m_{\dot{\alpha}}}\hat{\dot{\alpha}}(t)) \tag{A.18c}$$

$$\dot{\tilde{\boldsymbol{x}}}_{Y_\beta}(t) = \bar{\boldsymbol{A}}_{Y_\beta}\tilde{\boldsymbol{x}}_{Y_\beta}(t) + \bar{\boldsymbol{B}}_{Y_\beta}(C_{Y_\beta}\beta(t) + C_{Y_{\dot{\beta}}}\hat{\dot{\beta}}(t)) \tag{A.18d}$$

$$\dot{\tilde{\boldsymbol{x}}}_{l_\beta}(t) = \bar{\boldsymbol{A}}_{l_\beta}\tilde{\boldsymbol{x}}_{l_\beta}(t) + \bar{\boldsymbol{B}}_{l_\beta}(C_{l_\beta}\beta(t) + C_{l_{\dot{\beta}}}\hat{\dot{\beta}}(t)) \tag{A.18e}$$

$$\dot{\tilde{\boldsymbol{x}}}_{n_\beta}(t) = \bar{\boldsymbol{A}}_{n_\beta}\tilde{\boldsymbol{x}}_{n_\beta}(t) + \bar{\boldsymbol{B}}_{n_\beta}(C_{n_\beta}\beta(t) + C_{n_{\dot{\beta}}}\hat{\dot{\beta}}(t)) \tag{A.18f}$$

and the full longitudinal and lateral unsteady force and moment aerodynamic coefficients of Eq. (A.12) are:

$$C_Z(t) = C_{Z_0} + C_{Z_q}\hat{q}(t) + C_{Z_{\delta_e}}\delta_e(t) + \bar{\boldsymbol{C}}_{Z_\alpha}\tilde{\boldsymbol{x}}_{Z_\alpha}(t) + \bar{D}_{Z_\alpha}(C_{Z_\alpha}\alpha(t) + C_{Z_{\dot\alpha}}\hat{\dot{\alpha}}(t)) \tag{A.19a}$$

$$C_X(t) = C_{X_0} + C_{X_q}\hat{q}(t) + C_{X_{\delta_e}}\delta_e(t) + \bar{\boldsymbol{C}}_{X_\alpha}\tilde{\boldsymbol{x}}_{X_\alpha}(t) + \bar{D}_{X_\alpha}(C_{X_\alpha}\alpha(t) + C_{X_{\dot\alpha}}\hat{\dot{\alpha}}(t)) \tag{A.19b}$$

$$C_m(t) = C_{m_0} + C_{m_q}\hat{q}(t) + C_{m_{\delta_e}}\delta_e(t) + \bar{\boldsymbol{C}}_{m_\alpha}\tilde{\boldsymbol{x}}_{m_\alpha}(t) + \bar{D}_{m_\alpha}(C_{m_\alpha}\alpha(t) + C_{m_{\dot\alpha}}\hat{\dot{\alpha}}(t)) \tag{A.19c}$$

$$C_Y(t) = C_{Y_0} + C_{Y_p}\hat{p}(t) + C_{Y_r}\hat{r}(t) + C_{Y_{\delta_a}}\delta_a(t) + C_{Y_{\delta_r}}\delta_r(t) + \bar{\boldsymbol{C}}_{Y_\beta}\tilde{\boldsymbol{x}}_{Y_\beta}(t) + \bar{D}_{Y_\beta}(C_{Y_\beta}\beta(t) + C_{Y_{\dot\beta}}\hat{\dot{\beta}}(t)) \tag{A.19d}$$

$$C_l(t) = C_{l_0} + C_{l_p}\hat{p}(t) + C_{l_r}\hat{r}(t) + C_{l_{\delta_a}}\delta_a(t) + C_{l_{\delta_r}}\delta_r(t) + \bar{\boldsymbol{C}}_{l_\beta}\tilde{\boldsymbol{x}}_{l_\beta}(t) + \bar{D}_{l_\beta}(C_{l_\beta}\beta(t) + C_{l_{\dot\beta}}\hat{\dot{\beta}}(t)) \tag{A.19e}$$

$$C_n(t) = C_{n_0} + C_{n_p}\hat{p}(t) + C_{n_r}\hat{r}(t) + C_{n_{\delta_a}}\delta_a(t) + C_{n_{\delta_r}}\delta_r(t) + \bar{\boldsymbol{C}}_{n_\beta}\tilde{\boldsymbol{x}}_{n_\beta}(t) + \bar{D}_{n_\beta}(C_{n_\beta}\beta(t) + C_{n_{\dot\beta}}\hat{\dot{\beta}}(t)) \tag{A.19f}$$

The expressions on the left side of Eq. (A.14) are computed from flight data as follows:

$$C_X(t) = \frac{m}{\bar{q}(t)S}a_x(t) \tag{A.20a}$$

$$C_Y(t) = \frac{m}{\bar{q}(t)S}a_y(t) \tag{A.20b}$$

$$C_Z(t) = \frac{m}{\bar{q}(t)S}a_z(t) \tag{A.20c}$$

$$C_l(t) = \frac{1}{\bar{q}(t)bS}\left(I_{xx}\dot{p}(t) - I_{xz}(\dot{r}(t) + p(t)q(t)) + q(t)r(t)(I_{zz} - I_{yy})\right) \tag{A.20d}$$

$$C_m(t) = \frac{1}{\bar{q}(t)\bar{c}}\left(I_{yy}\dot{q}(t) + r(t)p(t)(I_{xx} - I_{zz}) + I_{xz}(p(t)^2 - r(t)^2)\right) \tag{A.20e}$$

$$C_n(t) = \frac{1}{\bar{q}(t)bS}\left(I_{zz}\dot{r}(t) - I_{xz}(\dot{p}(t) + q(t)r(t)) + p(t)q(t)(I_{yy} - I_{xx})\right) \tag{A.20f}$$

where $\bar{q}(t) = \frac{1}{2}\rho V_{\mathrm{r}}(t)^2$, $a_{(\cdot)}$ are the body-fixed aircraft accelerations, m is the mass of the aircraft, S is the aircraft's projected wing area, ρ is air density, and $I_{(\cdot)}$ are the aircraft's moments of inertia.

A.4 Flight Test Setup

The research aircraft used in this chapter, the My Twin Dream (MTD), is a radio-controlled (RC) twin-engine, electrically powered, and foam-structured fixed-wing aircraft manufactured by My Fly Dream described in Chapter 4.

A.4.1 Flight Test Inputs

The software tools for the input design, post-flight data processing, and parameter estimation used to identify the quasi-steady terms are available in a MATLAB® toolbox called System Identification Programs for Aircraft (SIDPAC), which is associated with [4]. A detailed discussion regarding the aircraft instrumentation, flight test, and system identification analysis is provided in [105, 106]. The transfer function signal processing and parameter estimations were done with the MATLAB® System Identification Toolbox [108].

Orthogonal Phase-Optimized Multisine Excitation

The maneuvers used to identify the quasi-steady parameters include the orthogonal phase-optimized multisine input perturbation [4, Ch. 8]. The perturbation input $\Delta\delta$ is applied to each input in the control surface deflection vector (δ_a,δ_e,δ_r), and each perturbation input is a summation of sinusoids:

$$\Delta\delta = \sum_{k\in[1,2,\ldots,N]} A_k \sin\left(\frac{2\pi kt}{T} + \phi_k\right) \tag{A.21}$$

where N is the total number of harmonic excitation frequencies, A_k is the amplitude for the kth sinusoidal component, t is time and T is the total duration of the excitation, and ϕ_k is a phase shift chosen to ensure that the overall signal amplitude and the resulting perturbations from nominal flight remain sufficiently small. A table of the multisine harmonics used for model identification in this chapter is shown in [105]. Generally, the pitch rate and angle of attack rate dependent parameters are correlated. To decorrelate the pitch rate and angle of attack rate dependent parameters, the phugoid mode of the aircraft must be excited. The phugoid mode is characterized by a slow oscillation in airspeed, pitch rate, and pitch angle at an approximately constant angle of attack. The phugoid and short period mode of the aircraft can be excited using a multisine excitation [18] to identify all parameters in Eq. (A.13).

Sharp Aerodynamic Angle Excitation

The *sharp aerodynamic angle excitation* involves flying the aircraft through a well characterized wind disturbance produced by an *artificial gust generator* (AGG) to be described in Section A.4.3; see Figure A.2. The aircraft is flown through this disturbance without artificial stabilization or feedback control, with constant thrust, and with all control surfaces set to trim conditions. This is done to record the response of the aircraft due to a sudden angle of attack and sideslip angle change. This disturbance excites the unsteady terms in Eq. (A.12). The experimental data from overflights of the AGG are used to directly determine the transfer functions $\bar{C}_{Z_\alpha}(s)$, $\bar{C}_{X_\alpha}(s)$, $\bar{C}_{m_\alpha}(s)$, $\bar{C}_{Y_\beta}(s)$, $\bar{C}_{l_\beta}(s)$ and $\bar{C}_{n_\beta}(s)$. Following Eq. (A.16), the transfer functions' outputs are the aerodynamic coefficients given by Eq. (A.15). The velocity disturbances generated by the AGG are superimposed onto the flight data and used as the input to the transfer functions; see Figure A.9.

A.4.2 Aircraft Trim Configuration

The aircraft trim condition was established for straight and level constant altitude flight. Both the quasi-steady and unsteady aerodynamic models were developed for this nominal condition. Each system identification data collection flight was configured to trim conditions given in Table A.1.

Table A.1: Aircraft trim condition

Attitude	**Velocity**	**Control surface**
$\phi = 0$ [rad]	$u = 18.0\cos(0.029)$ [m/s]	$\delta_a = 0.041$ [rad]
$\theta = 0.0294$ [rad]	$v = 0$ [m/s]	$\delta_e = 0.012$ [rad]
$\psi =$ Arbitrary	$w = 18.0\sin(0.029)$ [m/s]	$\delta_r = 0.056$ [rad]

A.4.3 Artificial Gust Generator (AGG)

The artificial gust generator (AGG) used here is designed to generate a large, sharp gust in an outdoor environment. It is similar in concept to the blower device used in [109] to disturb the flight of a micro-aerial vehicle and the water jet device described in [110] for towing basin experiments.

The AGG used here consists of 16 carpet blowers arranged in a 2×8 array and oriented such that the length of the array exceeds the wing span of the sUAS; a photograph of the AGG is shown in Figure A.2. The sUAS is flown over the array at a height between six and twelve feet above ground level. The lower altitude limit is selected based on the pilot's sense of safe operation; the upper limit is based on the strength of the generated gust, which diminishes with height. The closer the uncrewed aircraft flies to the array the stronger and sharper (narrower) the disturbance.

The carpet blowers used in the experiment are Ironton 1/8 HP Mini Air Movers; the specifi-

Table A.2: AGG technical specifications

Technical specification specification	**Kestrel 5 Series Anemometer**
Brand	Ironton
Model	Item number 52724
Volt/ Frequency	115 Volts / 60 Hz
Power	1/8 HP
Max Current	1.5 Amps
Airflow (on High)	500 CFM
RPM (on High)	1200
Technical specification specification	**Kestrel 5 Series Anemometer**
Sensor	wind speed
Accuracy	least significant digit
Resolution	0.1 m/s
Specification Range	0.6 m/s to 40.0 m/s

Figure A.2: MTD pass over the AGG

cations are given in Table A.2. The output of the AGG was characterized along the length, width, and height above its footprint with the array oriented vertically. Figure A.5 and Table A.3 provide average measurements of vertical wind speed along with a 95% confidence interval of the measurements at each coordinate point specified. The wind speed measurements were obtained using a Kestrel 5 series anemometer. A three-dimensional measurement grid was established along x, y, and z axes. The schematic in Figure A.3 provides an overhead view of the x-y measurement grid; the airflow is out of the page, emanating from the darker shaded blower nozzles. The annotation "CB: #" denotes a given carpet blower and "BN: #" denotes the corresponding blower's nozzle. The integer values of x and y represent measurement stations along the length and width of the array, respectively; the corresponding scale in meters is indicated in Figure A.3.

Five separate wind velocity measurements were taken every four to six seconds at each x, y, and z coordinate of the measurement grid. The flow from the AGG was assumed to be symmetric about the y-axis to reduce the total number of measurements taken. As a result, measurements at only $x \in \{-2, -1, 0, 1, 2\}$, $y \in \{-8, -7, -5, -3, -1, 0\}$, and z

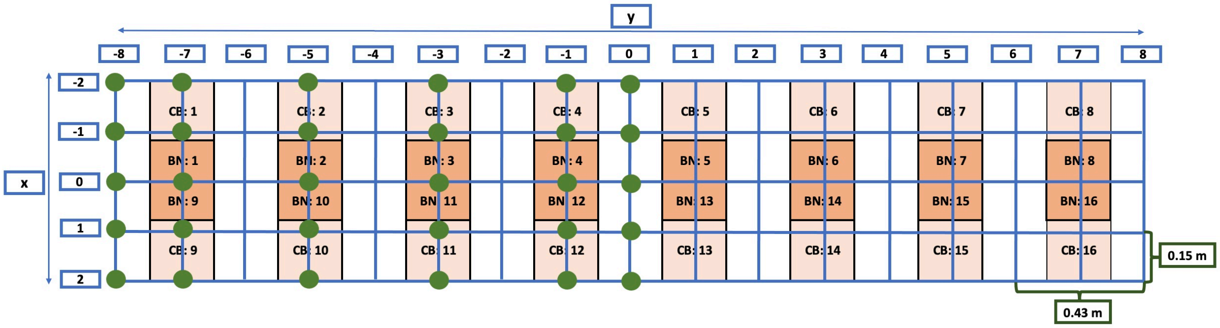

Figure A.3: AGG measurement grid, viewed from above.

$\in \{8, 7, 6, 5, 4, 3, 2\}$ were recorded which totaled 1050 measurements. The z coordinate points correspond to the height above the table on which the AGG is mounted: $z \in \{2.4\text{m}, 2.1\text{m}, 1.8\text{m}, 1.5\text{m}, 1.2\text{m}, 0.9\text{m}, 0.6\text{m}\}$. The flow emanating from these fans is a turbulent jet; the quoted vertical wind speeds are mean measurement values.

The plume characterization effort was conducted in Virginia Tech's indoor football practice facility, which is much larger than the AGG in every dimension and in which there is no measurable airflow. As a result, the ambient wind was calm, and the plume generated by the AGG was not disturbed. At 0.6 m above the base of the AGG the mean velocity is about 2.4 m/s and at 2.4 m above the base of the AGG the mean velocity is about 6 m/s. To further illustrate the effect of the plume generated by the AGG, the AGG was visually characterized using smoke plumes. This effort was conducted outdoors using smoke grenades; see Figure A.4.

A.4.4 Wind Conditions for Training and Validation Flight

In this chapter, three wind conditions were defined: calm, light, and severe. Wind speed fluctuations between 0 m/s and 2.5 m/s are classified as calm, see Figure A.6a, wind speed fluctuations between 2.5 m/s and 5.0 m/s are classified as light, see Figure A.6b, and wind

(a) Vertical AGG smoke visualization (b) Lateral AGG smoke visualization

Figure A.4: Artificial gust generator (AGG) visualization

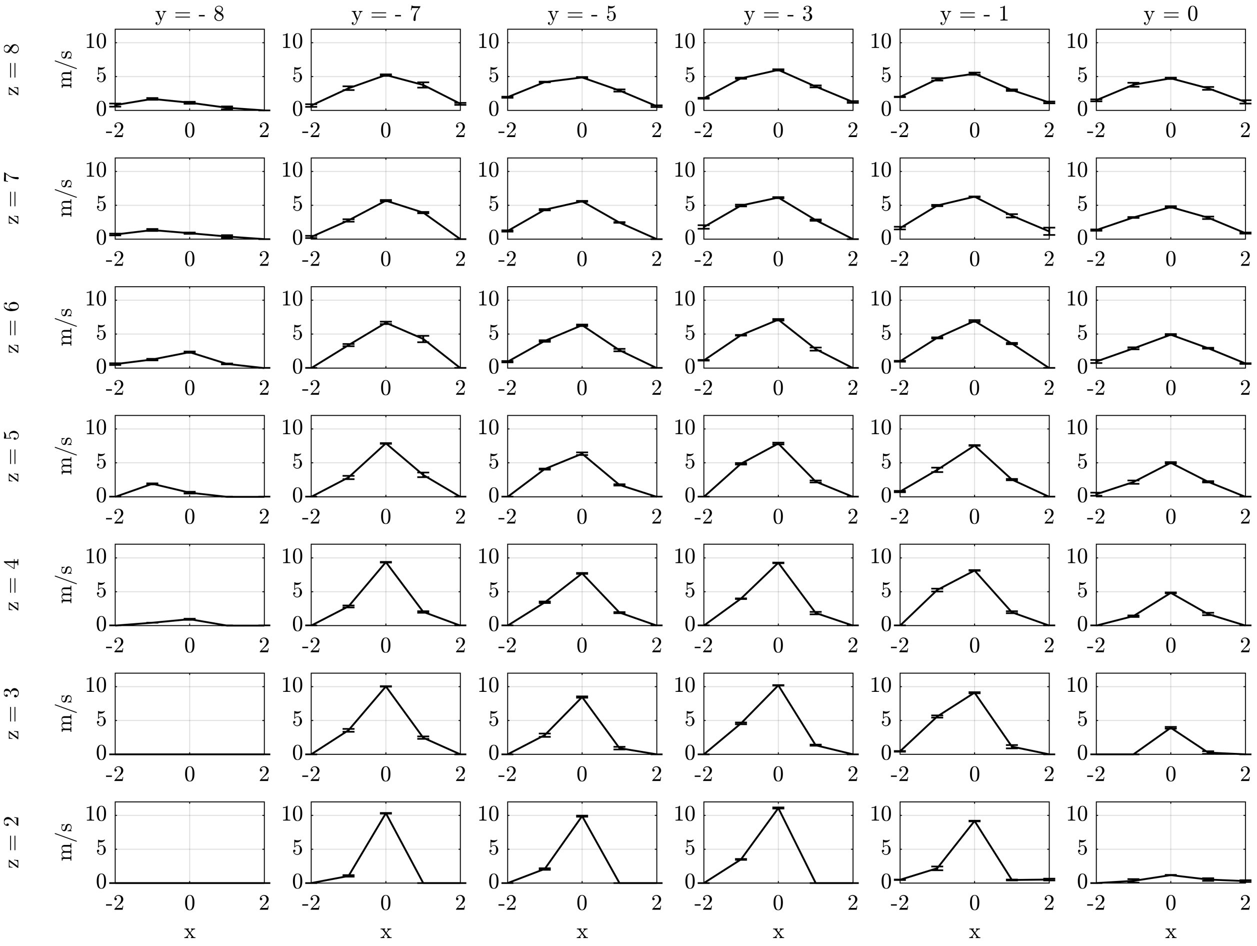

Figure A.5: AGG velocity measurement by vertical and lateral station; see Figure A.3.

Table A.3: Mean velocity and 95 % confidence intervals per coordinate point; see Figure A.3

			$y=-8$					$y=-7$		
	$x=2$	$x=1$	$x=0$	$x=-1$	$x=-2$	$x=2$	$x=1$	$x=0$	$x=-1$	$x=-2$
$z=-8$	0.8 ± 0.1	1.7 ± 0.1	1.1 ± 0.1	0.4 ± 0.1	0.0 ± 0.0	0.7 ± 0.1	3.3 ± 0.1	5.2 ± 0.1	3.7 ± 0.2	1.0 ± 0.1
$z=-7$	0.7 ± 0.1	1.3 ± 0.1	0.9 ± 0.1	0.4 ± 0.1	0.0 ± 0.0	0.3 ± 0.1	2.8 ± 0.1	5.7 ± 0.1	3.9 ± 0.1	0.0 ± 0.0
$z=-6$	0.6 ± 0.1	1.2 ± 0.1	2.3 ± 0.1	0.6 ± 0.0	0.0 ± 0.0	0.0 ± 0.0	3.4 ± 0.1	6.7 ± 0.1	4.3 ± 0.2	0.0 ± 0.0
$z=-5$	0.0 ± 0.0	1.9 ± 0.1	0.6 ± 0.1	0.0 ± 0.0	0.0 ± 0.0	0.0 ± 0.0	2.8 ± 0.1	7.9 ± 0.0	3.2 ± 0.2	0.0 ± 0.0
$z=-4$	0.0 ± 0.0	0.4 ± 0.0	0.9 ± 0.0	0.0 ± 0.0	0.0 ± 0.0	0.0 ± 0.0	2.8 ± 0.1	9.4 ± 0.0	2.0 ± 0.1	0.0 ± 0.0
$z=-3$	0.0 ± 0.0	0.0 ± 0.0	0.0 ± 0.0	0.0 ± 0.0	0.0 ± 0.0	0.0 ± 0.0	3.5 ± 0.1	10.0 ± 0.0	2.4 ± 0.1	0.0 ± 0.0
$z=-2$	0.0 ± 0.0	0.0 ± 0.0	0.0 ± 0.0	0.0 ± 0.0	0.0 ± 0.0	0.0 ± 0.0	1.0 ± 0.1	10.3 ± 0.0	0.0 ± 0.0	0.0 ± 0.0
			$y=-5$					$y=-3$		
	$x=2$	$x=1$	$x=0$	$x=-1$	$x=-2$	$x=2$	$x=1$	$x=0$	$x=-1$	$x=-2$
$z=-8$	1.9 ± 0.0	4.2 ± 0.0	4.9 ± 0.0	2.9 ± 0.1	0.6 ± 0.1	1.8 ± 0.0	4.7 ± 0.0	6.0 ± 0.1	3.5 ± 0.1	1.2 ± 0.0
$z=-7$	1.2 ± 0.1	4.3 ± 0.1	5.6 ± 0.0	2.4 ± 0.0	0.0 ± 0.0	1.8 ± 0.1	5.0 ± 0.1	6.1 ± 0.0	2.8 ± 0.1	0.0 ± 0.0
$z=-6$	0.9 ± 0.1	4.0 ± 0.1	6.3 ± 0.1	2.6 ± 0.1	0.0 ± 0.0	1.1 ± 0.0	4.8 ± 0.0	7.1 ± 0.1	2.8 ± 0.1	0.0 ± 0.0
$z=-5$	0.0 ± 0.0	4.1 ± 0.0	6.3 ± 0.1	1.7 ± 0.1	0.0 ± 0.0	0.0 ± 0.0	4.9 ± 0.1	7.8 ± 0.1	2.2 ± 0.1	0.0 ± 0.0
$z=-4$	0.0 ± 0.0	3.4 ± 0.1	7.7 ± 0.0	1.9 ± 0.1	0.0 ± 0.0	0.0 ± 0.0	4.0 ± 0.0	9.3 ± 0.0	1.8 ± 0.1	0.0 ± 0.0
$z=-3$	0.0 ± 0.0	2.8 ± 0.1	8.4 ± 0.1	0.9 ± 0.1	0.0 ± 0.0	0.0 ± 0.0	4.6 ± 0.1	10.2 ± 0.0	1.3 ± 0.0	0.0 ± 0.0
$z=-2$	0.0 ± 0.0	2.1 ± 0.1	9.9 ± 0.0	0.0 ± 0.0	0.0 ± 0.0	0.0 ± 0.0	3.5 ± 0.0	11.1 ± 0.0	0.0 ± 0.0	0.0 ± 0.0
			$y=-1$					$y=0$		
	$x=2$	$x=1$	$x=0$	$x=-1$	$x=-2$	$x=2$	$x=1$	$x=0$	$x=-1$	$x=-2$
$z=-8$	2.0 ± 0.0	4.6 ± 0.1	5.4 ± 0.1	3.0 ± 0.1	1.2 ± 0.1	1.5 ± 0.1	3.8 ± 0.2	4.7 ± 0.1	3.2 ± 0.1	1.2 ± 0.1
$z=-7$	1.6 ± 0.1	4.9 ± 0.1	6.3 ± 0.0	3.4 ± 0.1	1.1 ± 0.3	1.3 ± 0.1	3.2 ± 0.0	4.7 ± 0.1	3.1 ± 0.1	0.9 ± 0.0
$z=-6$	1.0 ± 0.0	4.4 ± 0.0	6.9 ± 0.1	3.6 ± 0.1	0.0 ± 0.0	1.0 ± 0.1	2.9 ± 0.1	4.9 ± 0.0	2.9 ± 0.0	0.7 ± 0.0
$z=-5$	0.8 ± 0.1	4.0 ± 0.2	7.6 ± 0.0	2.5 ± 0.1	0.0 ± 0.0	0.4 ± 0.1	2.2 ± 0.1	5.0 ± 0.1	2.2 ± 0.1	0.0 ± 0.0
$z=-4$	0.0 ± 0.0	5.2 ± 0.1	8.1 ± 0.0	2.0 ± 0.1	0.0 ± 0.0	0.0 ± 0.0	1.4 ± 0.1	4.8 ± 0.0	1.7 ± 0.1	0.0 ± 0.0
$z=-3$	0.4 ± 0.0	5.6 ± 0.1	9.1 ± 0.1	1.1 ± 0.1	0.0 ± 0.0	0.0 ± 0.0	0.0 ± 0.0	3.9 ± 0.1	0.2 ± 0.1	0.0 ± 0.0
$z=-2$	0.5 ± 0.0	2.2 ± 0.1	9.2 ± 0.0	0.4 ± 0.0	0.0 ± 0.0	0.0 ± 0.0	0.3 ± 0.1	1.2 ± 0.0	0.5 ± 0.1	0.3 ± 0.1

speed fluctuations above 5.0 m/s are classified as severe, see Figure A.6c.

The flight data used to train and validate the quasi-steady and the unsteady aerodynamic models given in Tables A.4-A.6 were collected in calm wind conditions; see Figures A.7-A.10. Additionally, three validation flights were conducted in the three wind conditions; see Figures A.11-A.13.

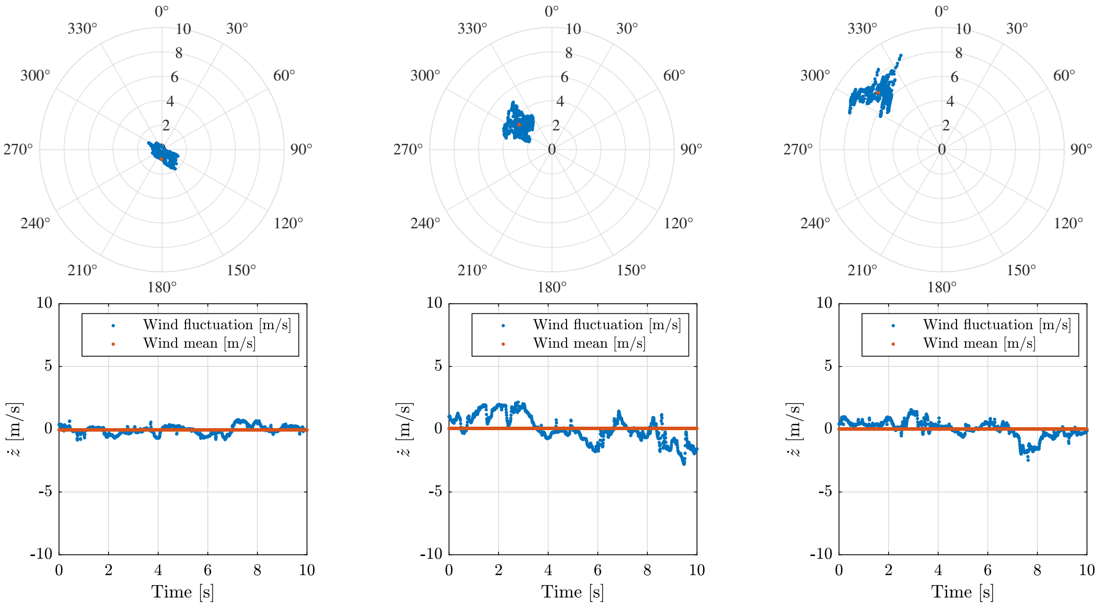

(a) Calm

(b) Light

(c) Severe

Figure A.6: Wind conditions for system identification training and validation flights from an Air Data Unit (ADU)

A.5 Results and Discussion

A.5.1 Quasi-steady Aerodynamic Parameters

Following the description from Section A.3.1, the aerodynamic longitudinal and lateral-directional force and moment coefficient equations acting on the aircraft can be expressed as:

$$C_X = C_{X_o} + C_{X_{\delta_{\mathrm{e}}}}\delta_{\mathrm{e}} + C_{X_\alpha}\alpha \tag{A.22a}$$

$$C_Z = C_{Z_o} + C_{Z_q}\hat{q} + (C_{Z_\alpha}\alpha + C_{Z_{\dot{\alpha}}}\hat{\dot{\alpha}})\mathcal{L}^{-1}\{\bar{C}_{Z_\alpha}(s)\} \tag{A.22b}$$

$$C_m = C_{m_o} + C_{m_{\delta_{\mathrm{e}}}}\delta_{\mathrm{e}} + C_{m_q}\hat{q} + (C_{m_\alpha}\alpha + C_{m_{\dot{\alpha}}}\hat{\dot{\alpha}})\mathcal{L}^{-1}\{\bar{C}_{m_\alpha}(s)\} \tag{A.22c}$$

$$C_Y = C_{Y_p}\hat{p} + C_{Y_r}\hat{r} + C_{Y_{\delta_{\mathrm{a}}}}\delta_{\mathrm{a}} + C_{Y_{\delta_{\mathrm{r}}}}\delta_{\mathrm{r}} + (C_{Y_\beta}\beta + C_{Y_{\dot{\beta}}}\hat{\dot{\beta}})\mathcal{L}^{-1}\{\bar{C}_{Y_\beta}(s)\} \tag{A.22d}$$

$$C_l = C_{l_p}\hat{p} + C_{l_{\delta_{\mathrm{a}}}}\delta_{\mathrm{a}} + (C_{l_\beta}\beta + C_{l_{\dot{\beta}}}\hat{\dot{\beta}})\bar{C}_{l_\beta}(s) \tag{A.22e}$$

$$C_n = C_{n_r}\hat{r} + C_{n_{\delta_{\mathrm{a}}}}\delta_{\mathrm{a}} + C_{n_{\delta_{\mathrm{r}}}}\delta_{\mathrm{r}} + C_{n_\beta}\beta \tag{A.22f}$$

Initially, only the quasi-steady parameters are identified, setting $\bar{C}_{Z_\alpha}(s) = 1$, $\bar{C}_{m_\alpha}(s) = 1$, $\bar{C}_{Y_\beta}(s) = 1$ and $\bar{C}_{l_\beta}(s) = 1$. Note that, the transfer functions $\bar{C}_{X_\alpha}(s)$ and $\bar{C}_{n_\beta}(s)$ are not in Eq. (A.22); because, $C_{X_{\dot{\alpha}}}$ and $C_{n_{\dot{\beta}}}$ were assessed to be insignificant during model structure determination.

Identified Quasi-steady Model

The identified quasi-steady parameters in Equations (A.22a)-(A.22f) are shown in Table A.4 and Table A.5. In these tables, $\hat{\theta}$ represents an estimate for the value of a given parameter value and σ represents the standard deviation in that estimate. Parameter estimation was accomplished with the output error method [4]. Parameter uncertainty estimates in Table A.4 and Table A.5 account for colored residuals [4]. The quasi-steady model is valid in the normal operating range, just prior to stall; it does not capture propulsion effects, as discussed in [107].

Table A.4: Quasi-steady model longitudinal parameter estimates

Term	$\hat{\theta} \pm \sigma$	Term	$\hat{\theta} \pm \sigma$	Term	$\hat{\theta} \pm \sigma$
C_{X_0}	+0.009 ± 0.026	C_{Z_0}	-0.255 ± 0.074	C_{m_0}	+0.008 ± 0.006
C_{X_α}	+0.282 ± 0.000	C_{Z_α}	-4.436 ± 0.015	C_{m_α}	-0.444 ± 0.027
$C_{X_{\delta e}}$	+0.051 ± 0.025	C_{Z_q}	-12.540 ± 0.030	C_{m_q}	-14.019 ± 3.363
		$C_{Z_{\dot{\alpha}}}$	+4.614 ± 0.034	$C_{m_{\delta e}}$	-0.415 ± 0.058
				$C_{m_{\dot{\alpha}}}$	+0.514 ± 0.036

Table A.5: Quasi-steady model lateral-directional parameter estimates

Term	$\hat{\theta} \pm \sigma$	Term	$\hat{\theta} \pm \sigma$	Term	$\hat{\theta} \pm \sigma$
C_{Y_β}	-0.410 ± 0.115	C_{l_β}	-0.035 ± 0.004	C_{n_β}	+0.083 ± 0.020
C_{Y_p}	+0.221 ± 0.133	C_{l_p}	-0.386 ± 0.041	C_{n_r}	-0.119 ± 0.029
C_{Y_r}	+0.230 ± 0.547	$C_{l_{\delta_a}}$	-0.137 ± 0.010	$C_{n_{\delta_a}}$	+0.013 ± 0.009
$C_{Y_{\delta_a}}$	+0.118 ± 0.011	$C_{l_{\dot{\beta}}}$	-0.079 ± 0.042	$C_{n_{\delta_r}}$	-0.068 ± 0.006
$C_{Y_{\delta_r}}$	+0.136 ± 0.030				
$C_{Y_{\dot{\beta}}}$	+0.041 ± 0.533				

Quasi-steady Model Validation Results

Quasi-steady model validation flight data were collected with an automated elevator doublet to characterize pitching motion and a rudder doublet followed by aileron 1-2-1 maneuver to characterize lateral-directional motion. A comparison of the quasi-steady model predictions to the validation flight data is shown in Figure A.7 and Figure A.8. The model predictions show good matching to the validation flight data.

A.5.2 Unsteady Aerodynamic Parameters

Unsteady Model Training Data

The estimation of the parameters in the empirical transfer functions was accomplished based on the approach described in Section A.3.2 with MATLAB®'s System Identification toolbox. The training data used to identify the parameters were based on an AGG flight maneuver

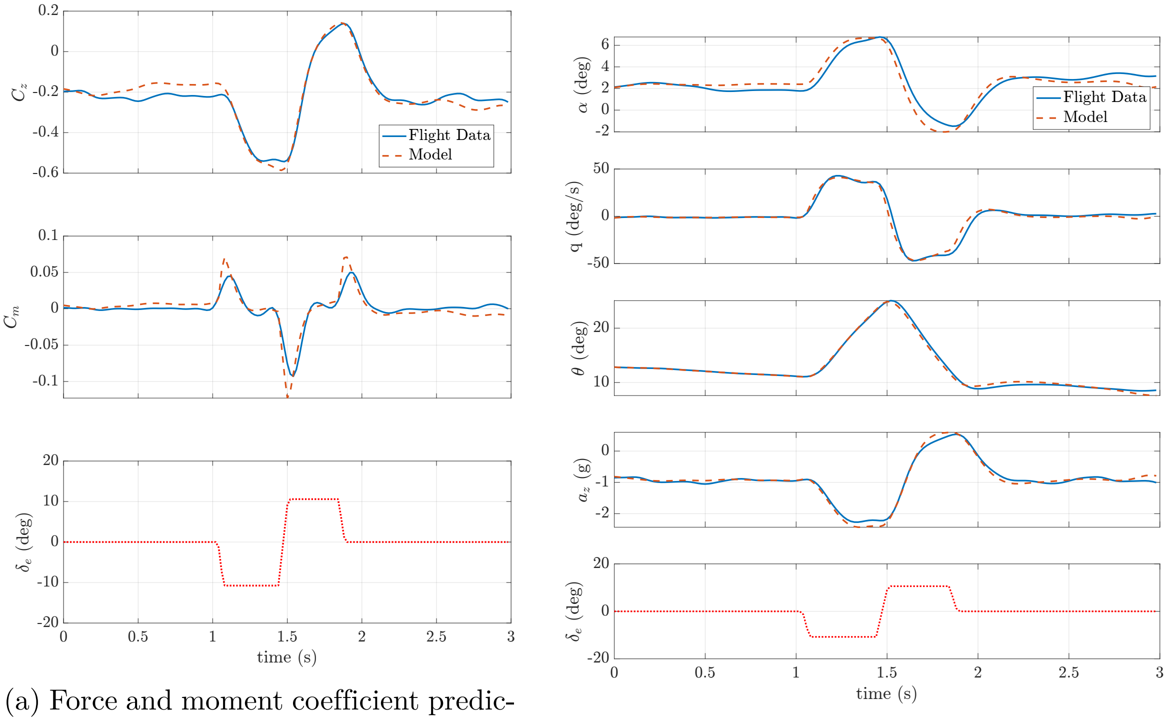

(a) Force and moment coefficient prediction

(b) Output prediction

Figure A.7: Validation results for the quasi-steady model for an elevator doublet maneuver in calm air.

described in Section A.4.1. The empirical transfer functions are identified after the quasi-steady parameters are estimated. In Figure A.9a, the angle of attack and sideslip values after the AGG values are superimposed are shown; these values are used to determine the quasi-steady aerodynamic coefficients ($C_{(\cdot)}^{\mathrm{QS}}$). In Figure A.9b, the circulatory aerodynamic coefficients ($C_{(\cdot)}^{\mathrm{circ}}$) and the quasi-steady aerodynamic coefficients ($C_{(\cdot)}^{\mathrm{QS}}$), which are the outputs and inputs to the empirical transfer functions described by Eq. (A.16), are shown. The roll moment coefficient ($C_l(t)$) shows very little response to an AGG pass. As a result, the unsteady effects in $C_l(t)$ were small enough to ignore; hence, $\bar{C}_{l_\beta}(s) = 1$. Based on the training flight data, shown in Figure A.9b, the parameters in the empirical transfer functions $\bar{C}_{Z_\alpha}(s)$, $\bar{C}_{Y_\beta}(s)$, and $\bar{C}_{m_{\alpha(s)}}$ were identified and given Table A.6; additionally, the realizations of the empirical transfer functions are given in Table A.7.

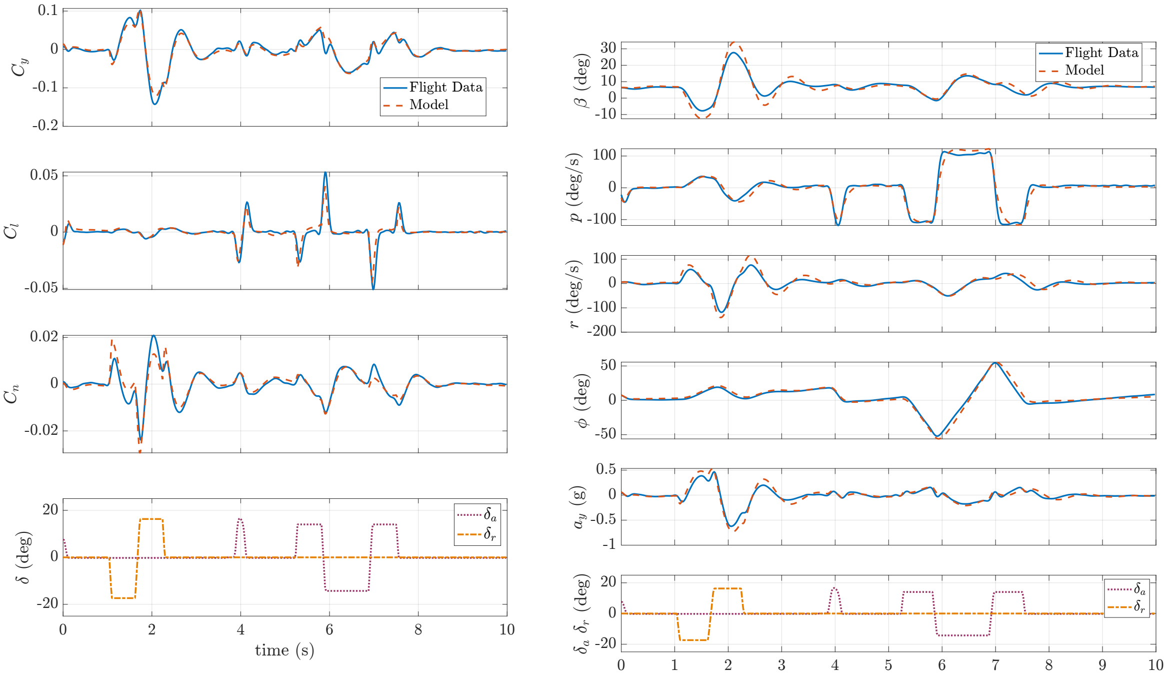

(a) Force and moment coefficient prediction

(b) Output prediction

Figure A.8: Validation results for the quasi-steady model for a rudder doublet, then aileron 1-2-1 maneuver.

Table A.6: Identified empirical rational transfer functions

$\bar{C}_{Y_\beta}(s)$:	$\dfrac{b_0 s^3 + b_1 s^2 + b_2 s + b_3}{a_0 s^3 + a_1 s^2 + a_2 s + a_3}$	$\bar{C}_{Z_\alpha}(s)$:	$\dfrac{b_0 s + b_1}{a_0 s + a_1}$	$\bar{C}_{m_\alpha}(s)$:	$\dfrac{b_0 s^2 + b_1 s + b_2}{a_0 s^2 + a_1 s + a_2}$
Term	$\hat{\theta} \pm \sigma$	Term	$\hat{\theta} \pm \sigma$	Term	$\hat{\theta} \pm \sigma$
b_0	$+0.19 \pm 0.17$	b_0	$+0.40 \pm 0.06$	b_0	$+0.02 \pm 0.10$
b_1	$+50.03 \pm 26.68$	b_1	$+51.78 \pm 55.58$	b_1	-41.18 ± 10.03
b_2	-3228 ± 1162	a_0	1	b_2	$+6663 \pm 750$
b_3	$+1.28e05 \pm 4.50e04$	a_1	$+99.16 \pm 112.3$	a_0	1
a_0	1			a_1	$+18.88 \pm 2.50$
a_1	$+54.34 \pm 18.34$			a_2	$+7666 \pm 229$
a_2	$+7237 \pm 795$				
a_3	$+1.94e05 \pm 9.11e04$				

Root Mean Square Error

In Sections A.5.2 and A.5.3, the root mean square error (RMSE) between the ”measured” and the predicted ”quasi-steady” and ”unsteady” aerodynamic coefficients are given. The

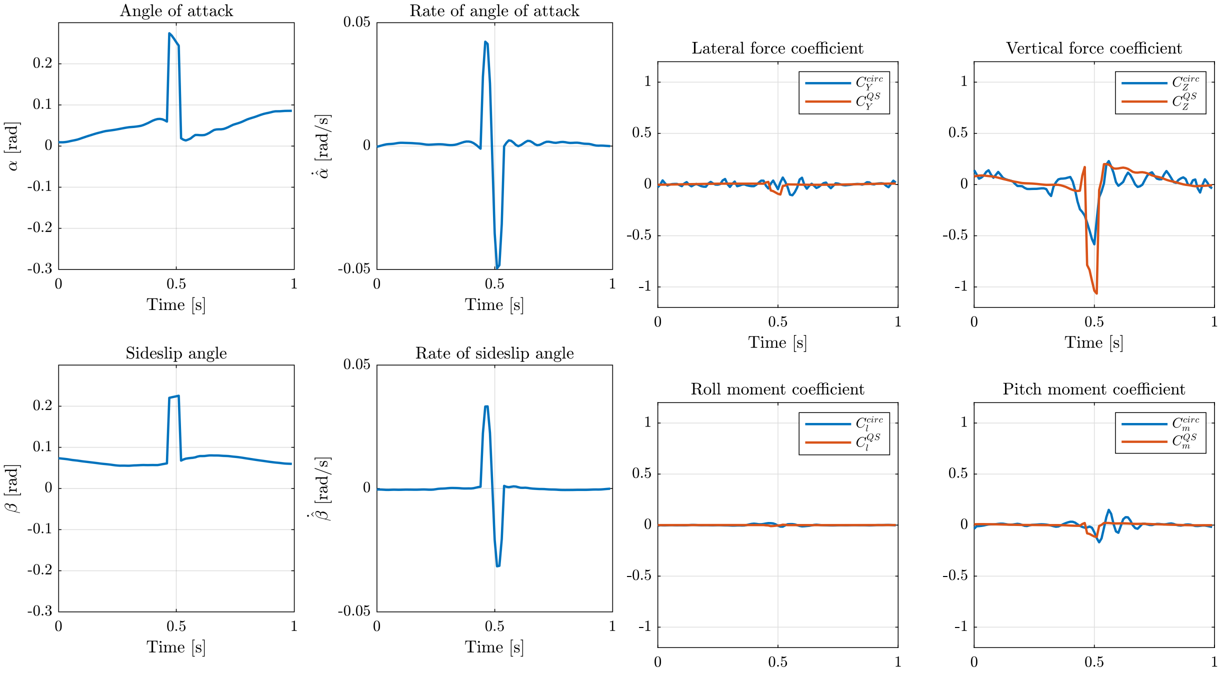

(a) Air data values after AGG velocities are superimposed

(b) Training data from an AGG flight

Figure A.9: Unsteady dynamic model system identification training data

Table A.7: Identified empirical rational transfer functions and the state-space representation

Aerodynamic parameters	Empirical rational transfer functions	State-space realization, $\left[\begin{array}{c\|c} \bar{\boldsymbol{A}} & \bar{\boldsymbol{B}} \\ \hline \bar{\boldsymbol{C}} & \bar{D} \end{array}\right]$
$\bar{C}_{Y_\beta}(s)$	$\dfrac{0.19s^3 + 50.03s^2 - 3228s + 1.28e05}{s^3 + 54.34s^2 + 7237s + 1.94e05}$	$\left[\begin{array}{ccc\|c} -54.34 & -7237 & -1.94 & 1 \\ 1 & 0 & 0 & 0 \\ 0 & 1 & 0 & 0 \\ \hline 40.00 & -4564 & 9.21e04 & 0.18 \end{array}\right]$
$\bar{C}_{Z_\alpha}(s)$	$\dfrac{0.40s + 51.78}{s + 99.16}$	$\left[\begin{array}{c\|c} -99.16 & 1 \\ \hline 12.24 & 0.40 \end{array}\right]$
$\bar{C}_{m_\alpha}(s)$	$\dfrac{0.02s^2 - 41.18s + 6663}{s^2 + 18.88s + 7666}$	$\left[\begin{array}{cc\|c} -18.88 & -7666 & 1 \\ 1 & 0 & 0 \\ \hline -41.48 & 6540 & 0.02 \end{array}\right]$

”measured” values are calculated using Eq. (A.20). The ”unsteady” model predictions are calculated using Eq. (A.22), and the ”quasi-steady” model predictions are calculated using Eq. (A.22) without the transfer function. The RMSEs from different validation flights are given in Figures A.10-A.13. All RMSE values are calculated with respect to the measured aerodynamic coefficients as follows:

$$\mathrm{RMSE}_{\mathrm{QS}} = \sqrt{\frac{1}{N}\sum_{i=1}^{N}\left(C_{(\cdot)}(t)_i^{\text{quasi-steady}} - C_{(\cdot)}(t)_i^{\text{measured}}\right)^2} \tag{A.23a}$$

$$\mathrm{RMSE}_{\mathrm{US}} = \sqrt{\frac{1}{N}\sum_{i=1}^{N}\left(C_{(\cdot)}(t)_i^{\text{unsteady}} - C_{(\cdot)}(t)_i^{\text{measured}}\right)^2} \tag{A.23b}$$

where N is the number of available data points, and $(\cdot)$ is either Z, Y, or m.

Unsteady Model Validation Result

A validation flight from an AGG pass was conducted to validate the unsteady aerodynamic force and moment models. The data collected were then used to compare the ”quasi-steady” and ”unsteady” model predictions to ”measured” values; see Figure A.10.

The results shown in Figure A.10 show that the unsteady aerodynamic models predict the forces and moment generated due to a sudden strong gust that perturbed the sUAS’s motion better than quasi-steady aerodynamic models. Note, for example, that the negative peak in the unsteady vertical force coefficient exhibits a slight delay and amplitude reduction relative to the quasisteady force coefficient. Furthermore, the RMSE values of the unsteady aerodynamic model, given in Figure A.10, are lower than the RMSE values of the quasi-steady aerodynamic model. As a result, we can conclude that the unsteady aerodynamic model captures the unsteady effect of the sharp vertical gust better than the quasi-steady aerodynamic model.

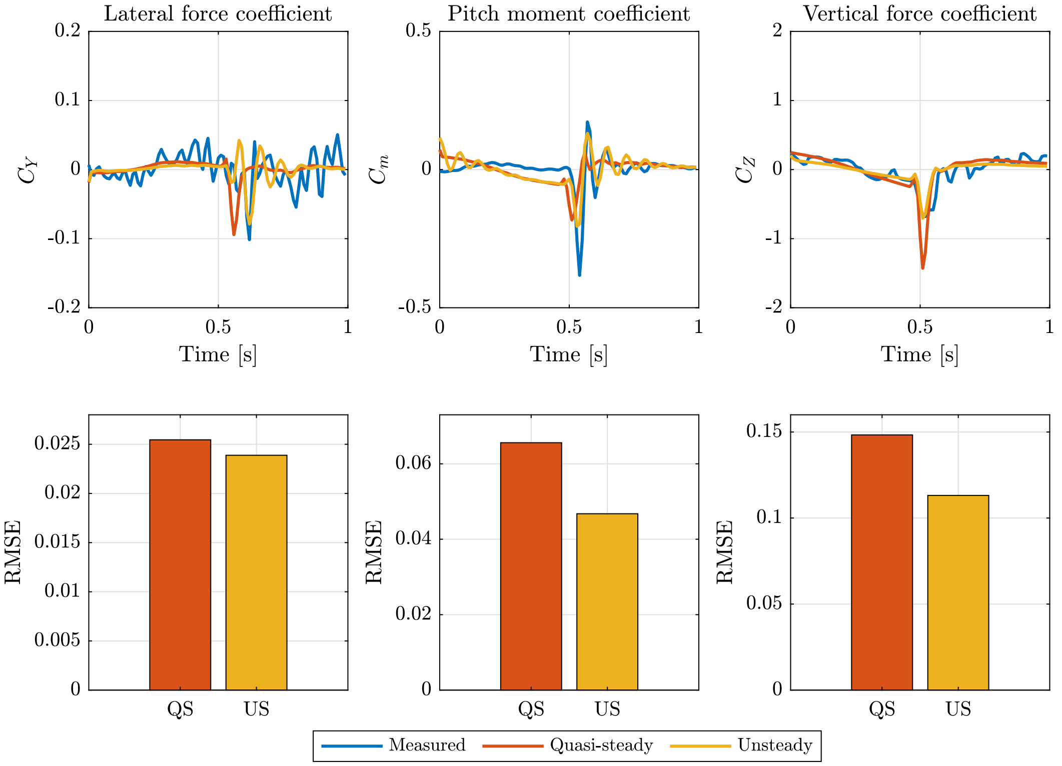

Figure A.10: Validation flight from an AGG pass

A.5.3 Quasi-Steady and Unsteady Aerodynamic Model Predictions in Natural Wind

Three additional validation flights were conducted in different wind conditions as a preliminary step toward the motivating application of model-based wind estimation.

In each flight, the aircraft was flown straight and level at a constant altitude. The data collected were then used to compare the ”quasi-steady” and ”unsteady” model predictions to ”measured” values, see Figures A.11-A.13. The results shown in Figures A.11-A.13 indicate that the RMSE values of the unsteady aerodynamic model are lower than the RMSE values of the quasi-steady aerodynamic model in all three wind conditions. Note that the model-based force and moment coefficients in Figure A.11 exhibit some trends that are

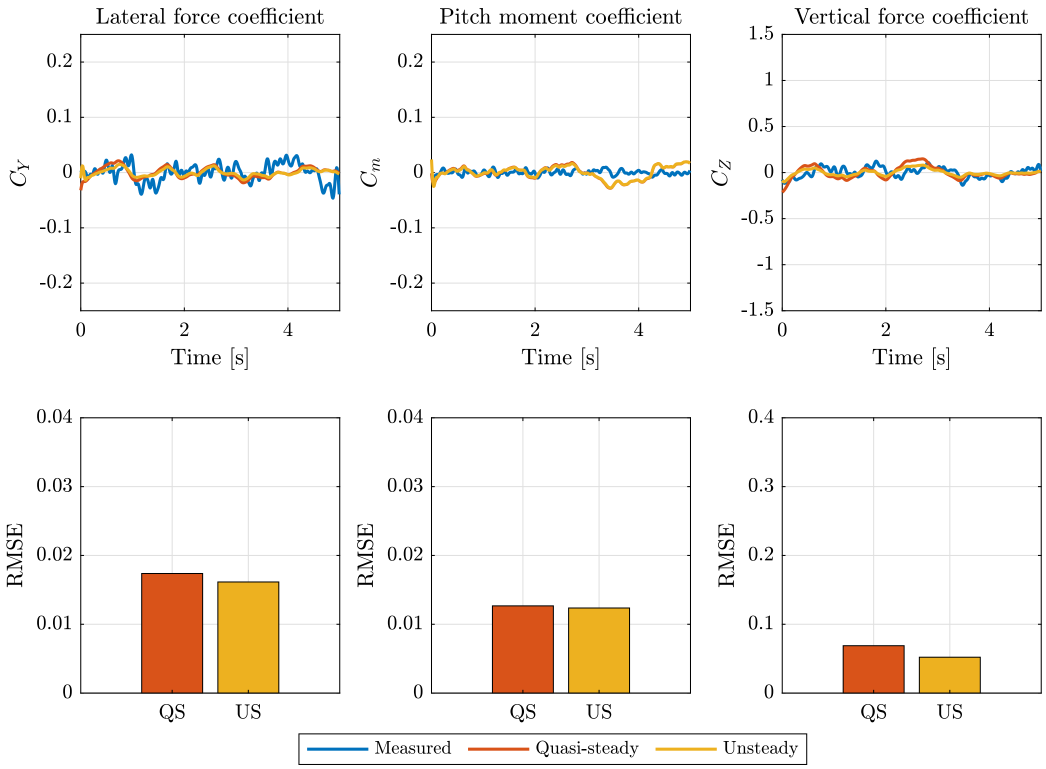

Figure A.11: Validation flight in calm winds

not reflected in the measurements. These disparities increase with increasing wind strength. These disparities may arise from the lack of a thrust model; thrust varies significantly in strongly varying winds. The disparities may also arise from the build-up approach used for modeling and parameter identification, in which quasi-steady terms were selected, and their parameters estimated, before moving on to estimate the unsteady parameters.

Summarizing the results, unsteady corrections to a quasi-steady flight dynamic model were obtained using sharp aerodynamic angle excitations from an artificial gust generator. The unsteady model was validated using data from independent passes of the aircraft through the AGG disturbance. While the flight dynamic models give plausible estimates of the disturbance force and moment due to wind fluctuations in calm wind, stronger wind conditions reveal that the models do not accurately capture the disturbances, though the unsteady

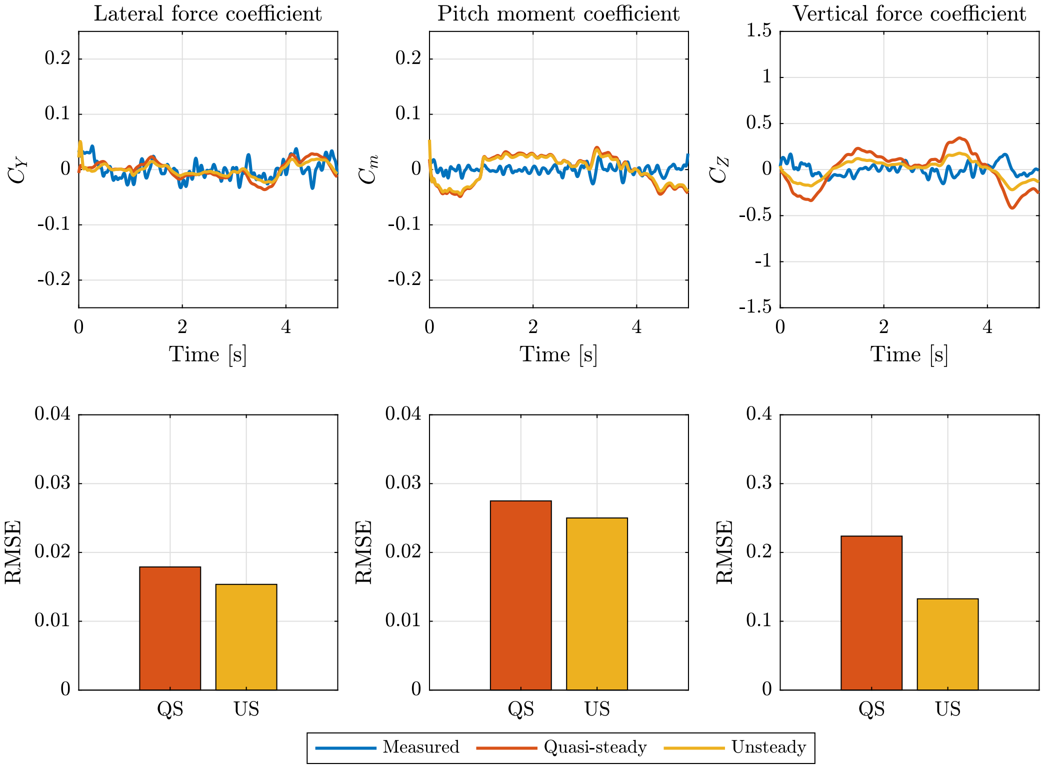

Figure A.12: Validation flight in light winds

model performs a little less poorly than the quasi-steady model in terms of RMSE.

A.6 Conclusion

After validating a baseline quasi-steady aerodynamic model for the longitudinal and lateral-directional forces and moments acting on a particular small fixed-wing uncrewed aircraft, an unsteady motion model was developed and validated. The unsteady aerodynamics are represented by state-space realizations of empirical transfer functions that were obtained from flight test data involving overflights of an artificial gust generator. These transfer functions correct force and moment contributions indicated by a quasi-steady model developed separately. In independently obtained validation data from the gust generator, the side

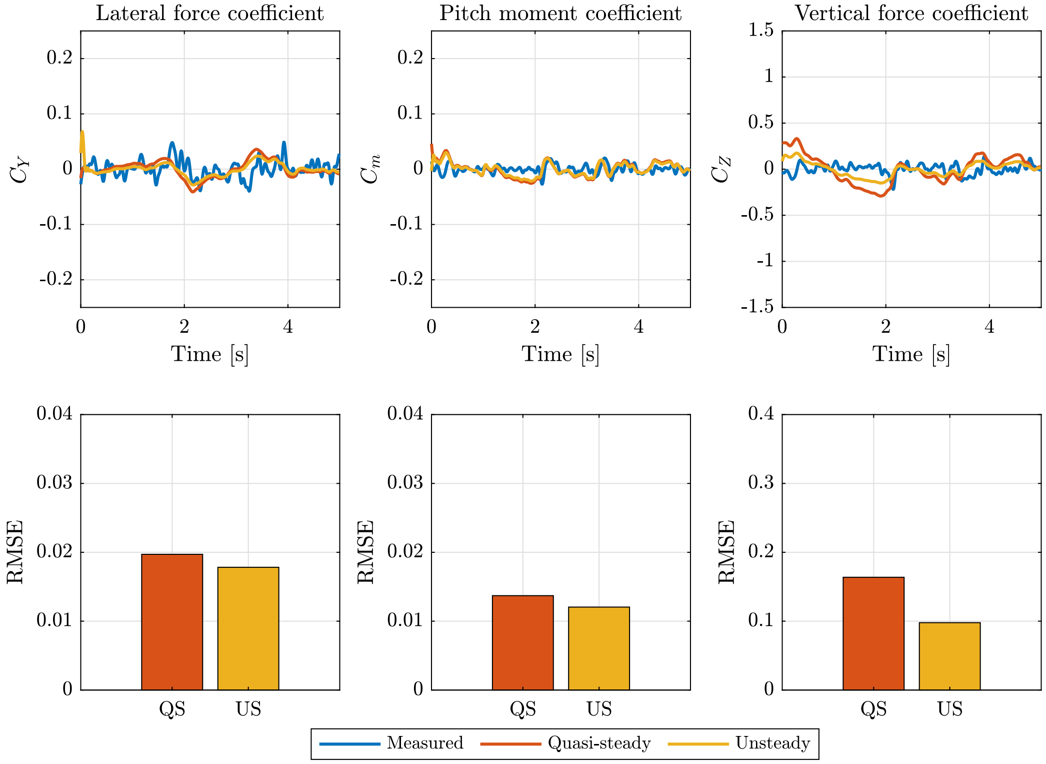

Figure A.13: Validation flight in severe conditions

force due to sideslip angle and the lift force and pitch moment due to angle of attack were found to differ substantially from quasi-steady predictions in ways that are well captured by the unsteady model. Quasi-steady and unsteady model predictions of force and moment were also computed using separate validation data obtained in calm, light, and severe wind conditions. The unsteady aerodynamic model predictions modestly outperformed the quasi-steady model predictions, but neither model performs well, which is especially evident as the wind conditions degrade from calm to severe. The relatively poor predictive performance of the models in natural wind may owe to the lack of a thrust model, to the build-up approach from quasi-steady to unsteady modeling, or to both.

Appendix B

Kalman Filter, Extended Kalman Filter, and Unscented Kalman Filter Algorithms

The following algorithms were utilized in this dissertation: the Kalman filter, extended Kalman filter, and unscented Kalman filter. A summary of these algorithms is provided here, while detailed explanations of their implementation can be found in Chapters 6 and 7. The discrete Kalman filter's algorithm is summarized in Table B.1. The continuous-discrete (hybrid) extended Kalman filter is summarized in Table B.2. Finally, the continuous-discrete (hybrid) unscented Kalman filter is summarized in Table B.3.

Table B.1: Discrete Kalman filter algorithm

Step 1: Initialization
Start with $\hat{\boldsymbol{x}}(t_0)$, and $\boldsymbol{P}(t_0)$
Set $t_k = 0$
Step 2: Dynamic propagation from sample t_k to t_{k+1}
$\bar{\boldsymbol{x}}(t_{k+1}) = \boldsymbol{F}\hat{\boldsymbol{x}}(t_k) + \boldsymbol{G}\boldsymbol{u}(t_k)$
$\bar{\boldsymbol{P}}(t_{k+1}) = \boldsymbol{F}\boldsymbol{P}(t_k)\boldsymbol{F}^{\mathrm{T}} + \boldsymbol{\Gamma}\boldsymbol{Q}\boldsymbol{\Gamma}^T$
Step 3: Measurement update at sample t_{k+1}
$\boldsymbol{\nu}(t_{k+1}) = \boldsymbol{z}(t_{k+1}) - \boldsymbol{H}\bar{\boldsymbol{x}}(t_{k+1})$
$\boldsymbol{S}(t_{k+1}) = \boldsymbol{H}(t_{k+1})\bar{\boldsymbol{P}}(t_{k+1})\boldsymbol{H}^T + \boldsymbol{R}(t_{k+1})$
$\boldsymbol{W}(t_{k+1}) = \bar{\boldsymbol{P}}(t_{k+1})\boldsymbol{H}^T\boldsymbol{S}^{-1}(t_{k+1})$
$\hat{\boldsymbol{x}}(t_{k+1}) = \bar{\boldsymbol{x}}(t_{k+1}) + \boldsymbol{W}(t_{k+1})\boldsymbol{\nu}(t_{k+1})$
$\boldsymbol{P}(t_{k+1}) = \bar{\boldsymbol{P}}(t_{k+1}) - \boldsymbol{W}(t_{k+1})\boldsymbol{S}(t_{k+1})\boldsymbol{W}^T(t_{k+1})$
Step 4: Replace t_k with t_{k+1} and return to Step 2

Table B.2: Continuous-discrete (hybrid) extended Kalman filter algorithm

Step 1: Initialization
Start with $\hat{\boldsymbol{x}}(t_0)$, and $\boldsymbol{P}(t_0)$
Set $t_k = 0$
Step 2: Dynamic propagation from sample t_k to sample t_{k+1}
$\bar{\boldsymbol{x}}(t_{k+1}) = \hat{\boldsymbol{x}}(t_k) + \int_{t_k}^{t_{k+1}} \boldsymbol{f}\left(\tau, \hat{\boldsymbol{x}}(\tau), \boldsymbol{\delta}(\tau)\right) d\tau$
$\boldsymbol{A}(t) = \frac{\partial \boldsymbol{f}}{\partial \boldsymbol{x}}\Big\vert_{[t,\hat{\boldsymbol{x}}(t),\boldsymbol{\delta}(t)]}$
$\bar{\boldsymbol{P}}(t_{k+1}) = \boldsymbol{P}(t_k) + \int_{t_k}^{t_{k+1}} \big(\boldsymbol{P}(\tau)\boldsymbol{A}(\tau) + \boldsymbol{A}^{\mathrm{T}}(\tau)\boldsymbol{P}(\tau) + \boldsymbol{Q}\big)\, d\tau$
Step 3: Measurement update at sample t_{k+1}
$\bar{\boldsymbol{z}}(t_{k+1}) = \boldsymbol{h}(t_{k+1}, \bar{\boldsymbol{x}}(t_{k+1}))$
$\boldsymbol{H} = \frac{\partial \boldsymbol{h}}{\partial \boldsymbol{x}(t_{k+1})}\bigg\vert_{[t_{k+1},\bar{\boldsymbol{x}}(t_{k+1})]}$
$\boldsymbol{\nu}(t_{k+1}) = \boldsymbol{z}(t_{k+1}) - \bar{\boldsymbol{z}}(t_{k+1})$
$\boldsymbol{S}(t_{k+1}) = \boldsymbol{H}\bar{\boldsymbol{P}}(t_{k+1})\boldsymbol{H}^T + \boldsymbol{R}(t_{k+1})$
$\boldsymbol{W}(t_{k+1}) = \bar{\boldsymbol{P}}(t_{k+1})\boldsymbol{H}^T\boldsymbol{S}^{-1}(t_{k+1})$
$\hat{\boldsymbol{x}}(t_{k+1}) = \bar{\boldsymbol{x}}(t_{k+1}) + \boldsymbol{W}(t_{k+1})\boldsymbol{\nu}(t_{k+1})$
$\boldsymbol{P}(t_{k+1}) = \bar{\boldsymbol{P}}(t_{k+1}) - \boldsymbol{W}(t_{k+1})\boldsymbol{S}(t_{k+1})\boldsymbol{W}^T(t_{k+1})$
Step 4: Replace t_k with t_{k+1} and return to Step 2

Table B.3: Continuous-discrete (hybrid) unscented Kalman filter algorithm

Step 1: Initialization Start with $\hat{\boldsymbol{x}}(t_0)$, and $\boldsymbol{P}(t_0)$
Step 2: Calculate $2(n+q)+1$ sigma points Set $\bar{\boldsymbol{x}} = \boldsymbol{x}_k$, $\boldsymbol{P}_{xx} = \boldsymbol{P}_k$, and $\boldsymbol{Q} = \boldsymbol{Q}(k)$ Set $n = \dim(\boldsymbol{x})$, $p = \dim(\boldsymbol{z})$, and $q = \dim(\tilde{\boldsymbol{w}})$ Set $\lambda = \alpha^2(n+q) - (n+q)\alpha$, typically $10^{-4} < \alpha < 1$ $\boldsymbol{\chi}_0 = \bar{\boldsymbol{x}}$ $\boldsymbol{\chi}_i = \bar{\boldsymbol{x}} + \sqrt{(n+p+q+\lambda)\boldsymbol{P}_{xx}}, \quad i = 1, \ldots, n$ $\boldsymbol{\chi}_i = \bar{\boldsymbol{x}} - \sqrt{(n+p+q+\lambda)\boldsymbol{P}_{xx}}, \quad i = n+1, \ldots, 2n$ $\boldsymbol{\chi}_i = \bar{\boldsymbol{x}}, \quad i = 2n+1, \ldots, 2n+2q$ $\boldsymbol{\chi}_i^w = \boldsymbol{0}, \quad i = 0, \ldots, 2n$ $\boldsymbol{\chi}_i^w = \sqrt{(n+p+q+\lambda)\boldsymbol{Q}(k)}, \quad i = 2n+1, \ldots, 2n+q$ $\boldsymbol{\chi}_i^w = -\sqrt{(n+p+q+\lambda)\boldsymbol{Q}(k)}, \quad i = 2n+q+1, \ldots, 2n+2q$
Step 3: Calculate the weights Set $\beta = 2$ for a Gaussian distribution $\boldsymbol{W}_0^m = \frac{\lambda}{n+q+\lambda}$ $\boldsymbol{W}_0^c = \frac{\lambda}{n+q+\lambda} + 1 - \alpha^2 + \beta$ $\boldsymbol{W}_i^m = \boldsymbol{W}_i^c = \frac{1}{2(\lambda+n+q)}, \quad i = 1, \ldots, 2n+2q$
Step 4: Dynamic propagation from sample t_k to t_{k+1} $\boldsymbol{\chi}(k+1) = \boldsymbol{f}(\boldsymbol{\chi}(k), \boldsymbol{u}(k), \boldsymbol{\chi}^w(k))$ $\bar{\boldsymbol{x}}(k+1) = \sum_{j=0}^{2(n+p)} \boldsymbol{W}_j^m \boldsymbol{\chi}(k+1)$ $\boldsymbol{\zeta}(k+1) = \boldsymbol{h}(\boldsymbol{\chi}(k), \boldsymbol{u}(k))$ $\bar{\boldsymbol{z}}(k+1) = \sum_{j=0}^{2(n+p)} \boldsymbol{W}_j^m \boldsymbol{\zeta}(k+1)$ $\boldsymbol{P}(k+1) = \sum_{j=0}^{2(n+q)} \boldsymbol{W}_j^c \left[\boldsymbol{\chi}_j(k+1) - \hat{\boldsymbol{x}}(k+1)\right] \left[\boldsymbol{\chi}_j(k+1) - \hat{\boldsymbol{x}}(k+1)\right]^T$ $\boldsymbol{P}_{xz}(k+1) = \sum_{j=0}^{2(n+q)} \boldsymbol{W}_j^c \left[\boldsymbol{\chi}_j(k+1) - \hat{\boldsymbol{x}}(k+1)\right] \left[\boldsymbol{\zeta}_j(k+1) - \hat{\boldsymbol{z}}(k+1\right]^T$ $\boldsymbol{P}_{zz}(k+1) = \sum_{j=0}^{2(n+q)} \boldsymbol{W}_j^c \left[\boldsymbol{\zeta}_j(k+1) - \hat{\boldsymbol{z}}(k+1)\right] \left[\boldsymbol{\zeta}_j(k+1) - \hat{\boldsymbol{z}}(k+1)\right]^T$
Step 5: Measurement update at sample t_{k+1} $\hat{\boldsymbol{x}}(k+1) = \bar{\boldsymbol{x}}(k+1) + \boldsymbol{P}_{xz}(k+1)\boldsymbol{P}_{zz}^{-1}(k+1)\left[\boldsymbol{z}(k+1) - \bar{\boldsymbol{z}}(k+1)\right]$ $\boldsymbol{P}(k+1) = \boldsymbol{P}(k+1) - \boldsymbol{P}_{xz}(k+1)\boldsymbol{P}_{zz}^{-1}(k+1)\boldsymbol{P}_{xz}^T(k+1)$
Step 6: Replace t_k with t_{k+1} and return to Step 4

Appendix C

MTD sUAS Flight Checklist

PREFLIGHT BRIEF

1. TIME HACK
2. ROLL CALL
3. ENVIRONMENT (WX, NOTAMS)
4. SYSTEM STATUS (AV, GS, DATA)
5. MISSION BRIEF
    a. OBJECTIVES
    b. POST-FLIGHT REQS
6. RISK MANAGEMENT & CRM
7. EP of the DAY

PRE-FLIGHT

BATTERIES	PLUGGED & SECURED
HATCHES	SECURED
CAMERA	SECURED
ADU VANES	INSPECTED
CONTROL HINGES	INSPECTED
PROPELLER	INSPECTED
MOTOR	SECURED, SPIN
TX RADIO POWER	ON, BATT CHECKED
TX RADIO CONNECTION	VERIFIED
GROUND STATION	ON
TELEM CONNECTION	VERIFIED
COMPASS CALIBRATION	AS REQ
PITOT TUBE CALIBRATION	AS REQ
GPS LOCK	VERIFIED
AUTO MISSION	VERIFIED
RTH LOCATION	VERIFIED
BATT FAILSAFE	VERIFIED
RTH FAILSAFE	VERIFIED
TX RADIO FAILSAFE	VERIFIED
BATTERY LEVELS	CHECKED
CONTROLS	CHECKED (ALL FLT MODES)

BEFORE TAKEOFF

CAMERA	ON
STROBE LIGHT	ON
THROTTLE	CHECKED (50%)
FLIGHT MODE	AS REQ
RWY/FLIGHT PATH	CLEAR
THROTTLE	0%
MOTOR	ARMED
ROLL CALL	GO / NO-GO

TAKEOFF

THROTTLE	*SMOOTHLY TO* ≈ 75%
FLY	*SAFE ALT & DIST*
CONTROLLABILITY	CHECK
TELEMETRY	VERIFIED

LANDING

FLIGHT MODE	AS REQ
RWY / FLIGHT PATH	CLEAR
WIND SPD & DIR	CHECKED
APPROACH SPEED	≈ *30 KIAS*

AFTER LANDING

MOTORS	DISARMED
TIME	RECORDED
GCS DATA	CAPTURED
CAMERA	OFF
STROBE LIGHT	OFF
BATTERIES PLUG	UNPLUGGED
TX RADIO	OFF
BATTERIES	REMOVED

POST FLIGHT

FLIGHT PLAN	CLOSED
FLIGHT LOG	COMPLETED
DATA LOGS	DOWNLOADED
VIDEO	DOWNLOADED
BATTERIES	BALANCED / STORED

GCS LINK LOSS

GCS ANT ORIENTATION .... VERIFIED
GCS ANT CONNECTION......... RECONNECTED
TELEMETRY.................................. MONITOR

LINK NOT RESTORED

AIRCRAFT................................ RTB (AS REQ)

LINK RESTORED

TELEMETRY.................................... VERIFIED

TX LINK LOSS

TX ORIENTATION .... ADJUSTED
TX POWER......................... CYCLED (AS REQ)

GPS LOSS

MODE SWITCH............................STABILIZED
AIRCRAFT................................ RTB (AS REQ)

PROPULSION LOSS

MODE SWITCH............................STABILIZED
THROTTLE .... 0% FOR 3 SEC, THEN 50%

PROPULSION NOT RESTORED

AIRCRAFT .... LAND AS SOON AS POSSIBLE

PROPULSION RESTORED

AIRCRAFT ...LAND AS SOON AS PRACTICABLE

CONTROLLABILITY LOSS

MODE SWITCH............................... MANUAL
CONTROLLABILITY CHECK......... PERFORMED

CONTROLLABILTY NOT AS EXPECTED

AIRCRAFT .... LAND AS SOON AS POSSIBLE

CONTROLLABILTY AS EXPECTED

AIRCRAFT ...LAND AS SOON AS PRACTICABLE

FLY AWAY CTAF OR ATC ALERT PROTOCOL

Towards and on VT Blacksburg (BCB) CTAF

Virginia Tech traffic UAS ground operator be advised lost link unmanned aircraft 10 miles west of Virginia tech airport 400 feet AGL heading ---- (East ---).

Towards and on New River Valley (PSK) CTAF

New river traffic UAS ground operator be advised lost link unmanned aircraft 5 miles east of new river valley airport 400 feet AGL heading ----- (West ---).

Bibliography

[1] J. Jacob, P. B. Chilson, A. L. Houston, J. O. Pinto, and S. Smith, "Real-time Weather Awareness for Enhanced Advanced Aerial Mobility Safety Assurance," in *AGU Fall Meeting 2020*, pp. A021–03, AGU, Dec. 2020.

[2] J. Jacob, "NASA TechPort - Project Data," 2020.

[3] A. Gelb, J. F. Kasper, R. A. Nash, C. F. Price, and A. A. Sutherland, *Applied Optimal Estimation*. MIT Press, May 1974.

[4] E. A. Morelli and V. Klein, *Aircraft System Identification: Theory and Practice*. Sunflyte Enterprises Williamsburg, VA, 2016.

[5] R. V. Jategaonkar, *Flight Vehicle System Identification: A Time Domain Methodology*. American Institute of Aeronautics and Astronautics, 2015.

[6] B. M. Simmons, J. L. Gresham, and C. A. Woolsey, "Flight-test system identification techniques and applications for small, low-cost, fixed-wing aircraft," *Journal of Aircraft*, vol. 60, pp. 1503–1521, Sept. 2023. Publisher: American Institute of Aeronautics and Astronautics.

[7] D. N. Axford, "On the accuracy of wind measurements using an inertial platform in an aircraft, and an example of a measurement of the vertical mesostructure of the atmosphere," *Journal of Applied Meteorology and Climatology*, vol. 7, pp. 645–666, Aug. 1968. Publisher: American Meteorological Society Section: Journal of Applied Meteorology and Climatology.

[8] K. Anderson and K. J. Gaston, “Lightweight unmanned aerial vehicles will revolutionize spatial ecology,” *Frontiers in Ecology and the Environment*, vol. 11, no. 3, pp. 138–146, 2013. _eprint: https://onlinelibrary.wiley.com/doi/pdf/10.1890/120150.

[9] S. W. Smith, P. B. Chilson, A. L. Houston, and J. D. Jacob, “Catalyzing Collaboration for Multi-Disciplinary UAS Development with a Flight Campaign Focussed on Meteorology and Atmospheric Physics,” in *AIAA Information Systems-AIAA Infotech @ Aerospace*, AIAA SciTech Forum, p. 1156, American Institute of Aeronautics and Astronautics, Jan. 2017.

[10] J. W. Langelaan, J. Spletzer, C. Montella, and J. Grenestedt, “Wind Field Estimation for Autonomous Dynamic Soaring,” in *2012 IEEE International Conference on Robotics and Automation*, pp. 16–22, May 2012. ISSN: 1050-4729.

[11] F. A. P. Lie and D. Gebre-Egziabher, “Synthetic air data system,” *Journal of Aircraft*, vol. 50, pp. 1234–1249, July 2013. Publisher: American Institute of Aeronautics and Astronautics.

[12] T. Larrabee, H. Chao, M. Rhudy, Y. Gu, and M. R. Napolitano, “Wind Field Estimation in UAV Formation Flight,” in *2014 American Control Conference*, pp. 5408–5413, June 2014. ISSN: 2378-5861.

[13] R. E. Kalman, “A New approach to linear filtering and prediction problems,” *Journal of Basic Engineering*, vol. 82, pp. 35–45, Mar. 1960.

[14] Y. Bar-Shalom, X. R. Li, and T. Kirubarajan, *Estimation with Applications to Tracking and Navigation: Theory Algorithms and Software.* John Wiley & Sons, Apr. 2004.

[15] E. Wan and R. Van Der Merwe, “The Unscented Kalman filter for Nonlinear Es-

timation," in *Proceedings of the IEEE 2000 Adaptive Systems for Signal Processing, Communications, and Control Symposium (Cat. No.00EX373)*, pp. 153–158, Oct. 2000.

[16] M. Tobak and L. B. Schiff, "On the formulation of the aerodynamic characteristics in aircraft dynamics," Jan. 1976. NTRS Author Affiliations: NASA Ames Research Center NTRS Meeting Information: Aircraft Stability and Control; 1975-05-12 to 1975-05-16; undefined NTRS Document ID: 19760007994 NTRS Research Center: Legacy CDMS (CDMS).

[17] S. L. Brunton and C. W. Rowley, "Empirical state-space representations for Theodorsen's lift model," *Journal of Fluids and Structures*, vol. 38, pp. 174–186, Apr. 2013.

[18] J. A. Grauer, E. A. Morelli, and D. G. Murri, "Flight-test techniques for quantifying pitch rate and angle-of-attack rate dependencies," *Journal of Aircraft*, vol. 54, pp. 2367–2377, Nov. 2017. Publisher: American Institute of Aeronautics and Astronautics.

[19] J. A. Grauer, "Aerodynamic parameter estimation using reconstructed turbulence measurements," *Journal of Aircraft*, vol. 58, pp. 1022–1033, Sept. 2021. Publisher: American Institute of Aeronautics and Astronautics.

[20] J. Sun, B. Li, C.-Y. Wen, and C.-K. Chen, "Model-aided wind estimation method for a tail-sitter aircraft," *IEEE Transactions on Aerospace and Electronic Systems*, vol. 56, pp. 1262–1278, Apr. 2020. Conference Name: IEEE Transactions on Aerospace and Electronic Systems.

[21] P. Tian and H. Chao, "Model Aided Estimation of Angle of Attack, Sideslip Angle, and 3D Wind without Flow Angle Measurements," in *2018 AIAA Guidance, Naviga-*

tion, and Control Conference, AIAA SciTech Forum, p. 1844, American Institute of Aeronautics and Astronautics, Jan. 2018.

[22] M. H. Halefom, J. L. Gresham, and C. A. Woolsey, "Wind Estimation from an Unsteady Aerodynamic Aircraft Motion Model," in *AIAA SCITECH 2022 Forum*, AIAA SciTech Forum, (San Diego, CA), p. 0554, American Institute of Aeronautics and Astronautics, 2022.

[23] M. H. Halefom and C. A. Woolsey, "Modeling and identification of unsteady aerodynamic dynamics of a small fixed-wing aircraft," *In Preparation for Jounal Publication*, 2024.

[24] M. H. Halefom, J. W. Hopwood, and C. A. Woolsey, "Unsteady aerodynamics in model-based wind estimation from fixed-wing aircraft motion," *Journal of Guidance, Control, and Dynamics*, pp. 1–13, May 2024. Publisher: American Institute of Aeronautics and Astronautics.

[25] Z. Ahmed, M. H. Halefom, and C. A. Woolsey, "A tutorial overview of indirect wind estimation using small uncrewed air vehicles.," *Journal of Aerospace Information Systems (To Appear)*, 2024.

[26] M. H. Halefom, Z. Ahmed, and C. A. Woolsey, "An Experimental Comparison of Wind Estimators for a Fixed-Wing Aircraft," *In Preparation for Jounal Publication*, 2024.

[27] "System Identification Programs for AirCraft (SIDPAC)(LAR-16100-1) | NASA Software Catalog," 2016.

[28] W. J. Rugh, *Linear System Theory.* Prentice Hall, 1993.

[29] D. Gebre-Egziabher and S. Gleason, *GNSS Applications and Methods.* Artech House, 2009.

[30] B. Etkin, *Dynamics of Atmospheric Flight.* Courier Corporation, Aug. 2012.

[31] "MIL-F-8785 C flying qualitues piloted airplanes," 1969.

[32] L. Arnold, *Stochastic Differential Equations: Theory and Applications.* Dover Publications, 1974.

[33] B. Etkin and L. D. Reid, *Dynamics of Flight: Stability and Control.* John Wiley & Sons, Oct. 1995.

[34] H. Wagner, "Über die entstehung des dynamischen auftriebes von tragflügeln," *ZAMM - Journal of Applied Mathematics and Mechanics / Zeitschrift für Angewandte Mathematik und Mechanik*, vol. 5, no. 1, pp. 17–35, 1925.

[35] T. Theodorsen, "General Theory of Aerodynamic Instability and the Mechanism of Flutter," Jan. 1949. NTRS Author Affiliations: National Advisory Committee for Aeronautics. Langley Aeronautical Lab. NTRS Document ID: 19930090935 NTRS Research Center: Legacy CDMS (CDMS).

[36] R. T. Jones, "The Unsteady Lift of a Finite Wing," tech. rep., National Aeronautics and Space Administration, Jan. 1939. NTRS Author Affiliations: NTRS Report/Patent Number: NACA-TN-682 NTRS Document ID: 19930081468 NTRS Research Center: Legacy CDMS (CDMS).

[37] R. T. Jones, "The Unsteady Lift of a Wing of Finite Aspect Ratio," tech. rep., National Aeronautics and Space Administration, Jan. 1940. NTRS Author Affiliations: NTRS Report/Patent Number: NACA-TR-681 NTRS Document ID: 19930091758 NTRS Research Center: Legacy CDMS (CDMS).

[38] I. E. Garrick, "On Some Reciprocal Relations in the Theory of Nonstationary Flows,"

Jan. 1938. NTRS Author Affiliations: NTRS Report/Patent Number: NACA-TR-629 NTRS Document ID: 19930091704 NTRS Research Center: Legacy CDMS (CDMS).

[39] R. T. Jones, "Operational Treatment of the Nonuniform-lift Theory in Airplane Dynamics," Oct. 1938. NTRS Author Affiliations: NTRS Report/Patent Number: NACA-TN-667 NTRS Document ID: 19930081472 NTRS Research Center: Legacy CDMS (CDMS).

[40] M. Tobak, "On the use of the indicial-function concept in the analysis of unsteady motions of wings and wing-tail combinations," Jan. 1954. NTRS Author Affiliations: NTRS Report/Patent Number: NACA-TR-1188 NTRS Document ID: 19930091106 NTRS Research Center: Legacy CDMS (CDMS).

[41] J. G. Leishman and K. Q. Nguyen, "State-space representation of unsteady airfoil behavior," *AIAA Journal*, vol. 28, no. 5, pp. 836–844, 1990. Publisher: American Institute of Aeronautics and Astronautics _eprint: https://doi.org/10.2514/3.25127.

[42] V. Klein and K. D. Noderer, "Modeling of aircraft unsteady aerodynamic characteristics. Part 1: Postulated models," Tech. Rep. NAS 1.15:109120, National Aeronautics and Space Administration, May 1994. NTRS Author Affiliations: George Washington Univ. NTRS Document ID: 19940028445 NTRS Research Center: Legacy CDMS (CDMS).

[43] V. Klein and K. D. Noderer, "Modeling of aircraft unsteady aerodynamic characteristics. Part 2: Parameters estimated from wind tunnel data," Tech. Rep. NAS 1.15:110161, National Aeronautics and Space Administration, Apr. 1995. NTRS Author Affiliations: Joint Inst. for Advancement of Flight Sciences NTRS Document ID: 19950021418 NTRS Research Center: Legacy CDMS (CDMS).

[44] P. C. Murphy, V. Klein, and N. T. Frink, “Nonlinear unsteady aerodynamic modeling using wind-tunnel and computational data,” *Journal of Aircraft*, vol. 54, pp. 659–683, 2017.

[45] K. Gahan, J. W. Hopwood, and C. A. Woolsey, “Wind Estimation using an H∞ Filter with Fixed-Wing Aircraft Flight Test Results,” in *AIAA SCITECH 2023 Forum*, AIAA SciTech Forum, pp. 1–12, American Institute of Aeronautics and Astronautics, Jan. 2023.

[46] P. Abichandani, D. Lobo, G. Ford, D. Bucci, and M. Kam, “Wind measurement and simulation techniques in multi-rotor small unmanned aerial vehicles,” *IEEE Access*, vol. 8, pp. 54910–54927, 2020.

[47] J. H. Lee, H. E. Sevil, A. Dogan, and D. Hullender, “Estimation of maneuvering aircraft states and time-varying wind with turbulence,” *Aerospace Science and Technology*, vol. 31, pp. 87–98, Dec. 2013.

[48] A. Wenz and T. A. Johansen, “Moving horizon estimation of air data parameters for UAVs,” *IEEE Transactions on Aerospace and Electronic Systems*, vol. 56, pp. 2101–2121, June 2020. Conference Name: IEEE Transactions on Aerospace and Electronic Systems.

[49] J. C. Kaimal, J. C. Wyngaard, Y. Izumi, and O. R. Coté, “Spectral characteristics of surface-layer turbulence,” *Quarterly Journal of the Royal Meteorological Society*, vol. 98, no. 417, pp. 563–589, 1972. _eprint: https://onlinelibrary.wiley.com/doi/pdf/10.1002/qj.49709841707.

[50] J. Mann, “The spatial structure of neutral atmospheric surface-layer turbulence,” *Journal of Fluid Mechanics*, vol. 273, pp. 141–168, Aug. 1994. Publisher: Cambridge University Press.

[51] J. Berg, A. Natarajan, J. Mann, and E. G. Patton, “Gaussian vs non-gaussian turbulence: impact on wind turbine loads,” *Wind Energy*, vol. 19, no. 11, pp. 1975–1989, 2016. _eprint: https://onlinelibrary.wiley.com/doi/pdf/10.1002/we.1963.

[52] J.-P. Condomines, M. Bronz, G. Hattenberger, and J.-F. Erdelyi, “Experimental Wind Field Estimation and Aircraft Identification,” in *IMAV 2015: International Micro Air Vehicles Conference and Flight Competition*, International Micro Air Vehicles Conference and Flight Competition (IMAV), Sept. 2015.

[53] J. González-Rocha, C. A. Woolsey, C. Sultan, and S. F. J. De Wekker, “Sensing wind from quadrotor motion,” *Journal of Guidance, Control, and Dynamics*, vol. 42, pp. 836–852, Apr. 2019. Publisher: American Institute of Aeronautics and Astronautics.

[54] H. Hong, M. Wang, F. Holzapfel, and S. Tang, “Wind Estimation for Fixed-Wing Aircraft Using Command Tracking Approach,” in *2018 26th Mediterranean Conference on Control and Automation (MED)*, pp. 1–6, June 2018. ISSN: 2473-3504.

[55] H. Hong, M. Wang, F. Holzapfel, and S. Tang, “Fast real-time three-dimensional wind estimation for fixed-wing aircraft,” *Aerospace Science and Technology*, vol. 69, pp. 674–685, Oct. 2017.

[56] R. T. Palomaki, N. T. Rose, M. v. d. Bossche, T. J. Sherman, and S. F. J. D. Wekker, “Wind estimation in the lower atmosphere using multirotor aircraft,” *Journal of Atmospheric and Oceanic Technology*, vol. 34, pp. 1183–1191, May 2017. Publisher: American Meteorological Society Section: Journal of Atmospheric and Oceanic Technology.

[57] A. R. Segales, B. R. Greene, T. M. Bell, W. Doyle, J. J. Martin, E. A. Pillar-Little, and P. B. Chilson, “The coptersonde: an insight into the development of a smart unmanned

aircraft system for atmospheric boundary layer research," *Atmospheric Measurement Techniques*, vol. 13, pp. 2833–2848, May 2020. Publisher: Copernicus GmbH.

[58] P. P. Neumann and M. Bartholmai, "Real-time wind estimation on a micro unmanned aerial vehicle using its inertial measurement unit," *Sensors and Actuators A: Physical*, vol. 235, pp. 300–310, Nov. 2015.

[59] A. Shelekhov, A. Afanasiev, E. Shelekhova, A. Kobzev, A. Tel'minov, A. Molchunov, and O. Poplevina, "High-resolution profiling of atmospheric turbulence using UAV autopilot data," *Drones*, vol. 7, p. 412, July 2023. Number: 7 Publisher: Multidisciplinary Digital Publishing Institute.

[60] J. Gonzalez-Rocha, C. A. Woolsey, C. Sultan, S. de Wekker, and N. Rose, "Measuring Atmospheric Winds from Quadrotor Motion," in *AIAA Atmospheric Flight Mechanics Conference*, AIAA SciTech Forum, p. 1189, American Institute of Aeronautics and Astronautics, Jan. 2017.

[61] J. González-Rocha, S. F. J. De Wekker, S. D. Ross, and C. A. Woolsey, "Wind profiling in the lower atmosphere from wind-induced perturbations to multirotor UAS," *Sensors*, vol. 20, p. 1341, Jan. 2020. Number: 5 Publisher: Multidisciplinary Digital Publishing Institute.

[62] G. Hattenberger, M. Bronz, and J.-P. Condomines, "Estimating wind using a quadrotor," *International Journal of Micro Air Vehicles*, vol. 14, p. 17568293211070824, Jan. 2022. Publisher: SAGE Publications Ltd STM.

[63] X. Xiang, Z. Wang, Z. Mo, G. Chen, K. Pham, and E. Blasch, "Wind Field Estimation through Autonomous Quadcopter Avionics," in *2016 IEEE/AIAA 35th Digital Avionics Systems Conference (DASC)*, pp. 1–6, Sept. 2016. ISSN: 2155-7209.

[64] J. Petrich and K. Subbarao, “On-Board Wind Speed Estimation for UAVs,” in *AIAA Guidance, Navigation, and Control Conference*, Guidance, Navigation, and Control and Co-located Conferences, p. 6223, American Institute of Aeronautics and Astronautics, Aug. 2011.

[65] A. J. Torgesen, J. P. How, and B. Cameron, “Airborne Sensing for Ship Air Wake Surveys with a Tethered Autonomous UAV,” in *AIAA Scitech 2021 Forum*, AIAA SciTech Forum, p. 0381, American Institute of Aeronautics and Astronautics, Jan. 2021.

[66] H. Chen, H. Bai, and C. N. Taylor, “Invariant-EKF design for Quadcopter Wind Estimation,” in *2022 American Control Conference (ACC)*, pp. 1236–1241, June 2022. ISSN: 2378-5861.

[67] V. S R Pappu, Y. Liu, J. Horn, and J. Cooper, “Wind Gust Estimation on a Small VTOL UAV,” in *Proceedings of the 7th AHS Technical Meeting on VTOL Unmanned Aircraft Systems and Autonomy*, pp. 24–26, American Helicopter Society, Jan. 2017.

[68] M. B. Rhudy, Y. Gu, and H. Chao, “Wind Field Velocity and Acceleration Estimation Using a Small UAV,” in *AIAA Modeling and Simulation Technologies Conference*, AIAA AVIATION Forum, p. 2647, American Institute of Aeronautics and Astronautics, June 2014.

[69] M. B. Rhudy, J. N. Gross, and Y. Gu, “Stochastic Wind Modeling and Estimation for Unmanned Aircraft Systems,” in *AIAA Aviation 2019 Forum*, AIAA AVIATION Forum, p. 3111, American Institute of Aeronautics and Astronautics, June 2019.

[70] J. Cooper, M. DeVore, J. Hopwood, C. Woolsey, and S. D. Wekker, “Intelligent Wind Estimation for Chemical Source Localization,” in *Vertical Flight Society Annual Forum & Technology Display - Forum 79*, pp. 1–20, The Vertical Flight Society, 2023.

[71] J. Velasco-Carrau, S. García-Nieto, J. V. Salcedo, and R. H. Bishop, "Multi-objective optimization for wind estimation and aircraft model identification," *Journal of Guidance, Control, and Dynamics*, vol. 39, pp. 372–389, Feb. 2016. Publisher: American Institute of Aeronautics and Astronautics.

[72] A. Asignacion, S. Suzuki, R. Noda, T. Nakata, and H. Liu, "Frequency-based wind gust estimation for quadrotors using a nonlinear disturbance observer," *IEEE Robotics and Automation Letters*, vol. 7, pp. 9224–9231, Oct. 2022. Conference Name: IEEE Robotics and Automation Letters.

[73] S. I. Azid, K. Kumar, M. Cirrincione, and A. Fagiolini, "Wind gust estimation for precise quasi-hovering control of quadrotor aircraft," *Control Engineering Practice*, vol. 116, p. 104930, Nov. 2021.

[74] J. W. Langelaan, N. Alley, and J. Neidhoefer, "Wind field estimation for small unmanned aerial vehicles," *Journal of Guidance, Control, and Dynamics*, vol. 34, pp. 1016–1030, July 2011. Publisher: American Institute of Aeronautics and Astronautics.

[75] M. Marinescu, A. Olivares, E. Staffetti, and J. Sun, "On the estimation of vector wind profiles using aircraft-derived data and gaussian process regression," *Aerospace*, vol. 9, p. 377, July 2022. Number: 7 Publisher: Multidisciplinary Digital Publishing Institute.

[76] G. Perozzi, D. Efimov, J.-M. Biannic, and L. Planckaert, "Using a quadrotor as wind sensor: time-varying parameter estimation algorithms," *International Journal of Control*, vol. 95, pp. 126–137, Jan. 2022. Publisher: Taylor & Francis _eprint: https://doi.org/10.1080/00207179.2020.1780324.

[77] A. Kumar and P. Ben-Tzvi, "Estimation of wind conditions utilizing RC helicopter

dynamics," *IEEE/ASME Transactions on Mechatronics*, vol. 24, pp. 2293–2303, Oct. 2019. Conference Name: IEEE/ASME Transactions on Mechatronics.

[78] G. Balmer, T. Muskardin, S. Wlach, and K. Kondak, "Enhancing Model-Free Wind Estimation for Fixed-Wing UAV," in *2018 International Conference on Unmanned Aircraft Systems (ICUAS)*, pp. 1242–1247, June 2018. ISSN: 2575-7296.

[79] A. Cho, J. Kim, S. Lee, and C. Kee, "Wind estimation and airspeed calibration using a UAV with a single-antenna GPS receiver and pitot-tube," *IEEE Transactions on Aerospace and Electronic Systems*, vol. 47, pp. 109–117, Jan. 2011. Conference Name: IEEE Transactions on Aerospace and Electronic Systems.

[80] A. Rautenberg, M. S. Graf, N. Wildmann, A. Platis, and J. Bange, "Reviewing Wind Measurement Approaches for Fixed-Wing Unmanned Aircraft," *Atmosphere*, vol. 9, p. 422, Nov. 2018. Number: 11 Publisher: Multidisciplinary Digital Publishing Institute.

[81] B. M. Witte, R. F. Singler, and S. C. C. Bailey, "Development of an unmanned aerial vehicle for the measurement of turbulence in the atmospheric boundary layer," *Atmosphere*, vol. 8, p. 195, Oct. 2017. Number: 10 Publisher: Multidisciplinary Digital Publishing Institute.

[82] Q. Zhang, Y. Xu, X. Wang, Z. Yu, and T. Deng, "Real-time wind field estimation and pitot tube calibration using an extended Kalman filter," *Mathematics*, vol. 9, p. 646, Jan. 2021. Number: 6 Publisher: Multidisciplinary Digital Publishing Institute.

[83] M. B. Rhudy, Y. Gu, J. N. Gross, and H. Chao, "Onboard Wind Velocity Estimation Comparison for Unmanned Aircraft Systems," *IEEE Transactions on Aerospace and Electronic Systems*, vol. 53, pp. 55–66, Feb. 2017. Conference Name: IEEE Transactions on Aerospace and Electronic Systems.

[84] A. Wenz, T. A. Johansen, and A. Cristofaro, “Combining Model-free and Model-based Angle of Attack Estimation for Small Fixed-wing UAVs using a Standard Sensor Suite,” in *2016 International Conference on Unmanned Aircraft Systems (ICUAS)*, pp. 624–632, June 2016.

[85] K. T. Borup, T. I. Fossen, and T. A. Johansen, “A nonlinear model-based wind velocity observer for unmanned aerial vehicles,” *IFAC-PapersOnLine*, vol. 49, pp. 276–283, Jan. 2016.

[86] S. Benders, A. Wenz, and T. A. Johansen, “Adaptive Path Planning for Unmanned Aircraft Using In-flight Wind Velocity Estimation,” in *2018 International Conference on Unmanned Aircraft Systems (ICUAS)*, pp. 483–492, June 2018.

[87] “Kentland experimental aerial systems (KEAS) laboratory.”

[88] “0.7m subsonic open jet wind tunnel.”

[89] M. P. Miller, “An accurate method of measuring the moments of inertia of airplanes,” Oct. 1930. NTRS Author Affiliations: NTRS Report/Patent Number: NACA-TN-351 NTRS Document ID: 19930081105 NTRS Research Center: Legacy CDMS (CDMS).

[90] J. L. Gresham, *Aerodynamic Modeling in Nonlinear Regions, including Stall Spins, for Fixed-Wing Unmanned Aircraft from Experimental Flight Data.* PhD thesis, Virginia Polytechnic Institute and State University, June 2022. Accepted: 2022-06-29T08:00:28Z Artwork Medium: ETD Interview Medium: ETD Publisher: Virginia Tech.

[91] J. A. Grauer and E. A. Morelli, “Generic global aerodynamic model for aircraft,” *Journal of Aircraft*, vol. 52, pp. 13–20, Jan. 2015. Publisher: American Institute of Aeronautics and Astronautics.

[92] B. M. Simmons, *Advances in Aero-Propulsive Modeling for Fixed-Wing and eVTOL Aircraft Using Experimental Data.* PhD thesis, Virginia Polytechnic Institute and State University, July 2023. Accepted: 2023-07-10T08:00:24Z Artwork Medium: ETD Interview Medium: ETD Publisher: Virginia Tech.

[93] E. A. Morelli, "Determining aircraft moments of inertia from flight test data," *Journal of Guidance, Control, and Dynamics*, vol. 45, pp. 4–14, Jan. 2022. Publisher: American Institute of Aeronautics and Astronautics.

[94] J. B. Brandt, R. W. Deters, G. K. Ananda, O. D. Dantsker, and M. S. Selig, "UIUC Propeller Data Site," 2022.

[95] P. Tian, H. Chao, M. Rhudy, J. Gross, and H. Wu, "Wind sensing and estimation using small fixed-wing unmanned aerial vehicles: a survey," *Journal of Aerospace Information Systems*, vol. 18, pp. 132–143, Mar. 2021. Publisher: American Institute of Aeronautics and Astronautics.

[96] I. de Boisblanc, N. Dodbele, L. Kussmann, R. Mukherji, D. Chestnut, S. Phelps, G. C. Lewin, and S. de Wekker, "Designing a hexacopter for the collection of atmospheric flow data," in *2014 Systems and Information Engineering Design Symposium (SIEDS)*, pp. 147–152, Apr. 2014.

[97] J. Gonzalez-Rocha, *Sensing Atmospheric Winds from Quadrotor Motion.* PhD thesis, Virginia Polytechnic Institute and State University, June 2020. Accepted: 2020-06-02T08:00:50Z Artwork Medium: ETD Interview Medium: ETD Publisher: Virginia Tech.

[98] M. B. Rhudy, T. Larrabee, H. Chao, Y. Gu, and M. Napolitano, "UAV Attitude, Heading, and Wind Estimation Using GPS/INS and an Air Data System," in *AIAA*

Guidance, Navigation, and Control (GNC) Conference, Guidance, Navigation, and Control and Co-located Conferences, pp. 1–11, American Institute of Aeronautics and Astronautics, Aug. 2013.

[99] J. A. Grauer, "Position Corrections for Airspeed and Flow Angle Measurements on Fixed-Wing Aircraft," Tech. Rep. L-20882, NASA Langley Research Center, Nov. 2017. NTRS Author Affiliations: NASA Langley Research Center NTRS Document ID: 20180000023 NTRS Research Center: Langley Research Center (LaRC).

[100] L. Rodriguez Salazar, J. A. Cobano, and A. Ollero, "Small UAS-based wind feature identification system part 1: integration and validation," *Sensors*, vol. 17, p. 8, Jan. 2017. Number: 1 Publisher: Multidisciplinary Digital Publishing Institute.

[101] J. W. Hopwood and C. A. Woolsey, "Passivity-Based Wind Estimation for Aircraft Maneuvering in Steady and Uniform Wind Fields," in *AIAA SCITECH 2024 Forum*, AIAA SciTech Forum, pp. 1–27, American Institute of Aeronautics and Astronautics, Jan. 2024.

[102] Z. Ahmed and C. A. Woolsey, "The Invariant Extended Kalman Filter for Wind Estimation using a Small Fixed-Wing UAV in Horizontal-Plane Flight," in *AIAA SCITECH 2024 Forum*, AIAA SciTech Forum, pp. 1–14, American Institute of Aeronautics and Astronautics, Jan. 2024.

[103] H. G. McClelland and C. A. Woolsey, "Effects of two modeling assumptions on wind reconstruction from longitudinal aircraft motion," *Journal of Guidance, Control, and Dynamics*, vol. 43, no. 6, pp. 1069–1081, 2020.

[104] J. Katz and A. Plotkin, *Low-Speed Aerodynamics.* Cambridge Aerospace Series, Cambridge: Cambridge University Press, 2 ed., 2001.

[105] J. L. Gresham, B. M. Simmons, J.-M. W. Fahmi, and C. A. Woolsey, “Remote Uncorrelated Pilot Inputs for Nonlinear Aerodynamic Model Identification from Flight Data,” in *AIAA AVIATION 2021 FORUM*, AIAA AVIATION Forum, p. 2792, American Institute of Aeronautics and Astronautics, July 2021.

[106] J. L. Gresham, J.-M. W. Fahmi, B. M. Simmons, J. W. Hopwood, W. Foster, and C. A. Woolsey, “Flight Test Approach for Modeling and Control Law Validation for Unmanned Aircraft,” in *AIAA SCITECH 2022 Forum*, AIAA SciTech Forum, p. 2406, American Institute of Aeronautics and Astronautics, Jan. 2022.

[107] B. M. Simmons, J. L. Gresham, and C. A. Woolsey, “Aero-propulsive modeling for propeller aircraft using flight data,” *Journal of Aircraft*, vol. 60, pp. 81–96, Jan. 2023. Publisher: American Institute of Aeronautics and Astronautics.

[108] L. Ljung, “System Identification Toolbox,” 1988.

[109] U. Saxena, M. R. Dorothy, and I. A. Faruque, “Gramian-aware control approach for atmospheric gust harvesting,” *Journal of Aerospace Information Systems*, vol. 19, no. 1, pp. 53–61, 2022. Publisher: American Institute of Aeronautics and Astronautics _eprint: https://doi.org/10.2514/1.I010951.

[110] X. Xu, A. Gementzopoulos, G. Sedky, A. R. Jones, and F. D. Lagor, “Iterative maneuver optimization in a transverse gust encounter,” *AIAA Journal*, vol. 61, pp. 2083–2099, May 2023. Publisher: American Institute of Aeronautics and Astronautics.